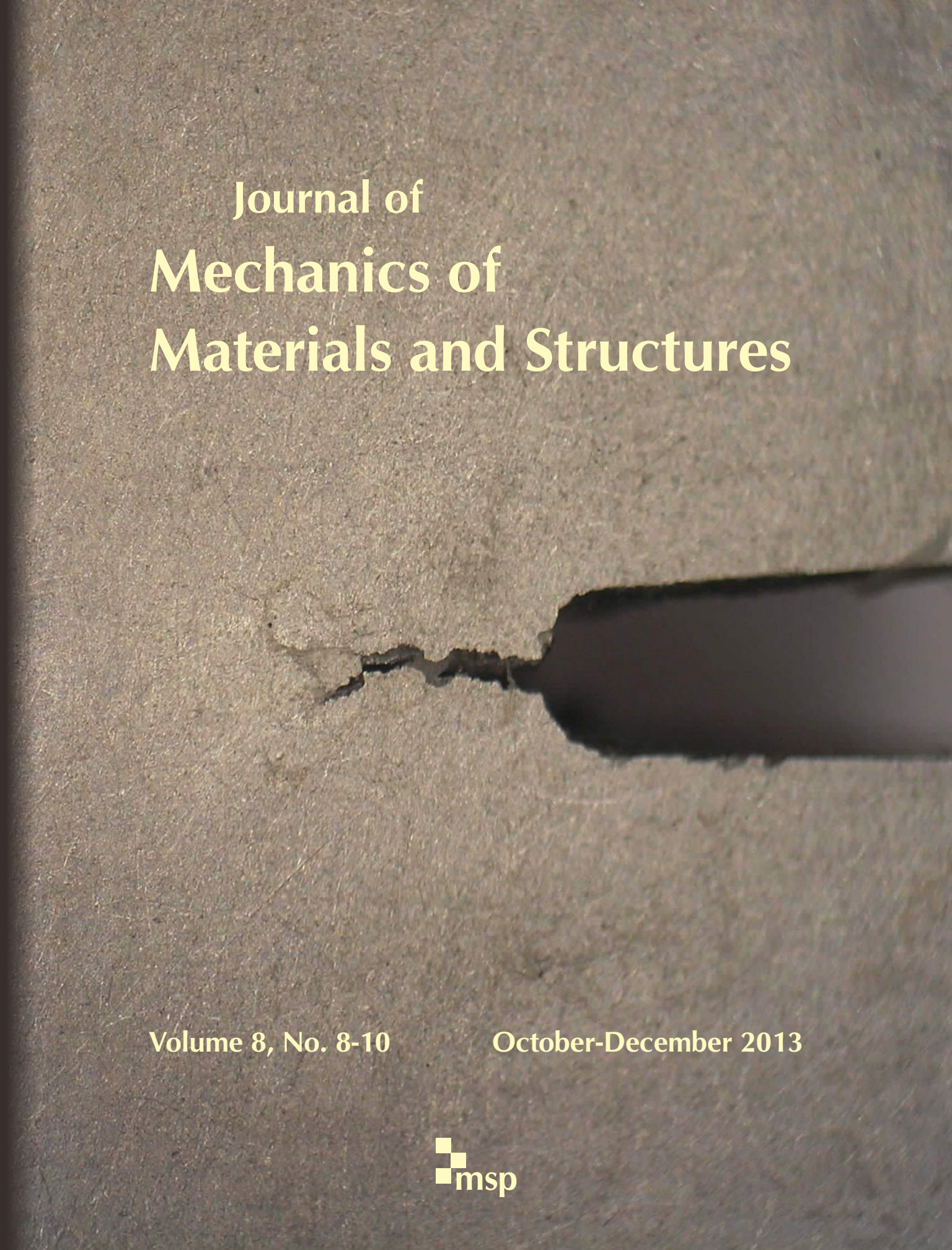

Journal of Mechanics of Materials and Structures

Volume 8, No. 8-10 October-December 2013

msp

JOURNAL OF MECHANICS OF MATERIALS AND STRUCTURES

msp.org/jomms

Founded by Charles R. Steele and Marie-Louise Steele

See msp.org/jomms for submission guidelines.

JoMMS (ISSN 1559-3959) at Mathematical Sciences Publishers, 798 Evans Hall #6840, c/o University of California, Berkeley, CA 94720-3840, is published in 10 issues a year. The subscription price for 2013 is US $555/year for the electronic version, and $705/year (+$60, if shipping outside the US) for print and electronic. Subscriptions, requests for back issues, and changes of address should be sent to MSP.

JoMMS peer-review and production is managed by EditFLOW® from Mathematical Sciences Publishers.

PUBLISHED BY

mathematical sciences publishers

nonprofit scientific publishing

http://msp.org/

JOURNAL OF MECHANICS OF MATERIALS AND STRUCTURES
Vol. 8, No. 8-10, 2013
dx.doi.org/10.2140/jomms.2013.8.385

msp

ANALYSIS OF PULL-IN INSTABILITY OF ELECTROSTATICALLY ACTUATED CARBON NANOTUBES USING THE HOMOTOPY PERTURBATION METHOD

MIR MASOUD SEYYED FAKHRABADI, ABBAS RASTGOO AND MOHAMMAD TAGHI AHMADIAN

This paper analyzes the deflection and pull-in behaviors of cantilever and doubly clamped carbon nanotubes (CNTs) under electrostatic actuation using the homotopy perturbation method. The effects of electrostatic force and interatomic interactions on the deflection and pull-in instabilities of CNTs with different lengths, diameters, and boundary conditions are investigated in detail. The results reveal that larger diameters and shorter lengths result in higher pull-in voltages. Moreover, CNTs with doubly clamped boundary conditions, in comparison with cantilever boundary conditions, are more resistant to pull-in.

1. Introduction

Research into micro- and nanoelectromechanical systems (MEMS/NEMS) has experienced tremendous growth in recent years. The main motivations for scientists to conduct research in these fields are their combined electrical and mechanical properties, which result in simpler structures in electrical systems. This can be utilized in different electronic circuits, communication devices, and in aerospace applications such as sensors, actuators, resonators, capacitors, switches, etc. [Mojahedi et al. 2011; Kahrobaiyan et al. 2011; Darvishian et al. 2012; Moeenfard and Ahmadian 2012; Moeenfard et al. 2012; Rahaeifard et al. 2012]. MEMS and NEMS are, in general, mechanical devices such as micro/nanobeams, shells, plates, or other similar structures sensed or actuated electrically. Electrothermal, piezoelectric, and electrostatic systems are the most common types of actuation systems applied in the field of MEMS and NEMS [Ansola et al. 2012; Tayyaba et al. 2012; Zand 2012]. However, in nanoscale applications, electrostatic actuation is more frequently used and applicable.

Krylov et al. [2005] showed that parametric actuation of microstructure has stabilizing effects. They proposed that using this technique would result in higher pull-in voltages. They utilized the Hill and Mathieu equations to analyze the parametric actuation of these structures and verified the outcomes with experimental data. In the system considered in their article, a microbeam was attached to the ground plate while embedded between two positive electrodes. The electrical potential difference between the microbeam and electrodes causes it to deflect towards the fixed electrode with higher voltage. In another study, Zhang and Zhao [2006] studied the pull-in behaviors of microstructures under electrostatic actuation using numerical and analytical techniques. They applied a one-DOF model of the microbeams and analyzed the governing equations via Taylor expansion.

Seyyed Fakhrabadi is the corresponding author.
Keywords: carbon nanotubes, pull-in phenomenon, nanoelectromechanical systems, homotopy perturbation method.

Batra et al. [2008] applied a reduced-order method to study the behaviors of rectangular and circular microplates in the presence of electrostatic actuation and Casimir effects. They used the nonlinear von Karman model to formulate the governing equations and presented the pull-in voltages for microstructures with different dimensions. Pirbodaghi et al. [2009] and Mojahedi et al. [2010] studied the static and dynamic behaviors of microbeams using the homotopy perturbation method. In the static case, the behaviors of the microbeams under electrostatic actuation were analyzed and pull-in voltages for different parameters were reported [Pirbodaghi et al. 2009]. For the dynamic case, the natural frequencies of microbeams under two cantilever and doubly clamped boundary conditions were extracted [Mojahedi et al. 2010].

Rezazadeh et al. [2011] studied the static and dynamic behaviors of microbeams using a one-DOF model and presented some equations to obtain the static and dynamic pull-in voltages. These relations could be used to estimate pull-in voltages without requiring solving the governing partial differential equations. Moghimi Zand et al. [2009] investigated the behaviors of microbeams under suddenly applied voltages and analyzed the effects of increments in voltages, residual stresses, and fringing fields using the homotopy perturbation method. Jia et al. [2011] studied the behaviors of microbeams in the presence of electrostatic actuation and Casimir forces considering geometrically nonlinear vibration on the pull-in phenomena.

The papers above show the depth of interest in MEMS; we now mention a few studies of NEMS. Technological progress has gone hand in hand with a decrease in the size of electrical devices embedded in electrical appliances such as cell phones, cameras, micro- and nanorobots, etc. Hence nanosystems have also been the object of intense attention. Nanobeams and nanotubes are the first choices one may consider in NEMS applications.

Ramezani et al. [2008a] studied the effects of Casimir forces on the electrostatic behaviors of nanobeams. They applied a Green's function to transform the nonlinear governing equation to an integrodifferential equation and considered an appropriate shape function to obtain an analytic relation for the deflection of nanobeams actuated electrostatically. They also investigated in [Ramezani et al. 2008b] the effects of van der Waals (vdW) force on the properties mentioned.

Abadyan et al. [2010] applied the homotopy perturbation method to investigate the effects of Casimir force on the pull-in instability of cantilever nanobeams. They studied the static pull-in of nanobeams using this method and compared the results with those reported in the literature. Soroush et al. [2010] studied the effects of Casimir and vdW forces on the pull-in instability of cantilevered nanobeams. They applied the Adomian decomposition method to obtain an analytical solution based on the distributed parameter model. In addition, Koochi et al. [2012] investigated the influence of surface effects including residual surface stress and surface elasticity on the size-dependent instability of nanobeams in the presence of Casimir forces using the Adomian decomposition technique.

There are fewer papers on electrostatically actuated nanobeams than there are for microbeams. However, electrostatic actuation of carbon nanotubes (CNTs), even in comparison with nanobeams, has not been investigated comprehensively and obviously deserves more attention.

Dequesnes et al. [2002] may be the first researchers to study the static pull-in behaviors of CNTs under electrostatic actuation and vdW force. They applied a one-DOF model in their research, which was a simplification and might have some deviation from the real systems. Ke and Espinosa [2005; 2005] presented two papers regarding CNT-based NEMS. The first focused on the quality of charge distribution, and the second was about stretching effects on doubly clamped CNTs. In addition, Ouakad and Younis

[2010] studied the nonlinear dynamic behaviors of CNTs under electrostatic actuation and presented the frequency response of these systems given different applied voltages.

In this paper, we study static and dynamic behaviors as well as pull-in instability of CNTs with different geometries and boundary conditions under electrostatic actuation. The governing equations, as presented in the following section, are nonlinear and may not be solved analytically by the typical approaches. Hence, either numerical or some special analytic or semianalytic techniques should be applied to analyze these phenomena in CNTs. He's homotopy perturbation method is applied in this paper. This technique has some advantages over other common methods, such as fast and safe convergence. Moreover, it doesn't need to discretize the space and time domains, unlike many other numerical techniques. Two other advantages are that less computational cost is needed, and solving nonlinear discrete systems of differential equations is not required.

2. Definition of the problem

This section defines the system under consideration and formulates governing equations. It also covers the description of the homotopy perturbation method that is to be applied to solve the resultant equations.

As shown in Figure 1, suppose that a CNT is suspended over some graphene sheets with an initial gap of G_0 (state 1 in Figure 1). With the CNT as the positive electrode and the graphene sheets as the negative electrode (ground plate), an electrical potential difference (V) is applied. The charge distributions over the electrodes create an attractive force between the positive and negative electrodes. This force along with the interatomic force between the electrodes leads to a deflection of the CNT towards the ground plate (state 2 in Figure 1). The deflection value ($w = w(x)$ in Figure 1) corresponds to the applied voltage up to where the elastic force of the CNT cannot tolerate the attractive force resulting from the applied voltage and the interatomic forces. Hence, it then drops suddenly on the ground plate. This phenomenon is called pull-in instability and the corresponding voltage is the pull-in voltage. Pull-in instability usually occurs at a deflection of about one third to one half of the gap distance.

In the following, formulation of the static and dynamic behaviors and pull-in instabilities of CNTs are conducted. The governing equations and solution methods of each item are presented.

2.1. ***Static pull-in.*** The deflation of a doubly clamped CNT actuated using a step DC voltage can be obtained from

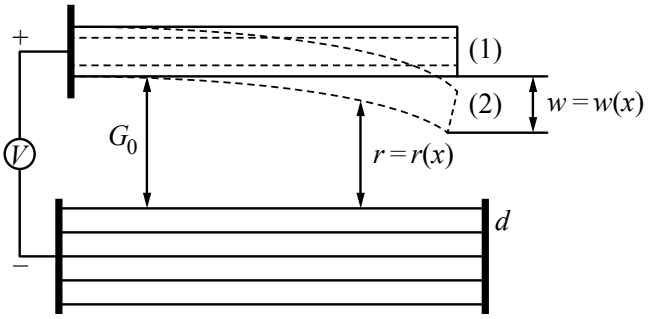

Figure 1. Deflection of a CNT under electrostatic actuation.

$$EI\frac{d^4w}{dx^4}-\left(\frac{EA}{2L}\int_0^L\left(\frac{dw}{dx}\right)^2dx\right)\frac{d^2w}{dx^2}=q_{\text{elec}}+q_{\text{vdW}}, \tag{1}$$

where, in the left-hand side of the equation, E is the elastic modulus, I is the moment of inertia, w is the deflection, x is the axial coordinate, A is the cross sectional area, and L is the length of the CNT. The right-hand side of the equation includes q_{elec} and q_{vdW}, which are the distributed forces applied by the electrostatic voltage and vdW interatomic effects, respectively.

The boundary conditions corresponding to the cantilever and doubly clamped CNTs are presented in (2) and (3). The second term in the left-hand side of (1) is due to midplane stretching and equals zero for the cantilevered CNTs:

$$\frac{\partial w(0,t)}{\partial x}=w(0,t)=\frac{\partial w(L,t)}{\partial x}=w(L,t)=0, \tag{2}$$

$$\frac{\partial w(0,t)}{\partial x}=w(0,t)=\frac{\partial^2 w(L,t)}{\partial x^2}=\frac{\partial^3 w(L,t)}{\partial x^3}=0. \tag{3}$$

The maximum deflections of the cantilever and doubly clamped CNTs are, respectively, at the tip and longitudinal center. Thus, the critical points to study the deflection of CNTs under the boundary conditions mentioned are these points.

The electrostatic force is formulated as [Dequesnes et al. 2002]

$$q_{\text{elec}}cl=\frac{\pi\epsilon_0V^2}{\sqrt{(G_0-w)(G_0-w+2R)}\operatorname{arccosh}^2(1+(G_0-w)/R)}, \tag{4}$$

where ϵ_0 is the electrical permittivity, V the voltage, R the radius of the CNT, and G_0 the initial gap.

The vdW force of the system can be formulated as [Dequesnes et al. 2002]

$$q_{\text{vdW}}=\frac{\pi^2c_6\sigma^2}{2}\sum_{n=1}^{N_G}\frac{R\begin{pmatrix}8(G_0+(n-1)d-w)^4+32(G_0+(n-1)d-w)^3R\\+72(G_0+(n-1)d-w)^2R^2+80(G_0+(n-1)d-w)R^3+35R^4\end{pmatrix}}{(G_0+(n-1)d-w)^{9/2}(G_0+(n-1)d-w+2R)^{9/2}}, \tag{5}$$

where c_6 and σ^2 are Lennard-Jones potential parameters describing the vdW force and N_G represents the number of graphene sheets.

In order to solve the governing equations of the deflection of the CNTs under electrostatic actuation, it is better to normalize the equations by considering the following nondimensional parameters:

$$\bar{w}=\frac{w}{G_0},\quad \bar{x}=\frac{x}{L},\quad \bar{R}=\frac{R}{G_0},\quad \bar{d}=\frac{d}{G_0}. \tag{6}$$

Replacing the above parameters into the terms of (1) and (5), we have

$$\frac{\partial^4\bar{w}}{\partial\bar{x}^4}-\alpha_1\frac{\partial^2\bar{w}}{\partial\bar{x}^2}+\beta_1\frac{\partial^2\bar{w}}{\partial\bar{t}^2}+\gamma_1\frac{\partial\bar{w}}{\partial\bar{t}}=\bar{q}_{\text{elec}}(\bar{w})+\bar{q}_{\text{vdW}}(\bar{w}), \tag{7}$$

where

$$\alpha_1=\left[\left(\alpha\int_0^1\left(\frac{d\bar{w}}{d\bar{x}}\right)^2d\bar{x}\right)\right];$$

here $\alpha=AG_0^2/(2I)$ for doubly clamped boundary conditions, $\alpha=0$ for cantilever boundary conditions,

and

$$\begin{aligned}
\beta_1 &= m_c \frac{L^4}{EIt^{*2}}, \quad \gamma_1 = \frac{cL^4}{EIt^*}, \quad \beta = \frac{\pi\epsilon_0 L^4}{EIG_0^2}, \\
\bar{q}_{\text{elec}}(\bar{w}) &= \frac{\beta V^2}{\sqrt{(1-\bar{w})(1-\bar{w}+2\bar{R})}\operatorname{arccosh}^2(1+(1-\bar{w})/\bar{R})}, \quad \gamma = \frac{\pi^2 c_6 \sigma^2 L^4}{2EIG_0^5}, \\
\bar{q}_{\text{vdW}}(\bar{w}) &= \gamma \sum_{n=1}^{N_G} \frac{\bar{R}\left(\begin{array}{l} 8(1+(n-1)\bar{d}-\bar{w})^4 + 32(1+(n-1)\bar{d}-\bar{w})^3\bar{R} \\ \quad + 72(1+(n-1)\bar{d}-\bar{w})^2\bar{R}^2 + 80(1+(n-1)\bar{d}-\bar{w})\bar{R}^3 + 35\bar{R}^4 \end{array}\right)}{(1+(n-1)\bar{d}-\bar{w})^{9/2}(1+(n-1)\bar{d}-\bar{w}+2\bar{R})^{9/2}}.
\end{aligned} \tag{8}$$

Expansion theory is applied at this stage to solve the governing equations. Suppose that deflection can be formulated as

$$\bar{w} = \sum_{i=1}^{n} a_i \phi_i(x), \tag{9}$$

where a_i are the coefficients and $\phi_i(x)$ are the shape modes. The shape modes corresponding to the cantilever and doubly clamped boundary conditions are presented in (10) and (11), respectively [Mojahedi et al. 2010]:

$$\phi(x) = \cosh\mu\bar{x} - \cos\mu\bar{x} - \frac{\cosh\mu + \cos\mu}{\sinh\mu + \sin\mu}(\sinh\mu\bar{x} - \sin\mu\bar{x}), \quad \mu_{1\text{st}} = 1.875, \tag{10}$$

$$\phi(x) = \cosh\lambda\bar{x} - \cos\lambda\bar{x} - \frac{\cosh\lambda - \cos\lambda}{\sinh\lambda - \sin\lambda}(\sinh\lambda\bar{x} - \sin\lambda\bar{x}), \qquad \lambda_{1\text{st}} = 4.73. \tag{11}$$

For static deflection of the CNT, the first mode is enough. Hence, (9) can be written as

$$\bar{w} = a\phi(\bar{x}). \tag{12}$$

By substituting (12) into (7), we have

$$a\frac{d^4\phi(\bar{x})}{d\bar{x}^4} - \alpha a^3 \phi''(\bar{x}) \int_0^1 \phi'(\bar{x})^2\, d\bar{x} = \bar{q}_{\text{elec}}(a\phi(\bar{x})) + \bar{q}_{\text{vdW}}(a\phi(\bar{x})). \tag{13}$$

The Galerkin method is applied to (13) to solve it. By multiplying all of the terms by $\phi(\bar{x})$ and integrating over the domain, we can write

$$k_1 a + k_2 a^3 - \int_0^1 \bar{q}_{\text{elec}}(a\phi(\bar{x}))\phi(\bar{x})\, d\bar{x} - \int_0^1 \bar{q}_{\text{vdW}}(a\phi(\bar{x}))\phi(\bar{x})\, d\bar{x} = 0, \tag{14}$$

where

$$k_{1s} = \int_0^1 \left(\frac{d^2\phi(\bar{x})}{d\bar{x}^2}\right)^2 d\bar{x}, \quad k_{2s} = \alpha\left(\int_0^1 \phi'(\bar{x})^2\, d\bar{x}\right)^2. \tag{15}$$

Equation (14) is the final governing formula for analyzing the static deflection of the CNT under electrostatic actuation. It should be solved to obtain the deflection of the CNT under different applied voltages as well as the pull-in voltage.

2.1.1. *The homotopy perturbation method for solving static deflection.* Here we are going to solve a nonlinear differential equation with the boundary conditions given as [Mojahedi et al. 2010]

$$A(u) - f(r) = 0, \quad r \in \Omega, \tag{16a}$$

$$B\left(u, \frac{\partial u}{\partial n}\right) = 0, \quad r \in \Gamma, \tag{16b}$$

where A denotes a general nonlinear operator, u an unknown function, $f(r)$ a given function of the variable r, Ω the problem domain, B a given function for the boundaries, n a given direction, and Γ the domain boundaries. The general nonlinear operator may be divided into linear, $L(u)$, and nonlinear, $N(u)$, parts. The main relation of the homotopy perturbation technique is

$$H(a, p) = L(a) - L(\bar{a}) + p(N(a) + L(\bar{a})) = 0, \tag{17}$$

where $\bar{a}$ is the initial guess satisfying the boundary conditions and a denotes the solution of the problem, which can be considered as

$$a = a_0 + pa_1 + p^2a_2 + p^3a_3 + p^4a_4 + p^5a_5 + \cdots. \tag{18}$$

Also, $p \in [0, 1]$ is an embedding parameter. A p value of zero causes a to correspond to the initial guess and a p value of one causes a to converge to the solution of the problem. In addition, $N(a)$ can be expanded in Taylor series as [Mojahedi et al. 2010]

$$\begin{aligned} N(a) = N(a_0) &+ N'(a_0)(pa_1 + p^2a_2 + p^3a_3 + p^4a_4 + p^5a_5) \\ &+ \frac{N''(a_0)}{2!}(pa_1 + p^2a_2 + p^3a_3 + p^4a_4 + p^5a_5)^2 \\ &+ \frac{N'''(a_0)}{3!}(pa_1 + p^2a_2 + p^3a_3 + p^4a_4 + p^5a_5)^3 \\ &+ \frac{N^{(4)}(a_0)}{4!}(pa_1 + p^2a_2 + p^3a_3 + p^4a_4 + p^5a_5)^4. \end{aligned} \tag{19}$$

Substituting (19) in (17), the coefficients of p^i, $i = 1, \ldots, 5$ are obtained as

$$\begin{aligned} &p^0 : L(a_0) - L(\bar{a}) = 0, \\ &p^1 : L(a_1) + N(a_0) + L(\bar{a}) = 0, \\ &p^2 : L(a_2) + a_1N'(a_0) = 0, \\ &p^3 : L(a_3) + a_2N'(a_0) + a_1\frac{N''(a_0)}{2!} = 0, \\ &p^4 : L(a_4) + a_3N'(a_0) + \frac{2a_1a_2}{2!}N''(a_0) + \frac{a_1^3}{3!}N'''(a_0) = 0, \\ &p^5 : L(a_5) + a_4N'(a_0) + \frac{2a_1a_3 + a_2^2}{2!}N''(a_0) + \frac{3a_1^2a_2}{3!}N'''(a_0) + \frac{a_1^4}{4!}N^{(4)}(a_0) = 0. \end{aligned} \tag{20}$$

For the current problem, according to (14), the linear and nonlinear parts are selected as

$$L(a) = k_{1s}a, \tag{21a}$$

$$N(a) = k_{2s}a^3 - \int_0^1 \bar{q}_{\text{elec}}(a\phi(\bar{x}))\phi(\bar{x})\,d\bar{x} - \int_0^1 \bar{q}_{\text{vdW}}(a\phi(\bar{x}))\phi(\bar{x})\,d\bar{x}. \tag{21b}$$

The above equations should be solved using the described technique in order to obtain the deflection and pull-in voltages of CNTs actuated electrostatically.

2.2. ***Dynamic pull-in.*** The deflation of the doubly clamped CNT applied a step DC voltage can be obtained from

$$EI\frac{\partial^4 w}{\partial x^4} - \left(\frac{EA}{2L}\int_0^L \left(\frac{\partial w}{\partial x}\right)^2 dx\right)\frac{\partial^2 w}{\partial x^2} + m\frac{\partial^2 w}{\partial t^2} = q_{\text{elec}} + q_{\text{vdW}}, \tag{22}$$

where m and t are, respectively, the mass of the CNT per length and time. Similarly to the static case, the second term equals zero for the cantilevered CNTs. The other variables were all introduced before. The first step in solving the above equation is nondimensionalization. The nondimensional parameters introduced in (6) and $\bar{t} = t/\sqrt{mL^4/EI}$ are applied for this purpose. The nondimensional form of (22) is obtained as

$$\frac{\partial^4 \bar{w}}{\partial \bar{x}^4} - \left(\alpha\int_0^1 \left(\frac{\partial \bar{w}}{\partial \bar{x}}\right)^2 d\bar{x}\right)\frac{\partial^2 \bar{w}}{\partial \bar{x}^2} + \eta\frac{\partial^2 \bar{w}}{\partial \bar{t}^2} = \bar{q}_{\text{elec}}(\bar{w}) + \bar{q}_{\text{vdW}}(\bar{w}), \tag{23}$$

where η equals

$$\frac{mL^4}{EIG_0} \Big/ \frac{mL^4}{EIG_0} = 1,$$

and other variables including α, q_{elec}, and q_{vdW} were introduced in previous equations.

The Taylor expansions of the right-hand terms of (23) are

$$\bar{q}_{\text{elec}}(\bar{w}) = \sum_{i=0}^{n} A_i w^i, \tag{24}$$

$$\bar{q}_{\text{vdW}}(\bar{w}) = \sum_{i=0}^{n} B_i w^i. \tag{25}$$

The coefficients A_i and B_i are obtained from the derivative terms of the Taylor expansions. We consider five terms for the expansions; the two first terms of $\bar{q}_{\text{elec}}(\bar{w})$ and $\bar{q}_{\text{vdW}}(\bar{w})$ are presented in (26) and (27). The others are not reported here for brevity. Our calculations show that considering more than five terms does not add any accuracy to the results. The first two terms are:

$$\begin{aligned} A_0 &= \frac{\beta V^2}{\sqrt{1+2R}\,\text{arccosh}^2((R+1)/R)}, \\ A_1 &= \frac{2\beta V^2}{(1+2R)\,\text{arccosh}^3((R+1)/R)} + \frac{\frac{1}{2}\dfrac{\beta V^2}{(1+2R)^{3/2}} + \frac{1}{2}\dfrac{\beta V^2}{\sqrt{1+2R}}}{\text{arccosh}^2((R+1)/R)}, \end{aligned} \tag{26}$$

and

$$B_0 = \gamma \sum_{n=1}^{N_G} \frac{\bar{R}\left(\begin{array}{l} 8(1+(n-1)\bar{d})^4 + 32(1+(n-1)\bar{d})^3\bar{R} \\ \quad +72(1+(n-1)\bar{d})^2\bar{R}^2 + 80(1+(n-1)\bar{d})\bar{R}^3 + 35\bar{R}^4 \end{array}\right)}{(1+(n-1)\bar{d})^{9/2}(1+(n-1)\bar{d}+2\bar{R})^{9/2}},$$

$$B_1 = \gamma \sum_{n=1}^{N_G} \left[\frac{9}{2} \frac{\bar{R}\left(\begin{array}{l} 8(1+(n-1)\bar{d})^4 + 32(1+(n-1)\bar{d})^3\bar{R} \\ \quad +72(1+(n-1)\bar{d})^2\bar{R}^2 + 80(1+(n-1)\bar{d})\bar{R}^3 + 35\bar{R}^4 \end{array}\right)}{(1+(n-1)\bar{d})^{9/2}(1+(n-1)\bar{d}+2\bar{R})^{11/2}} \right.$$

$$\left. + \frac{1}{(1+(n-1)\bar{d}+2\bar{R})^{\frac{9}{2}}} \left(\begin{array}{l} \dfrac{9}{2} \dfrac{\bar{R}\left(\begin{array}{l} 8(1+(n-1)\bar{d})^4+32(1+(n-1)\bar{d})^3\bar{R} \\ \quad +72(1+(n-1)\bar{d})^2\bar{R}^2+80(1+(n-1)\bar{d})\bar{R}^3+35\bar{R}^4 \end{array}\right)}{(1+(n-1)\bar{d})^{11/2}} \\ \qquad + \dfrac{\bar{R}(32((1+(n-1)\bar{d})(-2-2(n-1)\bar{d})-(1+(n-1)\bar{d})^2)\bar{R})}{(1+(n-1)\bar{d})^{9/2}} \\ + \dfrac{16(1+(n-1)\bar{d})^2(-2-2(n-1)\bar{d})-80\bar{R}^3+72(-2-2(n-1)\bar{d})\bar{R}^2}{(1+(n-1)\bar{d})^{9/2}} \end{array} \right) \right]. \tag{27}$$

The Taylor expansion applied at this stage is around $w = 0$. The results will show that the applied technique is in good agreement with previous studies, but it may have some inaccuracy for larger gaps. Suppose that $C_i = A_i + B_i$. Substituting (24), (25), and (28) into (23) and using the Galerkin method, we have the final governing equation in (29):

$$\bar{w} = \sum_{i=1}^{n} u_i(t)\phi_i(x), \tag{28}$$

$$k_{1d}\frac{d^2u(t)}{dt^2} + k_{2d}u(t) + k_{3d}u^3(t) = k_{4d} + k_{5d}u(t) + k_{6d}u^2(t) + k_{7d}u^3(t) + k_{8d}u^4(t) + k_{9d}u^5(t), \tag{29}$$

where

$$\begin{array}{lll} k_{1d} = \displaystyle\int_0^1 \eta\phi^2(x)\,dx, & k_{2d} = \displaystyle\int_0^1 \left(\frac{d^2\phi(x)}{dx^2}\right)^2 dx, & k_{3d} = \left[\displaystyle\int_0^1 \alpha\left(\frac{d\phi(x)}{dx}\right)^2 dx\right]^2, \\ k_{4d} = C_1\displaystyle\int_0^1 \phi(x)\,dx, & k_{5d} = C_2\displaystyle\int_0^1 \phi^2(x)\,dx, & k_{6d} = C_3\displaystyle\int_0^1 \phi^3(x)\,dx, \\ k_{7d} = C_4\displaystyle\int_0^1 \phi^4(x)\,dx, & k_{8d} = C_5\displaystyle\int_0^1 \phi^5(x)\,dx, & k_{9d} = C_5\displaystyle\int_0^1 \phi^6(x)\,dx. \end{array} \tag{30}$$

2.2.1. *The homotopy perturbation method for solving dynamic pull-in.* In order to solve the governing equation of the dynamic behavior of CNTs under step DC voltage, the following technique is applied. Although the concepts are similar to the previous description in Section 2.1.1, the formulations are arranged a little differently. Suppose that the nonlinear differential equation to be solved is

$$R(u(t)) = 0, \tag{31}$$

where R is the nonlinear operator and $u(t)$ is the unknown function [Moghimi Zand and Ahmadian 2009]. Using $q \in [0, 1]$ as an embedding parameter, the homotopy function can be written as

$$H(\Phi, q) = (1-q)L[\Phi(t,q) - u_0(t)] - qR[\Phi(t,q), \Omega(q)] = 0, \tag{32}$$

where $u_0(t)$ is the initial guess satisfying the boundary conditions, L is the nonzero auxiliary operator, and Ω is the frequency of the solution. This equation is similar to (17). As q increases from zero to one, $\Phi(t, q)$ changes from the initial guess $\Phi(t, 0) = u_0(t)$ to the exact solution $\Phi(t, 1) = u(t)$. Using Taylor expansion, $\Phi(t, q)$ can be expanded with respect to q as

$$\Phi(t,q) = \Phi(t,0) + \lim_{n\to\infty} \sum_{j=1}^{n} \frac{1}{j!} \frac{\partial^j \Phi(t,q)}{\partial q^j}\bigg|_{q=0} q^j = u_0(t) + \lim_{n\to\infty} \sum_{j=1}^{n} u_j(t) q^j, \tag{33}$$

where $u_j(t)$ is called the j-th order deformation derivative. Solving (33), we can write

$$(1-q)L[\Phi(t,q) - u_0(t)] = qR[\Phi(t,q), \Omega(q)], \tag{34a}$$

$$\Phi(0,q) = 0, \quad \frac{d\Phi(0,q)}{dt} = 0. \tag{34b}$$

If $q = 0$, then (34a) turns to the following relation to obtain the zero-order deformation:

$$L[\Phi(t,0) - u_0(t)] = 0. \tag{35}$$

Differentiating (34a) with respect to q and setting $q = 0$, the first-order deformation relation with zero initial conditions can be obtained:

$$L[u_1(t)] = qR[\Phi(t,q), \Omega(q)]\big|_{q=0}. \tag{36}$$

Taking the j-th order differential of (34a) and then setting $q = 0$ results in the j-th order deformation equation [Moghimi Zand and Ahmadian 2009]:

$$L[u_j(t) - \delta_j u_{j-1}(t)] = \frac{1}{(j-1)!} \frac{\partial^{j-1} R[\Phi(t,q), \Omega(q)]}{\partial q^{j-1}}\bigg|_{q=0}, \tag{37}$$

where

$$\delta_j = \begin{cases} 0, & \text{if } j \le 1, \\ 1, & \text{otherwise.} \end{cases} \tag{38}$$

Higher-order approximations of the exact solution can be achieved by solving (37).

At this stage, the homotopy perturbation method is applied to solve the governing equations of the CNT deflection and pull-in under step DC voltage. Using a new time scale $\tau = \omega t$, (30) can be rewritten as follows:

$$k_{1d}\omega^2 \frac{d^2u(\tau)}{d\tau^2} + k_{2d}u(\tau) + k_{3d}u^3(\tau) - k_{4d} - k_{5d}u(\tau) - k_{6d}u^2(\tau) - k_{7d}u^3(\tau) - k_{8d}u^4(\tau) - k_{9d}u^5(\tau) = 0. \tag{39}$$

The nonlinear and linear operators of (33) are defined as

$$R[\Phi(\tau,q),\Omega(q)] = k_{1d}\omega(q)^2\frac{\partial^2\Phi(\tau,q)}{\partial\tau^2} + k_{2d}\Phi(\tau,q) + k_{3d}\Phi(\tau,q)^3 - k_{4d} - k_{5d}\Phi(\tau,q) - k_{6d}\Phi(\tau,q)^2 - k_{7d}\Phi(\tau,q)^3 - k_{8d}\Phi(\tau,q)^4 - k_{9d}\Phi(\tau,q)^5, \quad (40)$$

$$L[\Phi(t,q)] = \omega_0^2\left(\frac{\partial^2\Phi(t,q)}{\partial\tau^2} + \Phi(t,q)\right). \quad (41)$$

The initial guess for the system deflection is considered $u_0(\tau) = 0$. The first-order approximation is obtained by solving (36):

$$u_1(t) = \frac{k_4}{\omega_0^2}(1-\cos(\tau)). \quad (42)$$

The governing equation of the undamped vibration of the CNT should be expressed based on the base functions

$$\cos(m\tau) = 0, \quad m = 1, 2, 3, \ldots. \quad (43)$$

Hence, in order to eliminate the secular terms in the j-th order approximation, the coefficients of $\cos(\tau)$ in the $(j-1)$-th order deformation equation should be set to zero. This fact results in an algebraic equation and its solution leads to ω_{j-2}. The second-order approximation is obtained from solving (37) as

$$u_2(\tau) = \frac{k_1k_4(1+k_1)(1-\cos(\tau))}{k_2+k_5}, \quad \omega_0 = \frac{\sqrt{k_1(k_2+k_5)}}{k_1}. \quad (44)$$

Successive solution of (37) for the higher-order approximations and setting $q = 1$ result in more-exact results according to

$$u(\tau) = \sum_{j=0}^{n+2} u_j(t), \quad \omega = \sum_{j=0}^{n}\omega_j. \quad (45)$$

3. Results and discussion

In this section, the results obtained from the above formulations are presented. The results cover the deflection of CNTs with different geometries and boundary conditions under electrostatic actuation in the presence of vdW effects as well as their pull-in voltages. The numerical values applied in the paper are presented in Table 1. They are fixed unless stated explicitly.

First of all, in order to verify the formulation and applied technique to solve the governing equations, we are going to compare some results of this paper with those reported in [Dequesnes et al. 2002]. Figure 2 illustrates the tip deflection of a cantilever and center-point deflection of a doubly clamped CNT studied in [ibid.] ($R_{\text{int}} = 6.65\,\text{A}$, $R_{\text{ext}} = 10\,\text{A}$, and $E = 1.2\,\text{TPa}$) versus voltage. The results obtained from the formulation presented in that paper are depicted in the same figures. The diagrams reveal good agreement between the results and confirm our formulation and applied solutions method. The inconsequential differences may be due to different solution techniques and various formulations. Duquesnes et al. considered a one-DOF model, while in this paper we consider a more real distributed model.

Parameter	Numerical value
Elastic modulus	1 TPa
Electric permittivity	$8.854 \times 10^{-12}\,\mathrm{C}^2/\mathrm{Nm}^2$
Gap distance	4 nm
Length	50 nm
Radius	6.785 A
Lennard-Jones (c_6)	$2.43 \times 10^{-78}\,\mathrm{Nm}^7$
Lennard-Jones (σ)	$1.14 \times 10^{29}\,\mathrm{m}^{-3}$

Table 1. Numerical values applied in the paper. For the parameters of the Lennard-Jones potential, see [Dequesnes et al. 2002].

As shown in Figure 2, the deflections of the CNTs increase with the voltage up to maximum values, and then suddenly drop on the ground plate. This phenomenon is called pull-in, and the corresponding voltage, as described before, is the pull-in voltage. The figures reveal that the vdW force decreases the pull-in voltage of the CNTs with both boundary conditions, but the effects are remarkably higher for the cantilevered CNTs. Hence, it has a very important role and cannot be disregarded in NEMS. There are several key points in the figures that we will discuss in detail. At zero voltage (the absence of electrostatic actuation), there is an initial deflection in the cantilevered CNTs. The deflection is the resulted of the vdW interaction between the CNT and substrate. Thus, the vdW force not only decreases the pull-in voltage but also applies an initial deflection to the system before any external actuation. However, this deflection is ignorable for the doubly clamped CNT due to its stiffer structure. Comparison between the two parts of Figure 2 reveals that the pull-in voltages of the doubly clamped CNTs are much larger than those of the cantilevered CNTs with same dimensions. This is also because of the weaker structures of the cantilevered CNTs in comparison with the doubly clamped CNTs. We now study the effects of variation in dimensions on the pull-in voltages of CNTs under cantilever and doubly clamped boundary conditions.

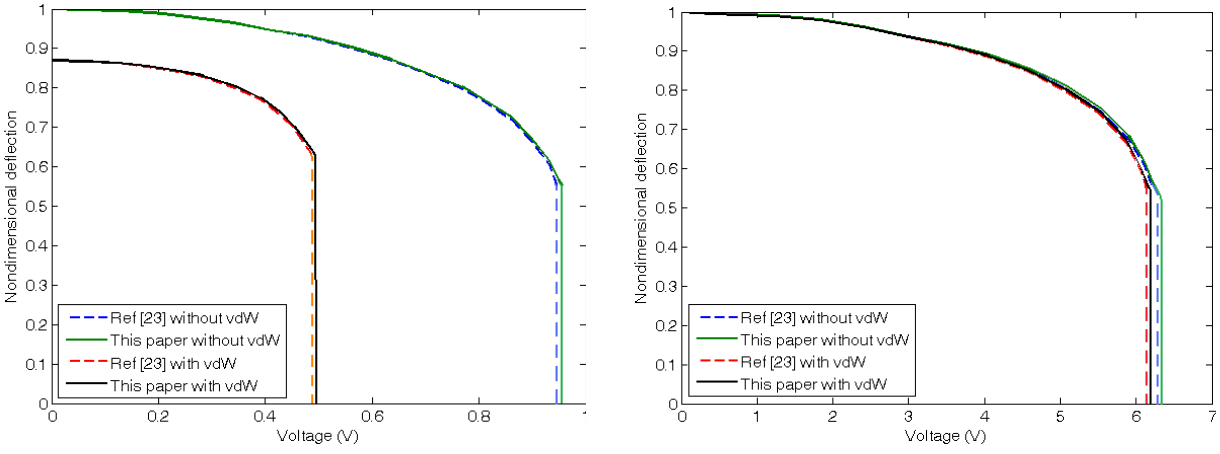

Figure 2. Deflection of CNTs with (left) cantilever and (right) doubly clamped boundary conditions under electrostatic actuation.

3.1. ***Deflection of CNTs under static DC actuation.*** We next discuss the effects of changes in the dimensions of CNTs on the static electrostatic actuation under the boundary conditions mentioned. Figure 3 shows the pull-in voltages of the cantilevered and doubly clamped CNTs versus length. The figure reveals that with increasing length of the CNT, the pull-in occurs at smaller voltages. It is worth noting that the longer cantilevered CNTs may encounter pull-in instability only by the vdW interaction. This means that in the absence of electrostatic actuation, vdW forces can make the longer nanosystems pull in. For example, a cantilevered CNT with length of 60 nm and other characteristics the same as those mentioned in Table 1 pulls in only because of vdW interactions.

Figure 4 illustrates the pull-in voltages of the systems with various radii. The results reveal that CNTs with larger radii have higher pull-in voltages. Thus, they deflect harder than those with smaller radii because larger radii lead to stiffer CNTs.

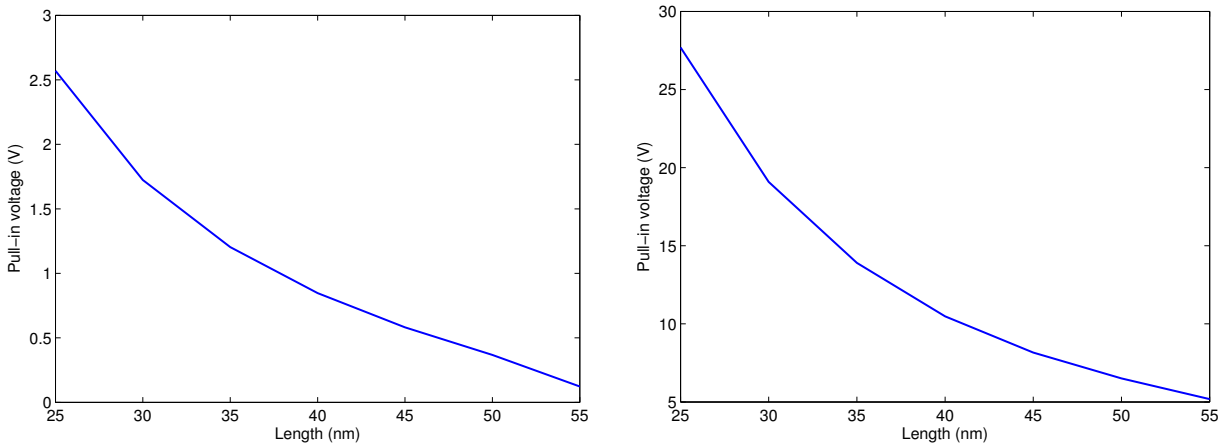

Figure 3. Static pull-in voltages versus length of CNTs with (left) cantilever and (right) doubly clamped boundary conditions.

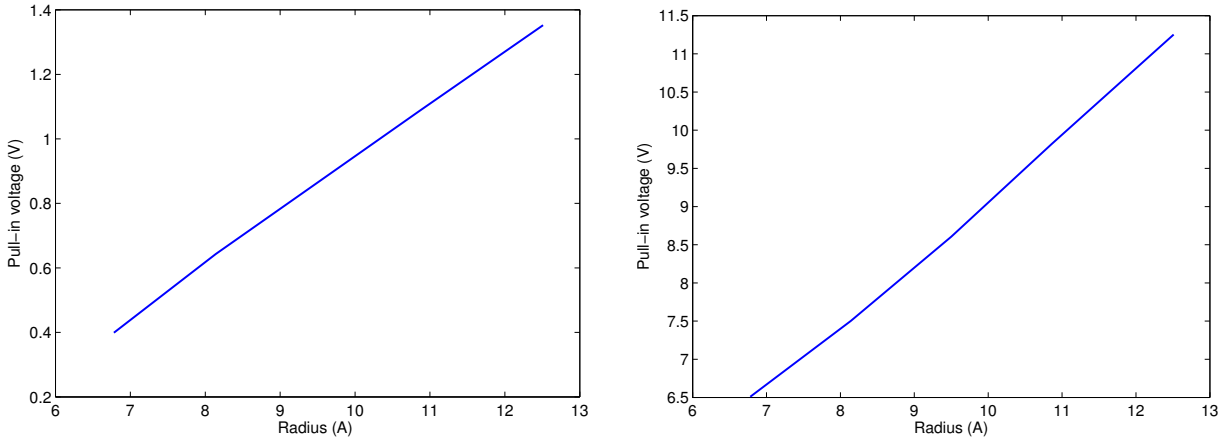

Figure 4. Static pull-in voltages versus radius of CNTs with (left) cantilever and (right) doubly clamped boundary conditions.

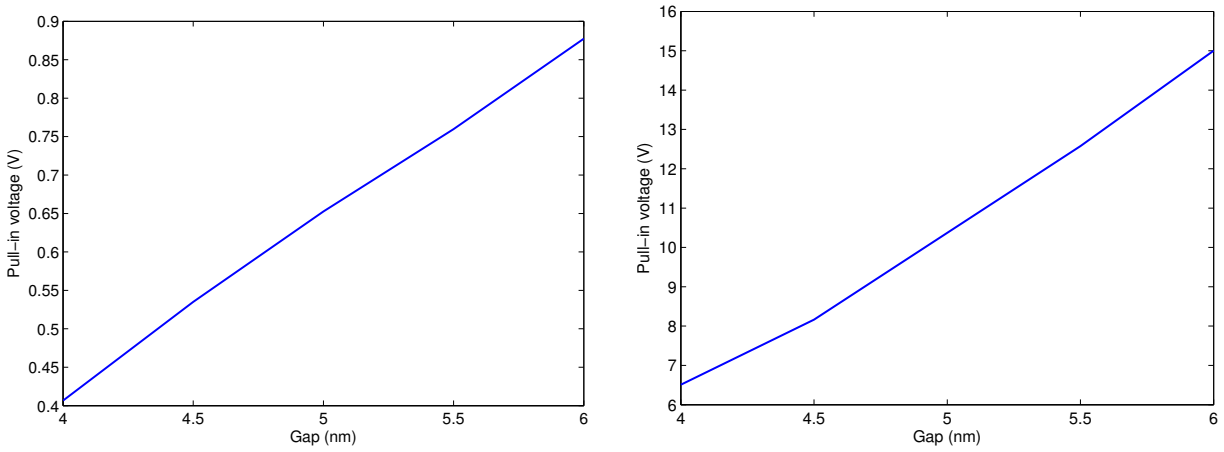

Figure 5. Static pull-in voltages versus gap between graphene sheets for CNTs with (left) cantilever and (right) doubly clamped boundary conditions.

The effects of gap increment on the static pull-in voltages of the CNTs are depicted in Figure 5. According to this figure, an increase in the gap increases the pull-in voltages of CNTs under both boundary conditions. Similarly to having longer CNTs, smaller gaps may lead to pull-in of the CNTs without application of electrostatic actuation, that is, only due to vdW effects. In general, the variation of each parameter resulting in a weaker structure, such as increasing length or decreasing radius or gap, may increase the possibility of occurrence of pull-in.

3.2. ***Vibration of CNTs under step DC voltage.*** The vibration behaviors of the cantilever and doubly clamped CNTs with dimensions as reported in [Dequesnes et al. 2002] are illustrated in Figure 6. In this figure, an increment in the applied voltage results in larger vibration amplitudes. This is correct for both boundary conditions. However, the variation of natural frequency leads to different behaviors. For cantilever boundary conditions, increasing the applied voltage leads to a decrease in the natural frequency.

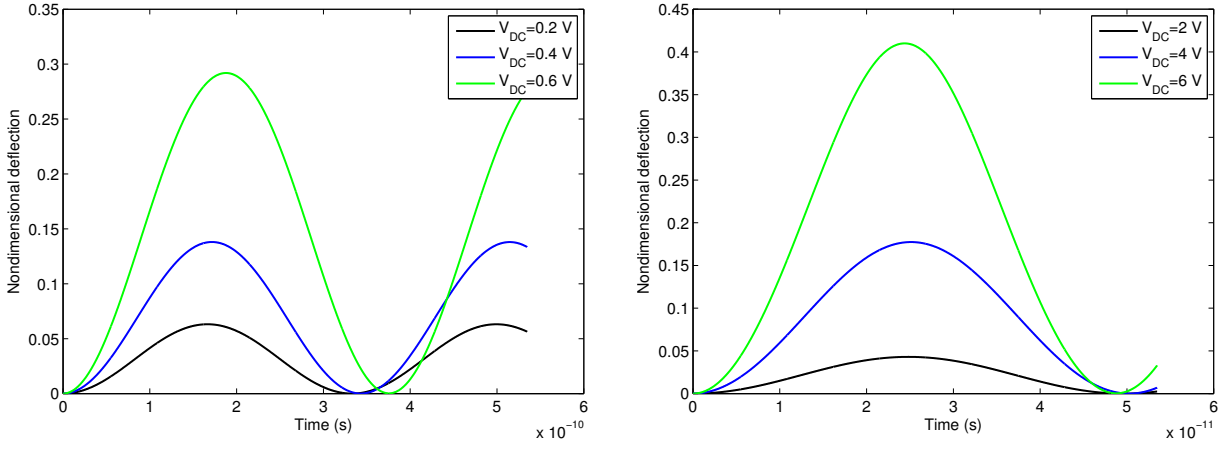

Figure 6. Vibration of CNTs with (left) cantilever and (right) doubly clamped boundary conditions under step DC voltage.

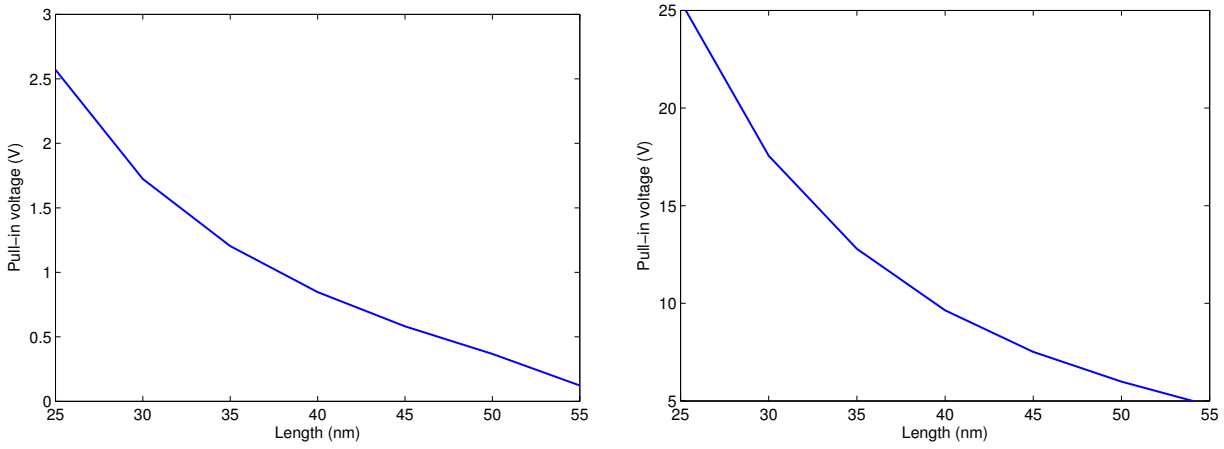

Figure 7. Dynamic pull-in voltages versus length of CNTs with (left) cantilever and (right) doubly clamped boundary conditions.

But, for the doubly clamped boundary conditions, in general, a voltage increment results in increasing frequency. Dependency of the natural frequency on the applied voltage or applied force is often a sign of a nonlinear system, because in linear systems the frequency does not depend on the applied force.

We next investigate the effects of changing the dimensions of the nanostructure on the dynamic pull-in voltages of CNTs under the boundary conditions mentioned. The physical and geometrical conditions of the CNTs studied in this subsection are same as those in the previous subsection.

Figure 7 show the variation of dynamic pull-in voltages versus length changes of CNTs under step DC voltage with cantilever and doubly clamped boundary conditions. According to this figure, we conclude that a length increment results in a decrease in dynamic pull-in voltage. However, the numerical range of variation is higher for doubly clamped boundary conditions.

Figure 8 shows the dynamic pull-in voltages versus radius increment of CNTs under step DC voltage with cantilever and doubly clamped boundary conditions. The figure reveals that, similarly to the static

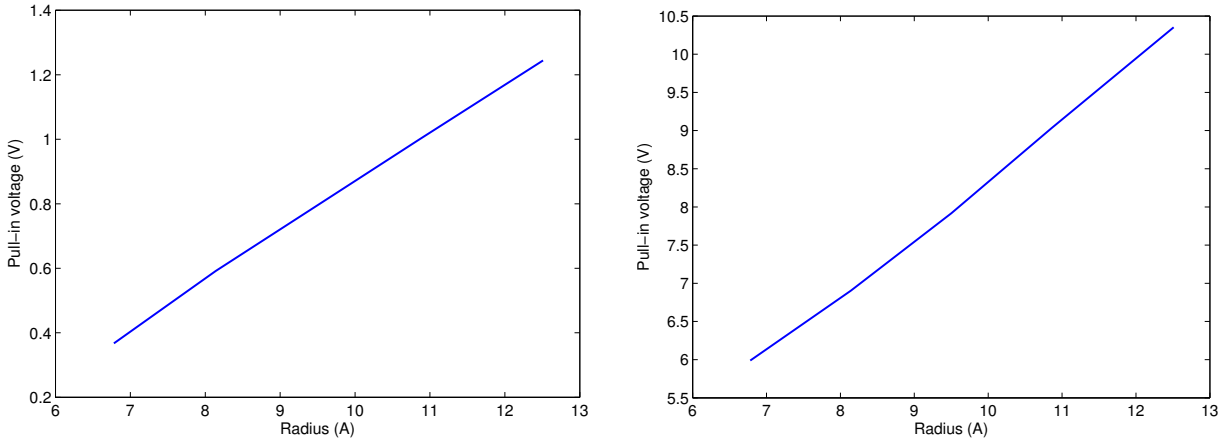

Figure 8. Dynamic pull-in voltages versus radius of CNTs with (left) cantilever and (right) doubly clamped boundary conditions.

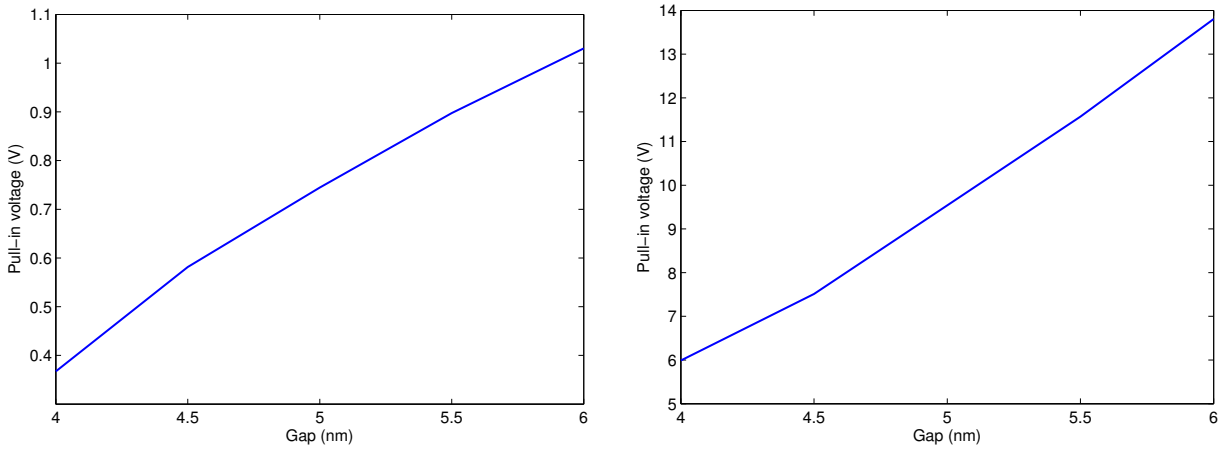

Figure 9. Dynamic pull-in voltages versus gap of CNTs with (left) cantilever and (right) doubly clamped boundary conditions.

case, the radius increment increases the dynamic pull-in voltages of CNTs with both boundary conditions. This can be attributed to the stiffer structures of CNTs with larger diameters. Comparison between the static and dynamic pull-in voltages show that the static pull-in voltages exceed the dynamic ones.

Figure 9 depicts the effects of gap increment on the dynamic pull-in voltages of CNTs with the considered boundary conditions. Based on this figure, it can be concluded that increasing the gap increases the dynamic pull-in voltages of CNTs with both boundary conditions. This fact can be attributed to weakening of the electrostatic and vdW forces with an increasing gap. Thus higher voltages should be applied to compensate for the weakening effects of increasing the gap to reach the pull-in behaviors.

4. Conclusion

This paper presents the static and dynamic deflection of carbon nanotubes (CNTs) under electrostatic actuation in the presence of vdW interactions. The homotopy perturbation method was applied to investigate the effects of diameter, length, and gap distance variations on CNTs with cantilever and doubly clamped boundary conditions. The results suggest that CNTs with longer lengths and smaller diameters were more vulnerable to pull-in. However, pull-in phenomena noticeably depended also on the gap distance between the CNT and the substrate. Smaller gaps resulted in lower pull-in voltages. Our figures suggest that decreasing the gap or increasing the length may lead to conditions in which the pull-in occurs only via vdW interaction, without electrostatic actuation. Similar investigations were conducted for nanostructures under step DC voltages and the dynamic behaviors were studied.

References

[Abadyan et al. 2010] M. Abadyan, A. Novinzadeh, and A. S. Kazemi, "Approximating the effect of the Casimir force on the instability of electrostatic nano-cantilevers", *Physica Scr.* **81**:1 (2010), Article ID #015801.

[Ansola et al. 2012] R. Ansola, E. Veguería, J. Canales, and C. Alonso, "Evolutionary optimization of compliant mechanisms subjected to non-uniform thermal effects", *Finite Elem. Anal. Des.* **57** (2012), 1–14.

[Batra et al. 2008] R. C. Batra, M. Porfiri, and D. Spinello, "Reduced-order models for microelectromechanical rectangular and circular plates incorporating the Casimir force", *Int. J. Solids Struct.* **45**:11–12 (2008), 3558–3583.

[Darvishian et al. 2012] A. Darvishian, H. Moeenfard, M. T. Ahmadian, and H. Zohoor, "A coupled two degree of freedom pull-in model for micromirrors under capillary force", *Acta Mech.* **223**:2 (2012), 387–394.

[Dequesnes et al. 2002] M. Dequesnes, S. V. Rotkin, and N. R. Aluru, "Calculation of pull-in voltages for carbon-nanotube-based nanoelectromechanical switches", *Nanotechnology* **13** (2002), 120–131.

[Jia et al. 2011] X. L. Jia, J. Yang, and S. Kitipornchai, "Pull-in instability of geometrically nonlinear micro-switches under electrostatic and Casimir forces", *Acta Mech.* **218**:1–2 (2011), 161–174.

[Kahrobaiyan et al. 2011] M. H. Kahrobaiyan, M. Rahaeifard, and M. T. Ahmadian, "Nonlinear dynamic analysis of a V-shaped microcantilever of an atomic force microscope", *Appl. Math. Model.* **35**:12 (2011), 5903–5919.

[Ke and Espinosa 2005] C. Ke and H. D. Espinosa, "Numerical analysis of nanotube-based NEMS devices, I: Electrostatic charge distribution on multiwalled nanotubes", *J. Appl. Mech.* (*ASME*) **72**:5 (2005), 721–725.

[Ke et al. 2005] C. Ke, H. D. Espinosa, and N. Pugno, "Numerical analysis of nanotube based NEMS devices, II: Role of finite kinematics, stretching and charge concentrations", *J. Appl. Mech.* (*ASME*) **72**:5 (2005), 726–731.

[Koochi et al. 2012] A. Koochi, A. S. Kazemi, F. Khandani, and M. Abadyan, "Influence of surface effects on size-dependent instability of nano-actuators in the presence of quantum vacuum fluctuations", *Physica Scr.* **85** (2012), Article ID #035804.

[Krylov et al. 2005] S. Krylov, I. Harari, and Y. Cohen, "Stabilization of electrostatically actuated microstructures using parametric excitation", *J. Micromech. Microeng.* **15**:6 (2005), 1188–1204.

[Moeenfard and Ahmadian 2012] H. Moeenfard and M. T. Ahmadian, "The influence of vertical deflection of the supports in modeling squeeze film damping in torsional micromirrors", *Microelectron. J.* **43**:8 (2012), 530–536.

[Moeenfard et al. 2012] H. Moeenfard, A. Darvishian, and M. T. Ahmaidan, "Static behavior of nano/micromirrors under the effect of Casimir force, an analytical approach", *J. Mech. Sci. Technol.* **26**:2 (2012), 537–543.

[Moghimi Zand and Ahmadian 2009] M. Moghimi Zand and M. T. Ahmadian, "Application of homotopy analysis method in studying dynamic pull-in instability of microsystems", *Mech. Res. Commun.* **36**:7 (2009), 851–858.

[Moghimi Zand et al. 2009] M. Moghimi Zand, M. T. Ahmadian, and B. Rashidian, "Semi-analytic solutions to nonlinear vibrations of microbeams under suddenly applied voltages", *J. Sound Vib.* **325**:1–2 (2009), 382–396.

[Mojahedi et al. 2010] M. Mojahedi, M. Moghimi Zand, and M. T. Ahmadian, "Static pull-in analysis of electrostatically actuated microbeams using homotopy perturbation method", *Appl. Math. Model.* **34**:4 (2010), 1032–1041.

[Mojahedi et al. 2011] M. Mojahedi, M. Moghimi Zand, M. T. Ahmadian, and M. Babaei, "Analytic solutions to the oscillatory behavior and primary resonance of electrostatically actuated microbridges", *Int. J. Struct. Stab. Dyn.* **11**:6 (2011), 1119–1137.

[Ouakad and Younis 2010] H. M. Ouakad and M. I. Younis, "Nonlinear dynamics of electrically actuated carbon nanotube resonators", *J. Comput. Nonlinear Dyn.* (*ASME*) **5**:1 (2010), Article ID #011009.

[Pirbodaghi et al. 2009] T. Pirbodaghi, M. T. Ahmadian, and M. Fesanghary, "On the homotopy analysis method for non-linear vibration of beams", *Mech. Res. Commun.* **36**:2 (2009), 143–148.

[Rahaeifard et al. 2012] M. Rahaeifard, M. H. Kahrobaiyan, M. T. Ahmadian, and K. Firoozbakhsh, "Size-dependent pull-in phenomena in nonlinear microbridges", *Int. J. Mech. Sci.* **54**:1 (2012), 306–310.

[Ramezani et al. 2008a] A. Ramezani, A. Alasty, and J. Akbari, "Analytical investigation and numerical verification of Casimir effect on electrostatic nano-cantilevers", *Microsyst. Technol.* **14**:2 (2008), 145–157.

[Ramezani et al. 2008b] A. Ramezani, A. Alasty, and J. Akbari, "Closed-form approximation and numerical validation of the influence of van der Waals force on electrostatic cantilevers at nano-scale separations", *Nanotechnology* **19**:1 (2008), Article ID #015501.

[Rezazadeh et al. 2011] G. Rezazadeh, M. Fathalilou, and M. Sadeghi, "Pull-in voltage of electrostatically-actuated microbeams in terms of lumped model pull-in voltage using novel design corrective coefficients", *Sens. Imaging Int. J.* **12**:3–4 (2011), 117–131.

[Soroush et al. 2010] R. Soroush, A. Koochi, A. S. Kazemi, A. Noghrehabadi, H. Haddadpour, and M. Abadyan, "Investigating the effect of Casimir and van der Waals attractions on the electrostatic pull-in instability of nano-actuators", *Physica Scr.* **82** (2010), Article ID #045801.

[Tayyaba et al. 2012] S. Tayyaba, N. Afzulpurkar, and M. W. Ashraf, "Simulation and design optimization of piezoelectricaly actuated valveless blood pump for hemofiltration system", *Sens. Transducers J.* **139**:4 (2012), 63–78.

[Zand 2012] M. M. Zand, "The dynamic pull-in instability and snap-through behavior of initially curved microbeams", *Mech. Adv. Mater. Struct.* **19**:6 (2012), 485–491.

[Zhang and Zhao 2006] Y. Zhang and Y. Zhao, "Numerical and analytical study on the pull-in instability of micro-structure under electrostatic loading", *Sens. Actuators A Phys.* **127**:2 (2006), 366–380.

Received 8 Feb 2013. Revised 20 Jun 2013. Accepted 1 Oct 2013.

MIR MASOUD SEYYED FAKHRABADI: msfakhrabadi@gmail.com
Karaj Branch, Islamic Azad University, Karaj, Iran

ABBAS RASTGOO: arastgo@ut.ac.ir
School of Mechanical Engineering, College of Engineering, University of Tehran, Tehran, Iran

MOHAMMAD TAGHI AHMADIAN: ahmadian@sharif.edu
Department of Mechanical Engineering, Sharif University of Technology, Tehran 11365-9567, Iran

JOURNAL OF MECHANICS OF MATERIALS AND STRUCTURES
Vol. 8, No. 8-10, 2013
dx.doi.org/10.2140/jomms.2013.8.403

THERMOELASTIC DAMPING IN AN AUXETIC RECTANGULAR PLATE WITH THERMAL RELAXATION: FORCED VIBRATIONS

BOGDAN T. MARUSZEWSKI, ANDRZEJ DRZEWIECKI,
ROMAN STAROSTA AND LILIANA RESTUCCIA

We analyze the forced vibrations of an auxetic rectangular thermoelastic plate. In contrast with the existing classical studies, two important phenomena have been considered: thermoelastic damping and second sound. In this way the presented model much better describes thermomechanical processes running in "negative" materials of finite extent.

1. Introduction

Thermoelastic interactions in classical continuous media of finite extent have been investigated by many authors [Boley and Weiner 1960; Nowacki 1962; 1975; Noda et al. 2003]. However, the definite geometry of a body can also be the origin of certain unusual phenomena that do not occur in infinite media. One of these, among others, is so-called thermoelastic damping, which does not arise from eventual viscous features of the body. The extra energy dissipation resulting from that phenomenon, not observed in a pure elastic infinite medium, comes from an additional heat flux occurring in bodies of finite extent (in the case of a plate the flux is normal to its limiting surfaces). The origin of that extra heat flux is a specific deformation of the plate: if we consider a vibration process, for instance, the upper and lower fibers are alternatively extended and compressed. Thus, any thermoelastic problem in a plate in bending is 2D–3D (the latter because of the extra heat flux normal to the middle surface). Here nD stands for "n-dimensional". The first idea which pointed out one of the mechanisms of thermoelastic damping was based on the stress heterogeneities which give rise to fluctuations of temperature [Zener 1937]. Zener focused his attention on 1D bodies. While his theory has been successful in explaining the measurements of internal friction in reeds and wires, it is incomplete in two respects:

(a) It is not consistent with the modern theory of thermoelasticity.

(b) It does not describe the thermoelastic behavior of bodies of arbitrary form, especially if coupling occurs between different vibration modes.

The complete thermodynamical model of that phenomenon has been presented in [Alblas 1961; 1981]. There you can find the general theory of thermoelastic internal friction in 3D bodies of finite extent and its application to thermoelastic damping during vibrations of beams of various cross-sections (1D–3D problems) which proves its consistency. Following that model, in [Maruszewski 1992] damping during vibrations of circular plates has been considered. Research on thermoelastic damping has continued for

The paper has been supported by the grants MNiSzW 2363/B/T02/2010/39 and 21-418/2013/DS..
Keywords: thermoelastic damping, thermal relaxation, auxetics.

many years as the phenomenon plays an important role in many applications. However, all the mentioned considerations were based on the classical irreversible thermodynamics. Within that model, the temperature distribution is described by the parabolic heat conduction equation [Bishop and Kinra 1993; 1994; Milligan and Kinra 1993; Kinra and Milligan 1994]. Since any physical signals propagate with finite velocity it is much better to base the above considerations on extended irreversible thermodynamics [Cattaneo 1958; Vernotte 1958; Chester 1963; Lebon 1982; Jou et al. 1988; Maruszewski 1988]. That idea has been, for the first time, applied to describe thermoelastic damping with the effect of second sound [Khisaeva and Ostoja-Starzewski 2006; Ignaczak and Ostoja-Starzewski 2010]. Such an approach is crucial in researching micro, nano, and macroengineering problems [Lifshitz and Roukes 2000; Nayfeh and Younis 2004; Vengallatore 2005; Prabhakar and Vengallatore 2008].

Fast technological development requires the use of unconventional materials with peculiar and unusual properties. Special interest has been recently focused on "negative" materials, that is, materials with negative Poisson's ratio, negative compressibility, negative stiffness, negative heat expansion coefficient, and the like [Almgren 1985; Lakes 1987; Wojciechowski 1989; Novikov and Wojciechowski 1999; Poźniak et al. 2010; Kołat et al. 2010; 2011]. Those unconventional features strongly influence the behavior of many mechanical structures, like bodies of finite extent, laminates, composite structures, weaved structures, and other multiphase structures. In contrast to [Khisaeva and Ostoja-Starzewski 2006], where the thermoelastic damping in a vibrating beam has been investigated with one relaxation time based only on the hyperbolic heterogeneous heat equations, we have focused in this paper on an analysis of the forced bending vibrations of an auxetic thermoelastic rectangular plate (a plate with negative Poisson's ratio) within coupled thermoelasticity. This research takes also into account thermoelastic damping and the relaxation features of the thermal field (second sound). The obtained results have been compared to those of the normal material of the plate and those without thermal relaxation.

2. Basic equations

Let us consider forced vibrations of a thermoelastic rectangular plate with $0 \le x_1 \le a$, $0 \le x_2 \le b$, $-h/2 \le x_3 \le h/2$, where h denotes the thickness, and $a, b \gg h$ (see Section 4). Following [Nowacki 1975; Alblas 1981; Ignaczak and Ostoja-Starzewski 2010] the basic equations for such a plate consisting of one relaxation time of the thermal field read

$$D_0 w_{,\alpha\alpha\beta\beta} + \rho h \ddot{w} + \frac{1}{1-\nu_T} M_{T,\alpha\alpha} = p, \tag{2-1}$$

$$\theta_{,ii} - \left(\tau \frac{\partial}{\partial t} + 1\right)\left(\frac{\rho c_v}{k}\dot{\theta} + \frac{m}{k} T_0 \dot{e}\right) = 0. \tag{2-2}$$

Here $w = w(x_1, x_2, t)$ and $\theta = \theta(x_1, x_2, x_3, t)$ with ranges of variables $0 \le x_1 \le a$, $0 \le x_2 \le b$, $-h/2 \le x_3 \le h/2$, and $0 \le t < \infty$, where $\alpha, \beta = 1, 2$, $i = 1, 2, 3$, τ is the thermal relaxation time, ρ is the constant plate density, and

$$D_0 = \frac{E_T h^3}{12(1-\nu_T^2)}, \quad m = \frac{E_T \alpha_T}{1-2\nu_T}.$$

Taking into account (2-1) on the one hand and (2-2) and (2-5) below on the other, we see that the problem is 2D–3D. The heat expansion coefficient is α_T, k is the heat conductivity, and the moment M_T due to

the temperature distribution is given by

$$M_T = \alpha_T E_T \int_{-h/2}^{h/2} \theta(x_1, x_2, x_3, t) x_3 \, dx_3. \tag{2-3}$$

The general form of the dilatation e for the thermoelastic plate is as follows:

$$e = \frac{1-2\nu}{1-\nu}(u_{,1} + v_{,2} - x_3 w_{,\alpha\alpha}) + \alpha_T \frac{1+\nu}{1-\nu}\theta. \tag{2-4}$$

T denotes the absolute temperature of the plate and θ is a small temperature variation coming from reciprocal thermoelastic interactions (see (2-1) and (2-2)), so we assume that $\theta = T - T_0$, $|\theta/T_0| \ll 1$. T_0 is the constant reference temperature (see (2-9) and (2-10)) and c_v is the specific heat, while u and v denote displacements corresponding to the elongation of the middle surface and w is the deflection of the plate. However, we confine ourselves to a simplified form of e in the sequel, i.e.,

$$e = -\frac{1-2\nu}{1-\nu} x_3 w_{,\alpha\alpha}, \tag{2-5}$$

assuming that the contribution of the remaining terms in (2-4) can be neglected in the case considered, of pure small bending (see [Khisaeva and Ostoja-Starzewski 2006]). Note that the coefficients E_T (the Young's modulus) and ν_T (the Poisson's ratio) are isothermal. The Poisson's ratio ν in (2-4) and (2-5) has an effective value dependent on the vibrational mode but does not much differ from ν_T [Alblas 1981]. So, we assume that $\nu = \nu_T$ in the sequel. For the model of interactions taken in this paper we also assume that changes in temperature come only from mechanical vibrations of the plate. The mass forces and heat sources have been neglected.

To obtain an exact solution of the problem we have to pose proper boundary conditions for the set (2-1) and (2-2), assuming that

- the plate is simply supported at all edges,
- the temperature at lateral surfaces $T = T_0$, and
- at the upper and lower surfaces temperature changes result from alternate compression and extension of the plate fibers; free heat exchange across those surfaces has been assumed.

Hence we have [Boley and Weiner 1960]

$$w(0, x_2, t) = w(a, x_2, t) = w(x_1, 0, t) = w(x_1, b, t) = 0, \tag{2-6}$$

$$w_{,11} + \frac{1}{D_0(1-\nu_T)} M_T = 0, \quad \text{at } x_1 = 0, a, \tag{2-7}$$

$$w_{,22} + \frac{1}{D_0(1-\nu_T)} M_T = 0, \quad \text{at } x_2 = 0, b, \tag{2-8}$$

$$\theta = 0, \quad \text{at } x_1 = 0, a, \tag{2-9}$$

$$\theta = 0, \quad \text{at } x_2 = 0, b, \tag{2-10}$$

$$\frac{\partial\theta}{\partial x_3} \pm \eta\left(\tau\frac{\partial}{\partial t} + 1\right)\theta = 0, \quad \text{at } x_3 = \pm\frac{h}{2}, \tag{2-11}$$

where η denotes the surface heat exchange coefficient.

From (2-3), (2-9), and (2-10) follows that $M_T = 0$ at $x_1 = 0, a$ and $x_2 = 0, b$.

3. Forced vibrations

Since we are interested in the description of the forced vibrations of a rectangular plate accompanied by thermoelastic damping, the general solutions of (2-1) and (2-2) with the boundary conditions (2-6)–(2-11) are looked for in the forms

$$w(x_1, x_2, t) = \sum_{m=1}^{\infty}\sum_{n=1}^{\infty} w_{00mn} \sin\Big(\frac{m\pi}{a}x_1\Big) \sin\Big(\frac{n\pi}{b}x_2\Big)e^{i\omega t}, \tag{3-1}$$

$$\theta(x_1, x_2, x_3, t) = \sum_{m=1}^{\infty}\sum_{n=1}^{\infty} \theta_{00mn}(x_3) \sin\Big(\frac{m\pi}{a}x_1\Big) \sin\Big(\frac{n\pi}{b}x_2\Big)e^{i\omega t}. \tag{3-2}$$

These solutions concern the situation that our problem is 2D–3D, as was mentioned before.

For the plate vibrations having a forced character we assume that the upper surface $x_3 = h/2$ is loaded by (see (2-1))

$$p(x_1, x_2, t) = \sum_{m=1}^{\infty}\sum_{n=1}^{\infty} p_{00mn} \sin\Big(\frac{m\pi}{a}x_1\Big) \sin\Big(\frac{n\pi}{b}x_2\Big)e^{i\omega t}. \tag{3-3}$$

For the sake of simplicity we take into consideration only the first terms of expansions (3-1)–(3-3), meaning in the sequel that $w_{0011} = w_{00}$, $\theta_{0011} = \theta_{00}$, and $p_{0011} = p_{00}$, confining us to only one solution for $\theta_{00}(x_3)$.

Making use now of (3-1)–(3-3) with (2-5) in (2-1) and (2-2), we arrive at the following result for displacement w_{00}:

$$w_{00} = \frac{\beta B + \bar{p}_{00}}{\omega_0^2 - \omega^2}, \tag{3-4}$$

where

$$\bar{p}_{00} = \frac{p_{00}}{\rho h}, \quad \beta = \frac{\alpha_T E_T H}{(1-\nu_T)\rho h}, \quad \omega_0^2 = \frac{D_0 H^2}{\rho h}, \quad H = \frac{\pi^2}{a^2} + \frac{\pi^2}{b^2}, \tag{3-5}$$

$$B = \int_{-h/2}^{h/2} x_3\theta_{00}\, dx_3 = \overline{C}\int_{-h/2}^{h/2} x_3\tilde{\theta}_{00}\, dx_3 = \overline{C}\,\overline{D}.$$

On using (3-4) in (2-2) the equation for $\theta_{00}(x_3)$ (which gives the solution for temperature distribution along the plate thickness within the third dimension) reads

$$\frac{\partial^2\theta_{00}}{\partial x_3^2} - \epsilon^2\theta_{00} = \overline{C}x_3. \tag{3-6}$$

Now, setting $\theta_{00} = \overline{C}\tilde{\theta}_{00}$, the solution of (3-6) is possible (see [Alblas 1981]) with the help of the modified condition (2-11) by the assumption that $\eta = +\infty$, that is, $(\tau\partial/\partial t + 1)\theta = 0$ for $0 \le x_1 \le a$, $0 \le x_2 \le b$, and $0 \le t < \infty$ at $x_3 = \pm h/2$, and postulating that $\theta_{00}(h/2) = \theta_{00}(-h/2) = 0$:

$$\tilde{\theta}_{00} = \frac{-h\exp\big[\frac{1}{2}(h-2x_3)\epsilon\big] + h\exp\big[\frac{1}{2}(h+2x_3)\epsilon\big] + 2x_3 - 2x_3\exp(h\epsilon)}{2\epsilon^2(-1+\exp(h\epsilon))}, \tag{3-7}$$

where $\epsilon = \sqrt{H + (i\omega - \tau\omega^2)\gamma}$ and $\gamma = \rho c_v/k$.

Thus way we have, from (3-5) and (3-7),

$$\overline{D} = -h\frac{12+h^2\epsilon^2-6h\epsilon\coth(h\epsilon/2)}{12\epsilon^4} \quad \text{and} \quad \overline{C} = \frac{\bar{p}_{00}(i\omega-\tau\omega^2)\delta}{\omega_0^2-\omega^2-\beta\delta(i\omega-\tau\omega^2)\overline{D}}, \tag{3-8}$$

where

$$\delta = \frac{E_T\alpha_T T_0 H}{k}\frac{1-2\nu}{1-2\nu_T}. \tag{3-9}$$

Therefore, the final solutions for the displacement amplitude w_{00} and temperature θ_{00} are

$$w_{00} = \frac{p_{00}}{\omega_0^2-\omega^2-\beta\overline{D}(i\omega-\tau\omega^2)}, \quad \theta_{00} = \overline{C}\tilde{\theta}_{00}. \tag{3-10}$$

4. Numerical results

Let us analyze the results obtained for a plate with the following thermomechanical properties:

$$E_T = 10^{11}\,\frac{\mathrm{N}}{\mathrm{m}^2}, \quad \alpha_T = 3\times10^{-6}\,\mathrm{K}^{-1}, \quad \rho = 7860\,\frac{\mathrm{kg}}{\mathrm{m}^3}, \quad k = 58\,\frac{\mathrm{J}}{\mathrm{s\,m\,K}}, \quad c_v = 460\,\frac{\mathrm{J}}{\mathrm{kg\,K}}, \tag{4-1}$$

$$h = 0.005\,\mathrm{m}, \quad a = 1\,\mathrm{m}, \quad b = 1\,\mathrm{m}, \quad T_0 = 100\,\mathrm{K}, \quad p_{00} = 1000\,\mathrm{N/m}^2. \tag{4-2}$$

The characteristic frequency, assuming a Poisson's ratio $\nu_T = 0.3$, reads $\omega_0 = 106.5313\,\mathrm{s}^{-1}$. The first eigenfrequency, as the root of the denominator of (3-10), is then $\omega_R = 106.5324\,\mathrm{s}^{-1}$.

In Figure 1 we see that the resonance frequency for auxetics, ω_{R1}, is lower than that for normal materials, ω_{R2}, and both amplitudes $\mathrm{Re}(w_{00})$ (top plot) and $\mathrm{Im}(w_{00})$ (bottom) are bigger for auxetics. Moreover $\mathrm{Re}(w_{00})$ and $\mathrm{Im}(w_{00})$ are phase-shifted by $\frac{3}{2}\pi$ for auxetics and $\frac{\pi}{2}$ for normal materials. However, much more interesting are the real and imaginary parts of the temperature distribution θ_{00} across the thickness of the plate, because that distribution is the direct origin of the thermoelastic damping.

Figure 2, top, shows that the above temperature parts are phase shifted with each other and their distributions are completely different across the thickness. We see that thermoelastic damping dominates in the vicinity of the resonance frequency. Detailed depictions of the more spectacular situations indicated in the figure are presented in 3D form in Figure 3. Figure 2, bottom, shows details of the two top panels of Figure 2 around the first eigenfrequency $\omega_R = \omega_{R2}$.

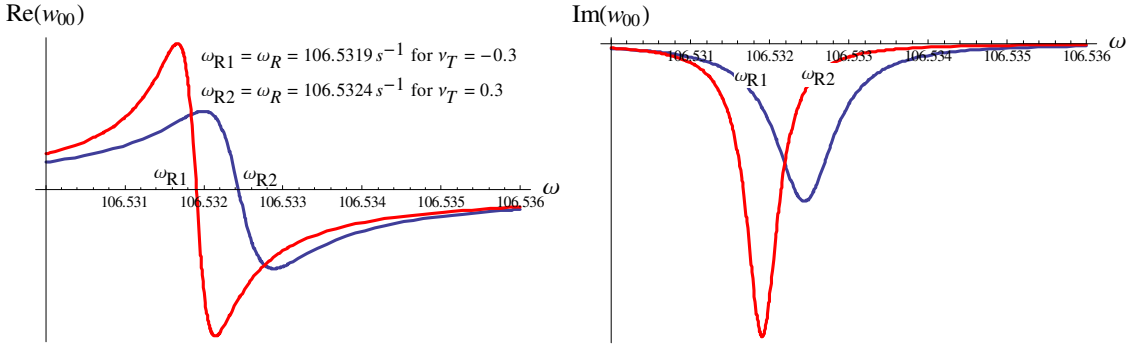

Figure 1. Bending displacement amplitudes w_{00} versus forcing frequency for $\nu_T = 0.3$ (blue) and $\nu_T = -0.3$ (red); $\tau = 10^{-10}$ s.

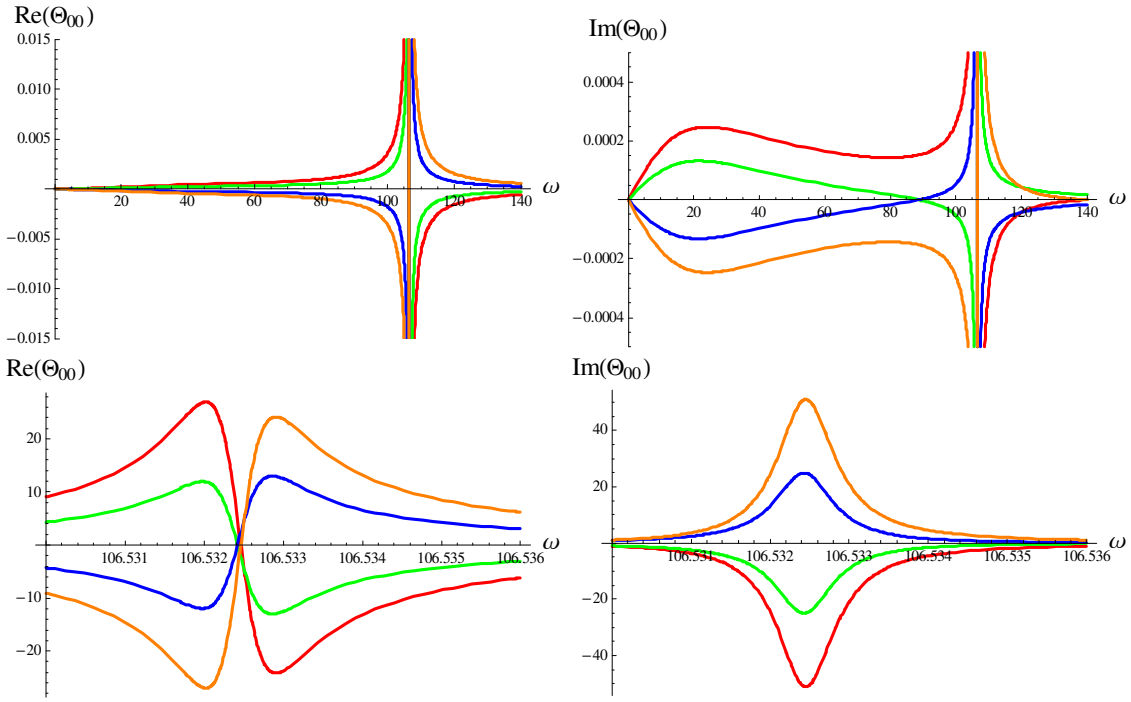

Figure 2. Temperature distribution amplitudes across plate thickness versus forcing frequency for $\nu_T = 0.3$ and $\tau = 10^{-10}$ s; $x_3 = -0.001$ m (red), $x_3 = -0.0005$ m (green), $x_3 = 0.0005$ m (blue), and $x_3 = 0.0001$ m (orange).

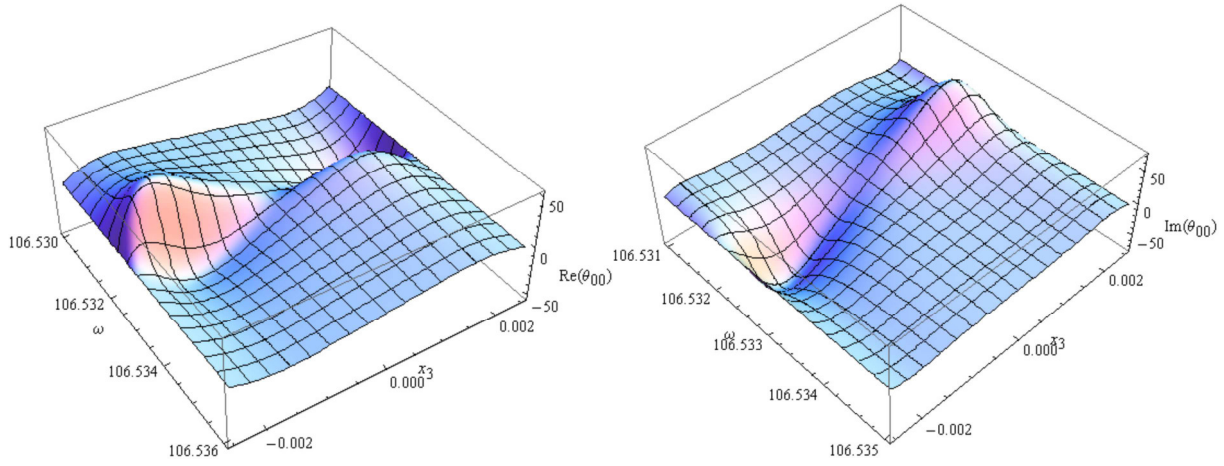

Figure 3. 3D presentation of real and imaginary parts of the temperature amplitude distribution across the thickness.

We remark that the results presented in Figures 2 and 3 are qualitatively comparable to those shown in [Khisaeva and Ostoja-Starzewski 2006].

We still have to analyze how the auxeticity and the relaxation of the thermal field influence mechanical bending and the amplitude distribution responsible for the thermoelastic damping temperature.

For greater legibility, Figures 4–7 show the amplitudes in limited ranges only, while the Poisson's ratios are shown in their full range. The amplitudes are actually represented by smooth functions, not asymptotic ones. The amplitude distributions are symmetric with respect to $\nu = 0$ only within the mathematical range, not within the physical one. For the first eigenfrequency $\omega < 101.625\,\mathrm{s}^{-1}$ there is no resonance in any normal and auxetic material. But for increasing ω if $\omega > 101.625\,\mathrm{s}^{-1}$ the resonance peaks follow increasing values of $|\nu|$. Beyond approximately $\omega = 120\,\mathrm{s}^{-1}$ the resonance occurs only for

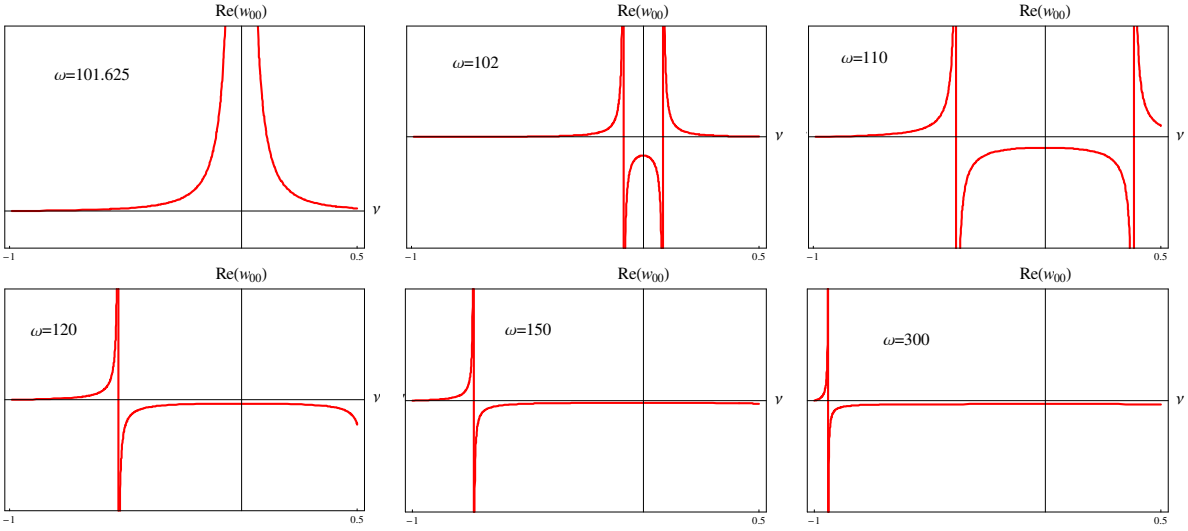

Figure 4. Distribution of w_{00} amplitudes versus Poisson's ratio for different ω.

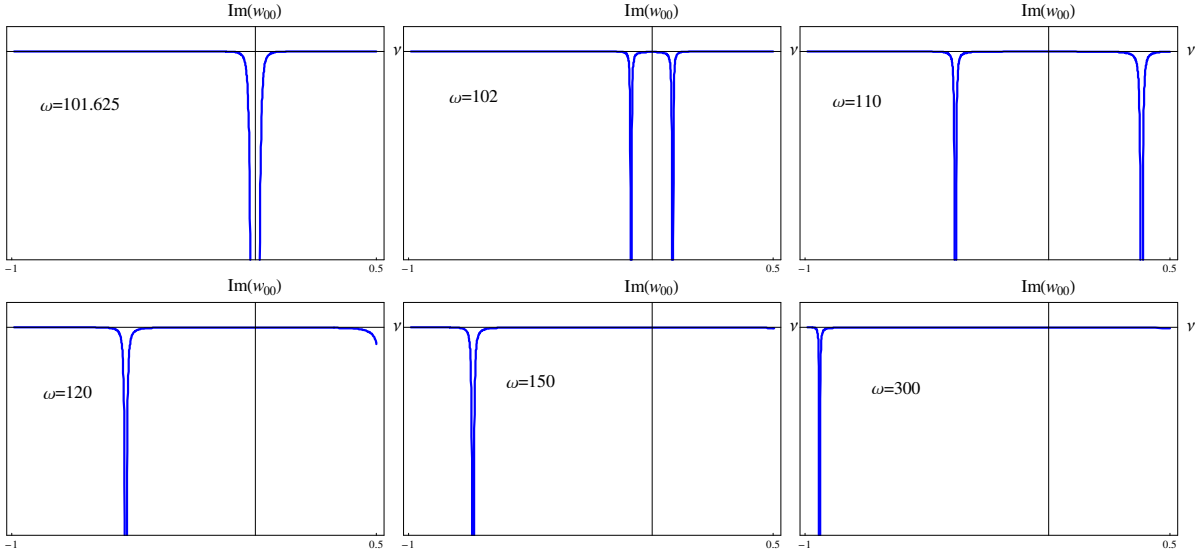

Figure 5. Bending amplitudes $\mathrm{Im}(w_{00})$ for different Poisson's ratios and different frequencies ω; phase-shifted $\pi/2$ with respect to $\mathrm{Re}(w_{00})$.

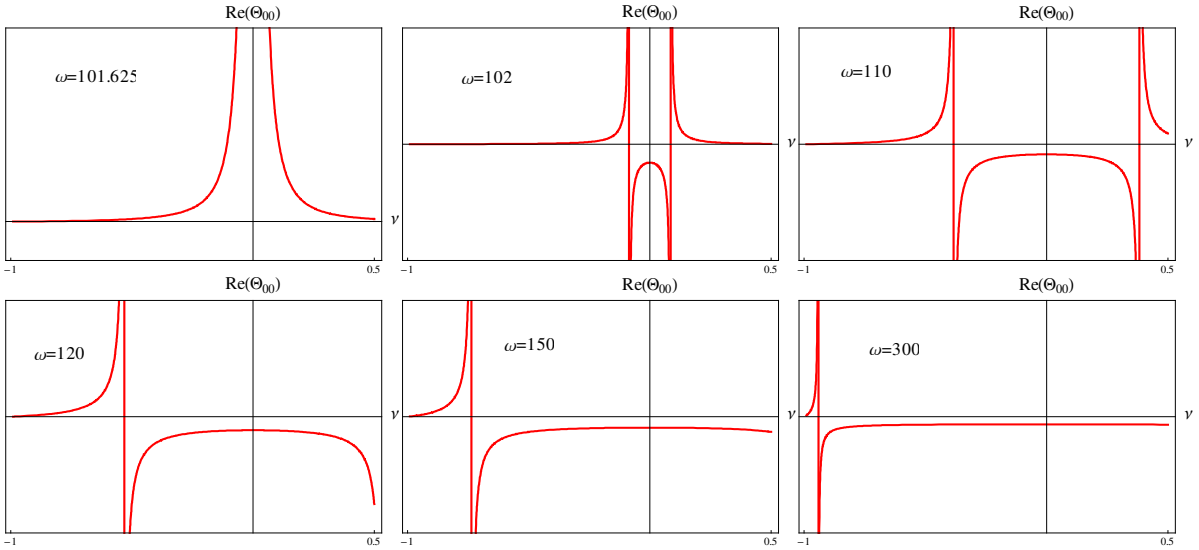

Figure 6. Temperature amplitudes $\mathrm{Re}(w_{00})$ for different forcing frequencies and various materials, for various Poisson's ratios ν.

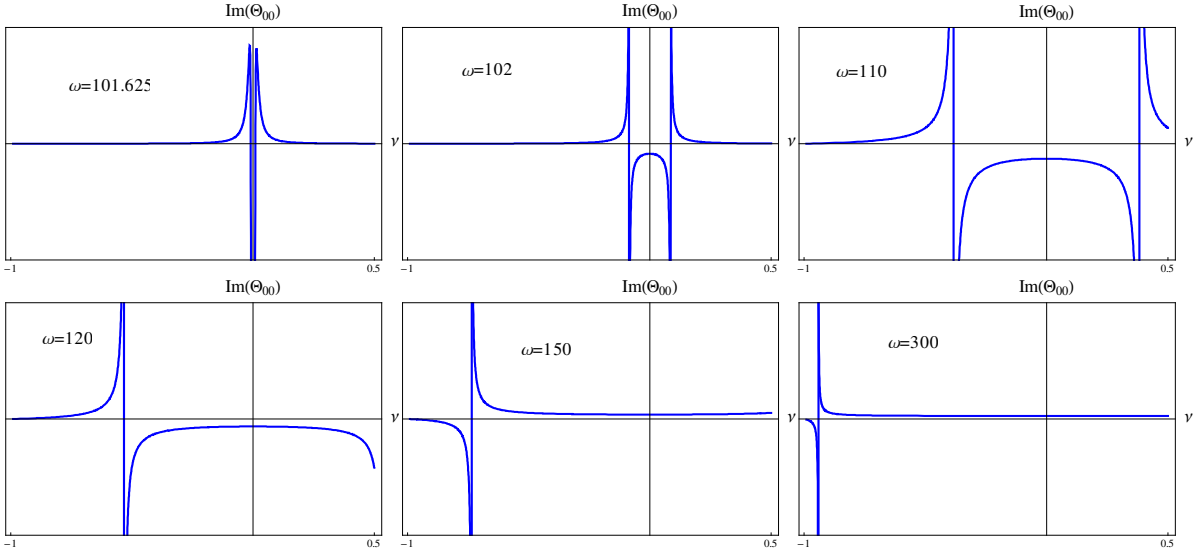

Figure 7. Temperature amplitudes $\mathrm{Im}(w_{00})$, phase-shifted $\pi/2$ with respect to $\mathrm{Re}(\theta_{00})$, for different frequencies and various materials, and various Poisson's ratios ν (continued on next page).

auxetics. Numerical analysis has indicated that for arbitrarily large values of $\omega > 101.625\,\mathrm{s}^{-1}$ resonances occur as the Poisson's ratio ν approaches -1. In the "normal material" ($\nu > 0$) sides of Figures 6 and 7 the character of the dependence temperature variations on the forcing frequency ω are also qualitatively comparable to the similar character of results presented in [Khisaeva and Ostoja-Starzewski 2006]. Note that the temperature distributions shown in Figures 6 and 7 have been calculated for fixed x_3.

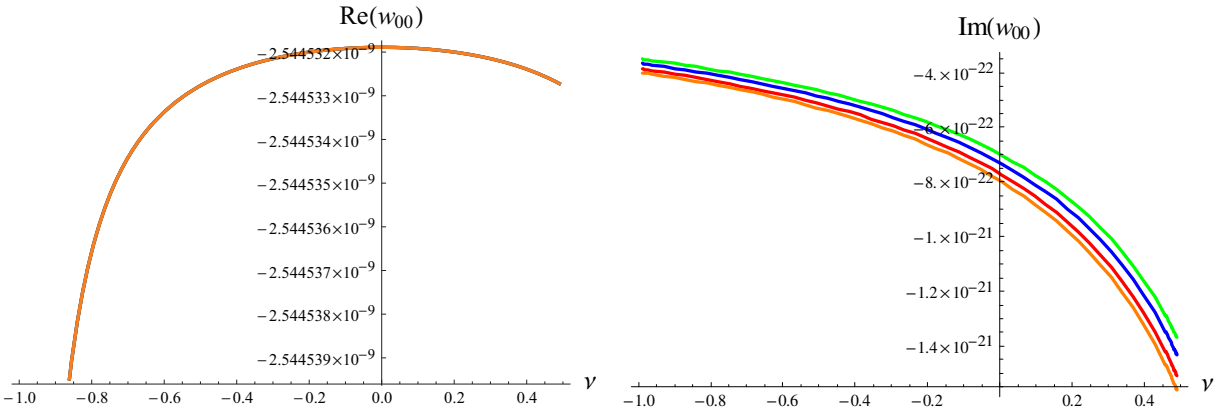

Figure 8. Real and imaginary parts of the bending w_{00} versus the Poisson's ratio for different thermal relaxation times, with high frequency $\omega = 10^5\,\mathrm{s}^{-1}$. On the left, the graph of $\mathrm{Re}(w_{00})$ remains essentially the same for $\tau = 10^{-10}$ s, $\tau = 10^{-8}$ s, $\tau = 10^{-6}$ s, and $\tau = 5 \times 10^{-6}$ s. On the right, $\tau = 10^{-8}$ s (blue), $\tau = 10^{-6}$ s (green), $\tau = 10^{-5}$ s (red), and $\tau = 5 \times 10^{-6}$ s (orange).

Analysis of these figures shows that thermoelastic damping decreases for increasing frequencies and comes from the thermoelastic damping occurring in the plate.

We see in Figure 8, left, that the mechanical vibrations described by the real part of the bending amplitude w_{00} are practically independent of the thermal relaxation time τ; its influence in that situation is negligible. Moreover, we see that amplitudes are very small because the frequency ω is high.

But for the mechanical vibrations phase-shifted $\pi/2$, described by the imaginary part of the bending amplitude w_{00}, the situation is different (see Figure 8, right). Although those amplitudes are extremely small, they depend on the thermal relaxation time τ and decrease if the Poisson's ratio ν approaches -1.

A similar situation occurs qualitatively for the temperature distribution $\mathrm{Re}(\theta_{00})$ (see Figure 9). This conclusion is very important because the distribution of $\theta_{00} = \theta_{00}(x_3)$ forms the origin of the thermoelastic damping. That damping increases for decreasing frequencies.

Comparison of Figures 8 and 9 shows that $\mathrm{Im}(w_{00})$ strongly depends on the Poisson's ratio being weakly dependent on the thermal relaxation time. But $\mathrm{Im}(\theta_{00})$ is constant for various Poisson's ratios which are strongly dependent on the thermal relaxation time.

5. Conclusions

The detailed analysis of thermoelastic damping during forced vibrations of an auxetic rectangular plate presented in this paper within the extended thermodynamical model shows that

- energy dissipation is lower in an auxetic material then in normal material,
- thermoelastic damping decreases if forcing frequency increases,
- unconventional behavior of materials occurs in the vicinity of the resonance frequency ω_R, and
- only the imaginary parts of the bending and temperature amplitudes depend on the thermal relaxation time.

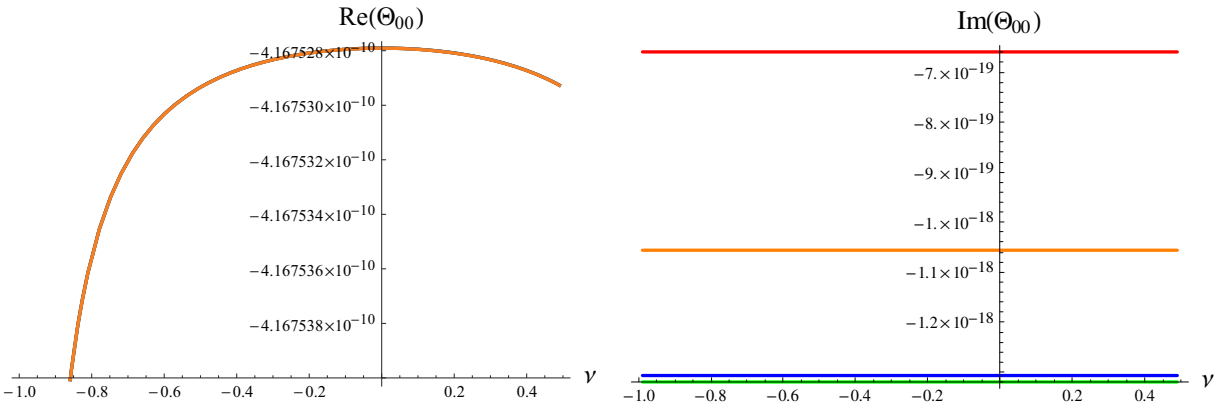

Figure 9. Real and imaginary parts of the temperature distribution θ_{00} versus the Poisson's ratio for different thermal relaxation times, with high frequency $\omega = 10^5\,\mathrm{s}^{-1}$. On the left, the graph of $\mathrm{Re}(\theta_{00})$ remains essentially the same for $\tau = 10^{-10}\,\mathrm{s}$, $\tau = 10^{-8}\,\mathrm{s}$, $\tau = 10^{-6}\,\mathrm{s}$, and $\tau = 5 \times 10^{-6}\,\mathrm{s}$. On the right, $\tau = 10^{-8}\,\mathrm{s}$ (blue), $\tau = 10^{-6}\,\mathrm{s}$ (green), $\tau = 10^{-5}\,\mathrm{s}$ (red), and $\tau = 5 \times 10^{-6}\,\mathrm{s}$ (orange).

References

[Alblas 1961] J. B. Alblas, "On the general theory of thermo-elastic friction", *Appl. Sci. Res. A* **10**:1 (1961), 349–362.

[Alblas 1981] J. B. Alblas, "A note on the theory of thermoelastic damping", *J. Therm. Stresses* **4**:3–4 (1981), 333–355.

[Almgren 1985] R. F. Almgren, "An isotropic three-dimensional structure with Poisson's ratio $= -1$", *J. Elasticity* **15**:4 (1985), 427–430.

[Bishop and Kinra 1993] J. E. Bishop and V. K. Kinra, "Thermoelastic damping of a laminated beam in flexure and extension", *J. Reinf. Plast. Compos.* **12**:2 (1993), 210–226.

[Bishop and Kinra 1994] J. E. Bishop and V. K. Kinra, "Elastothermodynamic damping in composite materials", *Mech. Compos. Mater. Struct.* **1**:1 (1994), 75–93.

[Boley and Weiner 1960] B. A. Boley and J. H. Weiner, *Theory of thermal stresses*, Wiley, New York, 1960.

[Cattaneo 1958] C. Cattaneo, "Sur une form de l'équation de la chaleur éliminant le paradoxe d'une propagation instantanée", *C. R. Hebd. Séances Acad. Sci.* **247** (1958), 431–433.

[Chester 1963] M. Chester, "Second sound in solids", *Phys. Rev.* **131**:5 (1963), 2013–2015.

[Ignaczak and Ostoja-Starzewski 2010] J. Ignaczak and M. Ostoja-Starzewski, *Thermoelasticity with finite wave speeds*, Oxford University Press, 2010.

[Jou et al. 1988] D. Jou, J. Casas-Vázquez, and G. Lebon, "Extended irreversible thermodynamics", *Rep. Prog. Phys.* **51**:8 (1988), 1105–1179.

[Khisaeva and Ostoja-Starzewski 2006] Z. F. Khisaeva and M. Ostoja-Starzewski, "Thermoelastic damping in nanomechanical resonators with finite wave speeds", *J. Therm. Stresses* **29**:3 (2006), 201–216.

[Kinra and Milligan 1994] V. K. Kinra and K. B. Milligan, "A second-law analysis of thermoelastic damping", *J. Appl. Mech.* (*ASME*) **61**:1 (1994), 71–76.

[Kołat et al. 2010] P. Kołat, B. T. Maruszewski, and K. W. Wojciechowski, "Solitary waves in auxetic plates", *J. Non-Cryst. Solids* **356**:37–40 (2010), 2001–2009.

[Kołat et al. 2011] P. Kołat, B. T. Maruszewski, K. V. Tretiakov, and K. W. Wojciechowski, "Solitary waves in auxetic rods", *Phys. Status Solidi B* **248**:1 (2011), 148–157.

[Lakes 1987] R. Lakes, "Foam structures with a negative Poisson's ratio", *Science* **235**:4792 (1987), 1038–1040.

[Lebon 1982] G. Lebon, "A generalized theory of thermoelasticity", *J. Tech. Phys.* **23** (1982), 37–46.

[Lifshitz and Roukes 2000] R. Lifshitz and M. L. Roukes, "Thermoelastic damping in micro- and nanomechanical systems", *Phys. Rev. B* **61**:8 (2000), 5600–5609.

[Maruszewski 1988] B. T. Maruszewski, "Evolution equations of thermodiffusion in paramagnets", *Int. J. Eng. Sci.* **26**:11 (1988), 1217–1230.

[Maruszewski 1992] B. T. Maruszewski, "Nonlinear thermoelastic damping in a circular plate", *Z. Angew. Math. Mech.* **72**:4 (1992), T75–T78.

[Milligan and Kinra 1993] K. B. Milligan and V. K. Kinra, "On the thermoelastic damping of a one-dimensional inclusion in a uniaxial bar", *Mech. Res. Commun.* **20**:2 (1993), 137–142.

[Nayfeh and Younis 2004] A. H. Nayfeh and M. I. Younis, "Modeling and simulations of thermoelastic damping in microplates", *J. Micromech. Microeng.* **14**:12 (2004), 1711–1717.

[Noda et al. 2003] N. Noda, R. B. Hetnarski, and Y. Tanigawa, *Thermal stresses*, 2nd ed., Taylor & Francis, New York, 2003.

[Novikov and Wojciechowski 1999] V. V. Novikov and K. W. Wojciechowski, "Negative Poisson's coefficients of fractal structures", *Phys. Solid State* **41**:12 (1999), 1970–1975.

[Nowacki 1962] W. Nowacki, *Thermoelasticity*, Pergamon, Oxford, 1962.

[Nowacki 1975] W. Nowacki, *Dynamic problems of thermoelasticity*, Noordhoff, Leyden, 1975.

[Poźniak et al. 2010] A. A. Poźniak, H. Kamiński, P. Kędziora, B. T. Maruszewski, T. Stręk, and K. W. Wojciechowski, "Anomalous deformation of constrained auxetic square", *Rev. Adv. Mater. Sci.* **23**:2 (2010), 169–174.

[Prabhakar and Vengallatore 2008] S. Prabhakar and S. Vengallatore, "Theory of thermoelastic damping in micromechanical resonators with two-dimensional heat conduction", *J. Micromech. Syst.* **17**:2 (2008), 494–502.

[Vengallatore 2005] S. Vengallatore, "Analysis of thermoelastic damping in laminated composite micromechanical beam resonators", *J. Micromech. Microeng.* **15**:12 (2005), 2398–2404.

[Vernotte 1958] P. Vernotte, "Les paradoxes de la théorie continue de l'équation de la chaleur", *C. R. Hebd. Séances Acad. Sci.* **246** (1958), 3154–3155.

[Wojciechowski 1989] K. W. Wojciechowski, "Two-dimensional isotropic system with a negative Poisson ratio", *Phys. Lett. A* **137**:1–2 (1989), 60–64.

[Zener 1937] C. Zener, "Internal friction in solids, I: Theory of internal friction in reeds", *Phys. Rev.* **52**:3 (1937), 230–235.

Received 8 Mar 2013. Revised 25 Sep 2013. Accepted 1 Oct 2013.

BOGDAN T. MARUSZEWSKI: bogdan.maruszewski@put.poznan.pl
Poznan University of Technology, Institute of Applied Mechanics, ul. Jana Pawła II 24, 60-965 Poznan, Poland

ANDRZEJ DRZEWIECKI: andrzej.drzewiecki@put.poznan.pl
Poznan University of Technology, Institute of Applied Mechanics, ul. Jana Pawła II 24, 60-965 Poznan, Poland

ROMAN STAROSTA: roman.starosta@put.poznan.pl
Poznan University of Technology, Institute of Applied Mechanics, ul. Jana Pawła II 24, 60-965 Poznan, Poland

LILIANA RESTUCCIA: lrestuccia@unime.it
University of Messina, Department of Mathematics, Contrada Papardo, Salita Sperone 31, 98166 Messina, Italy

JOURNAL OF MECHANICS OF MATERIALS AND STRUCTURES
Vol. 8, No. 8-10, 2013
dx.doi.org/10.2140/jomms.2013.8.415

WORST-CASE LOAD IN PLASTIC LIMIT ANALYSIS OF FRAME STRUCTURES

YOSHIHIRO KANNO

This paper addresses the plastic limit analysis of a frame structure under uncertainty in the external load. Given a bounded set in which an external load can vary, we attempt to find the worst load that minimizes the limit load factor. It is shown that this problem can be formulated as a mixed-integer linear programming problem. The global optimal solution of this optimization problem can be found by using an existing algorithm, e.g., a branch-and-cut method. Guaranteed convergence to a global optimal solution is important because it implies that the proposed method yields neither overestimation nor underestimation in this uncertainty analysis problem. Two numerical examples illustrate that the worst scenario problem can be solved with modest computational effort. They also show that not only does the limit load factor depend on the level of uncertainty in the external load, but the collapse mode as well.

1. Introduction

This paper presents a numerical method for finding the worst-case loading in plastic limit analysis of a frame structure. Possibilistic (or bounded-but-unknown) models, rather than probabilistic models, are employed to represent the uncertainty in the external load. Then the worst scenario is defined as the external load with which the plastic limit load factor attains the minimum value.

Since real-world structures inevitably encounter various uncertainties stemming from manufacturing variability, aging, limitation of knowledge of input disturbance, etc., the concept of robustness to uncertainty is central in structural design [Zang et al. 2005; Beyer and Sendhoff 2007; Schuëller and Jensen 2008; Valdebenito and Schuëller 2010]. Probabilistic and possibilistic methods for analysis and design of structures under uncertainties have been compared in the literature [Langley 2000; Nikolaidis et al. 2004]. If a reliable statistical property of uncertainty is available, then probabilistic reliability analysis can be performed. In contrast, a possibilistic model of uncertainty might be applicable to problems without reliable stochastic information, because it requires only bounds for the input data to define the uncertainty and hence is often less information intensive. In this case, the key is to analyze the worst scenario, that is, the most severe scenario among a given set of scenarios, in order to assess the robustness of the structure [Ben-Haim and Elishakoff 1990; Hlaváček et al. 2004; Ben-Haim 2006]. The problem of finding the worst scenario, called the *worst scenario problem*, is formulated as an optimization problem, and the worst scenario corresponds to its optimal solution. It is worth noting that the worst scenario

This work is supported in part by Grant-in-Aid for Scientific Research (C) 23560663 from the Japan Society for the Promotion of Science.

Keywords: robustness, uncertainty, worst scenario detection, plastic limit analysis, global optimization, mixed-integer programming.

problem should be solved by an algorithm with guaranteed global convergence, because, obviously, a local (but not global) optimal solution is not necessarily the worst scenario. In this paper attention is focused on development of a global optimization method for the worst scenario problem.

There exists a vast literature on numerical methods for worst scenario problems. The so-called convex modeling approach [Ben-Haim and Elishakoff 1990] is one of the best-known methods and has been applied in many areas. Interval arithmetic, originally developed for finding bounds on round-off errors [Neumaier 1990; Alefeld and Mayer 2000], has also been applied to various problems in mechanics [McWilliam 2001; Chen et al. 2002; De Gersem et al. 2007; Neumaier and Pownuk 2007; Degrauwe et al. 2010]. It finds a conservative bound, i.e., an outer bound, for the response of a structural system with uncertainty; for details, as well as surveys on other nonprobabilistic uncertainty analyses, see [Moens and Vandepitte 2005], [Möller and Beer 2008], and [Moens and Hanss 2011]. Since the worst scenario problem is formulated as an optimization problem, it might be natural to use an optimization algorithm for finding the worst scenario. However, direct use of a conventional nonlinear programming approach is not guaranteed to provide a conservative solution, unless the worst scenario problem is convex. Also, metaheuristics including genetic algorithms, which have been applied to complex engineering systems [Biondini et al. 2004; Catallo 2004], do not necessarily converge to the global optimal solution and hence their solutions are on the unsafe side in general. For nonconvex worst scenario problems, two nontraditional approaches have been recently developed to ensure conservativeness: one is to construct a convex approximation problem that provides a conservative bound, while the other is to reformulate the original worst scenario problem to another equivalent optimization problem for which an algorithm with guaranteed convergence to the global optimal solution is available. Taking the former approach, semidefinite programming approximations have been developed for static problems [Kanno and Takewaki 2006; 2008; Guo et al. 2009; 2011] and a dynamic steady-state problem [Kanno and Takewaki 2009]. With the latter approach, *mixed-integer linear programming* (MILP) formulations have been studied for static analysis [Guo et al. 2008] and plastic limit analysis of trusses [Kanno and Takewaki 2007; Kanno 2012]. Although this MILP approach is applicable only in some specific cases, its distinguishing feature is guaranteed convergence to the exact worst case; in other words, it returns neither overestimation nor underestimation.

In [Kanno and Takewaki 2007] an MILP formulation was developed to solve the worst scenario problem in the plastic limit analysis of a truss, where the external load was considered uncertain and assumed to be included in a given convex set. In a continuation of this work, we extend the result to frame structures. It is shown that the worst scenario problem of a frame structure can also be converted to an MILP problem, provided that the yield surface is represented by a piecewise linear function of the axial force and the end moment. The global optimal solution of an MILP problem can be found with, e.g., a branch-and-cut algorithm; several well-developed software packages, e.g., Gurobi Optimizer [Gurobi 2013] and CPLEX [IBM ILOG 2011], are available for this purpose. Guaranteed convergence to a global optimal solution implies that the exact worst case can be found by the proposed method. Since we restrict ourselves to the case of piecewise linear yield functions, the problem for frame structures in this paper is not much different from the one for trusses in [Kanno and Takewaki 2007] from a mathematical point of view. For instance, the limit analysis problems of both structures can be formulated as *linear programming* (LP) problems, although, due to the effect of interaction between the axial force and the end moment, the formulation for frame structures is slightly more complicated. From an engineering

point of view, however, limit analysis that can deal with frame structures has more significance than analysis that is limited to trusses. Also, in [Kanno and Takewaki 2007] the worst-case load is found by solving a MILP problem with generation of some disjunctive cuts and a subsequent naive branch-and-bound method with depth-first search. Accordingly, the size of problems that could be solved was limited. In contrast, in this paper the efficiency of a commercial software package, CPLEX [IBM ILOG 2011], is examined.

Note that an MILP problem is a minimization, or maximization, problem of a linear function under linear constraints, where some of the variables are constrained to be integers and the remaining variables are considered to be continuous real variables. Specifically, the MILP problem solved in this paper is of the form

$$\text{Minimize } \boldsymbol{c}^{\mathrm{T}}\boldsymbol{x} + \boldsymbol{g}^{\mathrm{T}}\boldsymbol{y} \tag{1a}$$

$$\text{subject to } \boldsymbol{A}\boldsymbol{x} + \boldsymbol{F}\boldsymbol{y} = \boldsymbol{b}, \tag{1b}$$

$$\boldsymbol{x} \in \{0, 1\}^n, \tag{1c}$$

$$\boldsymbol{y} \geq \boldsymbol{0}. \tag{1d}$$

Here $\boldsymbol{x} \in \mathbb{R}^n$ and $\boldsymbol{y} \in \mathbb{R}^p$ are variables to be optimized, $\boldsymbol{A} \in \mathbb{R}^{m\times n}$ and $\boldsymbol{F} \in \mathbb{R}^{m\times p}$ are constant matrices, and $\boldsymbol{c} \in \mathbb{R}^n$, $\boldsymbol{g} \in \mathbb{R}^p$, and $\boldsymbol{b} \in \mathbb{R}^m$ are constant vectors. Problem (1) is also called a mixed 0-1 linear programming problem, because the integer variables, $x_1, \ldots, x_n$, are restricted to being either 0 or 1. If we replace the binary constraints, (1c), with linear inequality constraints, $0 \leq x_j \leq 1$ $(j = 1, \ldots, n)$, then the resulting relaxation problem is an LP problem. By virtue of this property, a global solution of (1) can be found by enumerating all possible realizations of binary variables, $x_1, \ldots, x_n$. To make this enumeration more efficient, a branch-and-bound method discards hopeless candidates by making use of upper and lower bounds on the objective function. Efficient software packages for solving MILP usually implement a branch-and-cut method, which is a combination of a branch-and-bound method and a cutting-plane method. A cutting-plane method iteratively generates valid inequalities of (1), called cuts, to refine the feasible set of the relaxation problem; see, for example, [Wolsey 1998], [Faigle et al. 2002], and [Aardal et al. 2005] for fundamentals of MILP and related algorithms.

Limit analysis under probabilistic uncertainties has been studied within several frameworks. For evaluating the probability of plastic collapse, the first and second-order methods in reliability analysis were employed in [Bjerager 1989; Wang et al. 1994; Staat and Heitzer 2003; Trần et al. 2009] and the stochastic programming approach was applied in [Sikorski and Borkowski 1990; Marti and Stoeckl 2004; Marti 2008]. When the yield strengths are assumed to be stochastic variables, the conditional probability of collapse, that is, the probability of plastic collapse under the given load, was evaluated in [Caddemi et al. 2002; Alibrandi and Ricciardi 2008]. The classical optimal plastic design is to find a structural design that minimizes the total structural volume under the constraint on the plastic limit load factor. For this problem, fuzzy LP approaches were proposed in [Munro and Chuang 1986; Jung and Pulmano 1996], where uncertainty was modeled by employing fuzzy set theory. Unlike those studies, this paper addresses possibilistic uncertainty models in the external load and attempts to find the worst loading scenario.

This paper is organized as follows. Section 2 prepares LP formulations for the conventional limit analysis of frame structures. Section 3 presents our main result: The worst scenario problem in limit

analysis is reformulated to an MILP problem. Two numerical experiments are performed in Section 4. We conclude in Section 5. Proofs of propositions appear in the Appendix.

A few words regarding notation. All vectors are assumed to be column vectors. The $(m+n)$-dimensional column vector $(\boldsymbol{v}^{\mathrm{T}}, \boldsymbol{x}^{\mathrm{T}})^{\mathrm{T}}$ consisting of $\boldsymbol{v} \in \mathbb{R}^m$ and $\boldsymbol{x} \in \mathbb{R}^n$ is often written simply as $(\boldsymbol{v}, \boldsymbol{x})$. For two vectors $\boldsymbol{x} = (x_1, \ldots, x_n)^{\mathrm{T}} \in \mathbb{R}^n$ and $\boldsymbol{y} = (y_1, \ldots, y_n)^{\mathrm{T}} \in \mathbb{R}^n$, we write $\boldsymbol{x} \geq \boldsymbol{y}$ if $x_i \geq y_i$ $(i = 1, \ldots, n)$. Particularly, $\boldsymbol{x} \geq \boldsymbol{0}$ means $x_i \geq 0$ $(i = 1, \ldots, n)$. The ℓ^1-norm and the ℓ^∞-norm of vector $\boldsymbol{x} \in \mathbb{R}^n$ are defined by

$$\|\boldsymbol{x}\|_1 = \sum_{i=1}^{n} |x_i|, \quad \|\boldsymbol{x}\|_\infty = \max_{i=1,\ldots,n} |x_i|.$$

We use $\boldsymbol{1} = (1, 1, \ldots, 1)^{\mathrm{T}}$ to denote the all-ones vector.

2. Fundamentals of limit analysis

This section summarizes LP formulations of the conventional limit analysis of frame structures. Section 2A describes the yield conditions that we adopt in this paper. Section 2B presents an LP formulation of the lower bound principle. The dual problem which corresponds to the upper bound principle is presented in Section 2C.

2A. ***Yield conditions.*** In this paper we consider only planar frame structures for simplicity. Spatial frames can be dealt with in the same manner.

Suppose that the frame structure consists of E beam elements. Let $\boldsymbol{s}_e \in \mathbb{R}^3$ denote the generalized stress vector of member e $(e = 1, \ldots, E)$. For example, the components of $\boldsymbol{s}_e \in \mathbb{R}^3$ can be chosen as

$$\boldsymbol{s}_e = \begin{bmatrix} q_e \\ m_e^{(1)} \\ m_e^{(2)} \end{bmatrix},$$

where q_e is the axial force and $m_e^{(1)}$ and $m_e^{(2)}$ are the end moments. The yield condition of member e is assumed to be written in the form

$$\|\boldsymbol{A}_{e,j}\boldsymbol{s}_e\|_1 \leq R_{e,j}, \quad j = 1, \ldots, J. \tag{2}$$

Two concrete examples of (2) are given in Examples 2.1 and 2.2.

Example 2.1. Suppose that the dependence of the yield condition on the shear force is negligible. Consider a piecewise linear yield surface in Figure 1, which involves the simple effect of interaction between the axial force and the end moment. This yield condition is written as

$$\frac{|q_e|}{q_e^{\mathrm{y}}} + \frac{|m_e^{(1)}|}{m_e^{\mathrm{y}}} \leq 1, \tag{3a}$$

$$\frac{|q_e|}{q_e^{\mathrm{y}}} + \frac{|m_e^{(2)}|}{m_e^{\mathrm{y}}} \leq 1, \tag{3b}$$

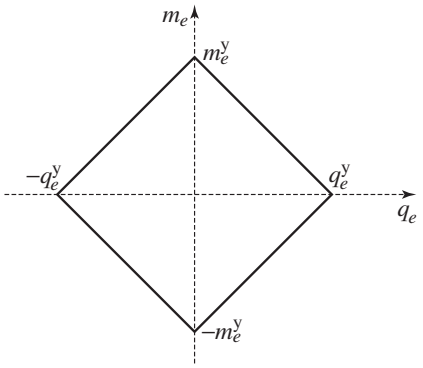

Figure 1. Yield surface of a beam element in Example 2.1.

where q_e^{y} and m_e^{y} are admissible absolute values of the axial force and the end moment, respectively. Let $J = 2$. Define matrices $\boldsymbol{A}_{e,j}$ $(j = 1, 2)$ by

$$\boldsymbol{A}_{e,1} = \begin{bmatrix} 1/q_e^{\mathrm{y}} & 0 & 0 \\ 0 & 1/m_e^{\mathrm{y}} & 0 \end{bmatrix}, \quad \boldsymbol{A}_{e,2} = \begin{bmatrix} 1/q_e^{\mathrm{y}} & 0 & 0 \\ 0 & 0 & 1/m_e^{\mathrm{y}} \end{bmatrix},$$

and constants $R_{e,j}$ $(j = 1, 2)$ by

$$R_{e,1} = R_{e,2} = 1.$$

Then yield condition (3) is written in the form of (2).

Example 2.2. As a piecewise linear model slightly more complex than Example 2.1, consider the yield surface depicted in Figure 2. Here $\kappa \in (1, \sqrt{2})$ is a constant.[1] This yield condition is formulated as

$$\frac{|q_e|}{\kappa q_e^{\mathrm{y}}} + \frac{|m_e^{(1)}|}{\kappa m_e^{\mathrm{y}}} \le 1, \quad \left|\frac{q_e}{2q_e^{\mathrm{y}}} + \frac{m_e^{(1)}}{2m_e^{\mathrm{y}}}\right| + \left|\frac{-q_e}{2q_e^{\mathrm{y}}} + \frac{m_e^{(1)}}{2m_e^{\mathrm{y}}}\right| \le 1, \tag{4a}$$

$$\frac{|q_e|}{q_e^{\mathrm{y}}} + \frac{|m_e^{(2)}|}{m_e^{\mathrm{y}}} \le 1, \quad \left|\frac{q_e}{2q_e^{\mathrm{y}}} + \frac{m_e^{(2)}}{2m_e^{\mathrm{y}}}\right| + \left|\frac{-q_e}{2q_e^{\mathrm{y}}} + \frac{m_e^{(2)}}{2m_e^{\mathrm{y}}}\right| \le 1. \tag{4b}$$

Let $J = 4$ and define $\boldsymbol{A}_{e,j}$ by

$$\boldsymbol{A}_{e,1} = \begin{bmatrix} 1/\kappa q_e^{\mathrm{y}} & 0 & 0 \\ 0 & 1/\kappa m_e^{\mathrm{y}} & 0 \end{bmatrix}, \quad \boldsymbol{A}_{e,3} = \begin{bmatrix} 1/2q_e^{\mathrm{y}} & 1/2m_e^{\mathrm{y}} & 0 \\ -1/2q_e^{\mathrm{y}} & 1/2m_e^{\mathrm{y}} & 0 \end{bmatrix}, \tag{5a}$$

$$\boldsymbol{A}_{e,2} = \begin{bmatrix} 1/\kappa q_e^{\mathrm{y}} & 0 & 0 \\ 0 & 0 & 1/\kappa m_e^{\mathrm{y}} \end{bmatrix}, \quad \boldsymbol{A}_{e,4} = \begin{bmatrix} 1/2q_e^{\mathrm{y}} & 0 & 1/2m_e^{\mathrm{y}} \\ -1/2q_e^{\mathrm{y}} & 0 & 1/2m_e^{\mathrm{y}} \end{bmatrix}, \tag{5b}$$

and $R_{e,j}$ by

$$R_{e,1} = R_{e,2} = R_{e,3} = R_{e,4} = 1.$$

Then (4) is expressed by (2).

[1] If $\kappa \le 1$, then (4) is reduced to (3) in Example 2.1. On the other hand, if $\kappa \ge \sqrt{2}$, (4) is reduced to a box constraint, i.e., $|q_e| \le q_e^{\mathrm{y}}$, $|m_e^{(1)}| \le m_e^{\mathrm{y}}$, and $|m_e^{(2)}| \le \mu_e^{\mathrm{y}}$, which does not involve interaction between the axial force and the end moment.

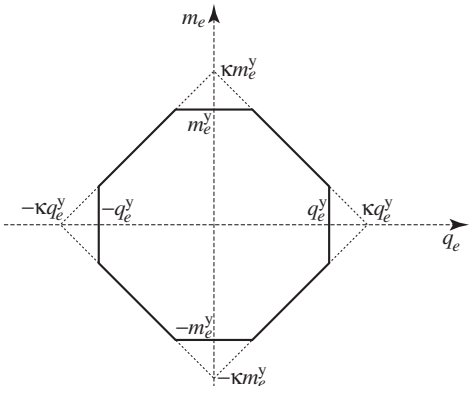

Figure 2. Piecewise linear yield surface in Example 2.2.

2B. ***Lower bound principle.*** Suppose that the external load consists of a constant part, denoted by $\boldsymbol{p}$, and a proportionally increasing part, expressed as $\lambda \boldsymbol{f}$. The constant vector $\boldsymbol{f} \in \mathbb{R}^d \setminus \{\boldsymbol{0}\}$ is called the *reference load*, where d is the number of displacement degrees of freedom. The parameter $\lambda \in \mathbb{R}$ is called the *load factor*. The force-balance equation is written as

$$\boldsymbol{H}\boldsymbol{s} = \boldsymbol{p} + \lambda \boldsymbol{f}, \tag{6}$$

where $\boldsymbol{H} \in \mathbb{R}^{d\times 3E}$ is the equilibrium matrix and $\boldsymbol{s} = (\boldsymbol{s}_1^{\mathrm{T}}, \ldots, \boldsymbol{s}_E^{\mathrm{T}}) \in \mathbb{R}^{3E}$.

From the lower bound principle, the limit load factor, denoted $\bar{\lambda}$, is defined as the maximum value of λ under the yield condition (2) and the force-balance equation (6). Specifically, $\bar{\lambda}$ is the optimal value of the following optimization problem:

$$\begin{aligned} &\text{Maximize } \lambda \text{ over } \lambda, \boldsymbol{s} \\ &\text{subject to} \quad \boldsymbol{H}\boldsymbol{s} = \boldsymbol{p} + \lambda \boldsymbol{f}, \\ &\qquad\qquad \|\boldsymbol{A}_{e,j}\boldsymbol{T}_e\boldsymbol{s}\|_1 \le R_{e,j}, \quad e = 1, \ldots, E, \ \ j = 1, \ldots, J. \end{aligned} \tag{7}$$

Here for each $e = 1, \ldots, E$, $\boldsymbol{T}_e \in \mathbb{R}^{3\times 3E}$ is a constant matrix satisfying

$$\boldsymbol{T}_e\boldsymbol{s} = \begin{bmatrix} q_e \\ m_e^{(1)} \\ m_e^{(2)} \end{bmatrix}.$$

Throughout the paper we assume that problem (7) is feasible and its optimal value is bounded above.

Remark 2.3. Problem (7) can be solved as an LP problem. To see this, it suffices to show that constraint $\|\boldsymbol{A}_{e,j}\boldsymbol{T}_e\boldsymbol{s}\|_1 \le R_{e,j}$ can be converted to some linear inequality constraints. We begin with the following slightly simpler form:

$$\|\boldsymbol{x}\|_1 = \sum_{i=1}^{n} |x_i| \le b. \tag{8}$$

For each $i = 1, \ldots, n$, let ξ_i be an additional variable that serves as an upper bound for $|x_i|$, that is, $|x_i| \le \xi_i$. This relation is written as the following linear inequality constraints:

$$-\xi_i \le x_i \le \xi_i, \quad i = 1, \ldots, n. \tag{9}$$

Then $\sum_{i=1}^{n} \xi_i$ becomes an upper bound for $\|\boldsymbol{x}\|_1$. Therefore, (8) is rewritten as (9) and

$$\sum_{i=1}^{n} \xi_i \le b. \tag{10}$$

In the same manner, the constraint $\|\boldsymbol{A}_{e,j}\boldsymbol{T}_e\boldsymbol{s}\|_1 \le R_{e,j}$ in problem (7) can be converted to finitely many linear inequality constraints. Let $|\boldsymbol{A}_{e,j}\boldsymbol{T}_e\boldsymbol{s}|$ be a vector of the absolute values of the components of $\boldsymbol{A}_{e,j}\boldsymbol{T}_e\boldsymbol{s}$. Use a vector of additional variables, $\boldsymbol{\eta}_{e,j}$, to express upper bounds for components of $|\boldsymbol{A}_{e,j}\boldsymbol{T}_e\boldsymbol{s}|$, that is, $|\boldsymbol{A}_{e,j}\boldsymbol{T}_e\boldsymbol{s}| \le \boldsymbol{\eta}_{e,j}$. Then, the sum of components of $\boldsymbol{\eta}_{e,j}$, that is, $\mathbf{1}^{\mathrm{T}}\boldsymbol{\eta}_{e,j}$, serves as an upper bound for $\|\boldsymbol{A}_{e,j}\boldsymbol{T}_e\boldsymbol{s}\|_1$. Therefore, problem (7) can be rewritten as

$$\begin{aligned} &\text{Maximize } \lambda \text{ over } \lambda, \boldsymbol{s}, \boldsymbol{\eta} \\ &\text{subject to} \quad \boldsymbol{H}\boldsymbol{s} = \boldsymbol{p} + \lambda \boldsymbol{f}, \\ &\qquad\qquad R_{e,j} \ge \mathbf{1}^{\mathrm{T}}\boldsymbol{\eta}_{e,j}, \qquad\qquad j = 1, \ldots, J, \quad e = 1, \ldots, E, \\ &\qquad\qquad -\boldsymbol{\eta}_{e,j} \le \boldsymbol{A}_{e,j}\boldsymbol{T}_e\boldsymbol{s} \le \boldsymbol{\eta}_{e,j}, \quad j = 1, \ldots, J, \quad e = 1, \ldots, E, \end{aligned} \tag{11}$$

which is clearly an LP problem.

2C. ***Upper bound principle.*** In Section 2B we have formulated the limit analysis problem, (7), based on the lower bound principle. The upper bound principle corresponds to the dual problem. In Section 3 we shall use the upper bound principle to formulate the worst scenario problem.

Let $\boldsymbol{u} \in \mathbb{R}^d$ denote the vector of nodal displacements. We use $\boldsymbol{z}_{e,j}$ to denote the generalized strain vector that is conjugate to $\boldsymbol{A}_{e,j}\boldsymbol{T}^{\mathrm{T}}\boldsymbol{s}$. The dual problem of problem (7) can be formulated in variables $\boldsymbol{u}$, $\gamma_{e,j}$, and $\boldsymbol{z}_{e,j}$ ($e = 1, \ldots, E$ and $j = 1, \ldots, J$) as

$$\begin{aligned} &\text{Minimize } -\boldsymbol{p}^{\mathrm{T}}\boldsymbol{u} + \sum_{e=1}^{E}\sum_{j=1}^{J} R_{e,j}\gamma_{e,j} \text{ over } \boldsymbol{u}, \boldsymbol{\gamma}, \boldsymbol{z} \\ &\text{subject to} \quad \boldsymbol{f}^{\mathrm{T}}\boldsymbol{u} = 1, \\ &\qquad\qquad \sum_{e=1}^{E}\sum_{j=1}^{J} (\boldsymbol{A}_{e,j}\boldsymbol{T}_e)^{\mathrm{T}}\boldsymbol{z}_{e,j} = \boldsymbol{H}^{\mathrm{T}}\boldsymbol{u}, \\ &\qquad\qquad \gamma_{e,j} \ge \|\boldsymbol{z}_{e,j}\|_\infty, \quad e = 1, \ldots, E, \ j = 1, \ldots, J. \end{aligned} \tag{12}$$

See Section A.1 for the derivation of (12). At the optimal solution we obtain $\gamma_{e,j} = \|\boldsymbol{z}_{e,j}\|_\infty$ ($e = 1, \ldots, E$; $j = 1, \ldots, J$), because $R_{e,j}\gamma_{e,j}$ is minimized under constraint $\gamma_{e,j} \ge \|\boldsymbol{z}_{e,j}\|_\infty$. Thus $\gamma_{e,j}$ becomes equal to the sum of the absolute values of the generalized plastic strain at the j-th end of member e.

Remark 2.4. Problem (12) can be solved as an LP problem. Indeed, the constraint $\gamma_{e,j} \ge \|\boldsymbol{z}_{e,j}\|_\infty$ of (12) can be rewritten as

$$-\gamma_{e,j}\mathbf{1} \le \boldsymbol{z}_{e,j} \le \gamma_{e,j}\mathbf{1},$$

which is a system of linear inequalities.

With reference to Remarks 2.3 and 2.4, the duality theory of LP implies that problems (7) and (12) share the same optimal value, because we assume that (7) has an optimal solution. In short, the optimal value of (12) is equal to $\bar{\lambda}$.

3. Worst scenario detection

In Section 3A we formally define the worst-case load, where the ℓ^∞-norm of uncertain parameters is bounded. Section 3B shows that the worst-case load can be obtained as the optimal solution of an MILP problem. This problem can be solved globally by using an existing algorithm, e.g., a branch-and-bound method. Section 3C explores the worst scenario problem in which the ℓ^1-norm of uncertain parameters is bounded.

3A. ***Definition of worst-case load.*** As summarized in Section 2, the limit load factor, $\bar{\lambda}$, of a given frame structure is determined when the load vectors, $\boldsymbol{p}$ and $\boldsymbol{f}$, are specified. In the following, $\bar{\lambda}$ is considered a function of $\boldsymbol{p}$, i.e., $\bar{\lambda}(\boldsymbol{p})$, while $\boldsymbol{f}$ is assumed to be fixed. In other words, we suppose that only $\boldsymbol{p}$ is uncertain.

Uncertainty in $\boldsymbol{p}$ is modeled as follows. Let $\tilde{\boldsymbol{p}} \in \mathbb{R}^d$ denote the nominal value, or the best estimate, of $\boldsymbol{p}$. We use an unknown vector $\boldsymbol{\zeta} \in \mathbb{R}^L$ $(L \le d)$ to express uncertainty in $\boldsymbol{p}$. Suppose that $\boldsymbol{p}$ depends on $\boldsymbol{\zeta}$ affinely as

$$\boldsymbol{p} = \tilde{\boldsymbol{p}} + \boldsymbol{Q}\boldsymbol{\zeta} \tag{13}$$

and that the norm of $\boldsymbol{\zeta}$ is known to be bounded. Here $\boldsymbol{Q} \in \mathbb{R}^{d\times L}$ is a constant matrix satisfying rank $\boldsymbol{Q} = L$. The unknown vector $\boldsymbol{Q}\boldsymbol{\zeta} \in \mathbb{R}^d$ corresponds to the difference between the actual load, $\boldsymbol{p}$, and the estimated load, $\tilde{\boldsymbol{p}}$. The number of independently varying components of uncertain load, $\boldsymbol{Q}\boldsymbol{\zeta}$, is L. The set of all such loading scenarios is given by

$$P(\alpha, \tilde{\boldsymbol{p}}) = \{\tilde{\boldsymbol{p}} + \boldsymbol{Q}\boldsymbol{\zeta} \mid \|\boldsymbol{\zeta}\|_\infty \le \alpha\}, \tag{14}$$

where $\alpha \ge 0$ is a constant. We call $P(\alpha, \tilde{\boldsymbol{p}})$ the *uncertainty set* of the load. Parameter α, called the *uncertainty parameter*, expresses the level of uncertainty in the following sense [Ben-Haim 2006]:

(i) $P(0, \tilde{\boldsymbol{p}}) = \{\tilde{\boldsymbol{p}}\}$ and

(ii) $\alpha \le \alpha'$ implies $P(\alpha, \tilde{\boldsymbol{p}}) \subseteq P(\alpha', \tilde{\boldsymbol{p}})$.

Namely, (i) only the nominal loading scenario is considered at $\alpha = 0$ and (ii) the range of possible scenarios of external loads increases as α increases.

For given α and $\tilde{\boldsymbol{p}}$, vector $\boldsymbol{p}$ takes any value in $P(\alpha, \tilde{\boldsymbol{p}})$. The limit load factor in the worst scenario is then defined as the minimum value of $\bar{\lambda}(\boldsymbol{p})$. Formally, the *worst-case limit load factor*, denoted $\lambda_{\min}(\alpha, \tilde{\boldsymbol{p}})$, for a given α and $\tilde{\boldsymbol{p}}$ is defined by

$$\lambda_{\min}(\alpha, \tilde{\boldsymbol{p}}) = \min\{\bar{\lambda}(\boldsymbol{p}) \mid \boldsymbol{p} \in P(\alpha, \tilde{\boldsymbol{p}})\}. \tag{15}$$

Accordingly, the worst-case load, denoted $\boldsymbol{p}_{\mathrm{w}}$, is defined as the optimal solution of this maximization problem, i.e.,

$$\boldsymbol{p}_{\mathrm{w}} \in \arg\min\{\bar{\lambda}(\boldsymbol{p}) \mid \boldsymbol{p} \in P(\alpha, \tilde{\boldsymbol{p}})\}. \tag{16}$$

It is worth noting that this optimization problem should be solved by an algorithm with guaranteed convergence to a global optimal solution, because, obviously, a local (but not global) optimal solution is not the most severe scenario. In Section 3B, we shall reduce problem (16) to an MILP problem, the global optimal solution of which can be found with an existing algorithm.

Remark 3.1. Since both the set of admissible (generalized) stress vectors and the set of uncertain external loads are polytopes, the worst-case load, $\boldsymbol{p}_{\mathrm{w}}$, in (16) can be found by enumerating all vertices of polytope $P(\alpha, \tilde{\boldsymbol{p}})$. Actually this is similar to what is often done in shakedown analysis; see, for example, [Polizzotto 1982], [Ngo and Tin-Loi 2007], [Simon and Weichert 2012], and references therein. However, enumeration of all vertices immediately becomes inexecutable when L, i.e., the number of independently varying components of the uncertain load, increases, because $P(\alpha, \tilde{\boldsymbol{p}})$ has 2^L vertices. For instance, in the numerical example of Section 4A we suppose $L = 55$, which results in $2^{55} \simeq 3.6 \times 10^{16}$ vertices. We use an MILP approach to deal with such problems.

Remark 3.2. The notion of the worst-case load has been introduced as the loading scenario when uncertainty is pernicious. Alternatively, uncertainty may be propitious, in the sense that the limit load factor can possibly increase with some $\boldsymbol{p}$ belonging to $P(\alpha, \tilde{\boldsymbol{p}})$. Finding such a case, called the opportune case by some authors [Ben-Haim 2006], together with the worst case will provide us with the range of the structural response under uncertainty. The opportune-case limit load factor is defined by

$$\lambda_{\max}(\alpha, \tilde{\boldsymbol{p}}) = \max\{\bar{\lambda}(\boldsymbol{p}) \mid \boldsymbol{p} \in P(\alpha, \tilde{\boldsymbol{p}})\}, \tag{17}$$

where minimization in (15) has been replaced by maximization. Computing $\lambda_{\max}(\alpha, \tilde{\boldsymbol{p}})$ is much easier than computing $\lambda_{\min}(\alpha, \tilde{\boldsymbol{p}})$. Recall that, for a fixed $\boldsymbol{p}$, the lower bound principle is given by problem (14), the optimal value of which is $\bar{\lambda}(\boldsymbol{p})$. From this and the definition in (14) of $P(\alpha, \tilde{\boldsymbol{p}})$, we immediately see that $\lambda_{\max}(\alpha, \tilde{\boldsymbol{p}})$ is the optimal value of the following problem:

$$\begin{aligned} &\text{Maximize } \lambda \text{ over } \lambda, \boldsymbol{s}, \boldsymbol{\zeta} \\ &\text{subject to} \quad \boldsymbol{H}\boldsymbol{s} = \tilde{\boldsymbol{p}} + \boldsymbol{Q}\boldsymbol{\zeta} + \lambda \boldsymbol{f}, \\ &\qquad\qquad \|\boldsymbol{A}_{e,j}\boldsymbol{T}_e\boldsymbol{s}\|_1 \le R_{e,j}, \qquad e = 1, \dots, E, \;\; j = 1, \dots, J, \\ &\qquad\qquad \alpha \ge \|\boldsymbol{\zeta}\|_\infty. \end{aligned} \tag{18}$$

Here λ, $\boldsymbol{s}$, and $\boldsymbol{\zeta}$ are variables to be optimized. In a manner similar to Remark 2.3, we can rewrite problem (18) as

$$\begin{aligned} &\text{Maximize } \lambda \text{ over } \lambda, \boldsymbol{s}, \boldsymbol{\zeta}, \boldsymbol{\eta} \\ &\text{subject to} \quad \boldsymbol{H}\boldsymbol{s} = \tilde{\boldsymbol{p}} + \boldsymbol{Q}\boldsymbol{\zeta} + \lambda \boldsymbol{f}, \\ &\qquad\qquad R_{e,j} \ge \mathbf{1}^{\mathrm{T}}\boldsymbol{\eta}_{e,j}, \qquad\qquad j = 1, \dots, J, \quad e = 1, \dots, E, \\ &\qquad\qquad -\boldsymbol{\eta}_{e,j} \le \boldsymbol{A}_{e,j}\boldsymbol{T}_e\boldsymbol{s} \le \boldsymbol{\eta}_{e,j}, \qquad j = 1, \dots, J, \quad e = 1, \dots, E, \\ &\qquad\qquad -\alpha\mathbf{1} \le \boldsymbol{\zeta} \le \alpha\mathbf{1}, \end{aligned} \tag{19}$$

which is an LP problem in variables λ, $\boldsymbol{s}$, $\boldsymbol{\zeta}$, and $\boldsymbol{\eta}$. Let $(\bar{\lambda}, \bar{\boldsymbol{s}}, \bar{\boldsymbol{\zeta}}, \bar{\boldsymbol{\eta}})$ denote the optimal solution of (19). The opportune-case load, defined as the optimal solution of problem (17), is then obtained straightforwardly as $\tilde{\boldsymbol{p}} + \boldsymbol{Q}\bar{\boldsymbol{\zeta}}$. In short, $\lambda_{\max}(\alpha, \tilde{\boldsymbol{p}})$ and the corresponding load can be obtained by solving LP problem (19).

Remark 3.3. In this paper we assume that only the fixed load, $\boldsymbol{p}$, is uncertain and that the reference load, $\boldsymbol{f}$, is known precisely. Introducing uncertainties in $\boldsymbol{f}$ might require more careful consideration. The worst case is characterized as the case with the minimum value of the limit load factor, and $\boldsymbol{f}$ is multiplied by the load factor. Therefore, if we allow that the norm of $\boldsymbol{f}$ can change due to uncertainty, then it affects the limit load factor. For instance, suppose that $\boldsymbol{f}$ is proportionally increased as $\beta\boldsymbol{f}$

($\beta > 1$). Then the limit load factor is multiplied by $1/\beta$, i.e., it is decreased. From a physical point of view, however, this does not mean that load $\beta \boldsymbol{f}$ is worse than load $\boldsymbol{f}$; the collapse loads in these two cases are the same. This observation may suggest that, when we consider uncertainty in $\boldsymbol{f}$, the loads included in the uncertainty set should be normalized in some manner. The method of normalization suitable for worst-case analysis may possibly be nontrivial and an interesting subject of study. This issue, however, is not pursued further in this paper.

3B. ***MILP formulation.*** In Section 3A we defined the worst-case limit load factor by (15). The uncertainty model of $\boldsymbol{p}$ has been given by (14). The following proposition presents a nonlinear programming formulation of the worst scenario problem.

Proposition 3.4. *The worst-case limit load factor*, $\lambda_{\min}(\alpha, \tilde{\boldsymbol{p}})$, *is equal to the optimal value of the following optimization problem*:

$$\begin{aligned} &\text{Minimize } -\alpha \| \boldsymbol{Q}^{\mathrm{T}} \boldsymbol{u} \|_1 - \tilde{\boldsymbol{p}}^{\mathrm{T}} \boldsymbol{u} + \sum_{e=1}^{E} \sum_{j=1}^{J} R_{e,j} \gamma_{e,j} \text{ over } \boldsymbol{u}, \boldsymbol{\gamma}, \boldsymbol{z} \\ &\text{subject to} \quad \boldsymbol{f}^{\mathrm{T}} \boldsymbol{u} = 1, \\ &\qquad \sum_{e=1}^{E} \sum_{j=1}^{J} (\boldsymbol{A}_{e,j} \boldsymbol{T}_e)^{\mathrm{T}} \boldsymbol{z}_{e,j} = \boldsymbol{H}^{\mathrm{T}} \boldsymbol{u}, \\ &\qquad \gamma_{e,j} \geq \| \boldsymbol{z}_{e,j} \|_\infty, \quad e = 1, \ldots, E, \ j = 1, \ldots, J. \end{aligned} \tag{20}$$

Here $\boldsymbol{u}$, $\boldsymbol{\gamma}$, *and* $\boldsymbol{z}$ *are variables to be optimized.*

A proof of Proposition 3.4 appears in Section A.2.

Let $(\bar{\boldsymbol{u}}, \bar{\boldsymbol{\gamma}}, \bar{\boldsymbol{z}})$ be an optimal solution of problem (20). Here $\bar{\boldsymbol{u}}$ is the collapse mode corresponding to the worst-case load. The worst-case load itself is obtained from $\bar{\boldsymbol{u}}$ as follows. As shown in the proof of Proposition 3.4 (see (42)), $\bar{\boldsymbol{\xi}}$ satisfies

$$\bar{\boldsymbol{\xi}} \in \arg\min_{\boldsymbol{\zeta}} \{ -(\boldsymbol{Q}^{\mathrm{T}} \bar{\boldsymbol{u}})^{\mathrm{T}} \boldsymbol{\zeta} \mid \alpha \geq \| \boldsymbol{\zeta} \|_\infty \}. \tag{21}$$

This is an LP problem in terms of $\boldsymbol{\zeta}$ and its optimal solution is given by

$$\bar{\zeta}_l \in \begin{cases} \{\alpha\} & \text{if } \boldsymbol{q}_l^{\mathrm{T}} \bar{\boldsymbol{u}} > 0, \\ [-\alpha, \alpha] & \text{if } \boldsymbol{q}_l^{\mathrm{T}} \bar{\boldsymbol{u}} = 0, \\ \{-\alpha\} & \text{if } \boldsymbol{q}_l^{\mathrm{T}} \bar{\boldsymbol{u}} < 0. \end{cases} \tag{22}$$

Here $\boldsymbol{q}_1, \ldots, \boldsymbol{q}_L \in \mathbb{R}^d$ are column vectors of $\boldsymbol{Q}$, i.e.,

$$\boldsymbol{Q} = \left[\boldsymbol{q}_1 \middle| \boldsymbol{q}_2 \middle| \cdots \middle| \boldsymbol{q}_L \right].$$

Accordingly, from definition (13) of $\boldsymbol{p}$, the worst-case load, denoted $\bar{\boldsymbol{p}}$, is obtained as

$$\bar{\boldsymbol{p}} = \tilde{\boldsymbol{p}} + \boldsymbol{Q} \bar{\boldsymbol{\zeta}}.$$

Problem (20) is a nonconvex optimization problem, because $-\alpha \| \boldsymbol{Q}^{\mathrm{T}} \boldsymbol{u} \|_1$ is a nonconvex function of $\boldsymbol{u}$. This problem should be solved by an algorithm with guaranteed global convergence, because, obviously,

a local (but not global) optimal solution is not the worst scenario. Unfortunately, it is difficult to solve problem (20) globally due to its nonconvexity. This difficulty motivates the following proposition, which converts problem (20) to an MILP problem.

Proposition 3.5. *The optimal solution of problem* (20) *is also optimal for the following optimization problem*:

$$\begin{aligned}
&\text{Minimize } -\alpha \sum_{l=1}^{L} w_l - \tilde{\boldsymbol{p}}^{\mathrm{T}}\boldsymbol{u} + \sum_{e=1}^{E}\sum_{j=1}^{J} R_{e,j}\gamma_{e,j} \text{ over } \boldsymbol{t}, \boldsymbol{u}, \boldsymbol{\gamma}, \boldsymbol{z}, \boldsymbol{w} \\
&\text{subject to} \quad \boldsymbol{f}^{\mathrm{T}}\boldsymbol{u} = 1, \\
&\qquad \sum_{e=1}^{E}\sum_{j=1}^{J} (\boldsymbol{A}_{e,j}\boldsymbol{T}_e)^{\mathrm{T}}\boldsymbol{z}_{e,j} = \boldsymbol{H}^{\mathrm{T}}\boldsymbol{u}, \\
&\qquad \gamma_{e,j} \geq \|\boldsymbol{z}_{e,j}\|_\infty, \quad e = 1, \ldots, E, \ j = 1, \ldots, J, \\
&\qquad \boldsymbol{w} \leq \boldsymbol{Q}^{\mathrm{T}}\boldsymbol{u} + M\boldsymbol{t}, \\
&\qquad \boldsymbol{w} \leq -\boldsymbol{Q}^{\mathrm{T}}\boldsymbol{u} + M(\boldsymbol{1} - \boldsymbol{t}), \\
&\qquad \boldsymbol{t} \in \{0, 1\}^L,
\end{aligned} \tag{23}$$

where $M \gg 0$ *is a sufficiently large constant.*

A proof of Proposition 3.5 appears in Section A.3. In problem (23), $\boldsymbol{w}$ and $\boldsymbol{t}$ are additional variables used for reformulation. At an optimal solution, these variables are related to the collapse mode, $\bar{\boldsymbol{u}}$, as

$$\bar{w}_l = |\boldsymbol{q}_l^{\mathrm{T}}\bar{\boldsymbol{u}}|, \quad \bar{t}_l \in \begin{cases} \{0\} & \text{if } \boldsymbol{q}_l^{\mathrm{T}}\bar{\boldsymbol{u}} > 0, \\ \{0, 1\} & \text{if } \boldsymbol{q}_l^{\mathrm{T}}\bar{\boldsymbol{u}} = 0, \\ \{1\} & \text{if } \boldsymbol{q}_l^{\mathrm{T}}\bar{\boldsymbol{u}} < 0. \end{cases} \tag{24}$$

Problem (23) is an MILP problem, because all the constraints other than the integrality constraints on $\boldsymbol{t}$ are linear constraints and the objective function is a linear function. Therefore, it can be solved by using an algorithm with guaranteed convergence to a global optimal solution. A branch-and-cut method is an example of such algorithms [Wolsey 1998; Aardal et al. 2005]. Moreover, several well-developed software packages, e.g., Gurobi Optimizer [Gurobi 2013] and CPLEX [IBM ILOG 2011], are available for solving this optimization problem.

3C. ***Another uncertainty set.*** In Sections 3A and 3B we assumed that the uncertainty of the external load, $\boldsymbol{p}$, is defined by (14). Instead of the ℓ^∞-norm used in (14), this section addresses an uncertain model defined by using the ℓ^1-norm, that is,

$$P(\alpha) = \{\tilde{\boldsymbol{p}} + \boldsymbol{Q}\boldsymbol{\zeta} \mid \|\boldsymbol{\zeta}\|_1 \leq \alpha\}. \tag{25}$$

In (14), the components of $\boldsymbol{\zeta}$ can perturb independently; for instance, when $\zeta_i = \alpha$, ζ_j $(j \neq i)$ can take any value in $[-\alpha, \alpha]$. In contrast, (25) takes into account some sort of correlation; for instance, $\zeta_i = \alpha$ implies $\zeta_j = 0$ $(j \neq i)$. In other words, (14) is somewhat more pessimistic (or more conservative) than (25). In the following we show that uncertainty set (25) also allows MILP reformulation of the worst scenario detection problem.

The worst scenario detection problem is defined by (15) with (25). Analogous to Proposition 3.4, we can show that this problem is converted to the following nonlinear programming problem:

$$\begin{aligned}
&\text{Minimize } -\alpha\|\boldsymbol{Q}^{\mathrm{T}}\boldsymbol{u}\|_\infty - \tilde{\boldsymbol{p}}^{\mathrm{T}}\boldsymbol{u} + \sum_{e=1}^{E}\sum_{j=1}^{J} R_{e,j}\gamma_{e,j} \text{ over } \boldsymbol{u}, \boldsymbol{\gamma}, z \\
&\text{subject to} \quad \boldsymbol{f}^{\mathrm{T}}\boldsymbol{u} = 1, \\
&\qquad \sum_{e=1}^{E}\sum_{j=1}^{J}(\boldsymbol{A}_{e,j}\boldsymbol{T}_e)^{\mathrm{T}}\boldsymbol{z}_{e,j} = \boldsymbol{H}^{\mathrm{T}}\boldsymbol{u}, \\
&\qquad \gamma_{e,j} \geq \|\boldsymbol{z}_{e,j}\|_\infty, \quad e = 1, \ldots, E,\ j = 1, \ldots, J.
\end{aligned} \tag{26}$$

Compared with problem (20), nonconvex term $-\alpha\|\boldsymbol{Q}^{\mathrm{T}}\boldsymbol{u}\|_1$ in the objective function is replaced by $-\alpha\|\boldsymbol{Q}^{\mathrm{T}}\boldsymbol{u}\|_\infty$. This is because the ℓ^1-norm (in (25)) is the dual norm of the ℓ^∞-norm (in (14)).

In a manner similar to Proposition 3.5, problem (26) also can be reformulated as an MILP problem. The result is formally stated as follows.

Proposition 3.6. *The optimal solution of problem* (26) *is also optimal for the following optimization problem*:

$$\begin{aligned}
&\text{Minimize } -\alpha v - \tilde{\boldsymbol{p}}^{\mathrm{T}}\boldsymbol{u} + \sum_{e=1}^{E}\sum_{j=1}^{J} R_{e,j}\gamma_{e,j} \text{ over } \boldsymbol{t}, \boldsymbol{y}, \boldsymbol{u}, \boldsymbol{\gamma}, \boldsymbol{z}, \boldsymbol{w}, v \\
&\text{subject to} \quad \boldsymbol{f}^{\mathrm{T}}\boldsymbol{u} = 1, \\
&\qquad \sum_{e=1}^{E}\sum_{j=1}^{J}(\boldsymbol{A}_{e,j}\boldsymbol{T}_e)^{\mathrm{T}}\boldsymbol{z}_{e,j} = \boldsymbol{H}^{\mathrm{T}}\boldsymbol{u}, \\
&\qquad \gamma_{e,j} \geq \|\boldsymbol{z}_{e,j}\|_\infty, \qquad e = 1, \ldots, E,\ j = 1, \ldots, J, \\
&\qquad \boldsymbol{w} \leq \boldsymbol{Q}^{\mathrm{T}}\boldsymbol{u} + M\boldsymbol{t}, \\
&\qquad \boldsymbol{w} \leq -\boldsymbol{Q}^{\mathrm{T}}\boldsymbol{u} + M(\boldsymbol{1} - \boldsymbol{t}), \\
&\qquad v \leq w_l + M(1 - y_l), \qquad l = 1, \ldots, L, \\
&\qquad \sum_{l=1}^{L} y_l = 1, \\
&\qquad \boldsymbol{t} \in \{0, 1\}^L, \quad \boldsymbol{y} \in \{0, 1\}^L.
\end{aligned} \tag{27}$$

A proof of Proposition 3.6 is slightly more complicated than one for Proposition 3.5; see Section A.4.

Let $(\bar{\boldsymbol{t}}, \bar{\boldsymbol{y}}, \bar{\boldsymbol{u}}, \bar{\boldsymbol{\gamma}}, \bar{\boldsymbol{z}}, \bar{\boldsymbol{w}}, \bar{v})$ denote the optimal solution of problem (27). Auxiliary variables, $\bar{w}_l$ and $\bar{t}_l$, are related to $\bar{\boldsymbol{u}}$ by (24). Moreover, $\bar{v}$ and $\bar{\boldsymbol{w}}$ satisfy $\bar{v} = \max\{\bar{w}_1, \ldots, \bar{w}_L\}$ and $\bar{y}_l = 1$ implies $\bar{v} = \bar{w}_l$.

4. Numerical experiments

The worst loading scenarios of two planar frame structures were found by solving MILP problem (23). Computation was carried out on a Core i5 (2.6 GHz) processor with 8.0 GB RAM. The data of the MILP

problems were prepared in the CPLEX LP file format [IBM ILOG 2011] with MATLAB 7.13. Then the MILP problems were solved with CPLEX Version 12.4 under the parameter setting "aggressive cuts".

4A. ***Eccentrically braced five-story frame.*** Consider the five-story plane frame in Figure 3. The nominal load, $\tilde{\boldsymbol{p}}$, is defined as vertical point forces as shown in Figure 3, where $\tilde{p}_{\mathrm{a}} = 180\,\mathrm{kN}$ and $\tilde{p}_{\mathrm{b}} = 90\,\mathrm{kN}$. The proportionally increasing load, $\lambda \boldsymbol{f}$, is given as horizontal forces (in kN) as shown in Figure 3. The frame consists of $E = 65$ beam elements and $d = 120$ degrees of freedom, where each of the long beams is divided into two Euler–Bernoulli beam elements.

We adopt the following steel sections:

- A beam has cross-sectional area 7,000 mm^2 and plastic section modulus 850,000 mm^3, which approximately corresponds to an H-section with depth 294 mm, width 200 mm, web thickness 8 mm, and flange thickness 12 mm.
- A column has cross-sectional area 10,000 mm^2 and plastic section modulus 1,150,000 mm^3, which approximately corresponds to a square hollow section with edge length 300 mm and thickness 9 mm.
- A brace has cross-sectional area 10,000 mm^2 and plastic section modulus 825,000 mm^3, which approximately corresponds to a circular hollow section with external diameter 267.4 mm and thickness 12.7 mm.

The yield condition is defined by (4) with $\kappa = 0.85\sqrt{2}$. Here q_e^{y} and m_e^{y} are defined by $q_e^{\mathrm{y}} = \sigma^{\mathrm{y}} a_e$ and $m_e^{\mathrm{y}} = \sigma^{\mathrm{y}} Z_e^{\mathrm{p}}$, where a_e and Z_e^{p} denote the cross-sectional area and the plastic section modulus, respectively, and $\sigma^{\mathrm{y}} = 300\,\mathrm{N/mm^2}$ is the material yield strength.

The nominal limit load factor of the frame is $\bar{\lambda}(\tilde{\boldsymbol{p}}) = \lambda_{\min}(0) = 1126.5710$. The uncertainty model of $\boldsymbol{p}$ is defined by (14). The coefficient matrix $\boldsymbol{Q}$ is defined so that uncertain horizontal and vertical forces within the range $[-\alpha, \alpha]$ (in kN) possibly present at the nodes subjected to $\tilde{p}_{\mathrm{a}}$. However, at the leftmost nodes only vertical forces are considered uncertain, because horizontal proportionally increasing forces are applied to these nodes. We suppose that no external moments are applied. Then $\boldsymbol{Q}$ results in a 120×55 matrix, the components of which are either 0 or 1 kN. For a given level of uncertainty $\alpha > 0$, the worst-case limit load factor, $\lambda_{\min}(\alpha)$, is computed by solving problem (23).

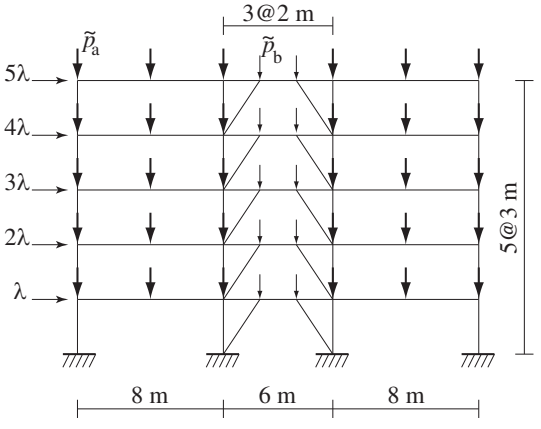

Figure 3. A five-story braced frame.

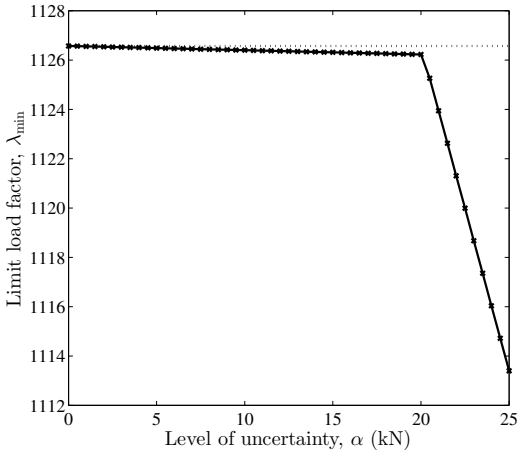

Figure 4. The variation of $\lambda_{\min}$ for the five-story frame.

The variation of $\lambda_{\min}(\alpha)$ with respect to α is depicted as a solid line in Figure 4. The dotted line shows the variation of the maximum limit load factor, $\lambda_{\max}(\alpha)$, which was obtained by solving problem (19). In this example, $\lambda_{\max}(\alpha)$ is constant within the range $0 \leq \alpha \leq 25\,\mathrm{kN}$. Concerning the worst-case limit load factor, at $\alpha = 18$ and $25\,\mathrm{kN}$ we obtain $\lambda_{\min}(18) = 1126.2593$ and $\lambda_{\min}(25) = 1113.3987$. CPLEX needed 7.4 s and 3.5 s to solve these two problems. Figure 5 depicts the collapse modes in the worst

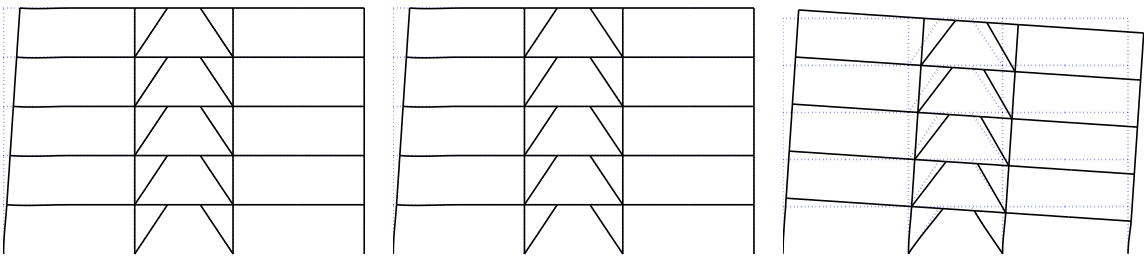

Figure 5. The collapse modes of the five-story frame, for various values of α.

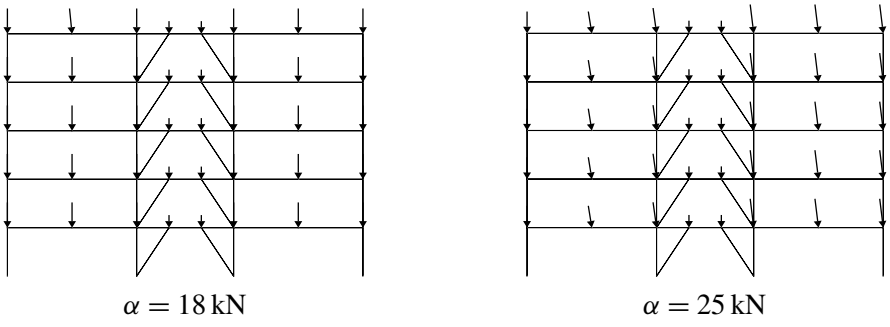

Figure 6. The worst-case loads for the five-story frame.

cases for $\alpha = 0$, 18, and 25 kN. It is observed that the collapse mode at $\alpha = 18$ kN is the same as that at $\alpha = 0$, while the collapse mode at $\alpha = 25$ kN is very different. Figure 6 shows the worst-case loads for $\alpha = 18$ kN and $\alpha = 25$ kN. Here the worst-case load is obtained using (22), choosing $\bar{\zeta}_l = 0$ for l satisfying $\boldsymbol{q}_l^{\mathrm{T}} \bar{\boldsymbol{u}} = 0$. In accordance with the difference of collapse modes, the worst-case loads of these two cases are also different.

4B. ***Seven-story portal frame.*** We next consider the seven-story plane frame in Figure 7. The nominal load, $\tilde{\boldsymbol{p}}$, is defined as vertical point forces with $\tilde{p}_{\mathrm{a}} = 3000$ kN. The proportionally increasing load, $\lambda \boldsymbol{f}$, is given as horizontal forces λ kN applied at the leftmost nodes. The frame consists of $E = 49$ beam elements and $d = 105$ degrees of freedom, where each beam is divided into two beam elements.

We use the following steel sections:

- A beam on the lower three stories has cross-sectional area 5,000 mm^2 and plastic section modulus 370,000 mm^3, which approximately corresponds to an H-section with depth 175 mm, width 175 mm, web thickness 7.5 mm, and flange thickness 11 mm.
- A beam on the upper stories has cross-sectional area 2,000 mm^2 and plastic section modulus 90,000 mm^3, which approximately corresponds to an H-section with depth 100 mm, width 100 mm, web thickness 6 mm, and flange thickness 8 mm.
- A column on the lower three stories has cross-sectional area 24,000 mm^2 and plastic section modulus 2,970,000 mm^3, which approximately corresponds to a square hollow section with edge length 350 mm and thickness 19 mm.
- A column on the upper stories has cross-sectional area 13,000 mm^2 and plastic section modulus 1,440,000 mm^3, which approximately corresponds to a square hollow section with edge length 300 mm and thickness 12 mm.

The yield condition is defined by (4) with $\kappa = 0.85\sqrt{2}$ and $\sigma^{\mathrm{y}} = 300\,\mathrm{N/mm^2}$ in the same manner as in Section 4A.

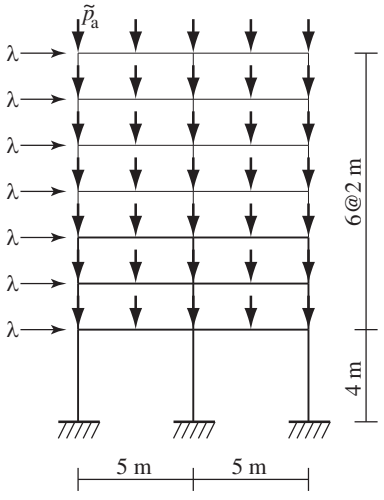

Figure 7. A seven-story portal frame.

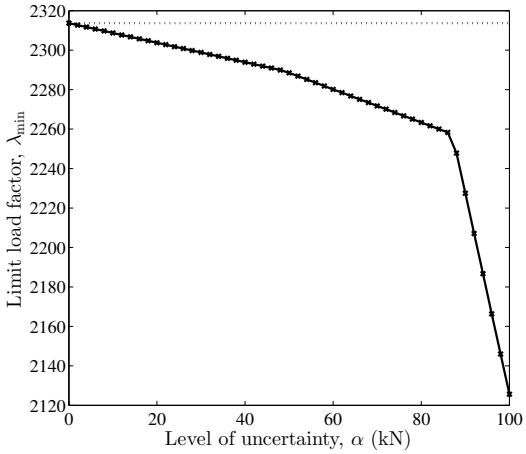

Figure 8. The variation of $\lambda_{\min}$ for the seven-story frame.

The nominal limit load factor of the frame is $\bar{\lambda}(\tilde{\boldsymbol{p}}) = \lambda_{\min}(0) = 2313.6687$. The uncertainty model of $\boldsymbol{p}$ is defined by (14). The coefficient matrix $\boldsymbol{Q}$ is defined so that uncertain horizontal and vertical forces within the range $[-\alpha, \alpha]$ (in kN) possibly present at the nodes. However, at the leftmost nodes only vertical forces are considered uncertain. Then $\boldsymbol{Q}$ results in a 105×63 matrix.

The solid line in Figure 8 shows the variation of the worst-case limit load factor, $\lambda_{\min}(\alpha)$, with respect to α. The dotted line shows the variation of the maximum limit load factor, $\lambda_{\max}(\alpha)$, which is constant within the range $0 \leq \alpha \leq 100\,\text{kN}$. Concerning the worst-case limit load factor, at $\alpha = 20$, 80, and 100 kN we obtain $\lambda_{\min}(20) = 2303.7830$, $\lambda_{\min}(80) = 2263.3615$, and $\lambda_{\min}(100) = 2125.5923$. CPLEX needed 0.8 s, 4.0 s, and 10.4 s, respectively, to solve these three problems. Figure 9 collects the collapse modes in the worst scenarios obtained . The mode at $\alpha = 20\,\text{kN}$ is the same as that in the nominal case ($\alpha = 0$). However, the modes at $\alpha = 80\,\text{kN}$ and $\alpha = 100\,\text{kN}$ are different from that in the nominal case. Thus the collapse mode in the most severe scenario depends on the level of uncertainty, α. The worst-case loads, $\boldsymbol{p}_{\text{w}}$, are shown in Figure 10. It may be observed in Figure 8 that the graph of $\lambda_{\min}(\alpha)$ has two angular

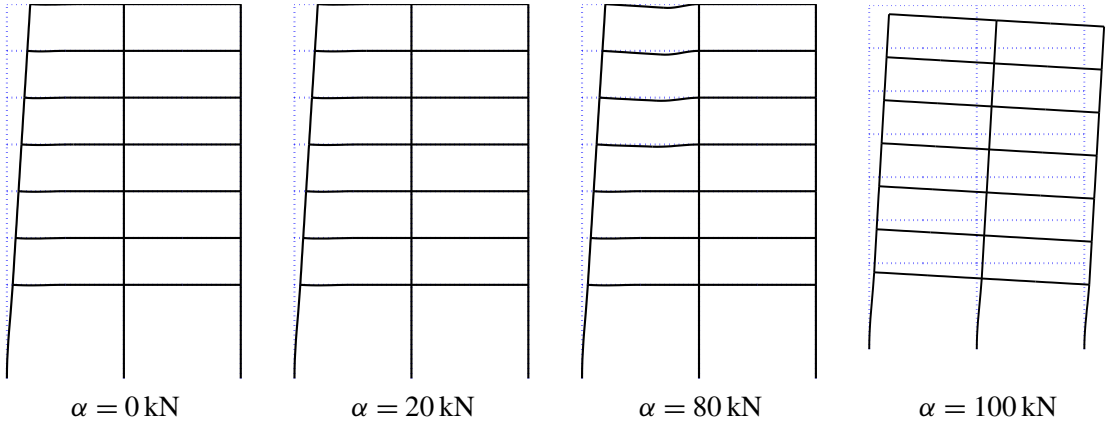

Figure 9. The collapse modes of the seven-story frame.

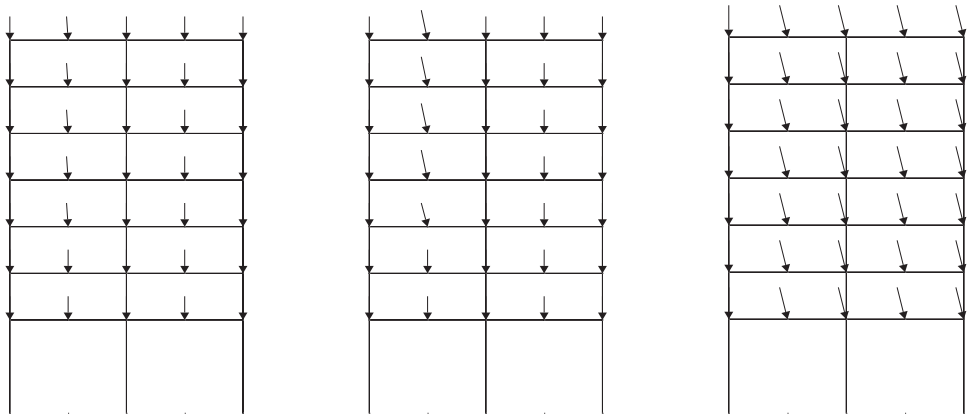

Figure 10. The worst-case loads for the seven-story frame.

points. Similarly, the curve in Figure 4 has one angular point. It seems that these sudden changes of the slope of the curve are due to changes of the collapse modes corresponding to $\lambda_{\min}(\alpha)$.

5. Conclusions

Evaluating robustness against uncertainty is a key to many design methodologies of structures. In some engineering problems including severe uncertainty, e.g., uncertainty in large earthquakes [Takewaki et al. 2013], knowledge of uncertain parameters is fundamentally limited and reliable stochastic data on uncertain parameters is unavailable. Nonprobabilistic uncertainty analysis, rather than probabilistic, might be applicable in grasping the critical response of a structure to estimate the safety level. This paper has developed a solid numerical method for finding the worst-case load at which the plastic limit load factor of a given frame structure attains the worst value.

Finding the worst scenario among a given set of possible scenarios is formulated in general as an optimization problem. In this paper this worst scenario problem has been converted to a mixed-integer linear programming (MILP) problem. Several well-developed software packages are available for finding a global optimal solution of an MILP problem. Guaranteed convergence to a global optimal solution warrants that the proposed method provides the precisely worst response of the structure; that is, neither overestimate nor underestimate arises. In addition, algorithms specifically designed for uncertainty analysis are not required. Also, implementation of optimization algorithms is not necessary.

This paper has assumed that yield conditions are represented as piecewise linear functions in terms of generalized stresses. Moreover, the uncertainty set of external loads has been restricted to polyhedra with specific forms. Extensions to curved yield surfaces and/or more general uncertainty sets remain to be explored. Also, extensions to shakedown analysis, possibly taking into account work-hardening effects [Maier 1970; Polizzotto et al. 1991] and dynamic loads [Corradi and Maier 1973–1974; Polizzotto et al. 1993], could be made. In the numerical examples it has been shown that the collapse mode in the worst case can possibly depend on the level of uncertainty in the external load. Numerical analysis using

more realistic structural designs could be performed for in-depth study of the influence of uncertainty on real-world structures.

Appendix: Proofs

A.1 ***Derivation of dual limit analysis problem.*** This section shows that problem (12) is derived as the Fenchel dual problem of problem (7).

For notational convenience, suppose that $\boldsymbol{A}_{1,1}, \ldots, \boldsymbol{A}_{E,J}$ are all $a \times 3$ matrices. Define vectors $\boldsymbol{x}$ and $\boldsymbol{y}$ by

$$\boldsymbol{x} = \begin{bmatrix} \lambda \\ \boldsymbol{s} \end{bmatrix}, \quad \boldsymbol{y} = \left[\begin{array}{c} \boldsymbol{y}^{\mathrm{a}} \\ \hline \boldsymbol{y}^{\mathrm{b}} \\ \hline \boldsymbol{y}^{\mathrm{c}}_{1,1} \\ \vdots \\ \boldsymbol{y}^{\mathrm{c}}_{E,J} \end{array}\right],$$

with $\lambda \in \mathbb{R}$, $\boldsymbol{s} \in \mathbb{R}^{3E}$, $\boldsymbol{y}^{\mathrm{a}} \in \mathbb{R}^{d}$, $\boldsymbol{y}^{\mathrm{b}} \in \mathbb{R}^{EJ}$, and $\boldsymbol{y}^{\mathrm{c}}_{e,j} \in \mathbb{R}^{a}$ for all e and j. We write

$$X = \mathbb{R} \times \mathbb{R}^{3E}, \quad Y = \mathbb{R}^{d} \times \mathbb{R}^{EJ} \times \mathbb{R}^{aEJ},$$

for simplicity, where $\boldsymbol{x} \in X$ and $\boldsymbol{y} \in Y$. Define functions $f : X \to \mathbb{R}$ and $g : Y \to \mathbb{R} \cup \{+\infty\}$ by

$$f(\boldsymbol{x}) = -\lambda, \tag{28}$$

$$g(\boldsymbol{y}) = \begin{cases} 0 & \text{if } \boldsymbol{y}^{\mathrm{a}} = \boldsymbol{p},\ y^{\mathrm{b}}_{e,j} + R_{e,j} \geq \|\boldsymbol{y}^{\mathrm{c}}_{e,j}\|_1 \ \text{ for all } e \text{ and } j, \\ +\infty & \text{otherwise,} \end{cases} \tag{29}$$

which are proper convex functions. Define a matrix $\boldsymbol{\Lambda}$ by

$$\boldsymbol{\Lambda} = \left[\begin{array}{c|c} -\boldsymbol{f} & \boldsymbol{H} \\ \hline \boldsymbol{0} & \boldsymbol{O} \\ \hline \boldsymbol{0} & -\boldsymbol{A}_{1,1}\boldsymbol{T}_1 \\ \vdots & \vdots \\ \boldsymbol{0} & -\boldsymbol{A}_{E,J}\boldsymbol{T}_E \end{array}\right]. \tag{30}$$

With this setting, problem (7) is equivalently rewritten as

$$\max\{-f(\boldsymbol{x}) - g(\boldsymbol{\Lambda}\boldsymbol{x}) \mid \boldsymbol{x} \in X\}. \tag{31}$$

From standard results in Fenchel duality theory [Rockafellar 1970], the Fenchel dual problem of (31) is given by

$$\min\{f^*(\boldsymbol{\Lambda}^{\mathrm{T}}\boldsymbol{y}^*) + g^*(-\boldsymbol{y}^*) \mid \boldsymbol{y}^* \in Y\}. \tag{32}$$

Here $f^* : X \to \mathbb{R}$ and $g^* : Y \to \mathbb{R} \cup \{\infty\}$ are conjugate functions of f and g, respectively, and

$$\boldsymbol{y}^* = \begin{bmatrix} \boldsymbol{y}^{\mathrm{a}*} \\ \hline \boldsymbol{y}^{\mathrm{b}*} \\ \hline \boldsymbol{y}^{\mathrm{c}*}_{1,1} \\ \vdots \\ \boldsymbol{y}^{\mathrm{c}*}_{E,J} \end{bmatrix}.$$

In the following we show that problem (32) with f, g, and Λ defined by (28), (29), and (30) is equivalent to problem (12).

With the notation $\boldsymbol{x}^* = (\lambda^*, \boldsymbol{s}^*) \in X$, f^* is explicitly written as

$$\begin{aligned} f^*(\boldsymbol{x}^*) &= \sup\{\langle \boldsymbol{x}, \boldsymbol{x}^* \rangle - f(\boldsymbol{x}) \mid \boldsymbol{x} \in V\} \\ &= \sup_{\lambda}\{\lambda(\lambda^* + 1)\} + \sup_{\boldsymbol{s}}\{\boldsymbol{s}^{\mathrm{T}}\boldsymbol{s}^*\} \\ &= \begin{cases} 0 & \text{if } \lambda^* = -1 \text{ and } \boldsymbol{s}^* = \boldsymbol{0}, \\ +\infty & \text{otherwise.} \end{cases} \end{aligned} \tag{33}$$

The conjugate function of g in (29) is obtained as follows. For notational convenience, define $K \subseteq \mathbb{R}^{a+1}$ by

$$K = \{(r_0, \boldsymbol{r}_1) \in \mathbb{R} \times \mathbb{R}^a \mid r_0 \geq \|\boldsymbol{r}_1\|_1\}.$$

By the definition of a conjugate function, we obtain

$$\begin{aligned} g^*(\boldsymbol{y}^*) &= \sup\{\langle \boldsymbol{y}, \boldsymbol{y}^* \rangle \mid \boldsymbol{y} \in \operatorname{dom} g\} \\ &= \sup_{\boldsymbol{y}^{\mathrm{a}}}\{(\boldsymbol{y}^{\mathrm{a}})^{\mathrm{T}}\boldsymbol{y}^{\mathrm{a}*} \mid \boldsymbol{y}^{\mathrm{a}} = \boldsymbol{p}\} + \sup_{\boldsymbol{y}^{\mathrm{b}}, \boldsymbol{y}^{\mathrm{c}}} \sum_{e=1}^{E}\sum_{j=1}^{J} \left\{ \begin{bmatrix} y^{\mathrm{b}}_{e,j} \\ \boldsymbol{y}^{\mathrm{c}}_{e,j} \end{bmatrix}^{\mathrm{T}} \begin{bmatrix} y^{\mathrm{b}*}_{e,j} \\ \boldsymbol{y}^{\mathrm{c}*}_{e,j} \end{bmatrix} \,\middle|\, \begin{bmatrix} y^{\mathrm{b}}_{e,j} + R_{e,j} \\ \boldsymbol{y}^{\mathrm{c}}_{e,j} \end{bmatrix} \in K \right\} \\ &= \boldsymbol{p}^{\mathrm{T}}\boldsymbol{y}^{\mathrm{a}*} - \sum_{e=1}^{E}\sum_{j=1}^{J} R_{e,j}\, y^{\mathrm{b}*}_{e,j} + \sum_{e=1}^{E}\sum_{j=1}^{J} \sup_{y^{\mathrm{b}}_{e,j}, \boldsymbol{y}^{\mathrm{c}}_{e,j}} \left\{ \begin{bmatrix} y^{\mathrm{b}}_{e,j} + R_{e,j} \\ \boldsymbol{y}^{\mathrm{c}}_{e,j} \end{bmatrix}^{\mathrm{T}} \begin{bmatrix} y^{\mathrm{b}*}_{e,j} \\ \boldsymbol{y}^{\mathrm{c}*}_{e,j} \end{bmatrix} \,\middle|\, \begin{bmatrix} y^{\mathrm{b}}_{e,j} + R_{e,j} \\ \boldsymbol{y}^{\mathrm{c}}_{e,j} \end{bmatrix} \in K \right\}. \end{aligned} \tag{34}$$

Since the dual cone of K is given by (see, for example, [Boyd and Vandenberghe 2004, Example 2.25])

$$K^* = \{(r_0^*, \boldsymbol{r}_1^*) \in \mathbb{R} \times \mathbb{R}^a \mid r_0^* \geq \|\boldsymbol{r}_1^*\|_\infty\},$$

we have that

$$\sup_{r_0, \boldsymbol{r}_1} \left\{ \begin{bmatrix} r_0 \\ \boldsymbol{r}_1 \end{bmatrix}^{\mathrm{T}} \begin{bmatrix} r_0^* \\ \boldsymbol{r}_1^* \end{bmatrix} \,\middle|\, \begin{bmatrix} r_0 \\ \boldsymbol{r}_1 \end{bmatrix} \in K \right\} = \begin{cases} 0 & \text{if } -\begin{bmatrix} r_0^* \\ \boldsymbol{r}_1^* \end{bmatrix} \in K^*, \\ +\infty & \text{otherwise.} \end{cases}$$

With this observation we see that (34) is reduced to

$$g^*(\boldsymbol{y}^*) = \begin{cases} \boldsymbol{p}^{\mathrm{T}}\boldsymbol{y}^{\mathrm{a}*} - \displaystyle\sum_{e=1}^{E}\sum_{j=1}^{J} R_{e,j}\, y^{\mathrm{b}*}_{e,j} & \text{if } -y^{\mathrm{b}*}_{e,j} \geq \|-\boldsymbol{y}^{\mathrm{c}*}_{e,j}\|_\infty \text{ for all } e \text{ and } j, \\ +\infty & \text{otherwise.} \end{cases} \tag{35}$$

From definition (30) of $\boldsymbol{\Lambda}$, $\boldsymbol{\Lambda}^{\mathrm{T}}\boldsymbol{y}^*$ is written as

$$\boldsymbol{\Lambda}^{\mathrm{T}}\boldsymbol{y}^* = \begin{bmatrix} -\boldsymbol{f}^{\mathrm{T}}\boldsymbol{y}^{\mathrm{a}*} \\ \boldsymbol{H}^{\mathrm{T}}\boldsymbol{y}^{\mathrm{a}*} - \sum_{e=1}^{E}\sum_{j=1}^{J}(\boldsymbol{A}_{e,j}\boldsymbol{T}_e)^{\mathrm{T}}\boldsymbol{y}_{e,j}^{\mathrm{c}*} \end{bmatrix}. \tag{36}$$

By using (33), (35), and (36), we obtain

$$f^*(\boldsymbol{\Lambda}^{\mathrm{T}}\boldsymbol{y}^*) = \begin{cases} 0 & \text{if } -\boldsymbol{f}^{\mathrm{T}}\boldsymbol{y}^{\mathrm{a}*} = -1,\ \boldsymbol{H}^{\mathrm{T}}\boldsymbol{y}^{\mathrm{a}*} - \sum_{e=1}^{E}\sum_{j=1}^{J}(\boldsymbol{A}_{e,j}\boldsymbol{T}_e)^{\mathrm{T}}\boldsymbol{y}_{e,j}^{\mathrm{c}*} = \boldsymbol{0}, \\ +\infty & \text{otherwise,} \end{cases} \tag{37}$$

$$g^*(-\boldsymbol{y}^*) = \begin{cases} -\boldsymbol{p}^{\mathrm{T}}\boldsymbol{y}^{\mathrm{a}*} + \sum_{e=1}^{E}\sum_{j=1}^{J} R_{e,j}\, y_{e,j}^{\mathrm{b}*} & \text{if } y_{e,j}^{\mathrm{b}*} \geq \|\boldsymbol{y}_{e,j}^{\mathrm{c}*}\|_\infty \text{ for all } e \text{ and } j, \\ +\infty & \text{otherwise.} \end{cases} \tag{38}$$

From (37) and (38), the Fenchel dual problem in (32) is explicitly written as

$$\begin{aligned} \text{Minimize}\ \ & -\boldsymbol{p}^{\mathrm{T}}\boldsymbol{y}^{\mathrm{a}*} + \sum_{e=1}^{E}\sum_{j=1}^{J} R_{e,j}\, y_{e,j}^{\mathrm{b}*} \\ \text{subject to}\ \ & \boldsymbol{f}^{\mathrm{T}}\boldsymbol{y}^{\mathrm{a}*} = 1, \\ & \sum_{e=1}^{E}\sum_{j=1}^{J}(\boldsymbol{A}_{e,j}\boldsymbol{T}_e)^{\mathrm{T}}\boldsymbol{y}_{e,j}^{\mathrm{c}*} = \boldsymbol{H}^{\mathrm{T}}\boldsymbol{y}^{\mathrm{a}*}, \\ & y_{e,j}^{\mathrm{b}*} \geq \|\boldsymbol{y}_{e,j}^{\mathrm{c}*}\|_\infty, \quad e = 1, \ldots, E,\ \ j = 1, \ldots, J. \end{aligned} \tag{39}$$

By rewriting the dual variables as

$$\boldsymbol{y}^{\mathrm{a}*} = \boldsymbol{u}, \quad \boldsymbol{y}^{\mathrm{b}*} = \boldsymbol{\gamma}, \quad \boldsymbol{y}^{\mathrm{c}*} = \boldsymbol{z},$$

we see that problem (39) indeed coincides with problem (12). Thus problem (12) is obtained as the Fenchel dual problem of (7).

Note that problems (7) and (12) can be converted to LP problems; see Remarks 2.3 and 2.4. As mentioned in Section 2B, we assume that problem (7) has an optimal solution. Then the duality theory of LP guarantees that problems (7) and (12) share the same optimal value.

A.2 ***Proof of Proposition 3.4.*** Since $\bar{\lambda}(\boldsymbol{p})$ is the optimal value of problem (12), (15) can be rewritten as

$$\lambda_{\min}(\alpha, \tilde{\boldsymbol{p}}) = \min_{\boldsymbol{p}\in P(\alpha,\tilde{\boldsymbol{p}})}\left\{\min_{\boldsymbol{u},\boldsymbol{\gamma},z}\left\{-\boldsymbol{p}^{\mathrm{T}}\boldsymbol{u} + \sum_{e=1}^{E}\sum_{j=1}^{J} R_{e,j}\gamma_{e,j} \;\middle|\; (\boldsymbol{u}, \boldsymbol{\gamma}, z) \in U\right\}\right\}, \tag{40}$$

where U is the feasible set of problem (12). By reversing the order of the two minimizations in (40), we obtain

$$\lambda_{\min}(\alpha, \tilde{\boldsymbol{p}}) = \min_{(\boldsymbol{u},\boldsymbol{\gamma},z)\in U}\left\{\min_{\boldsymbol{p}}\left\{-\boldsymbol{p}^{\mathrm{T}}\boldsymbol{u} \;\middle|\; \boldsymbol{p} \in P(\alpha, \tilde{\boldsymbol{p}})\right\} + \sum_{e=1}^{E}\sum_{j=1}^{J} R_{e,j}\gamma_{e,j}\right\}. \tag{41}$$

By using (14) and the Hölder inequality [Steele 2004, Chapter 9], the inner minimization problem of (41) can be reduced to

$$\begin{aligned}\min_{\boldsymbol{p}}\{-\boldsymbol{p}^{\mathrm{T}}\boldsymbol{u} \mid \boldsymbol{p} \in P(\alpha, \tilde{\boldsymbol{p}})\} &= \min_{\boldsymbol{\zeta}}\{-(\boldsymbol{Q}^{\mathrm{T}}\boldsymbol{u})^{\mathrm{T}}\boldsymbol{\zeta} \mid \alpha \geq \|\boldsymbol{\zeta}\|_\infty\} - \tilde{\boldsymbol{p}}^{\mathrm{T}}\boldsymbol{u} \\ &= \min_{\boldsymbol{\zeta}}\{-\|\boldsymbol{Q}^{\mathrm{T}}\boldsymbol{u}\|_1\|\boldsymbol{\zeta}\|_\infty \mid \alpha \geq \|\boldsymbol{\zeta}\|_\infty\} - \tilde{\boldsymbol{p}}^{\mathrm{T}}\boldsymbol{u} \\ &= -\alpha\|\boldsymbol{Q}^{\mathrm{T}}\boldsymbol{u}\|_1 - \tilde{\boldsymbol{p}}^{\mathrm{T}}\boldsymbol{u}.\end{aligned} \tag{42}$$

Here the last equality is actually attained by choosing $\boldsymbol{\zeta}$ as

$$\zeta_l = \begin{cases} \alpha & \text{if } \boldsymbol{q}_l^{\mathrm{T}}\boldsymbol{u} > 0, \\ 0 & \text{if } \boldsymbol{q}_l^{\mathrm{T}}\boldsymbol{u} = 0, \\ -\alpha & \text{if } \boldsymbol{q}_l^{\mathrm{T}}\boldsymbol{u} < 0, \end{cases}$$

where $\boldsymbol{q}_1, \ldots, \boldsymbol{q}_L \in \mathbb{R}^d$ are column vectors of $\boldsymbol{Q}$, i.e.,

$$\boldsymbol{Q} = \left[\, \boldsymbol{q}_1 \,\middle|\, \boldsymbol{q}_2 \,\middle|\, \cdots \,\middle|\, \boldsymbol{q}_L \,\right].$$

Substitution of (42) into problem (41) results in problem (20).

A.3 ***Proof of Proposition 3.5.*** In the objective function of problem (20), only $-\alpha\|\boldsymbol{Q}^{\mathrm{T}}\boldsymbol{u}\|_1$ is a nonconvex term. This term is explicitly written as

$$-\alpha\|\boldsymbol{Q}^{\mathrm{T}}\boldsymbol{u}\|_1 = -\alpha\sum_{l=1}^{L}|\boldsymbol{q}_l^{\mathrm{T}}\boldsymbol{u}|, \tag{43}$$

where $\boldsymbol{q}_1, \ldots, \boldsymbol{q}_L \in \mathbb{R}^d$ are column vectors of $\boldsymbol{Q}$. For each $l = 1, \ldots, L$, let w_l be an additional variable that serves as a lower bound for $|\boldsymbol{q}_l^{\mathrm{T}}\boldsymbol{u}|$, i.e., $w_l \leq |\boldsymbol{q}_l^{\mathrm{T}}\boldsymbol{u}|$. Then minimizing (43) is equivalent to minimizing

$$-\alpha\sum_{l=1}^{L} w_l \tag{44}$$

under the constraints

$$(w_l \leq \boldsymbol{q}_l^{\mathrm{T}}\boldsymbol{u}) \vee (w_l \leq -\boldsymbol{q}_l^{\mathrm{T}}\boldsymbol{u}), \quad l = 1, \ldots, L. \tag{45}$$

Here $\vee$ denotes the logical "or". For each $l = 1, \ldots, L$, constraint (45) can be rewritten as

$$w_l \leq \boldsymbol{q}_l^{\mathrm{T}}\boldsymbol{u} + Mt_l, \tag{46a}$$

$$w_l \leq -\boldsymbol{q}_l^{\mathrm{T}}\boldsymbol{u} + M(1 - t_l), \tag{46b}$$

$$t_l \in \{0, 1\}, \tag{46c}$$

where $M \gg 0$ is a sufficiently large constant. The upshot is that minimizing (43) is equivalent to minimizing (44) under constraint (46), and hence problem (20) is reduced to problem (23).

A.4 ***Proof of Proposition 3.6.*** In the objective function of problem (26), only the term

$$-\alpha \| \boldsymbol{Q}^{\mathrm{T}} \boldsymbol{u} \|_{\infty} = -\alpha \max\{|\boldsymbol{q}_l^{\mathrm{T}} \boldsymbol{u}| \mid l = 1, \ldots, L\} \tag{47}$$

is nonconvex. To rewrite this term we introduce additional variables w_l $(l = 1, \ldots, L)$ and v, where w_l is a lower bound for $|\boldsymbol{q}_l^{\mathrm{T}} \boldsymbol{u}|$ and v is a lower bound for $\max\{w_1, \ldots, w_L\}$. Then minimizing (47) is equivalent to minimizing

$$-\alpha v \tag{48}$$

under the constraints

$$(v \le w_1) \vee \cdots \vee (v \le w_L), \tag{49a}$$

$$w_l \le |\boldsymbol{q}_l^{\mathrm{T}} \boldsymbol{u}|, \quad l = 1, \ldots, L, \tag{49b}$$

where $\vee$ denotes the logical "or". Furthermore, by introducing 0-1 variables $y_1, \ldots, y_L$, (49a) can be replaced with

$$v \le w_l + M(1 - y_l), \quad l = 1, \ldots, L, \tag{50a}$$

$$\sum_{l=1}^{L} y_l = 1, \tag{50b}$$

$$y_l \in \{0, 1\}, \qquad l = 1, \ldots, L, \tag{50c}$$

where $M \gg 0$ is a sufficiently large constant. Indeed, (50b) and (50c) imply that there exists unique $\hat{l} \in \{1, \ldots, L\}$ satisfying $y_{\hat{l}} = 1$ and $y_l = 0$ for all $l \ne \hat{l}$. Then (50a) reads

$$v \le w_{\hat{l}},$$

$$v \le w_l + M \ \text{ for all } l \ne \hat{l},$$

which allows $v > w_l$ for all $l \ne \hat{l}$. . Next, observe that (49b) can be rewritten as

$$(w_l \le \boldsymbol{q}_l^{\mathrm{T}} \boldsymbol{u}) \vee (w_l \le -\boldsymbol{q}_l^{\mathrm{T}} \boldsymbol{u}), \quad l = 1, \ldots, L. \tag{51}$$

By using 0-1 variables, (51) is rewritten as

$$w_l \le \boldsymbol{q}_l^{\mathrm{T}} \boldsymbol{u} + M t_l, \qquad l = 1, \ldots, L, \tag{52a}$$

$$w_l \le -\boldsymbol{q}_l^{\mathrm{T}} \boldsymbol{u} + M(1 - t_l), \quad l = 1, \ldots, L, \tag{52b}$$

$$t_l \in \{0, 1\}, \qquad l = 1, \ldots, L. \tag{52c}$$

As a consequence, we see that (49) is rewritten as (50) and (52). By using this, problem (26) is reduced to problem (27).

References

[Aardal et al. 2005] K. Aardal, G. L. Nemhauser, and R. Weismantel (editors), *Discrete optimization*, Handbooks in Operations Research and Management Science **12**, Elsevier, Amsterdam, 2005.

[Alefeld and Mayer 2000] G. Alefeld and G. Mayer, "Interval analysis: theory and applications", *J. Comput. Appl. Math.* **121**:1-2 (2000), 421–464.

[Alibrandi and Ricciardi 2008] U. Alibrandi and G. Ricciardi, "The use of stochastic stresses in the static approach of probabilistic limit analysis", *Int. J. Numer. Methods Eng.* **73**:6 (2008), 747–782.

[Ben-Haim 2006] Y. Ben-Haim, *Information-gap decision theory: decisions under severe uncertainty*, 2nd ed., Academic Press, San Diego, CA, 2006.

[Ben-Haim and Elishakoff 1990] Y. Ben-Haim and I. Elishakoff, *Convex models of uncertainty in applied mechanics*, Studies in Applied Mechanics **25**, Elsevier, Amsterdam, 1990.

[Beyer and Sendhoff 2007] H.-G. Beyer and B. Sendhoff, "Robust optimization: a comprehensive survey", *Comput. Methods Appl. Mech. Eng.* **196**:33-34 (2007), 3190–3218.

[Biondini et al. 2004] F. Biondini, F. Bontempi, and P. G. Malerba, "Fuzzy reliability analysis of concrete structures", *Comput. Struct.* **82**:13–14 (2004), 1033–1052.

[Bjerager 1989] P. Bjerager, "Plastic systems reliability by LP and FORM", *Comput. Struct.* **31**:2 (1989), 187–196.

[Boyd and Vandenberghe 2004] S. Boyd and L. Vandenberghe, *Convex optimization*, Cambridge University Press, Cambridge, 2004.

[Caddemi et al. 2002] S. Caddemi, G. Ricciardi, and C. Saccà, "Limit analysis of structures with stochastic strengths by a static approach", *Meccanica* **37**:6 (2002), 527–544.

[Catallo 2004] L. Catallo, "Genetic anti-optimization for reliability structural assessment of precast concrete structures", *Comput. Struct.* **82**:13-14 (2004), 1053–1065.

[Chen et al. 2002] S. Chen, H. Lian, and X. Yang, "Interval static displacement analysis for structures with interval parameters", *Int. J. Numer. Methods Eng.* **53**:2 (2002), 393–407.

[Corradi and Maier 1973–1974] L. Corradi and G. Maier, "Inadaptation theorems in the dynamics of elastic work-hardening structures", *Ing. Arch.* **43**:1 (1973–1974), 44–57.

[De Gersem et al. 2007] H. De Gersem, D. Moens, W. Desmet, and D. Vandepitte, "Interval and fuzzy dynamic analysis of finite element models with superelements", *Comput. Struct.* **85**:5–6 (2007), 304–319.

[Degrauwe et al. 2010] D. Degrauwe, G. Lombaert, and G. De Roeck, "Improving interval analysis in finite element calculations by means of affine arithmetic", *Comput. Struct.* **88**:3–4 (2010), 247–254.

[Faigle et al. 2002] U. Faigle, W. Kern, and G. Still, *Algorithmic principles of mathematical programming*, Kluwer Texts in the Mathematical Sciences **24**, Kluwer, Dordrecht, 2002.

[Guo et al. 2008] X. Guo, W. Bai, and W. Zhang, "Extreme structural response analysis of truss structures under material uncertainty via linear mixed 0–1 programming", *Int. J. Numer. Methods Eng.* **76**:3 (2008), 253–277.

[Guo et al. 2009] X. Guo, W. Bai, and W. Zhang, "Confidence extremal structural response analysis of truss structures under static load uncertainty via SDP relaxation", *Comput. Struct.* **87**:3–4 (2009), 246–253.

[Guo et al. 2011] X. Guo, J. Du, and X. Gao, "Confidence structural robust optimization by non-linear semidefinite programming-based single-level formulation", *Int. J. Numer. Methods Eng.* **86**:8 (2011), 953–974.

[Gurobi 2013] *Gurobi optimizer reference manual*, Gurobi Optimization, Houston, TX, 2013, Available at http://www.gurobi.com.

[Hlaváček et al. 2004] I. Hlaváček, J. Chleboun, and I. Babuška, *Uncertain input data problems and the worst scenario method*, North-Holland Series in Applied Mathematics and Mechanics **46**, Elsevier, Amsterdam, 2004.

[IBM ILOG 2011] *User's manual for CPLEX*, IBM ILOG, Armonk, NY, 2011, Available at http://www.ilog.com.

[Jung and Pulmano 1996] C. Y. Jung and V. A. Pulmano, "Improved fuzzy linear programming model for structure designs", *Comput. Struct.* **58**:3 (1996), 471–477.

[Kanno 2012] Y. Kanno, "Worst scenario detection in limit analysis of trusses against deficiency of structural components", *Eng. Struct.* **42** (2012), 33–42.

[Kanno and Takewaki 2006] Y. Kanno and I. Takewaki, "Confidence ellipsoids for static response of trusses with load and structural uncertainties", *Comput. Methods Appl. Mech. Eng.* **196**:1-3 (2006), 393–403.

[Kanno and Takewaki 2007] Y. Kanno and I. Takewaki, "Worst case plastic limit analysis of trusses under uncertain loads via mixed 0–1 programming", *J. Mech. Mater. Struct.* **2**:2 (2007), 245–273.

[Kanno and Takewaki 2008] Y. Kanno and I. Takewaki, "Semidefinite programming for uncertain linear equations in static analysis of structures", *Comput. Methods Appl. Mech. Eng.* **198**:1 (2008), 102–115.

[Kanno and Takewaki 2009] Y. Kanno and I. Takewaki, "Semidefinite programming for dynamic steady-state analysis of structures under uncertain harmonic loads", *Comput. Methods Appl. Mech. Eng.* **198**:41-44 (2009), 3239–3261.

[Langley 2000] R. S. Langley, "Unified approach to probabilistic and possibilistic analysis of uncertain systems", *J. Eng. Mech.* (*ASCE*) **126**:11 (2000), 1163–1172.

[Maier 1970] G. Maier, "A matrix structural theory of piecewise linear elastoplasticity with interacting yield planes", *Meccanica* **5**:1 (1970), 54–66.

[Marti 2008] K. Marti, "Limit load and shakedown analysis of plastic structures under stochastic uncertainty", *Comput. Methods Appl. Mech. Eng.* **198**:1 (2008), 42–51.

[Marti and Stoeckl 2004] K. Marti and G. Stoeckl, "Stochastic linear programming methods in limit load analysis and optimal plastic design under stochastic uncertainty", *Z. Angew. Math. Mech.* **84**:10–11 (2004), 666–677.

[McWilliam 2001] S. McWilliam, "Anti-optimization of uncertain structures using interval analysis", *Comput. Struct.* **79**:4 (2001), 421–430.

[Moens and Hanss 2011] D. Moens and M. Hanss, "Non-probabilistic finite element analysis for parametric uncertainty treatment in applied mechanics: recent advances", *Finite Elem. Anal. Des.* **47**:1 (2011), 4–16.

[Moens and Vandepitte 2005] D. Moens and D. Vandepitte, "A survey of non-probabilistic uncertainty treatment in finite element analysis", *Comput. Methods Appl. Mech. Eng.* **194**:12-16 (2005), 1527–1555.

[Möller and Beer 2008] B. Möller and M. Beer, "Engineering computation under uncertainty: capabilities of non-traditional models", *Comput. Struct.* **86**:10 (2008), 1024–1041.

[Munro and Chuang 1986] J. Munro and P.-H. Chuang, "Optimal plastic design with imprecise data", *J. Eng. Mech.* (*ASCE*) **112**:9 (1986), 888–903.

[Neumaier 1990] A. Neumaier, *Interval methods for systems of equations*, Encyclopedia of Mathematics and its Applications **37**, Cambridge University Press, 1990.

[Neumaier and Pownuk 2007] A. Neumaier and A. Pownuk, "Linear systems with large uncertainties, with applications to truss structures", *Reliab. Comput.* **13**:2 (2007), 149–172.

[Ngo and Tin-Loi 2007] N. S. Ngo and F. Tin-Loi, "Shakedown analysis using the p-adaptive finite element method and linear programming", *Eng. Struct.* **29**:1 (2007), 46–56.

[Nikolaidis et al. 2004] E. Nikolaidis, S. Chen, H. Cudney, R. T. Haftka, and R. Rosca, "Comparison of probability and possibility for design against catastrophic failure under uncertainty", *J. Mech. Des.* (*ASME*) **126**:3 (2004), 386–394.

[Polizzotto 1982] C. Polizzotto, "A unified treatment of shakedown theory and related bounding techniques", *Solid Mech. Arch.* **7** (1982), 19–75.

[Polizzotto et al. 1991] C. Polizzotto, G. Borino, S. Caddemi, and P. Fuschi, "Shakedown problems for material models with internal variables", *Eur. J. Mech. A Solids* **10**:6 (1991), 621–639.

[Polizzotto et al. 1993] C. Polizzotto, G. Borino, S. Caddemi, and P. Fuschi, "Theorems of restricted dynamic shakedown", *Int. J. Mech. Sci.* **35**:9 (1993), 787–801.

[Rockafellar 1970] R. T. Rockafellar, *Convex analysis*, Princeton Mathematical Series **28**, Princeton University Press, 1970.

[Schuëller and Jensen 2008] G. I. Schuëller and H. A. Jensen, "Computational methods in optimization considering uncertainties: an overview", *Comput. Methods Appl. Mech. Eng.* **198**:1 (2008), 2–13.

[Sikorski and Borkowski 1990] K. Sikorski and A. Borkowski, "Ultimate load analysis by stochastic programming", pp. 403–424 in *Mathematical programming methods in structural plasticity*, edited by D. L. Smith, CISM Courses and Lectures **299**, Springer, Wien, 1990.

[Simon and Weichert 2012] J.-W. Simon and D. Weichert, "Shakedown analysis with multidimensional loading spaces", *Comput. Mech.* **49**:4 (2012), 477–485.

[Staat and Heitzer 2003] M. Staat and M. Heitzer, "Probabilistic limit and shakedown problems", Chapter 7, pp. 217–268 in *Numerical methods for limit and shakedown analysis: deterministic and probabilistic problems*, edited by M. Staat and M. Heitzer, NIC Series **15**, John von Neumann Institute for Computing, Jülich, 2003.

[Steele 2004] J. M. Steele, *The Cauchy–Schwarz master class: an introduction to the art of mathematical inequalities*, Cambridge University Press, New York, 2004.

[Takewaki et al. 2013] I. Takewaki, K. Fujita, and S. Yoshitomi, "Uncertainties in long-period ground motion and its impact on building structural design: case study of the 2011 Tohoku (Japan) earthquake", *Eng. Struct.* **49** (2013), 119–134.

[Trần et al. 2009] T. N. Trần, R. Kraißig, and M. Staat, "Probabilistic limit and shakedown analysis of thin plates and shells", *Struct. Saf.* **31**:1 (2009), 1–18.

[Valdebenito and Schuëller 2010] M. A. Valdebenito and G. I. Schuëller, "A survey on approaches for reliability-based optimization", *Struct. Multidiscip. Optim.* **42**:5 (2010), 645–663.

[Wang et al. 1994] W. Wang, M. R. Ramirez, and R. B. Corotis, "Reliability analysis of rigid-plastic structures by the static approach", *Struct. Saf.* **15**:3 (1994), 209–235.

[Wolsey 1998] L. A. Wolsey, *Integer programming*, Wiley, New York, 1998.

[Zang et al. 2005] C. Zang, M. I. Friswell, and J. E. Mottershead, "A review of robust optimal design and its application in dynamics", *Comput. Struct.* **83**:4-5 (2005), 315–326.

Received 10 Mar 2013. Revised 19 Jul 2013. Accepted 19 Aug 2013.

YOSHIHIRO KANNO: kanno@mist.i.u-tokyo.ac.jp
Department of Mathematical Informatics, Graduate School of Information Science and Technology, University of Tokyo, Hongo 7-3-1, Bunkyo-ku, Tokyo 113-8656, Japan

JOURNAL OF MECHANICS OF MATERIALS AND STRUCTURES
Vol. 8, No. 8-10, 2013
dx.doi.org/10.2140/jomms.2013.8.441

A TWO-DIMENSIONAL PROBLEM IN MAGNETOTHERMOELASTICITY WITH LASER PULSE UNDER DIFFERENT BOUNDARY CONDITIONS

SUNITA DESWAL, SANDEEP SINGH SHEORAN AND KAPIL KUMAR KALKAL

This paper is concerned with the study of vibrations induced by a laser beam in the context of generalized magnetothermoelasticity. The basic governing equations for isotropic and homogeneous elastic solids are formulated under Green–Naghdi theory in the x-z plane. The temporal profile of the laser beam is considered as non-Gaussian. The governing nondimensional equations are solved using normal mode analysis. The obtained solution is then applied to two specific problems in the half-space, where the boundary is subjected to either a mechanical or thermal load. Numerical computations are performed for a specific model to calculate the displacement, temperature, and stress fields and the results are displayed. The effects of time and magnetic field on the variation of different field quantities are analyzed in the figures.

1. Introduction

The dynamical interactions between the thermal and mechanical fields in solids are important to many practical applications, such as modern aeronautics, nuclear reactors and high speed particle accelerators, etc. The classical theory of thermoelasticity finds stresses caused by a temperature field using the parabolic heat conduction equation. The absence of any elasticity term in the heat conduction equation for uncoupled thermoelasticity appears to be unrealistic, since, due to mechanical loading of an elastic body, the strain so produced causes variation in temperature field. Moreover, the parabolic nature of the heat conduction equation results in an infinite velocity of wave propagation, which also contradicts the actual physical phenomena.

Biot [1956] developed the coupled theory of thermoelasticity to overcome the paradox inherent in the uncoupled theory, that elastic changes have no effect on temperature. In this theory, the equations of elasticity and heat conduction are coupled. However, it shares the defect of the uncoupled theory in which it predicts an infinite speed of propagation for heat waves. Generalized thermoelastic theories have been developed with the objective of removing this defect of coupled theory. The development of these theories was accelerated by the advent of the experimental observation of the second sound effect in materials at very low temperatures by Ackerman et al. [1966] and Ackerman and Overton [1969]. In heat transfer problems involving very short time intervals and/or very high heat flux, the second sound effect in the coupled theory yields results that are realistic and very much different from those obtained from the classical theory of thermoelasticity.

Sandeep Singh Sheoran is thankful to the University Grants Commission, New Delhi, for financial support in the form of Junior Research Fellowship vide letter no. F. 17-11/2008 (SA-1).
Keywords: G-N theory, magnetic field, laser pulse, normal mode analysis.

It is well known that there are three major generalizations of the theory of thermoelasticity. The first is that made by Lord and Shulman [1967], known as L-S theory, which involves one relaxation time for a thermoelastic process. The second is due to Green and Lindsay [1972] and is known as G-L theory. It takes into account two parameters as relaxation times. L-S theory only modifies Fourier's heat conduction equation, while G-L theory modifies both the energy equation and the equation of motion. Dhaliwal and Sherief [1980] extended L-S theory by including the anisotropic case. Later on, by providing sufficient basic modifications to the constitutive equations to follow thermodynamical principles, Green and Naghdi [1991; 1992; 1993] produced an alternative theory which was divided into three different parts, referred to as G-N theory of types I, II, and III. The constitutive assumptions for the heat flux vector are different in each theory. The nature of these three types of constitutive equations is such that when the respective theories are linearized, type I is same as classical heat conduction theory (based on Fourier's heat conduction law), type II predicts the finite speed of heat propagation involving no energy dissipation, and type III indicates the propagation of thermal signals with finite speed. Hetnarski and Ignaczak [1999] presented a survey of various representative theories in the range of generalized thermoelasticity. Ezzat et al. [2004] discussed a problem in generalized thermoelasticity theory for isotropic media with temperature-dependent moduli of elasticity under L-S, G-L, and coupled theories. Youssef [2006] studied two-dimensional generalized thermoelasticity problem with a spherical cavity subjected to thermal shock and ramp-type heating.

During pulsed laser heating, a thermoelastic wave is generated due to thermal expansion in the near-surface region and propagates into the target. Because of the extremely short heating time, the laser-induced thermoelastic wave has an extremely high strain rate, which in turn causes strong coupling between the strain rate and the temperature field. This coupling damps the stress wave during its propagation and induces a localized temperature variation [Wang and Xu 2001; 2002]. Chen et al. [2004] developed a problem in which three different approaches, ultrafast thermoelasticity, Lord–Shulman theory, and classical thermoelasticity, are used to investigate thermoelastic stress waves in a gold medium. Sun et al. [2008] studied the coupled thermoelastic vibrations of a microscale beam resonator induced by laser pulse heating. The vibrations of deflection and thermal moments were calculated using an analytical numerical technique based on the Laplace transformation. The effect of laser pulse energy depth, the size effect, and the effects of different boundary conditions were analyzed.

Laser-induced vibration of microbeam resonators has attracted considerable attention recently due to many important technological applications in microelectromechanical systems (MEMS) and nanoelectromechanical systems (NEMS). The field equations for coupled thermoelastic vibration of Rayleigh and Timoshenko beams have been derived by Jones [1966]. Many authors have studied the vibration and heat transfer process of beams [Kidawa-Kukla 1997; 2003; Fang et al. 2007].

So-called ultrashort lasers are those with a pulse duration ranging from nanoseconds to femtoseconds, in general. In the case of ultrashort-pulsed laser heating, high-intensity energy flux and ultrashort duration laser beams have introduced situations in which very large thermal gradients or an ultrahigh heating speed may exist on the boundaries. In such cases, as pointed out by many investigators, the classical Fourier model, which leads to an infinite propagation speed of thermal energy, is no longer valid [Joseph and Preziosi 1989; Özişik and Tzou 1994; Tzou 1997; Tang and Araki 1999]. The non-Fourier effect of heat conduction takes into account the effect of mean free time (thermal relaxation time) in the energy carrier's

collision process, which can eliminate this contradiction. He et al. [2002] solved a boundary value problem for a one-dimensional semi-infinite piezoelectric rod with the left boundary subjected to a sudden heat flux using the theory of generalized thermoelasticity with one relaxation time. Youssef and Al-Felali [2012] investigated the induced temperature and stress fields when subjected to non-Gaussian laser heating in context with classical coupled thermoelasticity, Lord–Shulman theory and Green–Lindsay theory.

The theory of magnetothermoelasticity has received the attention of many researchers due to its applications in widely diverse fields such as geophysics, for understanding the effect of earth's magnetic field on seismic waves, damping of acoustic waves, emission of electromagnetic radiations from nuclear devices, optics, etc. The theory of magnetothermoelasticity was introduced by Knopoff [1955] and Chadwick [1957] and developed by Kaliski and Petykiewicz [1959]. The theoretical outline of the development of magnetothermoelasticity was discussed by Paria [1962]. Paria studied the propagation of plane magnetothermoelastic waves in an isotropic unbounded medium under the influence of a magnetic field acting transversely to the direction of propagation. Nayfeh and Nemat-Nasser [1972] studied the propagation of plane waves in a solid under the influence of an electromagnetic field. Sherief and Ezzat [1996] discussed a thermal shock problem in magnetothermoelasticity with thermal relaxation. Sherief and Helmy [2002] illustrated a two-dimensional half-space problem subjected to a nonuniform thermal shock in the context of electromagnetothermoelasticity theory. Ezzat and Youssef [2005] constructed a generalized magnetothermoelasticity problem in a perfectly conducting medium. Baksi et al. [2005] examined a magnetothermoelastic problem with thermal relaxation and a heat source in a three-dimensional, infinite rotating elastic medium. Deswal and Kalkal [2011] employed normal mode analysis to study a problem in the purview of magnetothermoviscoelasticity with diffusion.

The objective of present investigation is to study the phenomenon of wave propagation in generalized magnetothermoelasticity with pulsed heating of a microbeam. Normal mode analysis is employed for the general solution of the problem. The resulting formulation is then applied to the problem of an elastic half-space whose boundary is subjected to two types of loads, mechanical and thermal. Finally, a numerical example has been considered and the results are displayed graphically to highlight the effects of magnetic field and time on physical quantities. To the authors' best knowledge, the technique of normal mode analysis has never been applied to Green–Naghdi theory of type III. It is also pertinent that hardly any effort has been made to discuss the laser pulse problem in the above-mentioned theory. In addition, we have also studied magnetic effects on the field variables. The present model is not only of theoretical interest, but may have practical applications in various fields such as geophysics, plasma physics, and other related topics. The self-focusing of a circularly polarized laser pulse in the hot plasma is very much influenced by the application of an external magnetic field. The external magnetic field enhances self-focusing for right-hand polarization while for left-hand polarization it acts to reduce self-focusing [Javan and Nasirzadeh 2012].

2. Governing equations

The governing equations in the context of Green–Naghdi theory of type III with a laser pulse heat source and a magnetic field for a isotropic and homogeneous elastic medium are (see [Kumar and Mukhopadhyay 2009])

- the equation of motion

$$\rho \ddot{u}_i = \sigma_{ji,j} + F_i, \tag{1}$$

where u_i are the components of displacement vector $\vec{u}$, ρ is the density of the medium, σ_{ij} are the components of the stress tensor, and F_i are the components of the Lorentz body force vector;

- the heat conduction equation

$$k^*\theta_{,ii} + k\dot{\theta}_{,ii} = \rho C_E \ddot{\theta} + \beta_1 T_0 \ddot{u}_{i,i} - \frac{\partial Q}{\partial t}, \tag{2}$$

where $\theta = T - T_0$ with T the absolute temperature and T_0 is a reference temperature assumed to obey the inequality $|\theta/T_0| \ll 1$, C_E is the specific heat, k^* is material constant, k is the thermal conductivity, and $\beta_1 = (3\lambda + 2\mu)\alpha_t$ with α_t is the coefficient of linear thermal expansion;

- the constitutive relations

$$\sigma_{ij} = 2\mu e_{ij} + \lambda e \delta_{ij} - \beta_1 \theta \delta_{ij}, \tag{3}$$

$$e_{ij} = \tfrac{1}{2}(u_{i,j} + u_{j,i}), \tag{4}$$

where e_{ij} are the components of strain tensor, δ_{ij} is the Kronecker delta function, e is the cubical dilation, and λ and μ are the Lamé constants.

We take linearized Maxwell's equations governing the electromagnetic field for a perfectly conducting medium as

$$\operatorname{curl} \vec{h} = \vec{J} + \varepsilon_0 \frac{\partial \vec{E}}{\partial t}, \tag{5}$$

$$\operatorname{curl} \vec{E} = -\mu_0 \frac{\partial \vec{h}}{\partial t}, \tag{6}$$

$$\vec{E} = -\mu_0 \Big(\frac{\partial \vec{h}}{\partial t} \times \vec{H} \Big), \tag{7}$$

$$\operatorname{div} \vec{h} = 0, \tag{8}$$

where μ_0 is the magnetic permeability, ε_0 is the electric permittivity, $\vec{H}$ is the applied magnetic field, $\vec{h}$ is the induced magnetic field, $\vec{E}$ is the induced electric field, $\vec{J}$ is the current density vector, and Q is the laser pulse heat source.

3. Problem formulation

A rectangular cartesian coordinate system is chosen in such a way that the x-axis lies along the free boundary of a perfectly conducting homogeneous isotropic generalized thermoelastic half-space with a laser pulse heat source, subjected to a constant magnetic field $\vec{H}(0, H_0, 0)$ which produces an induced magnetic field $\vec{h}(0, h_2, 0)$ and induced electric field $\vec{E}(E_1, 0, E_3)$. Let the z-axis point vertically downward into the half-space so that it occupies the region $z \geq 0$. The surface ($z = 0$) of the half-space is subjected to mechanical and thermal loads, and all the considered quantities will be functions of the time variable t and of coordinates x and z. Also, the boundary plane ($z = 0$) of the half-space is heated

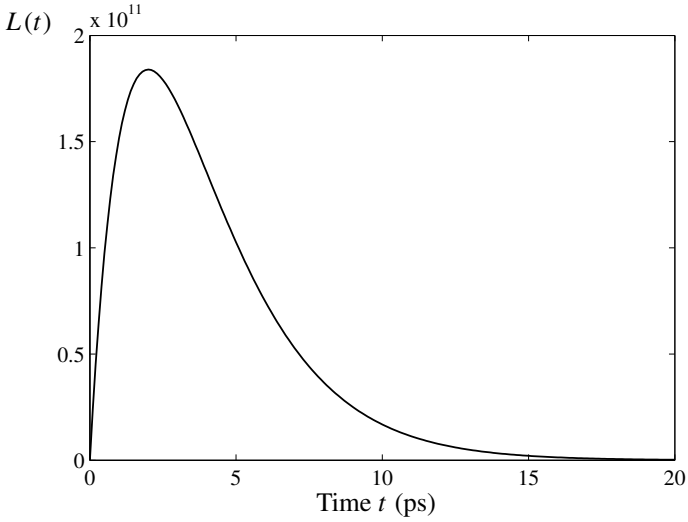

Figure 1. Temporal profile of $L(t)$ ($t_p = 2\,\text{ps}$).

uniformly by a laser pulse with non-Gaussian temporal profile [Sun et al. 2008]

$$L(t) = \frac{L_0 t}{t_p^2} \exp\Big(-\frac{t}{t_p}\Big), \tag{9}$$

where t_p is the time duration of a laser pulse and L_0 the laser intensity, which is defined as the total energy carried by a laser pulse per unit cross section of the laser beam. In the present study we take $t_p = 2\,\text{ps}$ as the time duration. According to [Tang and Araki 1999], the thermal conduction in the beam can be modeled as a one-dimensional problem with an energy source $Q(z, t)$ as

$$Q(z, t) = \frac{R_a}{\delta} \exp\Big(\frac{z - h/2}{\delta}\Big) L(t), \tag{10}$$

where δ is the absorption depth of the heating energy and R_a the absorptivity of the irradiated surface. For a two-dimensional problem in the x-z plane, the displacement components take the form

$$u = u(x, z, t), \quad v = 0, \quad w = w(x, z, t). \tag{11}$$

The strain components become

$$e_{xx} = \frac{\partial u}{\partial x}, \quad e_{zz} = \frac{\partial w}{\partial z}, \quad e_{xz} = \frac{1}{2}\Big(\frac{\partial u}{\partial z} + \frac{\partial w}{\partial x}\Big), \quad e_{xy} = e_{yz} = e_{yy} = 0. \tag{12}$$

The cubical dilatation e is thus given by

$$e = e_{xx} + e_{yy} + e_{zz} = \Big(\frac{\partial u}{\partial x} + \frac{\partial w}{\partial z}\Big). \tag{13}$$

The components of the initial magnetic field vector $\vec{H}$ are

$$H_x = 0, \quad H_y = H_0, \quad H_z = 0. \tag{14}$$

The electric intensity vector $\vec{E}$ is parallel to the current density vector $\vec{J}$, thus

$$E_x = E_1, \quad E_y = 0, \quad E_z = E_3, \tag{15}$$

$$J_x = J_1, \quad J_y = 0, \quad J_z = J_3. \tag{16}$$

From (5)–(8), we can obtain

$$E_1 = \mu_0 H_0 \frac{\partial w}{\partial t}, \qquad E_3 = -\mu_0 H_0 \frac{\partial u}{\partial t}, \tag{17}$$

$$h_1 = 0, \qquad h_2 = -H_0 e, \qquad h_3 = 0, \tag{18}$$

$$J_1 = -\varepsilon_0 \mu_0 H_0 \frac{\partial^2 w}{\partial t^2}, \quad J_3 = \varepsilon_0 \mu_0 H_0 \frac{\partial^2 u}{\partial t^2}. \tag{19}$$

The Lorentz's force $\vec{F}$ is given by the relation

$$\vec{F} = \mu_0 (\vec{J} \times \vec{H}). \tag{20}$$

Inserting (14) and (19) in (20), we can obtain the components of the Lorentz's force $\vec{F}$ as

$$F_x = -\varepsilon_0 \mu_0^2 H_0^2 \frac{\partial^2 u}{\partial t^2}, \quad F_y = 0, \quad F_z = -\varepsilon_0 \mu_0^2 H_0^2 \frac{\partial^2 w}{\partial t^2}. \tag{21}$$

Now, we will use the following nondimensional variables:

$$\begin{aligned} (x', z', u', w', \delta', h') &= c_0 \eta_0 (x, z, u, w, \delta, h), \qquad (t', t_p') = c_0^2 \eta_0 (t, t_p), \\ (\sigma_{ij}', p_1') &= \frac{1}{\lambda + 2\mu} (\sigma_{ij}, p_1), \qquad (\theta', p_2') = \frac{\beta_1}{(\lambda + 2\mu)} (\theta, p_2), \end{aligned} \tag{22}$$

where

$$c_0^2 = \frac{\lambda + 2\mu}{\rho}, \quad \eta_0 = \frac{\rho C_E}{k^*} \bar{\omega}, \quad \bar{\omega} = \frac{\rho C_E c_0^3}{k^* h^*},$$

and h^* is some standard length.

With the help of these nondimensional quantities, (1)–(3) take the following form (dropping the prime signs for convenience):

$$\alpha \frac{\partial^2 u}{\partial t^2} = \beta^2 \nabla^2 u + (1 - \beta^2) \frac{\partial e}{\partial x} - \frac{\partial \theta}{\partial x}, \tag{23}$$

$$\alpha \frac{\partial^2 w}{\partial t^2} = \beta^2 \nabla^2 w + (1 - \beta^2) \frac{\partial e}{\partial z} - \frac{\partial \theta}{\partial z}, \tag{24}$$

$$k^* \nabla^2 \theta + k (c_0^2 \eta_0) \nabla^2 \dot{\theta} = \rho C_E c_0^2 \frac{\partial^2 \theta}{\partial t^2} + \frac{\beta_1^2 T_0}{\rho} \frac{\partial^2 e}{\partial t^2} - \frac{\beta_1 c_0 \eta_0}{\rho} \frac{\partial Q}{\partial t}, \tag{25}$$

$$\sigma_{zx} = \beta^2 \Big(\frac{\partial u}{\partial z} + \frac{\partial w}{\partial x} \Big), \tag{26}$$

$$\sigma_{zz} = \frac{\partial w}{\partial z} + (1 - 2\beta^2) \frac{\partial u}{\partial x} - \theta, \tag{27}$$

where

$$\alpha = 1 + \frac{\varepsilon_0 \mu_0^2 H_0^2}{\rho}, \quad \beta^2 = \frac{\mu}{\lambda + 2\mu}.$$

Now, we introduce the displacement potentials $\phi(x, z, t)$ and $\psi(x, z, t)$, which are related to the displacement components as

$$u = \frac{\partial \phi}{\partial x} + \frac{\partial \psi}{\partial z}, \quad w = \frac{\partial \phi}{\partial z} - \frac{\partial \psi}{\partial x}. \tag{28}$$

By simplifying (23)–(25) using (28) along with (9) and (10), we obtain the following equations:

$$\frac{\partial^2 \phi}{\partial t^2} = \frac{1}{\alpha}(\nabla^2 \phi - \theta), \tag{29}$$

$$\frac{\partial^2 \psi}{\partial t^2} = \frac{1}{\alpha_0}\nabla^2 \psi, \tag{30}$$

$$k_1 \nabla^2 \theta + k_2 \nabla^2 \dot{\theta} = \frac{\partial^2 \theta}{\partial t^2} + \varepsilon_1 \nabla^2 \ddot{\phi} - \varepsilon_2 \frac{R_a L_0}{\delta t_p^2} \exp\left(\frac{z - h/2}{\delta} - \frac{t}{t_p}\right), \tag{31}$$

where

$$\alpha_0 = \frac{\alpha}{\beta^2}, \quad k_1 = \frac{k^*}{(\lambda + 2\mu)C_E}, \quad k_2 = \frac{k}{k^*}\bar{\omega}, \quad \varepsilon = \frac{\beta_1^2}{(\lambda + 2\mu)\rho}, \quad \varepsilon_1 = \frac{\varepsilon T_0}{C_E}, \quad \varepsilon_2 = \frac{\sqrt{\varepsilon}}{k^*}\bar{\omega}.$$

4. Normal mode analysis

The solution of the considered physical variables can be decomposed in terms of normal modes as

$$(u, w, \phi, \psi, \theta, \sigma_{ij})(x, z, t) = (u^*, w^*, \phi^*, \psi^*, \theta^*, \sigma_{ij}^*)(z) e^{(\omega t + \iota m x)}, \tag{32}$$

where ω is the complex time constant and m is the wave number in x-direction.

Using (32) in (29)–(31), we get

$$(D^2 - \varepsilon_3)\psi^* = 0, \tag{33}$$

$$(D^2 - \varepsilon_4)\phi^* = \theta^*, \tag{34}$$

$$(\varepsilon_5 D^2 - \varepsilon_6)\theta^* - \varepsilon_1 \omega^2 (D^2 - m^2)\phi^* + \varepsilon_2 \varepsilon_7 \exp\left(\frac{z - h/2}{\delta} - \frac{t}{t_p} - \omega t - \iota m x\right) = 0, \tag{35}$$

where

$$D \cong \frac{\partial}{\partial z}, \quad \varepsilon_3 = m^2 + \alpha_0 \omega^2, \quad \varepsilon_4 = m^2 + \alpha \omega^2, \quad \varepsilon_5 = k_1 + \omega k_2, \quad \varepsilon_6 = \varepsilon_5 m^2 + \omega^2, \quad \varepsilon_7 = \frac{R_a L_0}{t_p^2 \delta}.$$

Eliminating $\theta^*(z)$ between (34) and (35), we get the following fourth-order partial differential equation satisfied by $\phi^*(z)$:

$$(D^4 - AD^2 + B)\phi^*(z) = -CE \exp\left(\frac{z - h/2}{\delta} - \frac{t}{t_p} - \omega t - \iota m x\right), \tag{36}$$

where

$$A = \frac{\varepsilon_4 \varepsilon_5 + \varepsilon_1 \omega^2 + \varepsilon_6}{\varepsilon_5}, \quad B = \frac{\varepsilon_4 \varepsilon_6 + \varepsilon_1 m^2 \omega^2}{\varepsilon_5}, \quad C = \frac{\varepsilon_2 \varepsilon_7}{\varepsilon_5}, \quad E = 1 - \frac{(1 + \omega t_p)t}{t_p}.$$

Using the solutions of (33), (34), and (36) (which are assumed to be bounded as $z \to \infty$), we can express $\phi(x, z, t)$, $\psi(x, z, t)$, and $\theta(x, z, t)$ in the following forms:

$$\phi(x, z, t) = \left(\sum_{i=1}^{2} L_i e^{-\lambda_i z}\right) e^{(\omega t + \iota m x)} - \varepsilon_8 f_1(z, t), \tag{37}$$

$$\psi(x, z, t) = L_3 e^{-\lambda_3 z} e^{(\omega t + \iota m x)}, \tag{38}$$

$$\theta(x, z, t) = \left(\sum_{i=1}^{2} L_i' e^{-\lambda_i z}\right) e^{(\omega t + \iota m x)} - \varepsilon_9 f_1(z, t), \tag{39}$$

where L_i, L_i' $(i = 1, 2)$, and L_3 are parameters depending on m and ω and

$$f_1(z, t) = CE \exp\left(\frac{z - h/2}{\delta} - \frac{t}{t_p}\right), \qquad L_i' = (\lambda_i^2 - \varepsilon_3) L_i \quad (i = 1, 2),$$

$$\varepsilon_8 = \left(\frac{\delta^4}{\delta^4 B - \delta^2 A + 1}\right), \qquad \varepsilon_9 = \frac{1 - \varepsilon_4 \delta^2}{\delta^2}.$$

Here, λ_i $(i = 1, 2)$ are the positive roots of the characteristic equation

$$\lambda^4 - A\lambda^2 + B = 0,$$

and λ_3 is the root of the characteristic equation

$$\lambda^2 - \varepsilon_3 = 0.$$

Similarly, applying normal mode analysis and using the solutions of (33), (34), and (36) in (26)–(28), we get

$$u = \left(\iota m \sum_{i=1}^{2} L_i e^{-\lambda_i z} - \lambda_3 L_3 e^{-\lambda_3 z}\right) e^{(\omega t + \iota m x)} - \iota m \varepsilon_8 f_1(z, t), \tag{40}$$

$$w = -\left[\left(\sum_{i=1}^{2} L_i \lambda_i e^{-\lambda_i z} + (\iota m) L_3 e^{-\lambda_3 z}\right) e^{(\omega t + \iota m x)} + \varepsilon_8 \frac{f_1(z, t)}{\delta}\right], \tag{41}$$

$$\sigma_{zx} = -\beta^2 \left[\left(2\iota m \sum_{i=1}^{2} L_i \lambda_i e^{-\lambda_i z} - (\lambda_3^2 + m^2) L_3 e^{-\lambda_3 z}\right) e^{(\omega t + \iota m x)} + f_2(z, t)\right], \tag{42}$$

$$\sigma_{zz} = \left(\sum_{i=1}^{2} (\eta + \varepsilon_4) L_i e^{-\lambda_i z} - 2\iota m \beta^2 \lambda_3 L_3 e^{-\lambda_3 z}\right) e^{(\omega t + \iota m x)} + f_3(z, t), \tag{43}$$

where $\eta = (1 - 2\beta^2) m^2$, $f_2(z, t) = \varepsilon_8 (2\iota m/\delta) f_1(z, t)$, and $f_3(z, t) = (\eta - 1/\delta^2 - \varepsilon_9) \varepsilon_8 f_1(z, t)$.

5. Applications

We consider a homogeneous, isotropic magnetothermoelastic solid with laser pulse heating occupying the half-space $z \geq 0$. The boundary $z = 0$ of the half-space is subjected to mechanical and thermal loads.

Case (i): *Mechanical load.* For an isothermal boundary plane $z = 0$, subjected to a normal mechanical load, the boundary conditions are given as

$$\sigma_{zz}(x, 0, t) + \bar{\sigma}_{zz}(x, 0, t) = -p_1(x, t), \tag{44}$$

$$\sigma_{zx}(x, 0, t) + \bar{\sigma}_{zx}(x, 0, t) = 0, \tag{45}$$

$$\theta(x, 0, t) = 0, \tag{46}$$

where $p_1(x, t)$ is a given function of x and t, σ_{zj} is the mechanical stress, and $\bar{\sigma}_{zj}$ $(j = x, y, z)$ is the Maxwell stress, which is given as

$$\bar{\sigma}_{zj} = \mu_0[H_z h_j + H_j h_z - H_k h_k \delta_{zj}]. \tag{47}$$

Invoking the nondimensional form of (44)–(46) along with (26)–(28) and normal mode analysis as for (32), we obtain the system of equations

$$P_1 L_1 + P_2 L_2 + P_3 L_3 = P, \tag{48}$$

$$Q_1 L_1 + Q_2 L_2 + Q_3 L_3 = Q, \tag{49}$$

$$R_1 L_1 + R_2 L_2 = R, \tag{50}$$

whose coefficients are defined as follows, where $\eta_1 = \dfrac{\mu_0 H_0^2}{\lambda + 2\mu}$:

$$\begin{aligned}
&P_i = \lambda_i^2 \eta_1 + m^2(2\beta^2 - \eta_1) + \alpha\omega^2, \quad Q_i = -2\iota m \lambda_i, \quad R_i = \lambda_i^2 - \varepsilon_4, \quad i = 1, 2,\\
&P_3 = 2\iota m \lambda_3 \beta^2, \qquad\qquad Q_3 = \lambda_3^2 + m^2,\\
&P = -p_1^* + \left(\frac{1}{\delta^2}(1 + \eta_1) - \eta - m^2\eta_1 - \varepsilon_9\right)\varepsilon_8 f_1(z, t) e^{-(\omega t + \iota m x)},\\
&Q = \frac{2\iota m}{\delta}\varepsilon_8 f_1(z, t) e^{-(\omega t + \iota m x)}, \qquad R = \varepsilon_8 \varepsilon_9 f_1(z, t) e^{-(\omega t + \iota m x)}.
\end{aligned} \tag{51}$$

The solution of the system of linear equations (48)–(50) can be expressed as

$$L_1 = \frac{\Delta_1}{\Delta}, \quad L_2 = \frac{\Delta_2}{\Delta}, \quad L_3 = \frac{\Delta_3}{\Delta}, \tag{52}$$

where

$$\Delta_1 = -P R_2 Q_3 + Q R_2 P_3 + R(P_2 Q_3 - Q_2 P_3), \tag{53}$$

$$\Delta_2 = -P_1 R Q_3 + Q_1 R P_3 + R_1(P Q_3 - Q P_3), \tag{54}$$

$$\Delta_3 = P_1(Q_2 R - Q R_2) - Q_1(P_2 R - R_2 P) + R_1(P_2 Q - Q_2 P), \tag{55}$$

$$\Delta = -P_1 R_2 Q_3 + Q_1 R_2 P_3 + R_1(P_2 Q_3 - Q_2 P_3). \tag{56}$$

Substituting the values of L_1, L_2 and L_3 from (52) into (39)–(43), we get the expressions for the displacement components, temperature distribution, and stress components as

$$u = \frac{1}{\Delta}\left(\iota m \sum_{i=1}^{2} \Delta_i e^{-\lambda_i z} - \lambda_3 \Delta_3 e^{-\lambda_3 z}\right) e^{(\omega t + \iota m x)} - (\iota m)\varepsilon_8 f_1(z, t), \tag{57}$$

$$w = -\left[\frac{1}{\Delta}\left(\sum_{i=1}^{2}\Delta_i\lambda_i e^{-\lambda_i z} + \iota m\Delta_3 e^{-\lambda_3 z}\right)e^{(\omega t+\iota m x)} + \varepsilon_8\frac{f_1(z,t)}{\delta}\right], \tag{58}$$

$$\theta = \frac{1}{\Delta}\left(\sum_{i=1}^{2}(\lambda_i^2-\varepsilon_3)\Delta_i e^{-\lambda_i z}\right)e^{(\omega t+\iota m x)} - \varepsilon_8\varepsilon_9 f_1(z,t), \tag{59}$$

$$\sigma_{zx} = -\beta^2\left[\frac{1}{\Delta}\left(2\iota m\sum_{i=1}^{2}\Delta_i\lambda_i e^{-\lambda_i z} - \eta_2\Delta_3 e^{-\lambda_3 z}\right)e^{(\omega t+\iota m x)} + f_2(z,t)\right], \tag{60}$$

$$\sigma_{zz} = \frac{1}{\Delta}\left(\sum_{i=1}^{2}(\eta+\varepsilon_4)\Delta_i e^{-\lambda_i z} - 2\iota m\beta^2\lambda_3\Delta_3 e^{-\lambda_3 z}\right)e^{(\omega t+\iota m x)} + f_3(z,t), \tag{61}$$

where $\eta_2 = \lambda_3^2 + m^2$.

Case (ii): *Thermal load.* In this case the boundary conditions on the surface $z = 0$ are given by

$$\sigma_{zz}(x,0,t) + \bar{\sigma}_{zz}(x,0,t) = 0, \tag{62}$$

$$\sigma_{zx}(x,0,t) + \bar{\sigma}_{zx}(x,0,t) = 0, \tag{63}$$

$$\theta(x,0,t) = p_2(x,t), \tag{64}$$

where $p_2(x,t)$ is a given function of x and t.

Adopting the same procedure as in Case (i), that is, using the required expressions in (62)–(64) (the dimensionless forms) and normal mode analysis, we can get a system of linear equations:

$$P_1L_1 + P_2L_2 + P_3L_3 = P', \tag{65}$$

$$Q_1L_1 + Q_2L_2 + Q_3L_3 = Q, \tag{66}$$

$$R_1L_1 + R_2L_2 = R', \tag{67}$$

where

$$\begin{aligned} P' &= \left(\frac{1}{\delta^2}(1+\eta_1) - \eta - m^2\eta_1 - \varepsilon_9\right)\varepsilon_8 f_1(z,t)e^{-(\omega t+\iota m x)}, \\ R' &= p_2^* + \varepsilon_8\varepsilon_9 f_1(z,t)e^{-(\omega t+\iota m x)}. \end{aligned} \tag{68}$$

The corresponding expressions for the displacement components u and w, temperature distribution θ, and stress components σ_{zx} and σ_{zz} are given by (57)–(61) with (P, R) replaced by (P', R') in (53)–(55).

6. Limiting cases

6.1. *Neglecting the laser pulse effect.*

Case (i): *Mechanical load.* To obtain the expressions for u, w, θ, σ_{zx}, and σ_{zz} in the context of the generalized theory of magnetothermoelasticity due to a mechanical load applied on the isothermal boundary $z = 0$, we shall neglect the parameter corresponding to the laser pulse heat. For this, we put $L_0 = 0$, which implies that $\varepsilon_7 = 0$ and $f_1(z,t) = 0$. Now, substituting $f_1(z,t) = 0$ in (51), we get the following modifications in the expressions of P, Q, and R:

$$P = -p_1^*, \quad Q = 0, \quad R = 0. \tag{69}$$

Using (69) in (53)–(55), we get

$$\Delta_1 = -p_1^* R_2 Q_3, \quad \Delta_2 = -p_1^* R_1 Q_3, \quad \Delta_3 = -p_1^* (R_2 Q_1 - R_1 Q_2). \tag{70}$$

Hence, (57)–(61) take the form

$$u = \frac{1}{\Delta}\left(\iota m \sum_{i=1}^{2} \Delta_i e^{-\lambda_i z} - \lambda_3 \Delta_3 e^{-\lambda_3 z} \right) e^{(\omega t + \iota m x)}, \tag{71}$$

$$w = -\left[\frac{1}{\Delta}\left(\sum_{i=1}^{2} \Delta_i \lambda_i e^{-\lambda_i z} + \iota m \Delta_3 e^{-\lambda_3 z} \right) e^{(\omega t + \iota m x)} \right], \tag{72}$$

$$\theta = \frac{1}{\Delta}\left(\sum_{i=1}^{2} (\lambda_i^2 - \varepsilon_3) \Delta_i e^{-\lambda_i z} \right) e^{(\omega t + \iota m x)}, \tag{73}$$

$$\sigma_{zx} = -\beta^2 \left[\frac{1}{\Delta}\left(2\iota m \sum_{i=1}^{2} \Delta_i \lambda_i e^{-\lambda_i z} - \eta_2 \Delta_3 e^{-\lambda_3 z} \right) e^{(\omega t + \iota m x)} \right], \tag{74}$$

$$\sigma_{zz} = \frac{1}{\Delta}\left(\sum_{i=1}^{2} (\eta + \varepsilon_4) \Delta_i e^{-\lambda_i z} - 2\iota m \beta^2 \lambda_3 \Delta_3 e^{-\lambda_3 z} \right) e^{(\omega t + \iota m x)}. \tag{75}$$

Case (ii): *Thermal load.* Similarly, for a thermal load, the corresponding expressions for the field variables under generalized magnetothermoelasticity are given by (71)–(75) with Δ_i replaced by Δ_i^*, where

$$P' = 0, \quad Q = 0, \quad R' = p_2^*, \tag{76}$$

and

$$\Delta_1^* = p_2^* (P_2 Q_3 - Q_2 P_3), \tag{77}$$

$$\Delta_2^* = -p_2^* (P_1 Q_3 - Q_1 P_3), \tag{78}$$

$$\Delta_3^* = p_2^* (P_1 Q_2 - P_2 Q_1). \tag{79}$$

6.2. ***Neglecting the magnetic effect.*** Case (i): *Mechanical load.* For a mechanical load applied on the isothermal boundary $z = 0$, we take $H_0 = 0$ and thus obtain $\alpha = 1$, which provides the following modifications in (51):

$$P_i = 2\beta^2 m^2 + \omega^2, \quad P = -p_1^* + \left(\frac{1}{\delta^2} - \eta - \varepsilon_9 \right) \varepsilon_8 f_1(z,t) e^{-(\omega t + \iota m x)}, \quad i = 1, 2.$$

By considering these modifications in (53)–(56), we get the corresponding expressions for field variables from (57)–(61).

Case (ii): *Thermal load.* Similarly, in case of a thermal load, we assume that magnetic properties are absent from the medium. Then, by taking $H_0 = 0$ and $\alpha = 1$, we get the following changes in (68):

$$P_i = 2\beta^2 m^2 + \omega^2, \quad P' = \left(\frac{1}{\delta^2} - \eta - \varepsilon_9 \right) \varepsilon_8 f_1(z,t) e^{-(\omega t + \iota m x)}, \quad i = 1, 2.$$

Following the same procedure as described earlier in Section 5(ii) and considering the above modifications, the corresponding expressions for u, w, θ, σ_{zx}, and σ_{zz} are given by (57)–(61).

7. Numerical results and discussions

In this section, we carry out computational work in order to illustrate the results derived in Section 5 and examine the behavior of the displacement components u and w, temperature distribution θ, and stress components σ_{zx} and σ_{zz}.

For this purpose, the material is chosen as copper and the values of the relevant parameters are taken as follows:

$$
\begin{aligned}
&k = 386\,\mathrm{W m^{-1} K^{-1}}, && T_0 = 293\,\mathrm{K}, && \rho = 8954\,\mathrm{kg m^{-3}}, && \alpha_t = 1.78\times10^{-5}\,\mathrm{K^{-1}},\\
&C_E = 383.1\,\mathrm{J kg^{-1} K^{-1}}, && R_a = 0.5, && \mu_0 = 4\pi\times10^{-7}\,\mathrm{H m^{-1}}, && \varepsilon_0 = (10^{-9}/36\pi)\,\mathrm{F m^{-1}},\\
&H_0 = (10^7/4\pi)\,\mathrm{A m^{-1}}, && h = 0.01, && \delta = 0.01, && L_0 = 1\times10^{11}\,\mathrm{J m^{-1}},\\
&\lambda = 7.76\times10^{10}\,\mathrm{kg m^{-1} s^{-2}}, && m = 1.2, && \omega = 1. && \mu = 3.86\times10^{10}\,\mathrm{kg m^{-1} s^{-2}}.
\end{aligned}
$$

The computation is carried out for

$$t = 0.1, 0.3, 0.5; \quad p_1^* = 10;\ p_2^* = 10; \quad x = 1; \quad 0 \le z \le 4.5; \quad h^* = 10.$$

A comparison of the dimensionless form of the field variables for the cases of magnetothermoelasticity with a laser pulse (MTLP) and generalized thermoelasticity theory with a laser pulse (TLP) for three different values of time t, subjected to mechanical and thermal loads, is presented in Figures 2–9. The values of all the physical quantities for all the cases are displayed in the range $0 \le z \le 4.5$.

Case (i): *Mechanical load.* Figure 2 shows the variation of displacement component u with the distance z for MTLP and TLP for different values of t. We observe that all the curves show similar behavior, that is,

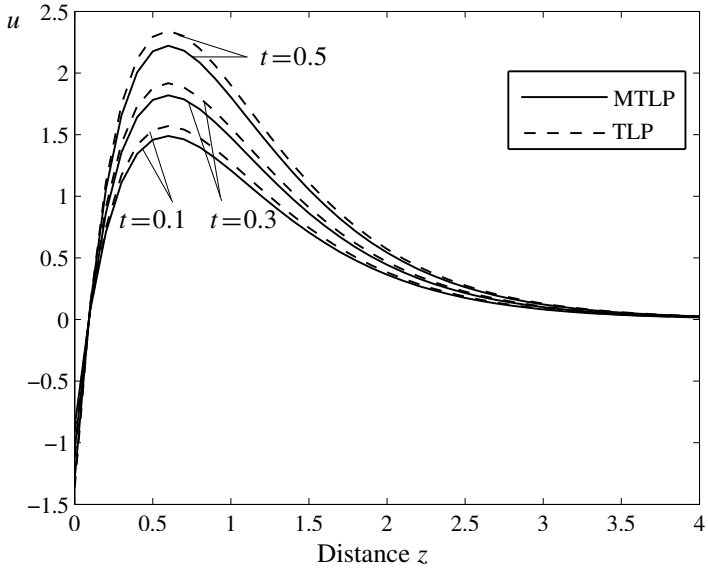

Figure 2. Variation of displacement u for a mechanical load.

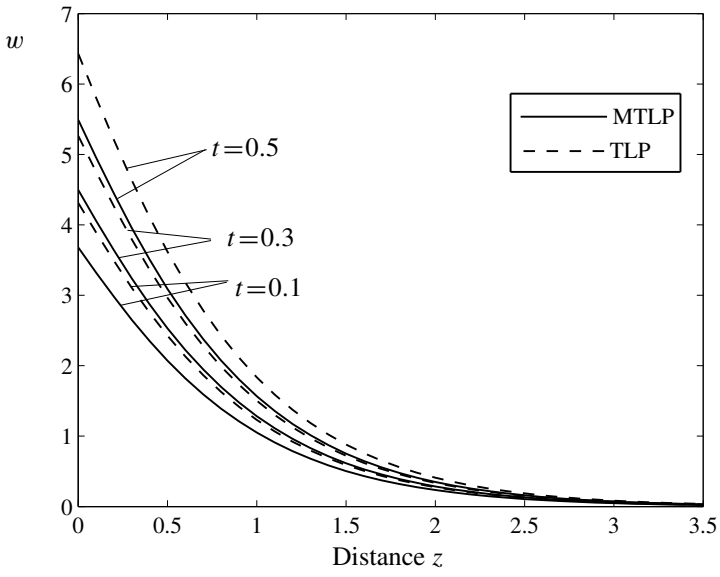

Figure 3. Variation of displacement w for a mechanical load.

all the curves start with negative values on the boundary of half-space, then rapidly increase to a maximal positive value and thereafter continuously decrease to zero value. Also, the effect of the magnetic field is significant for $0.5 \leq z \leq 2$ and the influence of time t is prominent in the range $0.3 \leq z \leq 3$.

Figure 3 shows the variation of displacement component w with distance z for MTLP and TLP for different values of t. We note that w starts with a positive value and then decreases continuously to zero value for all the cases in the range $0 \leq z \leq 3.5$. We see that the increment in time as well as the absence of magnetic field increase the magnitude of displacement component w. For MTLP and TLP at $t = 0.1, 0.3$, and 0.5, the effect is pronounced in the range $0 \leq z \leq 2$.

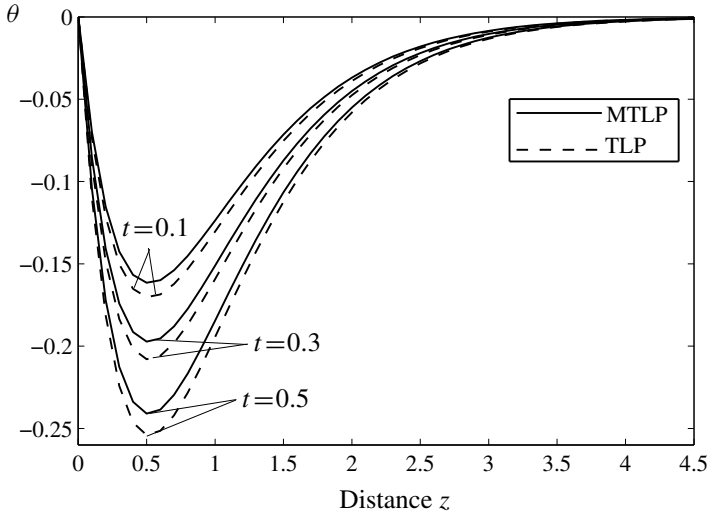

Figure 4. Variation of temperature distribution θ for a mechanical load.

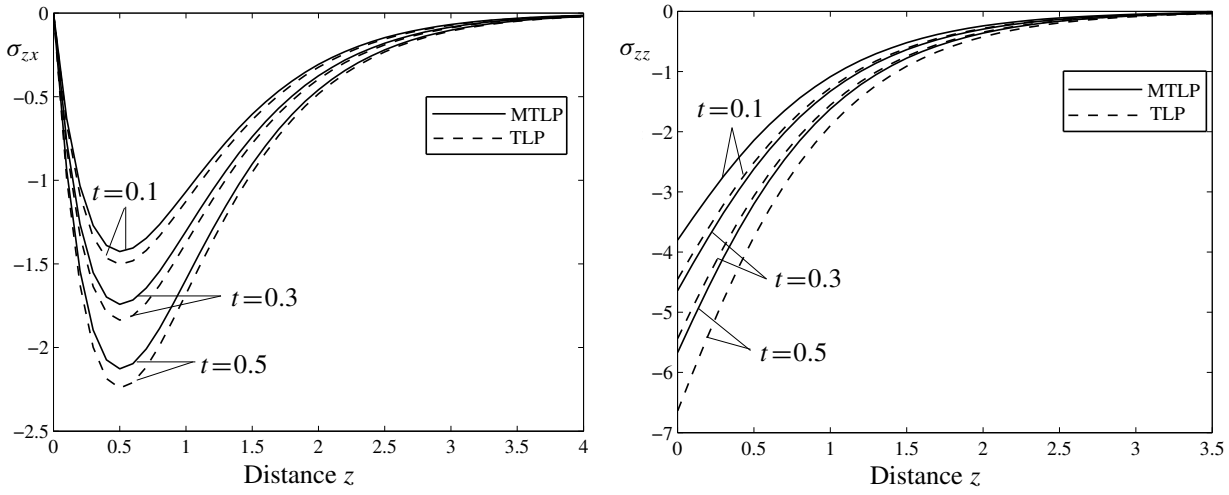

Figure 5. Variation of tangential stress σ_{zx} (left) and normal stress σ_{zz} (right) for a mechanical load.

Figure 4 shows the variation of θ with distance z for MTLP and TLP for different values of time t. It can be seen that the behavior of θ for all the three cases is similar: its magnitude increases in the range $0 \le z \le 0.5$ and then decreases in the range $0.5 \le z \le 4.5$. It is also seen that time strongly affects the temperature distribution θ; the difference is pronounced for both MTLP and TLP.

Figure 5 displays the variation of tangential stress σ_{zx} and normal stress σ_{zz} with distance z for MTLP and TLP for different values of t. In both cases the magnitude is greater for TLP than for MTLP, and it increases with t. It is also seen that all the curves show similar trends and the difference for time t is more pronounced than for a magnetic field.

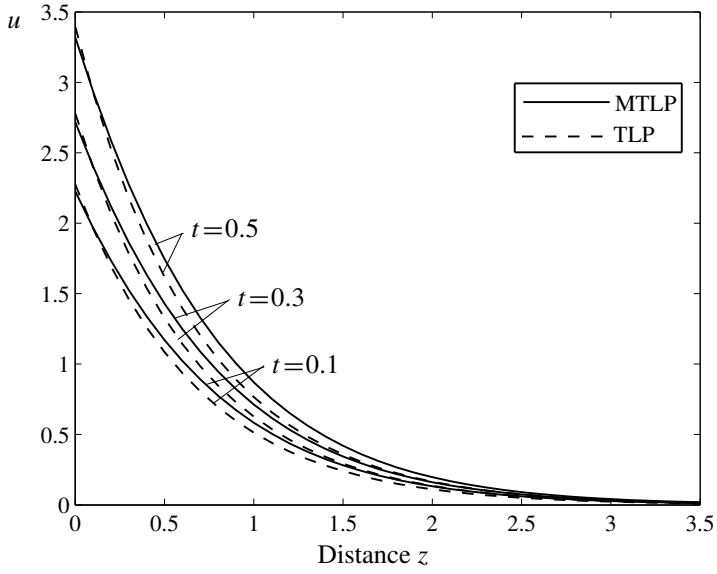

Figure 6. Variation of displacement u for a thermal load.

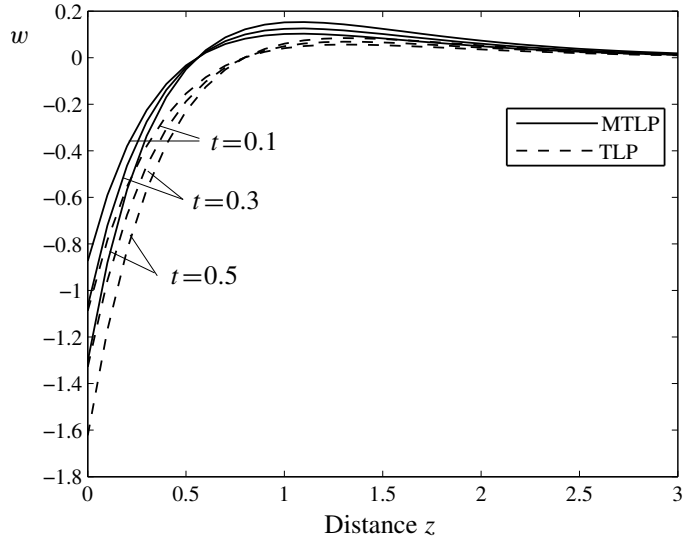

Figure 7. Variation of displacement w for a thermal load.

Case (ii): *Thermal load.* Figure 6 displays the variation of u with distance z for MTLP and TLP for different values of t. It is noticed that for all the cases the displacement component u behaves similarly. The values of u for TLP are found to be greater in the range $0 \leq z \leq 0.25$ and lesser in the range $0.25 \leq z \leq 3.5$, as compared to MTLP. Moreover, the value of u increases with time.

Figure 7 depicts the variation of w with distance z for MTLP and TLP for different values of t. The magnetic field acts to decrease the magnitude of displacement component w while an increment in time significantly enlarges the magnitude of w. Also, w shows a similar pattern for all the curves. The difference is clearly noticeable for MTLP and TLP in the range $0 \leq z \leq 2$.

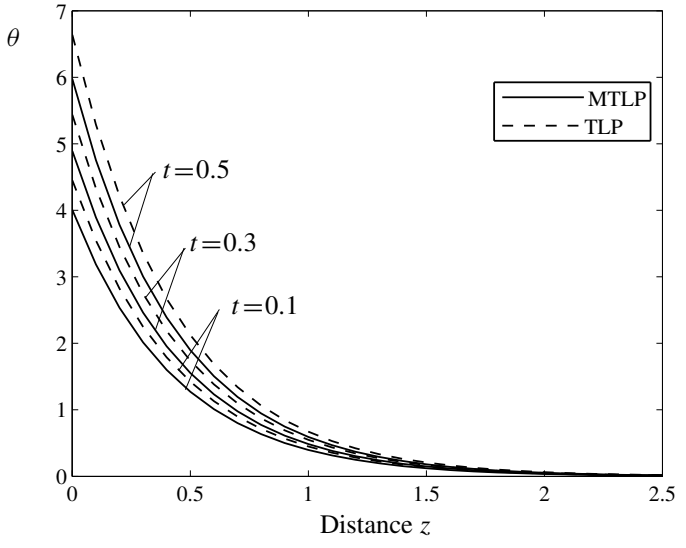

Figure 8. Variation of temperature distribution θ for a thermal load.

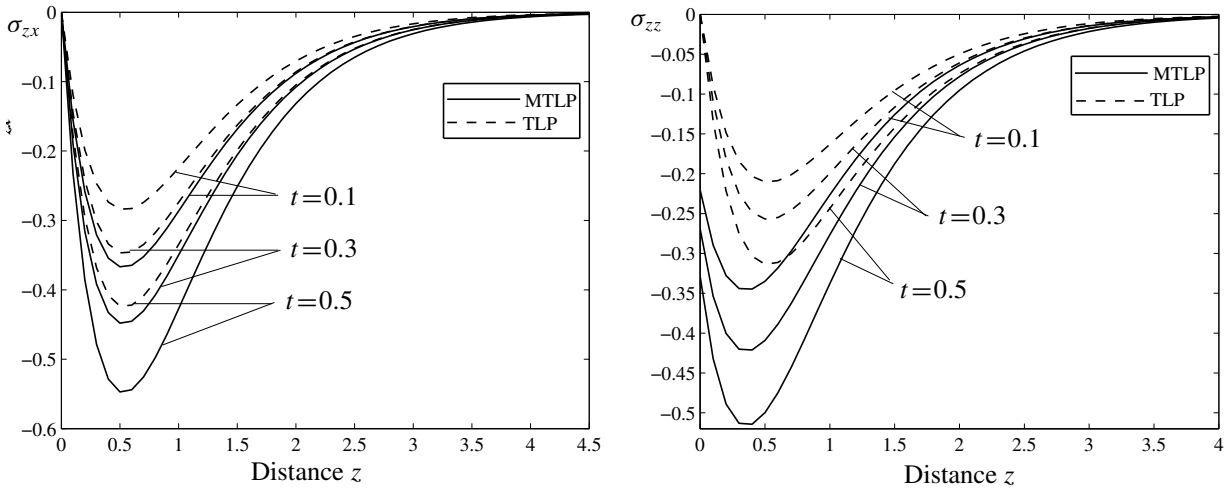

Figure 9. Variation of tangential stress σ_{zx} (left) and normal stress σ_{zz} (right) for a thermal load.

Figure 8 shows the variation of θ with distance z for MTLP and TLP for different values of t. We see that the trend of θ for all the cases is found to be similar. We notice that θ increases with time t while the presence of a magnetic field lowers the value of temperature. The effect of a magnetic field and time on temperature is prominent.

Figure 9 demonstrates the variation of σ_{zx} and σ_{zz} with distance z for MTLP and TLP for different values of t. We observe that σ_{zx} begins at zero value at $z = 0$ for all cases, then increases sharply to attain its highest value (in magnitude) at $z = 0.5$, and thereafter diminishes smoothly to zero. Hence, all the curves show similar trends. The magnitude of σ_{zx} for TLP is smaller than for MTLP; in both cases it increases with time. As for σ_{zz}, the curves for MTLP start at a negative value, while for TLP the curves begin with zero value. Normal stress shows significant sensitivity towards both factors. The magnitude of σ_{zz} decreases if we neglect the magnetic effect, and it increases with t.

8. Conclusions

The problem of investigating displacement components, temperature, and stress components in an infinite, homogeneous isotropic elastic half-space is studied in the purview of magnetothermoelasticity with a laser pulse. A normal mode analysis technique is employed to express the results mathematically. Theoretically obtained field variables are also exemplified through a specific model to present the results in graphical form.

The analysis of results permits some concluding remarks:

(1) It is clear from the figures that all the field variables have nonzero values only in the bounded region of space. Outside this region, the values vanish identically. This means that this outside region has not felt any thermal disturbance yet. Hence, all the results are in agreement with the generalized theory of thermoelasticity.

(2) The effect of the magnetic field is much pronounced in all the field variables except for the displacement component u and temperature field θ (however, it is still significant) in the case of a

thermal load. In case of a mechanical load being applied, the presence of a magnetic field decreases the magnitude of all the field variables, whereas it has both increasing and decreasing effects for thermal load.

(3) We see from the figures that the time t plays a significant role in all the field quantities. Changes in the value of time t cause significant changes in all the studied fields, and the magnitudes of all the field variables increase with an increase in time t.

(4) We can easily conclude from the figures that the curves for all the field variables show similar behaviors, for all the cases considered and for both type of loads applied.

(5) If the laser pulse effect is neglected, then the results are in agreement with [Das and Kanoria 2012] with appropriate modification in the boundary conditions.

(6) The temperature distribution θ shows a zero value for a mechanical load and a maximal value for a thermal load at the boundary of the surface, which is physically plausible and consistent with the theoretical boundary conditions of the problem.

The new model is employed in a homogeneous, isotropic thermoelastic medium as a new improvement in the field of thermoelasticity. The subject becomes more interesting because the use of a laser pulse with an extensive short duration or a very high heat flux has found numerous applications. The method used in this article is applicable to a wide range of problems in thermodynamics. By the obtained results, it is expected that the present model of equations will serve as more realistic and will provide motivation to investigate generalized magnetothermoelastic problems regarding laser pulse heat with high heat flux and/or short time duration.

References

[Ackerman and Overton 1969] C. C. Ackerman and W. C. Overton, Jr., "Second sound in solid helium-3", *Phys. Rev. Lett.* **22**:15 (1969), 764–766.

[Ackerman et al. 1966] C. C. Ackerman, B. Bertman, H. A. Fairbank, and R. A. Guyer, "Second sound in solid helium", *Phys. Rev. Lett.* **16**:18 (1966), 789–791.

[Baksi et al. 2005] A. Baksi, R. K. Bera, and L. Debnath, "A study of magneto-thermoelastic problems with thermal relaxation and heat sources in a three-dimensional infinite rotating elastic medium", *Int. J. Eng. Sci.* **43**:19-20 (2005), 1419–1434.

[Biot 1956] M. A. Biot, "Thermoelasticity and irreversible thermodynamics", *J. Appl. Phys.* **27** (1956), 240–253.

[Chadwick 1957] P. Chadwick, "Elastic wave propagation in a magnetic field", pp. 143–158 in *Proceedings of the 9th International Congress of Applied Mechanics* (Brussels, 1956), vol. 7, University of Brussels, 1957.

[Chen et al. 2004] J. K. Chen, J. E. Beraun, and C. L. Tham, "Ultrafast thermoelasticity for short-pulse laser heating", *Int. J. Eng. Sci.* **42**:8-9 (2004), 793–807.

[Das and Kanoria 2012] P. Das and M. Kanoria, "Magneto-thermo-elastic response in a perfectly conducting medium with three-phase-lag effect", *Acta Mech.* **223**:4 (2012), 811–828.

[Deswal and Kalkal 2011] S. Deswal and K. Kalkal, "A two-dimensional generalized electro-magneto-thermoviscoelastic problem for a half-space with diffusion", *Int. J. Therm. Sci.* **50**:5 (2011), 749–759.

[Dhaliwal and Sherief 1980] R. S. Dhaliwal and H. H. Sherief, "Generalized thermoelasticity for anisotropic media", *Quart. Appl. Math.* **33**:1 (1980), 1–8.

[Ezzat and Youssef 2005] M. A. Ezzat and H. M. Youssef, "Generalized magneto-thermoelasticity in a perfectly conducting medium", *Int. J. Solids Struct.* **42**:24-25 (2005), 6319–6334.

[Ezzat et al. 2004] M. A. Ezzat, M. Zakaria, and A. Abdel-Bary, "Generalized thermoelasticity with temperature dependent modulus of elasticity under three theories", *J. Appl. Math. Comput.* **14**:1-2 (2004), 193–212.

[Fang et al. 2007] D. Fang, Y. Sun, and A. K. Soh, "Advances in thermoelastic damping in micro- and nano- mechanical resonators: a review", *J. Solid Mech. Mater. Eng.* **1**:1 (2007), 18–34.

[Green and Lindsay 1972] A. E. Green and K. A. Lindsay, "Thermoelasticity", *J. Elasticity* **2**:1 (1972), 1–7.

[Green and Naghdi 1991] A. E. Green and P. M. Naghdi, "A re-examination of the basic postulates of thermomechanics", *Proc. R. Soc. Lond. A* **432**:1885 (1991), 171–194.

[Green and Naghdi 1992] A. E. Green and P. M. Naghdi, "On undamped heat waves in an elastic solid", *J. Therm. Stresses* **15**:2 (1992), 253–264.

[Green and Naghdi 1993] A. E. Green and P. M. Naghdi, "Thermoelasticity without energy dissipation", *J. Elasticity* **31**:3 (1993), 189–208.

[He et al. 2002] T. He, X. Tian, and Y. Shen, "State space approach to one-dimensional thermal shock problem for a semi-infinite piezoelectric rod", *Int. J. Eng. Sci.* **40**:10 (2002), 1081–1097.

[Hetnarski and Ignaczak 1999] R. B. Hetnarski and J. Ignaczak, "Generalized thermoelasticity", *J. Therm. Stresses* **22**:4-5 (1999), 451–476.

[Javan and Nasirzadeh 2012] N. S. Javan and Z. Nasirzadeh, "Self-focusing of circularly polarized laser pulse in the hot magnetized plasma in the quasi-neutral limit", *Phys. Plasmas* **19**:11 (2012), Article ID # 112304.

[Jones 1966] J. P. Jones, "Thermoelastic vibrations of a beam", *J. Acoust. Soc. Am.* **39** (1966), 542–548.

[Joseph and Preziosi 1989] D. D. Joseph and L. Preziosi, "Heat waves", *Rev. Mod. Phys.* **61**:1 (1989), 41–73.

[Kaliski and Petykiewicz 1959] S. Kaliski and J. Petykiewicz, "Equation of motion coupled with the field of temperature in a magnetic field involving mechanical and electrical relaxation for anisotropic bodies", *Proc. Vib. Probl.* **4** (1959), 1–12.

[Kidawa-Kukla 1997] J. Kidawa-Kukla, "Vibration of a beam induced by harmonic motion of a heat source", *J. Sound Vib.* **205**:2 (1997), 213–222.

[Kidawa-Kukla 2003] J. Kidawa-Kukla, "Application of the Green functions to the problem of the thermally induced vibration of a beam", *J. Sound Vib.* **262**:4 (2003), 865–876.

[Knopoff 1955] L. Knopoff, "The interaction between elastic wave motions and a magnetic field in electrical conductors", *J. Geophys. Res.* **60**:4 (1955), 441–456.

[Kumar and Mukhopadhyay 2009] R. Kumar and S. Mukhopadhyay, "Effects of three phase lags on generalized thermoelasticity for an infinite medium with a cylindrical cavity", *J. Therm. Stresses* **32**:11 (2009), 1149–1165.

[Lord and Shulman 1967] H. W. Lord and Y. A. Shulman, "A generalized dynamical theory of thermoelasticity", *J. Mech. Phys. Solids* **15**:5 (1967), 299–309.

[Nayfeh and Nemat-Nasser 1972] A. H. Nayfeh and S. Nemat-Nasser, "Electromagneto-thermoelastic plane waves in solids with thermal relaxation", *J. Appl. Mech.* (*ASME*) **39**:1 (1972), 108–113.

[Özişik and Tzou 1994] M. N. Özişik and D. Y. Tzou, "On the wave theory in heat conduction", *J. Heat Transf.* (*ASME*) **116**:3 (1994), 526–535.

[Paria 1962] G. Paria, "On magneto-thermo-elastic plane waves", *Math. Proc. Cambridge Philos. Soc.* **58**:3 (1962), 527–531.

[Sherief and Ezzat 1996] H. H. Sherief and M. A. Ezzat, "A thermal-shock problem in magneto-thermoelasticity with thermal relaxation", *Int. J. Solids Struct.* **33**:30 (1996), 4449–4459.

[Sherief and Helmy 2002] H. H. Sherief and K. A. Helmy, "A two-dimensional problem for a half-space in magneto-thermoelasticity with thermal relaxation", *Int. J. Eng. Sci.* **40**:5 (2002), 587–604.

[Sun et al. 2008] Y. Sun, D. Fang, M. Saka, and A. K. Soh, "Laser-induced vibrations of micro-beams under different boundary conditions", *Int. J. Solids Struct.* **45**:7-8 (2008), 1993–2013.

[Tang and Araki 1999] D. W. Tang and N. Araki, "Wavy, wavelike, diffusive thermal responses of finite rigid slabs to high-speed heating of laser-pulses", *Int. J. Heat Mass Transf.* **42**:5 (1999), 855–860.

[Tzou 1997] D. Y. Tzou, *Macro-to-micro scale heat transfer: the lagging behavior*, Taylor and Francis, Bristol, 1997.

[Wang and Xu 2001] X. Wang and X. Xu, "Thermoelastic wave induced by pulsed laser heating", *Appl. Phys. A Mater. Sci. Process.* **73**:1 (2001), 107–114.

[Wang and Xu 2002] X. Wang and X. Xu, "Thermoelastic wave in metal induced by ultrafast laser pulses", *J. Therm. Stresses* **25**:5 (2002), 457–473.

[Youssef 2006] H. M. Youssef, "Two-dimensional generalized thermoelasticity problem for a half-space subjected to ramp-type heating", *Eur. J. Mech. A Solids* **25**:5 (2006), 745–763.

[Youssef and Al-Felali 2012] H. M. Youssef and A. S. Al-Felali, "Generalized thermoelasticity problem of material subjected to thermal loading due to laser pulse", *Appl. Math.* **3**:2 (2012), 142–146.

Received 22 Mar 2013. Revised 29 May 2013. Accepted 1 Sep 2013.

SUNITA DESWAL: spannu_gju@yahoo.com
Department of Mathematics, Guru Jambheshwar University of Science & Technology, Hisar 125001, Haryana, India

SANDEEP SINGH SHEORAN: sandeep_gjtu@yahoo.co.in
Department of Mathematics, Guru Jambheshwar University of Science & Technology, Hisar 125001, Haryana, India

KAPIL KUMAR KALKAL: kapilkalkal_gju@rediffmail.com
Department of Mathematics, Guru Jambheshwar University of Science & Technology, Hisar 125001, Haryana, India

JOURNAL OF MECHANICS OF MATERIALS AND STRUCTURES
Vol. 8, No. 8-10, 2013
dx.doi.org/10.2140/jomms.2013.8.461

RAPID SLIDING CONTACT IN THREE DIMENSIONS BY DISSIMILAR ELASTIC BODIES: EFFECTS OF SLIDING SPEED AND TRANSVERSE ISOTROPY

LOUIS MILTON BROCK

An isotropic elastic sphere slides on the surfaces of transversely isotropic elastic half-spaces. In one case the material symmetry axis coincides with the half-space surface normal. In the other, the axis lies in the plane of the surface. In both cases sliding proceeds with constant subcritical speed along a straight path at an arbitrary angle to the principal material axes. A 3D dynamic steady state is considered. Exact solutions for contact zone traction are derived in analytic form, as well as formulas for contact zone geometry. Although a sphere is involved, the solution process is not based on the assumption of symmetry. Anisotropy is found to largely determine zone shape at low sliding speed, but direction of sliding becomes a major influence at higher speeds.

1. Introduction

The literature on the mechanics of contact is vast; see, for example, [Johnson 1985; Kalker 1990; Hills et al. 1993]. An important category is contact between dissimilar elastic bodies; see, for example, [Hertz 1882; Hartnett 1980; Ahmadi et al. 1983; Hills et al. 1993]. For sliding contact, if speed and resultant forces are constant, a dynamic steady state may be achieved for which contact zone and surface traction do not vary in the frame of the moving sphere. In [Brock 2012] the 3D problem of rapid sliding by a rigid ellipsoidal die on an isotropic half-space in the presence of friction is studied. Analytical solutions show that contact zone shape does not necessarily replicate a projection of the die profile onto the half-space surface. As sliding speed increases, the shape elongates in the direction of sliding, a result also seen in [Rahman 1996]. This problem is generalized by considering a transversely isotropic half-space [Brock 2013] and a die that slides in any direction with respect to the principal axes of the material. Again, contact zone shape may not replicate the die profile projection, but for low sliding speeds it is largely defined in terms of the principal axes. For higher speeds, the elongation effect seen in [Brock 2012] is exhibited. That is, as speed increases, the zone appears to rotate while undergoing elongation. In contrast to [Brock 2012], moreover, the Rayleigh speed may not be critical.

To ascertain whether the results of [Brock 2012; 2013] are a phenomenon of the rigid die, aspects of both studies are adapted here for two 3D cases of sliding by an isotropic elastic sphere on a transversely isotropic half-space. It is assumed (compare [Hills et al. 1993]) that the maximum contact zone width is much smaller than the radius r_0 of the sphere prior to deformation. Thus, the sphere is also treated as a half-space. With regard to the transversely isotropic half-space, the material symmetry axis is normal to the surface in one case, but lies in the plane of the surface in the other [Brock 2013]. In both cases, the sphere slides in an arbitrary direction with respect to the principal material axes. Sliding can be resisted

Keywords: 3D dynamic, sliding, transverse isotropy, contact zone geometry.

by friction, and sliding speeds are constant and subcritical. The solution for the unmixed boundary value problem of specified surface traction reduces the mixed contact problem to the solution of integral equations. To this end, governing equations for the elastic half-space, subjected to a translating zone of (somewhat) arbitrary traction over its surface, are given in Appendix A and in Section 2. Translation speed is constant and subcritical, and zone geometry and traction do not change during translation. Therefore, see [Brock 2012; 2013], a dynamic steady state is assumed. Cartesian coordinates are used, and an exact transform solution is obtained. Quasipolar coordinates, both in transform and spatial planes, are employed during the inversion process. These are defined by a polar angle that sweeps through 180° (π radians) and a radial coordinate that has both positive and negative directions. For points in the contact zone, the resulting displacement expressions reduce to double integrals whose limits are independent of the points. The imposed displacement conditions require that the integrands be solutions of Cauchy singular integral equations. The contact zone normal traction is then extracted analytically as a function of the quasipolar coordinates. This traction is required to vanish continuously on the contact zone boundary, and to render the resultant compression force as a stationary value for a given sliding speed. These requirements lead to expressions that define the contact zone geometry, and calculations for aspects of the geometry are given.

Solution expressions for anisotropic elasticity are often [Ting 1996] more complicated than for their isotropic counterparts. A cancellation of common factors in the numerator and denominator of solution transform terms is used for the 2D [Brock 2002] and 3D [Brock 2013] problems. The resulting expressions yield, upon inversion, more compact solution forms. The procedure is therefore used here for both the isotropic and transversely isotropic components of the transform solution.

2. General equations for the traction distribution problem

A linear elastic, anisotropic, and homogeneous half-space is defined as the region $x_3 > 0$. Here Cartesian coordinates $\boldsymbol{x}(x_k)$ also define the principal axes of the material. The half-space is undisturbed until a traction distribution is applied to a finite, simply connected area C of surface $x_3 = 0$. Its boundary is defined by contour $\Im(X, Y) = 0$, where

$$X = x_1 \cos\theta + x_2 \sin\theta, \quad Y = x_2 \cos\theta - x_1 \sin\theta, \quad |\theta| < \pi/2. \tag{1}$$

Here $\Im = 0$ defines a continuous closed curve that exhibits continuously varying tangent direction, and normal direction, and radius of curvature. Moreover, any span of C through origin $x_1 = x_2 = 0$ does not cross its boundary. Area C is then translated in the positive X-direction at constant subcritical speed V. This does not change the area, and the traction distribution remains invariant with respect to it. This suggests that a dynamic steady state can arise in which half-space response is invariant in the frame of translating C. It is therefore convenient to translate the Cartesian system with C, so that displacement $\boldsymbol{u}(u_k)$ and traction $\boldsymbol{T}(\sigma_{ik})$ vary with $\boldsymbol{x}(x_k)$ and time differentiation becomes $-V\partial_X$, where ∂_X signifies the X-derivative and is given by

$$\partial_X = \partial_1 \cos\theta + \partial_2 \sin\theta. \tag{2}$$

Here ∂_k signifies x_k-differentiation. The governing equations for the general anisotropic solid are given

in Appendix A. For $x_3 = 0$ the boundary conditions are

$$\sigma_{33} = \sigma, \quad \sigma_{31} = \tau_1, \quad \sigma_{32} = \tau_2, \quad (x_1, x_2) \in C, \tag{3a}$$

$$\sigma_{33} = \sigma_{31} = \sigma_{32} = 0, \qquad (x_1, x_2) \notin C. \tag{3b}$$

Here (σ, τ_1, τ_2) are piecewise continuous, bounded functions of (x_1, x_2). It is reasonable then to require that $|\boldsymbol{u}|$ remains bounded for $x_3 > 0$, $|\boldsymbol{x}| \to \infty$.

3. Transverse isotropy: Material symmetry axis normal to surface

Traction distribution problem: Transform. For this case the results in Appendix A involve five elastic constants [Jones 1999]:

$$C_{22} = C_{11}, \quad C_{44} = C_{55}, \quad C_{23} = C_{13}, \quad C_{33}, \quad C_{11} - C_{12} - 2C_{66} = 0. \tag{4}$$

The spherical die is isotropic, with only two elastic constants, so it is convenient to use its shear modulus μ_0, mass density ρ_0, and rotational wave speed v_0 as reference parameters, where

$$v_0 = \sqrt{\frac{\mu_0}{\rho_0}}. \tag{5}$$

Dimensionless parameters can then be defined:

$$d_1 = \frac{C_{11}}{\mu_0}, \quad d_3 = \frac{C_{33}}{\mu_0}, \quad d_5 = \frac{C_{55}}{\mu_0}, \quad d_6 = \frac{C_{66}}{\mu_0}, \quad d_{12} = \frac{C_{12}}{\mu_0}, \quad d_{13} = \frac{C_{13}}{\mu_0}, \tag{6a}$$

$$d_1 - d_{12} - 2d_6 = 0, \quad c = \sqrt{\frac{\rho}{\rho_0}}c_0, \quad c_0 = \frac{V}{v_0}. \tag{6b}$$

In view of (A.3) and (6) the linear momentum balance (A.5a) takes the form

$$\begin{bmatrix} d_5\partial_3^2 + \mathrm{X}_1 & (d_6 + d_{12})\partial_1\partial_2 & (d_5 + d_{13})\partial_1\partial_3 \\ (d_6 + d_{12})\partial_1\partial_2 & d_5\partial_3^2 + \mathrm{X}_2 & (d_5 + d_{13})\partial_2\partial_3 \\ (d_5 + d_{13})\partial_1\partial_3 & (d_5 + d_{13})\partial_2\partial_3 & d_3\partial_3^2 + \mathrm{X}_3 \end{bmatrix} \begin{bmatrix} u_1 \\ u_2 \\ u_3 \end{bmatrix} = 0, \tag{7a}$$

$$\mathrm{X}_1 = d_1\partial_1^2 + d_6\partial_2^2 - c^2\partial_X^2, \quad \mathrm{X}_2 = d_6\partial_1^2 + d_1\partial_2^2 - c^2\partial_X^2, \quad \mathrm{X}_3 = d_5(\partial_1^2 + \partial_2^2) - c^2\partial_X^2. \tag{7b}$$

The set of (3) and (7) is addressed by the double bilateral Laplace transform [Sneddon 1972]:

$$\hat{F} = \iint F(x_1, x_2) \exp(-p_1 x_1 - p_2 x_2)\, dx_1\, dx_2. \tag{8}$$

In (8) integration is over the entire x_1x_2-plane and transform variables (p_1, p_2) are imaginary. Its application to (7) for $x_3 > 0$ leads to the homogeneous solution

$$\hat{\boldsymbol{u}} = \boldsymbol{U}_+ \exp(-\Omega_+ x_3) + \boldsymbol{U}_- \exp(-\Omega_- x_3) + \boldsymbol{U}_6 \exp(-\Omega_6 x_3). \tag{9}$$

Exponential arguments $(\Omega_\pm, \Omega_6)$ are roots of the determinant of transformed (7a), that is,

$$(\Omega^2+\omega_6^2)[(d_5\Omega^2+\omega_1^2)(d_3\Omega^2+\omega_5^2)-\Omega^2P(d_5+d_{13})^2]=0, \tag{10a}$$

$$\omega_1=\sqrt{d_1P-c^2p_X^2},\quad \omega_5=\sqrt{d_5P-c^2p_X^2},\quad \omega_6=\sqrt{d_6P-c^2p_X^2}, \tag{10b}$$

$$P=p_1^2+p_2^2,\quad p_X=p_1\cos\theta+p_2\sin\theta. \tag{10c}$$

They are given by

$$\Omega_\pm=\frac{\omega_+\pm\omega_-}{2\sqrt{d_3d_5}}\sqrt{-1},\quad \Omega_6=\omega_6\sqrt{-1}, \tag{11a}$$

$$\omega_\pm=\sqrt{\left(\omega_1\sqrt{d_3}\pm\omega_5\sqrt{d_5}\right)^2-P(d_5+d_{13})^2}, \tag{11b}$$

$$\Omega_+\Omega_-=-\frac{\omega_1\omega_5}{\sqrt{d_3d_5}}. \tag{11c}$$

The components of the vector coefficients $(\boldsymbol{U}_\pm, \boldsymbol{U}_6)$ in (9) are

$$(U_1^\pm, U_2^\pm)=(d_5+d_{13})(p_1, p_2)\Omega_\pm U_\pm,\quad U_3^\pm=(d_5\Omega_\pm^2+\omega_1^2)U_\pm, \tag{12a}$$

$$U_1^6=-p_2U_6,\quad U_2^6=p_1U_6,\quad U_3^6=0. \tag{12b}$$

Here $(U_\pm, U_6)$ are arbitrary functions of (p_1, p_2). Result (9) is bounded for $x_3>0$ if $\mathrm{Re}(\Omega_++\Omega_-, \Omega_+-\Omega_-, \omega_1, \omega_5, \omega_6)>0$ in the cut p_1 and p_2-planes. Use of (A.1), (6), (9), and (12) gives the traction transforms for $x_3=0$:

$$\frac{1}{\mu_0}\begin{bmatrix}\hat\sigma_{33}\\ \hat\sigma_{31}\\ \hat\sigma_{32}\end{bmatrix}=\begin{bmatrix}C_3^+\Omega_+ & C_3^-\Omega_- & 0\\ d_5p_1D_3^+ & d_5p_1D_3^- & d_5p_2\Omega_6\\ d_5p_2D_3^+ & d_5p_2D_3^- & -d_5p_1\Omega_6\end{bmatrix}\begin{bmatrix}U_+\\ U_-\\ U_6\end{bmatrix}, \tag{13a}$$

$$C_3^\pm=d_{13}(d_5+d_{13})P-d_3(d_5\Omega_\pm^2+\omega_1^2),\quad D_3^\pm=\omega_1^2-d_{13}\Omega_\pm^2. \tag{13b}$$

Use of (13) in the transform of (3) gives equations for $(U_\pm, U_6)$. Application of the traction distribution solution to the sliding contact problem requires the normal displacement u_3^0 on surface $x_3=0$. Equation (9) and the solutions for $(U_\pm, U_6)$ are combined in Appendix B to construct its transform $\hat u_3^0$. The construction involves a factor cancellation procedure similar to that used in [Brock 2002; 2013] and some isotropic limit results are also given. In light of (11), (B.2b), and (B.3b), then, one can write the compact expressions for, respectively, the transversely isotropic and isotropic half-spaces:

$$\hat u_3^0=-\frac{\omega_1\omega_+\sqrt{-1}}{\sqrt{d_3d_5}M}\frac{\hat\sigma}{\mu_0}+\frac{N}{M}\left(p_1\frac{\hat\tau_1}{\mu_0}+p_2\frac{\hat\tau_2}{\mu_0}\right), \tag{14a}$$

$$(\hat u_3^0)'=-\frac{c_D^2\omega_D}{M_0\sqrt{-1}}(\omega_D+\omega)\frac{\hat\sigma'}{\mu_0}+\frac{N_0}{M_0}\left(p_1\frac{\hat\tau_1'}{\mu_0}+p_2\frac{\hat\tau_2'}{\mu_0}\right), \tag{14b}$$

$$M_0=4(c_D^2-1)\omega-c_D^2(\omega_D+\omega)c_0^2p_X^2,\quad N_0=c_D^2\omega_D+(2-c_D^2)\omega. \tag{14c}$$

Traction distribution problem: Transform inversion. In view of (7) and [Sneddon 1972] the inversion operation for each traction term in (14) has the general form

$$\frac{1}{2\pi i}\int dp_1 \frac{1}{2\pi i}\int dp_2\, C_\Sigma \iint_C d\xi_1\, d\xi_2\, \Sigma \exp[p_1(x_1-\xi_1)+p_2(x_2-\xi_2)]. \tag{15}$$

In (15), $\Sigma = \Sigma(\xi_1, \xi_2)$ is a given traction term in (14) and $C_\Sigma = C_\Sigma(p_1, p_2)$ is its coefficient, for example, $C_\Sigma = Np_1/\mu_0 M$ for $\Sigma = \hat{\tau}_1$ in (14a). Integration is along the entire $\mathrm{Im}(p_1)$ and $\mathrm{Im}(p_2)$-axes, and suggests the transformations [Brock 2012; 2013]

$$p_1 = p\cos\psi, \qquad p_2 = p\sin\psi, \tag{16a}$$

$$x = x_1\cos\psi + x_2\sin\psi, \qquad y = x_2\cos\psi - x_1\sin\psi, \tag{16b}$$

$$\xi = \xi_1\cos\psi + \xi_2\sin\psi, \qquad \eta = \xi_2\cos\psi - \xi_1\sin\psi. \tag{16c}$$

In (16), $\mathrm{Re}(p) = 0+$, $-\infty < [\mathrm{Im}(p), x, y, \xi, \eta, \xi_1, \xi_2] < \infty$, and $|\psi - \theta| < \pi/2$. Parameters (p, ψ), $(x, \psi;\, y = 0)$, and $(\xi, \psi;\, \eta = 0)$ constitute quasipolar coordinate systems, that is,

$$dx_1\, dx_2 = |x|\, dx\, d\psi, \quad d\xi_1\, d\xi_2 = |\xi|\, d\xi\, d\psi, \quad dp_1\, dp_2 = |p|\, dp\, d\psi. \tag{17}$$

Use of (16a) in (11) and (12) leads to formulas related to (14a):

$$\Omega_\pm = B_\pm\sqrt{-p^2}, \quad \Omega_6 = B_6\sqrt{-p^2}, \tag{18a}$$

$$\omega_1 = A_1 p, \quad \omega_5 = B_5 p, \quad \omega_6 = B_6 p, \tag{18b}$$

$$\omega_\pm = \mathrm{P}_\pm p, \quad M = \mathrm{M}p^3, \quad N = \mathrm{N}p^2, \quad P = p^2. \tag{18c}$$

Equation (18) involves dimensionless terms

$$B_\pm = \frac{\mathrm{P}_+ \pm \mathrm{P}_-}{2\sqrt{d_3 d_5}}, \quad \mathrm{P}_\pm = \sqrt{\left(\sqrt{d_3}A_1 \pm \sqrt{d_5}B_5\right)^2 - (d_5 + d_{13})^2}, \tag{19a}$$

$$A_1 = \sqrt{d_1 - c_X^2}, \quad B_5 = \sqrt{d_5 - c_X^2}, \quad B_6 = \sqrt{d_6 - c_X^2}, \quad c_X = c\cos(\psi - \theta), \tag{19b}$$

$$\mathrm{M} = A_1 B_5\left(B_5 + \sqrt{\frac{d_3}{d_5}}A_1\right) - d_5 A_1 - \frac{d_{13}^2 B_5}{\sqrt{d_3 d_5}}, \quad \mathrm{N} = A_1 - \frac{d_{13}B_5}{\sqrt{d_3 d_5}}. \tag{19c}$$

For (14b)

$$\omega_D = Ap, \quad \omega = Bp, \quad M_0 = \mathrm{M}_0 p^3, \quad N_0 = \mathrm{N}_0 p^2, \tag{20a}$$

$$A = \sqrt{1 - \left(\frac{c_X^0}{c_D}\right)^2}, \quad B = \sqrt{1 - (c_X^0)^2}, \quad c_X^0 = c_0\cos(\psi - \theta), \tag{20b}$$

$$\mathrm{M}_0 = 4(c_D^2 - 1)B - c_D^2(A + B)(c_X^0)^2, \quad \mathrm{N}_0 = c_D^2 A + (2 - c_D^2)B. \tag{20c}$$

Critical speed. The terms in (19) are functions of $\psi - \theta$. Because $c_X < c$, both B_+ and A_1 are real and positive for $0 < c < \sqrt{d_1}$, and vanish at branch point $c_X = \sqrt{d_1}$. Terms (N, B_-, B_5) are real and positive for $0 < c < \sqrt{d_5}$ and (B_-, B_5) vanish at branch point $c_X = \sqrt{d_5}$. In addition, $\mathrm{M} \to 0+$ when $c_X = 0$ and vanishes for $c_X = (c_X)_R$, $0 < (c_X)_R < \sqrt{d_5}$, that is, M and $(c_X)_R$ correspond to a Rayleigh function and its nonzero root; see Appendix B. For $\psi = \theta$ this root gives the dimensionless Rayleigh speed c_R.

Although not present in (14a), term Ω_6 does appear in $(\hat{u}_1^0, \hat{u}_2^0)$, and its counterpart B_6 vanishes at branch point $c_X = \sqrt{d_6}$. Parameter $c_X^0 < c_0$ and (A, B) in (20) are real for, respectively, $c_0 < c_D$ and $c_0 < 1$. Term M_0 exhibits root $c_X^0 = (c_X^0)_R$ (see Appendix B) that gives Rayleigh speed $(c_0)_R$ when $\psi = \theta$. In summary, if sliding speed V is such that c or c_0 exceed a branch-point value, the corresponding term becomes imaginary, which represents a transonic situation, as in [Brock 2002; 2012; 2013]. If c or c_0 reaches its Rayleigh value, then (14a) or (14b) is singular. Thus, the critical sliding speed is here defined as the maximum V such that (c, c_0) do not exceed any branch point or Rayleigh values. It is noted that the possibility of a non-Rayleigh critical speed does not arise in the plane strain analysis of transverse isotropy, as in [Brock 2002].

Inversion for subcritical speed. In light of (16)–(20), general result (15) takes the form

$$\iint_C \Sigma\, d\xi\, d\eta \frac{1}{\pi i} \int_\Psi C_\Sigma\, d\psi \frac{1}{2\pi i} \int \frac{|p|}{p}\left(1, \frac{\sqrt{-p}}{\sqrt{p}}\right) \exp p(x-\xi)\, dp. \tag{21}$$

Now $\Sigma = \Sigma(\xi, \eta)$, $C_\Sigma = C_\Sigma(\psi, c_X)$, or $C_\Sigma = C_\Sigma(\psi, c_X^0)$, and subscript Ψ signifies integration over the range $\theta - \pi/2 < \psi < \theta + \pi/2$. The p-integration is over the positive side of the entire $\mathrm{Im}(p)$-axis (see Appendix B). For $(x_1, x_2) \in C$ the inverses of (14) follow as

$$u_3^0 = -\frac{1}{\pi} \int_\Psi d\psi \int_\mathrm{N} d\eta \left[\frac{A_1 \mathrm{P}_+}{\mu_0 \mathrm{M} \sqrt{d_3 d_5}\pi} (vp) \int_\Xi \sigma(\xi, \eta) \frac{d\xi}{\xi - x} + \frac{\mathrm{N}}{\mu_0 \mathrm{M}} \mathrm{T}(x, \eta) \right], \tag{22a}$$

$$(u_3^0)' = -\frac{1}{\pi} \int_\Psi d\psi \int_\mathrm{N} d\eta \left[\frac{c_D^2 A(A+B)}{\mu_0 \mathrm{M}_0 \pi} (vp) \int_\Xi \sigma'(\xi, \eta) \frac{d\xi}{\xi - x} + \frac{\mathrm{N}_0}{\mu_0 \mathrm{M}_0} \mathrm{T}'(x, \eta) \right], \tag{22b}$$

$$\mathrm{T}(\xi, \eta) = \tau_1(\xi, \eta) \cos\psi + \tau_2(\xi, \eta) \sin\psi, \tag{22c}$$

$$\mathrm{T}'(\xi, \eta) = \tau_1'(\xi, \eta) \cos\psi + \tau_2'(\xi, \eta) \sin\psi. \tag{22d}$$

Here (vp) signifies principal value integration and (N, Ξ) signify integration over the ranges $\eta_-(\psi) < \eta < \eta_+(\psi)$ and $x_-(\eta, \psi) < \xi < x_+(\eta, \psi)$, respectively. Limits $\eta_\pm(\psi)$ are points on the contour $\Im[X(\xi, \eta), Y(\xi, \eta)] = 0$ where $d\eta/d\xi = 0$, and limits $x_\pm(\eta, \psi)$ locate the ends of a line parallel to the ξ-axis that spans C for a given η. The restrictions on $(C, \Im)$ imply that $(x_\pm, \eta_\pm)$ exist and are continuous in ψ.

Sliding contact with friction. It is assumed that the maximum deflections of the half-space and sphere surfaces caused by mutual indentation during sliding, and the maximum width of the resulting contact zone, are orders of magnitude less than the original radius r_0 of the sphere. Thus (22b) is a valid approximation for a sphere. For both (22a) and (22b), the contact zone translates in the positive X-direction and $x_3 < 0$ defines the outward normal to the surface. Thus, the condition on $x_3 = 0$ that the deformed surfaces of the two bodies conform in the contact zone can be written for small deformations as

$$u_3^0 + (u_3^0)' = U_3 - \frac{X^2}{2r_0}(x_1, x_2) \in C. \tag{23}$$

The form of (23) is based on measuring (x_1, x_2) from the center of the translating sphere in its rest configuration. Thus U_3 is the rigid-body normal displacement of the sphere, and $(x_1, x_2) = 0$ is the initial contact point. If sliding is resisted by friction with kinetic coefficient γ, and sphere sliding and

slip are assumed to coincide, the resultant force system on the sphere is (F_X, F_Y, F_3) where $F_X = \gamma F_3$ and $F_Y = 0$. Thus in (22)

$$\tau_1 = \tau_X \cos\theta, \qquad \tau_2 = \tau_X \sin\theta, \qquad \tau_X = \gamma\sigma \quad (\sigma < 0), \tag{24a}$$

$$\tau_1' = -\tau_X \cos\theta, \quad \tau_2' = -\tau_X \sin\theta, \quad \sigma' = \sigma. \tag{24b}$$

In view of (1), (16), and (24), (23) becomes

$$-\frac{1}{\mu\pi}\int_\Psi d\psi \int_\mathrm{N} d\eta \left[\frac{\mathrm{K}}{\pi}(vp)\int_\Xi \sigma(\xi,\eta)\frac{d\xi}{\xi - x} + \Gamma\sigma(x,\eta)\right] = U_3 - \frac{X^2}{2r_0}, \tag{25a}$$

$$\mathrm{K} = \frac{A_1 \mathrm{P}_+}{\mathrm{M}\sqrt{d_3 d_5}} + \frac{c_D^2 A}{\mathrm{M}_0}(A + B), \tag{25b}$$

$$\Gamma = \gamma\left(\frac{\mathrm{N}}{\mathrm{M}} + \frac{\mathrm{N}_0}{\mathrm{M}_0}\right)\cos(\psi - \theta). \tag{25c}$$

In light of (16) and Appendix B the right-hand side of (25a) can be written as

$$-\frac{1}{\pi}\int_\Psi d\psi \int_\mathrm{N} d\eta \int_\Xi d\xi \frac{d}{dx}\delta(x - \xi)\left[U_3 - \frac{1}{2r_0}X^2(\xi,\eta)\right], \tag{26a}$$

$$X(\xi,\eta) = \xi\cos(\psi - \theta) + \eta\sin(\psi - \theta). \tag{26b}$$

Here δ is the Dirac function, and so (25a) reduces to matching the integrands of double integration in (ψ, η). Parameter ξ in $\sigma(\xi, \eta)$ is an integration variable representing parameter x, which itself depends on coordinate (x_1, x_2) and integration variable ψ. However, as noted in light of (16) for $y = 0$, (x_1, x_2) can be replaced by quasipolar coordinates $(x, \psi - \theta)$. Thus traction σ itself can be found by dropping η, and (25a) is reduced to

$$\frac{\mathrm{K}}{\pi}(vp)\int_\Xi \sigma(\xi, \psi - \theta)\frac{d\xi}{\xi - x} + \Gamma\sigma(x, \psi - \theta) = \mu_0\frac{x}{r_0}. \tag{27}$$

Equation (27) is a Cauchy singular integral equation [Erdogan 1978]. Following a procedure used in [Brock 2012; 2013] and requiring that contact zone traction be bounded on C gives the solution

$$\sigma(x, \psi - \theta) = -\frac{\mu_0 \mathrm{M}_0 \mathrm{M}}{r_0\sqrt{\mathrm{A}_K^2 + \mathrm{A}_\Gamma^2}}(x_+ - x)^{1+\Omega}(x - x_-)^{-\Omega}, \tag{28a}$$

$$x_+ = -\Omega L, \quad x_- = -(1 + \Omega)L. \tag{28b}$$

In (28) terms $(\Omega, \mathrm{A}_K, \mathrm{A}_\Gamma)$ are defined as

$$\Omega = -\frac{1}{2} + \frac{1}{\pi}\tan^{-1}\frac{\Gamma}{\mathrm{K}}, \tag{29a}$$

$$\mathrm{A}_K = \mathrm{M}_0\frac{A_1 \mathrm{P}_+}{\sqrt{d_3 d_5}} + c_D^2 \mathrm{M} A(A + B), \tag{29b}$$

$$\mathrm{A}_\Gamma = \gamma(\mathrm{M}_0\mathrm{N} + \mathrm{M}\mathrm{N}_0)\cos(\psi - \theta). \tag{29c}$$

It is noted that $-\frac{1}{2} < \Omega < 0$ and $(\mathrm{M}, \mathrm{M}_0) \geq 0$ for subcritical V, so that (28a) also guarantees contact and does not involve tensile stress.

Contour of C. Equation (28b) defines, in part, contour $\Im$ and, because $\Omega = -\frac{1}{2}$ when $|\psi - \theta| = \pi/2$ and is an even function of $\psi - \theta$, C exhibits the symmetry of the sphere with respect to X. The unknown contact zone span L depends on c_0 (or c) and is also an even function of $\psi - \theta$. It is determined by requiring that (28a) be consistent with the resultant force system acting on the die. Therefore, here $(x_\pm, \sigma)$ are even functions of $\psi - \theta$, and also Y. Thus condition $F_Y = 0$ is automatically satisfied. The condition that there are resultant forces $F_X = \gamma F_3$ and F_3 is met when

$$\int_\Psi d\psi \int_\Xi \sigma(\xi, \psi)|\xi|\, d\xi = -F_3. \tag{30}$$

Here F_3 is specified and (30), therefore, is an integral equation for L. For given (c_0, θ), F_3 should be stationary with respect to (28a); that is,

$$\int_\Psi d\psi \int_\Xi \delta\sigma(\xi, \psi)|\xi|\, d\xi = 0. \tag{31}$$

This requirement is satisfied when at every $x_- < x < x_+$, $|\psi - \theta| < \pi/2$

$$\delta\sigma = \frac{\partial\sigma}{\partial x}\,\delta x + \frac{\partial\sigma}{\partial\psi}\,\delta\psi = 0. \tag{32}$$

Here ψ and x are held constant in the first and second coefficients, respectively, and $(\delta x, \delta\psi)$ are arbitrary. Differentiation of (28a) shows that

$$x = -(1 + 2\Omega)L: \quad \frac{\partial\sigma}{\partial x} = 0, \quad \frac{\partial^2\sigma}{\partial x^2} > 0. \tag{33a}$$

The second term then vanishes for $x = -(1 + 2\Omega)L$ if

$$-\frac{\partial}{\partial\psi}\left(\frac{\mathrm{M_0M}}{\sqrt{\mathrm{A_K^2} + \mathrm{A_\Gamma^2}}}QL\right) = 0, \quad Q = (1 + \Omega)^{1+\Omega}(-\Omega)^{-\Omega}. \tag{33b}$$

Separation of variables and integration gives

$$L = \frac{Q_X}{Q}\,\frac{(\mathrm{M_0M})_X}{\mathrm{M_0M}}\,\frac{\sqrt{\mathrm{A_K^2} + \mathrm{A_\Gamma^2}}}{\sqrt{(\mathrm{A_K^2})_X + (\mathrm{A_\Gamma^2})_X}}L_X. \tag{34}$$

Subscript X signifies that a parameter is evaluated for $\psi = \theta$, that is, $c_X^0 = c_0$ (or $c_X = c$). For $L = L_Y$, that is, $|\psi - \theta| = \pi/2$, (34) gives

$$L_Y = \frac{Q_X(\mathrm{M_0M})_X}{\sqrt{(\mathrm{A_K^2})_X + (\mathrm{A_\Gamma^2})_X}}\left[c_D^2 + \frac{2\sqrt{d_1}\sqrt{2d_5 + \sqrt{d_1d_3} + d_{13}}}{\left(\sqrt{d_1d_3} + d_{13}\right)\sqrt{d_5}\sqrt{\sqrt{d_1d_3} - d_{13}}}\right]\frac{L_X}{c_D^2 - 1}. \tag{35}$$

Lengths (L_X, L_Y) are the span of contact zone C respectively along and perpendicular to the sliding path. The profile projected prior to sliding by a sphere on the plane $x_3 = 0$ is a circle. Equations (34) and (35) show that this shape is not preserved in the contact zone C. In addition, (28b) shows that only symmetry with respect to the sliding (positive X-)direction is preserved in the contact zone. Results (28) and (35), moreover, are sensitive to the dimensionless die sliding speed ($c_0 \neq 0$). To illustrate this behavior values

of the ratio L_Y/L_X are given in Table 1 for values of (γ, c_0). The sphere is ASTM-A913 Grade 450 steel with these properties [Beer et al. 2012]:

$$\mu_0 = 77.2\,\text{GPa}, \quad \rho_0 = 7860\,\text{kg/m}^3, \quad v_0 = 3134\,\text{m/s}.$$

The transversely isotropic half-space is a graphite epoxy with properties [Jones 1999]

$$C_{11} = 13.9\,\text{GPa}, \quad C_{33} = 160.7\,\text{GPa}, \quad C_{13} = 6.44\,\text{GPa}, \quad C_{12} = 6.92\,\text{GPa},$$
$$C_{55} = 7.07\,\text{GPa}, \quad C_{66} = 3.5\,\text{GPa}, \quad \rho = 1688\,\text{kg/m}^3.$$

In view of (5) and (6), the corresponding dimensionless parameters are

$$d_1 = 0.1803, \quad d_3 = 2.0816, \quad d_{13} = 0.0834, \quad d_{12} = 0.0896,$$
$$d_5 = 0.0916, \quad d_6 = 0.0453,$$
$$c_D = 1.8554, \quad c = 0.4634 c_0.$$

For $\psi = \theta$ the Rayleigh roots of $(\mathrm{M}, \mathrm{M}_0)$ are $c_0 = 0.9268$ and $c_0 = 0.6387$, respectively. Among terms (A, B, A_1, B_5, B_6), the branch point of B_6 is the minimum, which corresponds to $c_0 = 0.4595$. Thus, this value of c_0 is the maximum for subcritical sliding, that is, $V < 1440\,\text{m/s}$. Entries in Table 1 show contact zone geometry consistent with that for a rigid die sliding on an isotropic solid [Brock 2012] and on the surface of axial material symmetry for a transversely isotropic solid [Brock 2013]. That is, the contact zone is a noncircular oval, elongated in the direction of sliding. Such elongation is also found for an isotropic solid [Rahman 1996]. Table 1 entries show that, as in [Brock 2012; 2013], the elongation increases with sliding speed (c_0). Substitution of (28) and (34) in (30) gives, finally, an equation for L_X as a function of c_0:

$$F_3 = \frac{\mu_0}{r_0}\left(\frac{Q\mathrm{M}_0\mathrm{M}}{\sqrt{\mathrm{A}_\mathrm{K}^2 + \mathrm{A}_\Gamma^2}}\right)_X^3 L_X^3 \int_\Psi \frac{d\psi}{Q^2} \frac{\mathrm{A}_\mathrm{K}^2 + \mathrm{A}_\Gamma^2}{(\mathrm{M}_0\mathrm{M})^2} \int_\Omega^{1+\Omega} (1+\Omega-t)^{1+\Omega}(t-\Omega)^{-\Omega}|t|\,dt. \tag{36}$$

4. Transverse isotropy: Material symmetry axis in plane of surface

Traction distribution problem: Transform. In this case the material symmetry axis aligns with the positive x_2-direction, and elastic constants [Jones 1999] and related dimensionless parameters are given by

	$c_0 = 0.05$	$c_0 = 0.1$	$c_0 = 0.2$	$c_0 = 0.3$	$c_0 = 0.4$
$\gamma = 0.1$	0.5333	0.5282	0.5061	0.469	0.4102
$\gamma = 0.2$	0.5321	0.5271	0.5054	0.4678	0.4089
$\gamma = 0.5$	0.5197	0.5191	0.4974	0.4596	0.4007

Table 1. Ratio L_Y/L_X for values of γ and $c_0 < 0.4595$ $(c < \sqrt{d_6} = 0.2129)$.

(5) and

$$C_{33} = C_{11}, \quad C_{66} = C_{44}, \quad C_{23} = C_{12}, \quad C_{22}, \quad C_{11} - C_{13} - 2C_{55} = 0, \tag{37a}$$

$$d_1 = \frac{C_{11}}{\mu_0}, \quad d_2 = \frac{C_{22}}{\mu_0}, \quad d_4 = \frac{C_{44}}{\mu_0}, \quad d_5 = \frac{C_{55}}{\mu_0}, \quad d_{12} = \frac{C_{12}}{\mu_0}, \quad d_{13} = \frac{C_{13}}{\mu_0}, \tag{37b}$$

$$d_1 - d_{13} - 2d_5 = 0, \quad c = \sqrt{\frac{\rho}{\rho_0}} c_0, \quad c_0 = \frac{v}{v_0}. \tag{37c}$$

Equations (A.5) and (37) give the homogeneous equation set

$$\begin{bmatrix} d_5\partial_3^2 + \mathrm{X}_1 & (d_6 + d_{12})\partial_1\partial_2 & (d_5 + d_{13})\partial_1\partial_3 \\ (d_6 + d_{12})\partial_1\partial_2 & d_6\partial_3^2 + \mathrm{X}_2 & (d_6 + d_{12})\partial_2\partial_3 \\ (d_5 + d_{13})\partial_1\partial_3 & (d_6 + d_{12})\partial_2\partial_3 & d_1\partial_3^2 + \mathrm{X}_3 \end{bmatrix} \begin{bmatrix} u_1 \\ u_2 \\ u_3 \end{bmatrix} = 0, \tag{38a}$$

$$\mathrm{X}_1 = d_1\partial_1^2 + d_6\partial_2^2 - c^2\partial_X^2, \quad \mathrm{X}_2 = d_6\partial_1^2 + d_2\partial_2^2 - c^2\partial_X^2, \quad \mathrm{X}_3 = d_5\partial_1^2 + d_6\partial_2^2 - c^2\partial_X^2. \tag{38b}$$

The same procedure based on (8) gives, for $x_3 = 0$, in place of (9), (12), and (13):

$$\hat{\boldsymbol{u}} = \boldsymbol{U}_+ \exp(-\Omega_+ x_3) + \boldsymbol{U}_- \exp(-\Omega_- x_3) + \boldsymbol{U}_5 \exp(-\Omega_5 x_3), \tag{39a}$$

$$(U_1^\pm, U_3^\pm) = (d_6 + d_{12}) p_2(-p_1, \Omega_\pm) U_\pm, \quad U_2^\pm = \left(A_6 - \tfrac{1}{2} d_1 P_\pm\right) U_\pm, \tag{39b}$$

$$U_1^5 = \Omega_5 U_5, \quad U_2^5 = 0, \quad U_3^5 = p_1 U_5, \tag{39c}$$

$$\frac{1}{\mu_0} \begin{bmatrix} \hat{\sigma}_{33} \\ \hat{\sigma}_{31} \\ \hat{\sigma}_{32} \end{bmatrix} = \begin{bmatrix} p_2 C_3^+ & p_2 C_3^- & -2d_5 p_1 \Omega_5 \\ d_6 D_{13} \Omega_+ & d_6 D_{13} \Omega_- & T_5 \\ D_{32}^+ \Omega_+ & D_{32}^- \Omega_- & d_6 p_1 p_2 \end{bmatrix} \begin{bmatrix} U_+ \\ U_- \\ U_5 \end{bmatrix}. \tag{39d}$$

The matrix coefficients in (39d) are given by

$$C_3^\pm = (d_6 + d_{12}) T_5 - d_1(\Omega_\pm^2 + p_1^2) - A_6, \tag{40a}$$

$$D_{13} = 2d_5 p_1 p_2 (d_6 + d_{12}), \tag{40b}$$

$$D_{32}^\pm = (d_6 + d_{12}) p_2^2 - d_1(\Omega_\pm^2 + p_1^2) - A_6. \tag{40c}$$

For both (39) and (40) the following definitions hold:

$$\Omega_\pm = \sqrt{p_1^2 + \frac{P_\pm}{2d_1 d_6}} \sqrt{-1}, \quad \Omega_5 = \omega_5 \sqrt{-1}, \tag{41a}$$

$$P_\pm = d_1 A_2 + d_6 A_6 - (d_6 + d_{12})^2 p_2^2 \pm \sqrt{[d_1 A_2 + d_6 A_6 - (d_6 + d_{12})^2 p_2^2]^2 - 4 d_1 d_6 A_2 A}, \tag{41b}$$

$$A_6 = p_2^2 - c^2 p_X^2, \quad A_2 = d_2 p_2^2 - c^2 p_X^2, \quad \omega_5 = \sqrt{p_1^2 + \frac{A_6}{d_5}}. \tag{41c}$$

As in the first problem, coefficients $(U_\pm, U_5)$ are obtained as functions of (p_1, p_2) by imposing the transform of condition (3) on the transforms given by (39). The transform $\hat{u}_3^0$ of the normal displacement for $x_3 = 0$ can then be written.

Transform inversion and sliding contact problem. Results (40) and (41) are relatively complicated in comparison with (10) and (11). For the purposes of illustration, therefore, the frictionless limit ($\gamma = 0$) is treated. Results analogous to those in Appendix A obtain, and the same transform inversion process used above is then used to reduce the sliding contact problem to a singular integral equation. The result is a normal contact zone traction that is bounded for $x_3 = 0$, $(x_1, x_2) \in C$:

$$\sigma(x, \psi, \psi - \theta) = \frac{\mu_0}{2\mathrm{K}r_0}\sqrt{L^2 - 4x^2}, \quad x_\pm = \pm\frac{L}{2}. \tag{42}$$

In (42), definition (19c) and (25b) are replaced with

$$\mathrm{K} = \left|\frac{\mathrm{A}_6}{\mathrm{M}}\right|\mathrm{B}_+\mathrm{B}_-(\mathrm{B}_+ + \mathrm{B}_-) + \frac{c_D^2 A}{\mathrm{M}_0}(A + B), \tag{43a}$$

$$\mathrm{M} = 4d_5^2 B_5 B_+ B_-(\mathrm{B}_+ + \mathrm{B}_-)\cos^2\psi - d_6 A_6(B_1^2 + \mathrm{B}_+\mathrm{B}_-)\sin^2\psi - Q_\mathrm{B}\mathrm{T}_5^2. \tag{43b}$$

Terms that arise in (42) and (43) are

$$\mathrm{T}_5 = \mathrm{A}_6 + 2d_5\cos^2\psi, \quad Q_\mathrm{B} = \frac{1}{d_1 d_6}(d_6 + d_{12})^2\sin^2\psi - \cos^2\psi - \frac{\mathrm{A}_2}{d_6} - \mathrm{B}_+\mathrm{B}_-, \tag{44a}$$

$$B_5 = \sqrt{\cos^2\psi + \frac{\mathrm{A}_6}{d_5}}, \quad B_1 = \sqrt{\cos^2\psi + \frac{\mathrm{A}_6}{d_1}}, \quad \mathrm{B}_\pm = \sqrt{\cos^2\psi + \frac{\mathrm{P}_\pm}{2d_1 d_6}}, \tag{44b}$$

$$\mathrm{P}_\pm = d_1\mathrm{A}_2 + d_6\mathrm{A}_6 - (d_6 + d_{12})^2\sin^2\psi \pm \sqrt{[d_1\mathrm{A}_2 + d_6\mathrm{A}_6 - (d_6 + d_{12})^2\sin^2\psi]^2 - 4d_1 d_6\mathrm{A}_2\mathrm{A}_6}, \tag{44c}$$

$$\mathrm{A}_6 = d_6\sin^2\psi - c_X^2, \quad \mathrm{A}_2 = d_2\sin^2\psi - c_X^2, \quad c_X = c\cos(\psi - \theta). \tag{44d}$$

Here $\mathrm{B}_+\mathrm{B}_-(\mathrm{B}_+ + \mathrm{B}_-) > 0$ for $(B_1, B_5, \mathrm{B}_\pm)$ real, and $(\mathrm{M}, \mathrm{A}_6)$ vanish for $|\psi, \theta| < \pi/2$ if

$$\tan\psi + \frac{c\cos\theta}{c\sin\theta \pm \sqrt{d_6}} = 0. \tag{45}$$

Thus, the first term in (43a) always gives a finite value. The second term in (43a) shows that A_6 cancels from u_3^0 in the isotropic limit. In any event (42) is finite and continuous, and guarantees a nontensile contact zone.

The anisotropy of the half-space surface is manifest in the definition (42)–(44). In particular, solution behavior now depends on orientation with respect to principal axes of both points in C and the path of the sliding sphere. Moreover, the definition of the critical sliding speed in terms of branch-point values and roots of $(\mathrm{M}, \mathrm{M}_0)$ is θ-dependent. The branch points of $(B_5, \mathrm{B}_\pm)$ are relevant and are given, respectively, in terms of dimensionless speed c_0 as

$$(c_0)_{56} = \sqrt{\frac{\rho_0}{\rho}}\sqrt{d_6\sin^2\theta + d_5\cos^2\theta}, \tag{46a}$$

$$(c_0)_\pm = \frac{1}{2}\sqrt{\frac{\rho_0}{\rho}}\left[\sqrt{d_6 + \mathrm{P} + \mathrm{P}_6} \pm \sqrt{d_6 + \mathrm{P} - \mathrm{P}_6}\right], \tag{46b}$$

$$\mathrm{P} = d_1\cos^2\theta + d_2\sin^2\theta, \tag{46c}$$

$$\mathrm{P}_6 = \sqrt{4\mathrm{P}^2 + [d_6^2 - 2d_1 d_2 - (d_6 + d_{12})^2]\sin^2 2\theta}. \tag{46d}$$

$\theta =$	$0°$	$30°$	$45°$	$60°$	$90°$
$(c_{56})_0$	0.4595	0.5147	0.5646	0.6104	0.653
$(c_+)_0$	0.9163	1.6743	2.2576	2.7193	3.113
$(c_-)_0$	0.653	0.8222	0.7719	0.7153	0.653

Table 2. Values of c_0 associated with solution branch points for various θ. Note that $A(1.8554) = 0$, $B(1) = 0$, and $\mathrm{M}_0(0.9268) = 0$.

Contour C. Expressions analogous to (34) and (36) can be obtained for this case:

$$L = \frac{\mathrm{K}}{\mathrm{K}_X} L_X, \quad F_3 = \frac{L_X^3}{12\mathrm{K}_X^3} \frac{\mu_0}{r_0} \int_\Xi d\psi \, \mathrm{K}^2. \tag{47}$$

In (47) subscript X signifies a quantity evaluated for $\psi = \theta$. In this case, however, terms in (43) and (44) are not, in general, even functions with respect to the X-direction; for example, for $\mathrm{M}(\psi, \psi - \theta)$ we have $\mathrm{M}(\theta + \phi, \phi) \neq \mathrm{M}(\theta - \phi, \phi)$ for $\phi \neq \pi/2$. Thus contact zone C symmetry may not involve the (X, Y)-axes. In this case, therefore, it is perhaps more illustrative to study the ratio

$$L_\Phi / L_X = \mathrm{K}_\Phi / \mathrm{K}_X. \tag{48}$$

As in (34) and (47) L_X is the contact zone span along the direction θ of sliding. Length L_Φ is the span along lines that make an angle ϕ with respect to the X-direction, that is, $\psi = \theta + \phi$ where $|\phi| \leq \pi/2$. The sphere has the same properties as used for the first problem, but orientation of the graphite epoxy [Jones 1999] now gives dimensionless parameters

$$d_1 = 0.1831, \quad d_2 = 2.0816, \quad d_{13} = 0.0896, \quad d_{12} = 0.0834, \quad d_5 = 0.0453, \quad d_6 = 0.0916.$$

Based on these, Table 2 presents dimensionless parameters $(c_0)_{56}$ and $(c_0)_\pm$ associated with various values of θ. It is noted that $(c_0)_{56} \leq (c_0)_\pm$. It can also be shown that ratio $|\mathrm{M}/\mathrm{A}_6| \neq 0$ for $0 < c_0 < (c_0)_{56}$ and that the second (isotropic) term in (43a) does not become singular until $c_0 = 0.9268$. Therefore $v = (c_0)_{56} v_0$ defines the critical sliding speed. Table 3 presents values of ratio (48) for $\theta = 45°$ and various values of ϕ. Table 2 shows that critical sliding speed for this direction is 1769 m/s. In the first problem the value was 1440 m/s for all sliding directions.

Entries in Table 1 depicted the contact zone as a noncircular oval, elongated in the direction of sliding. In this problem $\phi = 0°$ and $\phi = \pm 90°$ define the direction of sliding and its normal, and $\phi = \pm 45°$ define the (x_2, x_1)-principal material axes. Entries in Table 3 show that the contact zone for $c_0 = 0.05$ has an oval shape, but elongation is defined in terms of the principal axes, not the sliding direction ($\theta = 45°$). As c_0 is increased, however, the contact zone "rotates" and forms an oval elongated in the sliding direction, as in the first problem. This behavior is consistent with that for the rigid sliding sphere [Brock 2013]; that is, for low sliding speed the contact zone contour is largely determined by the orientation of the in-plane principal axes. For higher speeds, the direction of sliding becomes important.

5. Summary and comments

Combining quasipolar coordinates with an analysis defined in terms of Cartesian coordinates does result in solutions of a hybrid nature. However, analytical expressions for contact zone traction in the quasipolar

ϕ°	$c_0 = 0.05$	$c_0 = 0.1$	$c_0 = 0.2$	$c_0 = 0.3$	$c_0 = 0.4$
90	1.0218	1.0002	0.9113	0.7917	0.5945
67.5	0.8743	0.856	0.7859	0.6913	0.5279
45	0.823	0.8098	0.7536	0.6797	0.5403
22.5	0.8778	0.8668	0.8233	0.7748	0.6657
0	1.0	1.0	1.0	1.0	1.0
−22.5	1.2124	1.21	1.2103	1.257	1.4348
−45	1.2274	1.2168	1.1705	1.1286	1.023
−67.5	1.2058	1.1842	1.0937	0.973	0.7557
−90	1.2168	1.191	1.0852	0.9428	0.7079

Table 3. Ratio L_Φ/L_X for $\gamma = 0$, $\theta = 45^\circ$, ϕ and $c_0 < (c_0)_{56} = 0.5646$. Note that $\psi = \theta + \phi$.

system are readily extracted. In any event, the approach is adopted here in order to address problems that may not exhibit axial symmetry. The factor cancellation procedure adopted here follows that of the 2D analysis of sliding on a transversely half-plane surface [Brock 2002]. A more compact solution expression is the result, but care must then be used in comparing it with that for the isotropic limit case, for example, as in [Rahman 1996].

The assumption that key geometric features of the projection of die profile onto the contact surface are preserved in the contact zone shape, or that the zone is essentially elliptical, is often accurate [Johnson 1985; Hills et al. 1993]. Here, however, in addition to requiring a bounded traction on the zone boundary, the resultant compressive force is required to be stationary with respect to the traction. The expressions for contact zone geometry that result from these requirements, and calculations based on them, indicate that the contact zone is often a distortion of the projection. This result is consistent with those in [Brock 2012; 2013].

For the case of the material symmetry axis for a transversely isotropic material coinciding with the half-space surface normal, the contact zone shape represents in a sense an elongation of a sphere profile along the line of sliding; see [Rahman 1996; Brock 2012; 2013]. The effect is sensitive to sliding speed, and the presence of friction prevents replication by the contact zone of projection symmetry, other than that with respect to this line.

For the case of the material symmetry axis lying in the surface plane, solution response in the contact zone depends on both sliding direction orientation and location in the contact zone with respect to the principal material axes. Contact zone elongation is along a principal material axis for low sliding speeds. As sliding speed is increased, however, elongation is more consistent with isotropic behavior, that is, elongation is in the sliding direction. This behavior is also consistent with [Brock 2013] but the changes in shape during the transition from one behavior to the other are more pronounced here. This contrast suggests that analysis based on the rigid die is indeed a first step.

For frictionless sliding by a sphere, calculations for L_Y/L_X in Table 1 could be used to provide semiminor and semimajor axis measures for the elliptical contact zone model, for example, as in [Johnson 1985]. As noted above, friction may preserve profile symmetry only with respect to translation direction. However, the data in Table 1 indicates that the elliptical contact zone model may still be a useful approximation. In the second problem treated here, contact zone symmetry may not coincide with

that exhibited by the circular profile for the sphere. Calculations in Table 3 might still prove useful for the contact zone shape that is assumed; similar conclusions are reached in [Brock 2012; 2013].

This study also shows that, in a 3D analysis of transverse isotropy, Rayleigh speeds may not be critical. Specifically, the Rayleigh speeds for both a sphere and a half-space whose surface normal is the axis of material symmetry can be obtained. However, for the graphite epoxy material [Jones 1999] chosen for calculation, the value corresponds to a transonic speed, and the speed for steel exceeds that value. For the surface that contains the material symmetry axis, the Rayleigh function for such a material does not vanish in the subsonic sliding speed range. Again, moreover, the Rayleigh speed for steel corresponds to a transonic speed in the half-space.

In closing, it is recognized that sliding contact between an isotropic sphere and a transversely isotropic half-space with a surface that coincides with a principal material plane is a special case. A more tractable mathematical problem arises and, as a result, so does a solution in a simple analytical form. Nevertheless, anisotropic bodies are often composites, and shaped so that their surfaces do coincide with a principal plane [Jones 1999]. Moreover, the second problem may give insight into the response of materials with greater degrees of anisotropy.

Appendix A

For the homogeneous and linear elastic anisotropic solid, the stress and strain measure (σ_k, ϵ_k) in contracted notation is related by [Jones 1999]:

$$\sigma_k = C_{kl}\epsilon_l, \quad C_{kl} = C_{lk}. \tag{A.1}$$

Indices (k, l) take on values $(1, 2, 3, 4, 5, 6)$ and the 21 elastic parameters are constants. These measures correspond to those in the Cartesian basis, for $k = (1, 2, 3)$, as

$$\sigma_k = \sigma_{kk}, \quad \epsilon_k = \partial_k u_k. \tag{A.2}$$

For $k = (4, 5, 6)$, the correspondence is

$$\sigma_4 = \sigma_{23} = \sigma_{32}, \quad \epsilon_4 = \partial_2 u_3 + \partial_3 u_2, \tag{A.3a}$$

$$\sigma_5 = \sigma_{31} = \sigma_{13}, \quad \epsilon_5 = \partial_3 u_1 + \partial_1 u_3, \tag{A.3b}$$

$$\sigma_6 = \sigma_{12} = \sigma_{21}, \quad \epsilon_6 = \partial_1 u_2 + \partial_2 u_1. \tag{A.3c}$$

Here (u_k, ∂_k) are k-components of the displacement and gradient vector $(\boldsymbol{u}, \nabla)$. The strain energy density is positive for (A.1) when $\epsilon_k^T C_{kl}\epsilon_l > 0$. This condition, in turn, is satisfied when [Hohn 1965; Ting 1996]

$$\begin{vmatrix} C_{11} & C_{21} & \cdots & C_{1n} \\ C_{21} & C_{22} & \cdots & C_{2n} \\ \vdots & \vdots & \ddots & \vdots \\ C_{n1} & C_{2n} & \cdots & C_{nn} \end{vmatrix} > 0 \quad (n \le 6). \tag{A.4}$$

In view of (1), (2), and (A.1)–(A.3), the linear momentum balance in the translating Cartesian basis takes the form

$$\nabla_{kl}\epsilon_l - \rho v^2 \partial_X^2 u_k = 0, \tag{A.5a}$$

$$\begin{bmatrix} \nabla_{1l} \\ \nabla_{2l} \\ \nabla_{3l} \end{bmatrix} = \begin{bmatrix} C_{l1} & C_{l6} & C_{l5} \\ C_{l6} & C_{l2} & C_{l4} \\ C_{l5} & C_{l4} & C_{l3} \end{bmatrix} \begin{bmatrix} \partial_1 \\ \partial_2 \\ \partial_3 \end{bmatrix}. \tag{A.5b}$$

Here ρ is the mass density, $k = (1, 2, 3)$, $l = (1, 2, 3, 4, 5, 6)$, and the summation convention applies.

Appendix B

For $x_3 = 0$, (9) and (12) give the formal result

$$\hat{u}_3^0 = (d_5\Omega_+^2 + \omega_1^2)U_+ + (d_5\Omega_-^2 + \omega_1^2)U_-. \tag{B.1}$$

In view of (13) the solutions for $(U_\pm, U_6)$ and, therefore, the coefficients in (B.1) are functions of polynomials in $(\Omega_\pm, \Omega_6)$. These can be factored so that

$$\hat{u}_3^0 = d_5^2(d_5 + d_{13})(\Omega_+ - \Omega_-)\Omega_6\omega_1 \frac{P}{\Delta}\left[N\left(p_1\frac{\hat{\tau}_1}{\mu_0} + p_2\frac{\hat{\tau}_2}{\mu_0}\right) - \omega_1(\Omega_+ + \Omega_-)\frac{\hat{\sigma}}{\mu_0}\right], \tag{B.2a}$$

$$N = \omega_1 - \frac{d_{13}\omega_5}{\sqrt{d_3 d_5}}. \tag{B.2b}$$

Term Δ is the determinant of the matrix in (13a) and can also be factored:

$$\Delta = d_5^2(d_5 + d_{13})\omega_1\Omega_6 P(\Omega_+ - \Omega_-)M, \tag{B.3a}$$

$$M = \omega_1\omega_5\left(\omega_5 + \sqrt{\frac{d_3}{d_5}}\omega_1\right) - \left(d_5\omega_1 + \frac{d_{13}^2\omega_5}{\sqrt{d_3 d_5}}\right)P. \tag{B.3b}$$

Use of (B.3a) in (B.2a) leads, upon factor cancellation, to a more compact form. Similar results hold for the isotropic solid with mass density ρ_0, the shear modulus μ_0, and the rotational wave speed v_0, that is,

$$d_2 = d_1 = c_D^2, \quad d_5 = d_6 = 1, \quad d_{12} = d_{13} = c_D^2 - 2. \tag{B.4}$$

It can be shown that (11) and (12) reduce to

$$\Omega_+ = \omega_D\sqrt{-1}, \qquad \Omega_- = \Omega_6 = \omega\sqrt{-1}, \qquad T = 2P - c_0^2 p_X^2, \tag{B.5a}$$

$$\omega_D = \sqrt{P - \frac{c_0^2}{c_D^2}p_X^2}, \qquad \omega_5 = \omega = \sqrt{P - c_0^2 p_X^2}, \tag{B.5b}$$

$$C_3^+ = -(c_D^2 - 1)T\omega_D\sqrt{-1}, \quad D_3^+ = 2(c_D^2 - 1)\omega^2, \tag{B.5c}$$

$$C_3^- = -2(c_D^2 - 1)\omega P\sqrt{-1}, \quad D_3^- = (c_D^2 - 1)T. \tag{B.5d}$$

Parameter c_D is the dimensionless dilatational wave speed, and the determinant corresponding to Δ is

$$\omega_D\omega P(c_D^2 - 1)^2(4P\omega_D\omega - T^2). \tag{B.6}$$

The last term is the isotropic Rayleigh function [Brock 2012]. This term and the isotropic limit of (B.3b) can be written as, respectively,

$$\frac{\omega_D-\omega}{c_D^2-1}\times\omega[c_D^4\omega_D^2-(c_D^2-1)^2P]-\omega_D c_D^2 c_0^2 p_X^2, \tag{B.7a}$$

$$\frac{\omega}{c_D}[c_D^4\omega_D^2-(c_D^2-1)^2P]-\omega_D c_D c_0^2 p_X^2. \tag{B.7b}$$

Equation (B.7a) demonstrates that the nonzero roots of the isotropic Rayleigh function are also roots of the second factor. This implies that Δ is the transversely isotropic Rayleigh function, and that its nonzero roots will also be roots of factor M, where dimensionless sliding speeds (c, c_0) are related by (6b).

Appendix C

Consider integrals involving real parameters (X, Y) over the entire $\mathrm{Im}(p)$-axis P:

$$\frac{1}{2\pi i}\int_{\mathrm{P}}|p|\left(1,\frac{\sqrt{-p}}{\sqrt{p}}\right)\exp[pX-Y\sqrt{-p}\sqrt{p}\,]\frac{dp}{p}\quad(Y\ge 0). \tag{C.1}$$

$\mathrm{Re}(\sqrt{\pm p})\ge 0$ in the p-plane with, respectively, branch cuts $\mathrm{Im}(p)=0, \mathrm{Re}(p)<0$ and $\mathrm{Im}(p)=0$, $\mathrm{Re}(p)>0$. Specifically, for $\mathrm{Re}(p)=0+$ and, respectively, $\mathrm{Im}(p)=q>0$ and $\mathrm{Im}(p)=q<0$:

$$\sqrt{-p}=\left|\frac{q}{2}\right|^{1/2}(1\mp i),\quad \sqrt{p}=\left|\frac{q}{2}\right|^{1/2}(1\pm i). \tag{C.2}$$

Use of (C.2) reduces (C.1) to

$$\frac{1}{i\pi}\int_0^\infty(\cos qX,\sin qX)\exp(-Yq)\,dq. \tag{C.3}$$

From the standard [Peirce and Foster 1956] tables (C.3) is evaluated as

$$\frac{1}{i\pi}\left(\frac{Y}{X^2+Y^2},\frac{X}{X^2+Y^2}\right). \tag{C.4}$$

It is noted in [Stakgold 1967] that

$$\frac{1}{\pi}\frac{Y}{X^2+Y^2}\to\delta(X)\quad(Y\to 0). \tag{C.5}$$

Here δ is the Dirac function.

References

[Ahmadi et al. 1983] N. Ahmadi, L. M. Keer, and T. Mura, "Non-Hertzian contact stress analysis for an elastic half-space: normal and sliding contact", *Int. J. Solids Struct.* **19**:4 (1983), 357–373.

[Beer et al. 2012] F. P. Beer, E. R. Johnston, Jr., J. T. DeWolf, and D. F. Mazurek, *Mechanics of materials*, 6th ed., McGraw-Hill, New York, 2012.

[Brock 2002] L. M. Brock, "Exact analysis of dynamic sliding indentation at any constant speed on an orthotropic or transversely isotropic half-space", *J. Appl. Mech.* (*ASME*) **69**:3 (2002), 340–345.

[Brock 2012] L. M. Brock, "Two cases of rapid contact on an elastic half-space: sliding ellipsoidal die, rolling sphere", *J. Mech. Mater. Struct.* **7**:5 (2012), 469–483.

[Brock 2013] L. M. Brock, "Rapid sliding contact in 3D by an ellipsoidal die on transversely isotropic half-spaces with surfaces on different principal planes", *J. Appl. Mech.* (*ASME*) **81**:3 (2013), Article ID #031005.

[Erdogan 1978] F. Erdogan, "Mixed boundary value problems in mechanics", pp. 1–86 in *Mechanics today*, vol. 4, edited by S. Nemat-Nasser, Pergamon, New York, 1978.

[Hartnett 1980] M. J. Hartnett, "A general numerical programming method for design of elastic bodies in contact", pp. 51–66 in *Solid contact and lubrication* (Chicago, 1980), edited by H. S. Cheng and L. M. Keer, Applied Mechanics Division **39**, American Society of Mechanical Engineers, New York, 1980.

[Hertz 1882] H. Hertz, "Ueber die Berührung fester elastischer Körper", *J. Reine Angew. Math.* **1882**:92 (1882), 156–171. Translated as "On the contact of elastic solids", pp. 146–162 in *Miscellaneous papers*, edited by P. Lenard, Macmillan, London, 1896.

[Hills et al. 1993] D. A. Hills, D. Nowell, and A. Sackfield, *Mechanics of elastic contacts*, Butterworth-Heinemann, Oxford, 1993.

[Hohn 1965] F. E. Hohn, *Elementary matrix algebra*, Macmillan, New York, 1965.

[Johnson 1985] K. L. Johnson, *Contact mechanics*, Cambridge University Press, 1985.

[Jones 1999] R. M. Jones, *Mechanics of composite materials*, 2nd ed., Taylor & Francis, Philadelphia, 1999.

[Kalker 1990] J. J. Kalker, *Three-dimensional elastic bodies in rolling contact*, Kluwer, Dordrecht, 1990.

[Peirce and Foster 1956] B. O. Peirce and R. M. Foster, *A short table of integrals*, 4th ed., Ginn, New York, 1956.

[Rahman 1996] M. Rahman, "Hertz problem for a rigid punch moving across the surface of a semi-infinite elastic solid", *Z. Angew. Math. Mech.* **47**:4 (1996), 601–615.

[Sneddon 1972] I. N. Sneddon, *The use of integral transforms*, McGraw-Hill, New York, 1972.

[Stakgold 1967] I. S. Stakgold, *Boundary value problems of mathematical physics*, vol. 1, Macmillan, New York, 1967. Reprinted in *Classics in Applied Mathematics* **29**, SIAM, Philadelphia, 2000.

[Ting 1996] T. C. T. Ting, *Anisotropic elasticity: theory and applications*, Oxford Engineering Science Series **45**, Oxford University Press, New York, 1996.

Received 10 Jun 2013. Accepted 23 Sep 2013.

LOUIS MILTON BROCK: louis.brock@uky.edu
Mechanical Engineering, University of Kentucky, 265 RGAN, Lexington, KY 40506-0503, United States

JOURNAL OF MECHANICS OF MATERIALS AND STRUCTURES
Vol. 8, No. 8-10, 2013
dx.doi.org/10.2140/jomms.2013.8.479

msp

WEIGHT FUNCTION APPROACH TO A CRACK PROPAGATING ALONG A BIMATERIAL INTERFACE UNDER ARBITRARY LOADING IN AN ANISOTROPIC SOLID

LEWIS PRYCE, LORENZO MORINI AND GENNADY MISHURIS

The focus of this paper is the study of the dynamic steady-state propagation of interfacial cracks in anisotropic bimaterials under general, nonsymmetric loading conditions. Symmetric and skew-symmetric weight functions, defined as singular nontrivial solutions of a homogeneous traction-free crack problem, have been recently derived for a quasistatic semiinfinite crack at the interface between two dissimilar anisotropic materials. In this paper, the expressions for the weight functions are generalized to the case of a dynamic steady-state crack between two anisotropic media. A functional matrix equation, through which it is possible to evaluate the stress intensity factors and the energy release rate at the crack tip, is obtained. A general method for calculating the asymptotic coefficients of the displacement and traction fields, without any restrictions regarding the loading applied on the crack faces, is developed. The proposed approach is applied for the computing stress intensity factors and higher-order asymptotic terms corresponding to two different example loading configurations acting on the crack faces in an orthotropic bimaterial.

1. Introduction

Evaluation of stress intensity factors and higher-order asymptotic terms of displacement and stress fields represents a crucial issue for perturbative analysis of many interfacial crack problems [Bercial-Velez et al. 2005; Piccolroaz et al. 2010]. Recently, using a procedure based on Betti's reciprocal theorem together with weight functions [Bueckner 1985; 1989], a general method for calculating the coefficients of the asymptotic displacements and stresses corresponding to an arbitrary loading acting on crack faces has been developed in [Piccolroaz et al. 2009] for quasistatic cracks between dissimilar isotropic media, and in [Morini et al. 2013] for interfacial cracks in two-dimensional anisotropic bimaterials. The aim of this paper is to generalize these results to the case of dynamic steady-state crack propagation at the interface between two dissimilar anisotropic media, and to develop a general method for explicitly computing the coefficients in the asymptotic representations of the displacements and stresses and the energy release rate for dynamic interfacial crack problems, without any restrictions regarding the loading applied at the crack faces.

The article is organized as follows: Section 2 includes some preliminary results which are used in the proposed analysis. The Stroh representation [Stroh 1962] of displacements and stress fields is reported together with the Riemann–Hilbert formulation of interfacial cracks in anisotropic bimaterials developed in [Suo 1990; Yang et al. 1991]. Explicit expressions for symmetric and skew-symmetric weight functions for quasistatic plane crack problems derived in [Morini et al. 2013] and the Betti integral formula

Keywords: interfacial crack, steady-state propagation, weight functions, stress intensity factors, energy release rate.

are introduced. In Section 3, weight function matrices for a semiinfinite crack propagating at a constant speed at the interface between two dissimilar orthotropic materials under plane deformation are derived. In Section 4, using explicit weight functions together with Betti's integral theorem, general formulas for stress intensity factors and higher-order asymptotic terms are obtained. By means of the developed approach, both symmetric and skew-symmetric loading configurations acting on the crack faces can be considered, and higher-order asymptotic terms can also be computed for nonsmooth loading functions. The derived stress intensity factors are then used to evaluate the energy release rate. Two illustrative examples of numerical computations for a specific asymmetric load are presented in Section 5. The effects of the loading asymmetry on the energy release rate and the dependence of stress intensity factors on the crack tip velocity are finally discussed, and possible physical implications of these results on the continuing propagation of the crack are explored.

2. Preliminary results

In this section the mathematical framework of the model is introduced. Preliminary results concerning interfacial cracks in two-dimensional anisotropic elastic bimaterials used for further analysis in this paper are also reported. A semiinfinite crack propagating at a constant speed, v, along a perfect interface between two semiinfinite anisotropic materials is considered. The crack is said to be occupying the region $x_1 - vt < 0$, $x_2 = 0$, as illustrated in Figure 1.

Considering the Cartesian coordinate system shown in Figure 1, the traction on the crack faces is defined as

$$\sigma_{2j}(x_1 - vt, 0^{\pm}) = p_j^{\pm}(x_1 - vt), \quad \text{for} \quad x_1 - vt < 0, \tag{1}$$

and the body forces are assumed to be zero. The only restriction on the loading considered in this paper is that it must vanish within the region of the crack tip.

The closed-form solution to the problem of a semiinfinite crack at an interface between two dissimilar anisotropic materials has been derived by means of Stroh formalism [1962] in both the static [Suo 1990] and the steady-state [Yang et al. 1991] cases, where the variation of angular stresses for different crack

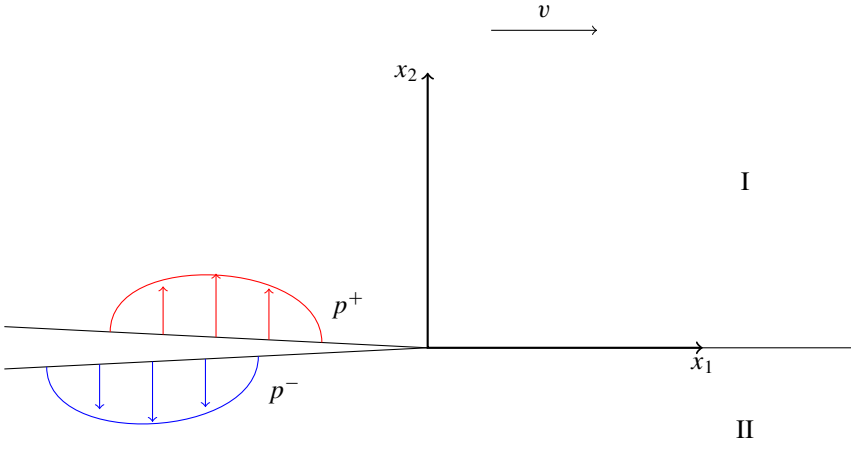

Figure 1. Geometry.

velocities was plotted. The expressions for the stress field along the interface and the displacement along the crack line derived in these papers, which are used in further analysis, are reported in Section 2.1. In Section 2.2 the weight function defined in [Willis and Movchan 1995] is introduced and, finally, in Section 2.3, it is shown how the Betti formula can be used to relate the weight functions and the physical solutions for a problem concerning a propagating crack.

2.1. ***Steady-state interfacial crack: Stroh formalism.*** For both anisotropic elastic media, occupying the upper and lower half-planes in Figure 1, Hooke's law is given by

$$\sigma_{ij} = C_{ijkl}\epsilon_{kl} = C_{ijkl}\frac{\partial u_k}{\partial x_l}, \quad \text{for} \quad i, j, k, l = 1, 2, \tag{2}$$

where σ is the stress, ϵ is the strain, C is the stiffness tensor for the material, v is the speed at which the crack is moving, and ρ is the material density. The following relationship relating the stress and displacement is also used:

$$\sum_{j=1}^{2} \frac{\partial \sigma_{ij}}{\partial x_j} = \rho \frac{\partial^2 u_i}{\partial t^2}. \tag{3}$$

Combining (2) and (3) gives

$$C_{ijkl}\frac{\partial^2 u_k}{\partial x_j \partial x_l} = \rho \frac{\partial^2 u_i}{\partial t^2}. \tag{4}$$

A new coordinate system is now introduced: $(\tilde{x}_1 = x_1 - vt, \tilde{x}_2 = x_2)$. The following relationship is therefore found in this new coordinate system:

$$\tilde{C}_{ijkl}\frac{\partial^2 u_k}{\partial \tilde{x}_j \partial \tilde{x}_l} = 0, \tag{5}$$

where $\tilde{C}_{ijkl} = C_{ijkl} - \rho v^2 \delta_{ik}\delta_{1j}\delta_{1l}$.

From here on, for convenience, the moving coordinates will be written as $\tilde{x}_1 = x$ and $\tilde{x}_2 = y$. In order to find expressions for the displacement and stress fields in both of the materials, the Stroh formalism can be applied, and a solution in the form $u_i = A_i f(x + py)$ derived. Introducing this expression into the balance equations (5), the following eigenvalue problem is obtained:

$$(\boldsymbol{Q} + p(\boldsymbol{R} + \boldsymbol{R}^T) + p^2 \boldsymbol{T})\boldsymbol{A} = 0, \tag{6}$$

where $\boldsymbol{Q} = C_{i1k1} - \rho v^2 \delta_{ik}$ depends on the material constants and the crack speed. However, $\boldsymbol{R} = C_{i1k2}$ and $\boldsymbol{T} = C_{i2k2}$ depend only on elastic constants of the material. This eigenvalue problem was solved in [Ting 1996], and general expressions for the traction and displacement fields can be found therein. At this stage the following matrices are also defined:

$$\boldsymbol{L} = (\boldsymbol{R}^T + p\boldsymbol{T})\boldsymbol{A}, \quad \boldsymbol{B} = i\boldsymbol{A}\boldsymbol{L}^{-1},$$

where $\boldsymbol{B}$ is the surface admittance tensor of the material. It is also important, for further analysis, to introduce the bimaterial matrices $\boldsymbol{H}$ and $\boldsymbol{W}$:

$$\boldsymbol{H} = \boldsymbol{B}_{\mathrm{I}} + \overline{\boldsymbol{B}}_{\mathrm{II}}, \quad \boldsymbol{W} = \boldsymbol{B}_{\mathrm{I}} - \overline{\boldsymbol{B}}_{\mathrm{II}}, \tag{7}$$

where the subscript I or II determines which material the matrix relates to. It is important to note that, in the considered dynamic steady-state case, the matrices $\boldsymbol{A}$, $\boldsymbol{L}$, $\boldsymbol{B}$, $\boldsymbol{H}$, and $\boldsymbol{W}$ all depend on both the elastic constants for the materials and the crack speed, v.

The analysis performed in [Suo 1990] considered the static, homogeneous traction-free form of the physical problem shown in Figure 1, with continuous traction and displacement across the interface ($x_1 > 0$). Suo's work has been extended to the steady-state crack in [Yang et al. 1991] using the new coordinates x and y. Considering the traction-free condition, the following Riemann–Hilbert problem is satisfied along the negative portion of the real axis [Suo 1990]:

$$\boldsymbol{h}^+(x) + \overline{\boldsymbol{H}}^{-1}\boldsymbol{H}\boldsymbol{h}^-(x) = 0, \quad -\infty < x < 0. \tag{8}$$

Here, $\boldsymbol{h}(z)$ is a function found in the form

$$\boldsymbol{h}(z) = \boldsymbol{w} z^{-1/2+i\epsilon}.$$

The branch cut of $\boldsymbol{h}(z)$ is placed along the negative real axis. Combining this solution with (8) gives the eigenvalue problem

$$\overline{\boldsymbol{H}}\boldsymbol{w} = e^{2\pi\epsilon}\boldsymbol{H}\boldsymbol{w}, \tag{9}$$

which can be used to find ϵ and $\boldsymbol{w}$, both of which depend on the crack velocity [Yang et al. 1991].

For the positive part of the real axis the following expression for the physical traction was found in [Suo 1990]:

$$\boldsymbol{t}(x) = \boldsymbol{h}^+(x) + \overline{\boldsymbol{H}}^{-1}\boldsymbol{H}\boldsymbol{h}^-(x), \quad 0 < x < \infty. \tag{10}$$

Combining this with the results from (9), Suo found the following expression for the traction ahead of the crack tip:

$$\boldsymbol{t}(x) = \frac{1}{\sqrt{2\pi x}}\,\mathrm{Re}(K x^{i\epsilon}\boldsymbol{w}), \tag{11}$$

where $K = K_1 + iK_2$ is the complex stress intensity factor, and includes both mode I and mode II contributions to the traction.

The displacement jump across the crack, defined as $[\boldsymbol{u}] = \boldsymbol{u}(x, 0^+) - \boldsymbol{u}(x, 0^-)$, was also found in [Suo 1990] for $x < 0$:

$$[\boldsymbol{u}](x) = \left(\frac{2(-x)}{\pi}\right)^{\frac{1}{2}} \frac{(\boldsymbol{H} + \overline{\boldsymbol{H}})}{\cosh \pi\epsilon}\,\mathrm{Re}\left(\frac{K(-x)^{i\epsilon}\boldsymbol{w}}{1 + 2i\epsilon}\right). \tag{12}$$

For the physical problem with forces acting on the crack faces the asymptotic expansions of the physical traction and the jump in displacement across the interface, as $x \to 0$, can be written as follows [Morini et al. 2013]:

$$[\boldsymbol{u}](x) = \frac{(-x)^{1/2}}{\sqrt{2\pi}}\mathcal{U}(x)\boldsymbol{K} + \frac{(-x)^{3/2}}{\sqrt{2\pi}}\mathcal{U}(x)\boldsymbol{Y}_2 + \frac{(-x)^{5/2}}{\sqrt{2\pi}}\mathcal{U}(x)\boldsymbol{Y}_3 + \mathcal{O}((-x)^{7/2}), \tag{13}$$

$$\boldsymbol{t}(x) = \frac{x^{-1/2}}{2\sqrt{2\pi}}\mathcal{T}(x)\boldsymbol{K} + \frac{x^{1/2}}{2\sqrt{2\pi}}\mathcal{T}(x)\boldsymbol{Y}_2 + \frac{x^{3/2}}{2\sqrt{2\pi}}\mathcal{T}(x)\boldsymbol{Y}_3 + \mathcal{O}(x^{5/2}), \tag{14}$$

where $\boldsymbol{K} = [K, \overline{K}]$ and $\boldsymbol{Y}_i = [Y_i, \overline{Y}_i]$. The Y_i are constants derived in the same manner as the stress

intensity factor K in order to find further terms in the asymptotic expansions. The matrices $\mathcal{U}(x)$ and $\mathcal{T}(x)$ are represented as

$$\mathcal{U}(x) = \frac{2(\boldsymbol{H} + \overline{\boldsymbol{H}})}{\cosh \pi\epsilon}\left[\frac{\boldsymbol{w}(-x)^{i\epsilon}}{1+2i\epsilon}, \frac{\overline{\boldsymbol{w}}(-x)^{-i\epsilon}}{1-2i\epsilon}\right], \quad \mathcal{T}(x) = 2[\boldsymbol{w}x^{i\epsilon}, \overline{\boldsymbol{w}}x^{-i\epsilon}]. \tag{15}$$

An explicit formula for computing the stress intensity factor for symmetric loading was given in [Suo 1990]. It was shown that

$$\boldsymbol{K}^S = -\left(\frac{2}{\pi}\right)^{1/2} \cosh \pi\epsilon \int_{-\infty}^{0} (-x)^{-1/2-i\epsilon} \langle \boldsymbol{p}_1 \rangle(x)\, \mathrm{d}x, \tag{16}$$

where the vector $\langle \boldsymbol{p}_1 \rangle(x)$ is related to the applied traction $\boldsymbol{p}(x)$ in the following way:

$$\langle \boldsymbol{p}_1 \rangle = \frac{\overline{\boldsymbol{w}}^T \boldsymbol{H} \langle \boldsymbol{p} \rangle}{\overline{\boldsymbol{w}}^T \boldsymbol{H} \boldsymbol{w}}.$$

Note here that the work in [Suo 1990] only studied symmetric loading, which is why the formula above only shows the part of the stress intensity factor corresponding to the symmetric part of the loading $\langle \boldsymbol{p}_1 \rangle$. For symmetric loading the asymmetric contribution to the loading, $[\boldsymbol{p}_1]$, is equal to 0.

Another key component in the analysis of fracture mechanics is the determination of the energy release rate (ERR) when a unit area of interface is cracked. An expression was found for the ERR, denoted G, in [Irwin 1957]:

$$G = \frac{1}{2\Delta} \int_0^{\Delta} \boldsymbol{t}^T (\Delta - r)[\boldsymbol{u}](r)\, \mathrm{d}r, \tag{17}$$

where Δ is an arbitrary length scale. It was stated in [Yu and Suo 2000] that this equation can still be used with an arbitrary Δ as long as the crack is moving at subsonic speeds. It was shown in [Suo 1990], using (11) and (12), that the ERR can be written as

$$G = \frac{\overline{\boldsymbol{w}}^T (\boldsymbol{H} + \overline{\boldsymbol{H}}) \boldsymbol{w} |K|^2}{4 \cosh^2(\pi\epsilon)}. \tag{18}$$

The value of G will change as the crack moves at different speeds. This is one of the key features this paper will be studying, with the results shown in Section 5.

2.2. ***Weight functions.*** The weight function $\boldsymbol{U}$ is now defined in the same vein as in [Willis and Movchan 1995]. We now consider $\boldsymbol{U} = (U_1, U_2)^T$, the singular displacement field obtained in the problem where the steady-state crack occupies the region of the x-axis with $x > 0$. Thus $\boldsymbol{U}$ is discontinuous over the positive portion of the real axis. The symmetric and skew-symmetric parts of the weight function are given by

$$[\boldsymbol{U}](x) = \boldsymbol{U}(x, 0^+) - \boldsymbol{U}(x, 0^-), \tag{19}$$

$$\langle \boldsymbol{U} \rangle(x) = \tfrac{1}{2}(\boldsymbol{U}(x, 0^+) + \boldsymbol{U}(x, 0^-)). \tag{20}$$

The traction field associated with the displacement field, $\boldsymbol{U}$, is denoted by $\Upsilon = (\Upsilon_1, \Upsilon_2)^T$ and is taken to be continuous over the interface ($x < 0$); the zero traction condition is imposed on the crack faces.

Therefore, the following Riemann–Hilbert problem stands along the positive section of the real axis for this problem, as seen in [Morini et al. 2013]:

$$\boldsymbol{h}_+(x) + \overline{\boldsymbol{H}}^{-1}\boldsymbol{H}\boldsymbol{h}_-(x) = 0, \quad 0 < x < \infty. \tag{21}$$

A solution for $\boldsymbol{h}(z)$ is found in the form

$$\boldsymbol{h}(z) = \boldsymbol{v}z^{-3/2+i\epsilon}, \tag{22}$$

where the branch cut is now said to be along the positive x-axis. This gives the eigenvalue problem

$$\overline{\boldsymbol{H}}\boldsymbol{v} = e^{-2\pi\epsilon}\boldsymbol{H}\boldsymbol{v}. \tag{23}$$

$\boldsymbol{H}$ is positive-definite hermitian, and therefore it is clear, by comparing (23) with (9), that $\boldsymbol{v} = \overline{\boldsymbol{w}}$.

An expression for Υ along the negative real axis is given by

$$\Upsilon(x) = \boldsymbol{h}_+(x) + \overline{\boldsymbol{H}}^{-1}\boldsymbol{H}\boldsymbol{h}_-(x), \quad -\infty < x < 0. \tag{24}$$

Therefore the singular traction in the steady state has the form [Morini et al. 2013]

$$\Upsilon(x) = \frac{(-x)^{-3/2}}{\sqrt{2\pi}}\,\mathrm{Re}(R(-x)^{i\epsilon}\overline{\boldsymbol{w}}), \tag{25}$$

where $R = R_1 + iR_2$ is an arbitrary, complex number in a similar fashion as the stress intensity factor for the physical problem. By considering the results obtained for Υ when $\{R_1 = 1, R_2 = 0\}$ and $\{R_1 = 0, R_2 = 1\}$ it is possible to obtain two linearly independent vectors, and therefore a 2×2 matrix, representing Υ [Piccolroaz et al. 2009].

An expression relating the Fourier transform, defined as

$$\hat{f}(\chi) = \int_{-\infty}^{\infty} f(x)e^{i\chi x}\,\mathrm{d}x,$$

of the symmetric and skew-symmetric weight functions was found in [Morini et al. 2013] following from the work seen in [Piccolroaz et al. 2007]:

$$[\hat{\boldsymbol{U}}]^+(\chi) = \frac{1}{|\chi|}(i\,\mathrm{sign}(\chi)\mathrm{Im}(\boldsymbol{H}) - \mathrm{Re}(\boldsymbol{H}))\hat{\Upsilon}^-(\chi), \tag{26}$$

$$\langle\hat{\boldsymbol{U}}\rangle(\chi) = \frac{1}{2|\chi|}(i\,\mathrm{sign}(\chi)\mathrm{Im}(\boldsymbol{W}) - \mathrm{Re}(\boldsymbol{W}))\hat{\Upsilon}^-(\chi). \tag{27}$$

Here the superscripts $\pm$ denote whether the function is analytic in the upper or lower half-plane.

2.3. ***The Betti formula.*** It was mentioned previously that there are now two displacement fields to consider: the physical displacement, $\boldsymbol{u}$, and the singular displacement, $\boldsymbol{U}$. However, $\boldsymbol{U}$ is discontinuous across the x-axis for $x > 0$ whereas $\boldsymbol{u}$ is discontinuous across the x-axis for $x < 0$. Also considered is the traction associated with $\boldsymbol{U}$, given by Υ, which is continuous when $x < 0$, and the traction $\boldsymbol{t}$ associated with $\boldsymbol{u}$, which is continuous when $x > 0$.

It was shown in [Willis and Movchan 1995] that the Betti formula still holds for a steady-state crack in isotropic materials. Using the same method it can be shown that the Betti formula still holds for the moving coordinate system in anisotropic materials. Therefore, the following expressions are found along

the upper and lower parts of the real axis, respectively:

$$\int_{-\infty}^{\infty} \{\boldsymbol{U}^T(x'-x,0^+)\mathcal{R}\boldsymbol{\sigma}(x,0^+) - \Upsilon^T(x'-x,0^+)\mathcal{R}\boldsymbol{u}(x,0^+)\}\,\mathrm{d}x = 0, \tag{28}$$

$$\int_{-\infty}^{\infty} \{\boldsymbol{U}^T(x'-x,0^-)\mathcal{R}\boldsymbol{\sigma}(x,0^-) - \Upsilon^T(x'-x,0^-)\mathcal{R}\boldsymbol{u}(x,0^-)\}\,\mathrm{d}x = 0, \tag{29}$$

where

$$\mathcal{R} = \begin{pmatrix} -1 & 0 \\ 0 & 1 \end{pmatrix}.$$

The homogeneous case of (8) is now considered. Combined with the applied traction on the crack faces, $\boldsymbol{p}(x)$, we obtain for the traction

$$\boldsymbol{\sigma}(x, y=0^+) = \boldsymbol{p}^+(x) + \boldsymbol{t}(x), \quad \boldsymbol{\sigma}(x, y=0^-) = \boldsymbol{p}^-(x) + \boldsymbol{t}(x). \tag{30}$$

Subtracting (29) from (28) and using (30), along with the definition of the symmetric and skew-symmetric parts of the weight function, the following formula is obtained:

$$\int_{-\infty}^{\infty} \{[\boldsymbol{U}]^T(x'-x)\mathcal{R}\boldsymbol{t}(x) - \Upsilon^T(x'-x,0)\mathcal{R}[\boldsymbol{u}](x)\}\,\mathrm{d}x = -\int_{-\infty}^{\infty} \{[\boldsymbol{U}]^T(x'-x)\mathcal{R}\langle\boldsymbol{p}\rangle(x) + \langle\boldsymbol{U}\rangle^T(x'-x)\mathcal{R}[\boldsymbol{p}](x)\}\,\mathrm{d}x. \tag{31}$$

Here, $\langle\boldsymbol{p}\rangle$ and $[\boldsymbol{p}]$ refer to the symmetric and skew-symmetric parts of the loading, respectively.

Using the Fourier convolution theorem the following identity, which relates the Fourier transforms of the weight functions and the solutions of the physical problem, is obtained [Piccolroaz et al. 2007; Morini et al. 2013]:

$$[\hat{\boldsymbol{U}}]^{+T}\mathcal{R}\hat{\boldsymbol{t}}^+ - \hat{\Upsilon}^{-T}\mathcal{R}[\hat{\boldsymbol{u}}]^- = -[\hat{\boldsymbol{U}}]^{+T}\mathcal{R}\langle\hat{\boldsymbol{p}}\rangle - \langle\hat{\boldsymbol{U}}\rangle^T\mathcal{R}[\hat{\boldsymbol{p}}], \tag{32}$$

where the $\pm$ denotes whether the transform is analytic in the upper or lower half-plane.

Further work performed in [Piccolroaz et al. 2007] and [Morini et al. 2013], combining (26), (27), and (32), found an explicit expression for finding the stress intensity factor, $\boldsymbol{K}$, using the weight functions and the loading applied on the crack faces. The expression obtained was

$$\boldsymbol{K} = \frac{1}{2\pi i}\mathscr{Z}_1^{-1}\int_{-\infty}^{\infty} [\hat{\boldsymbol{U}}]^{+T}(\tau)\mathcal{R}\langle\hat{\boldsymbol{p}}\rangle(\tau) + \langle\hat{\boldsymbol{U}}\rangle^T(\tau)\mathcal{R}[\hat{\boldsymbol{p}}](\tau)\,\mathrm{d}\tau, \tag{33}$$

where $\mathscr{Z}_1$ is a constant matrix derived from the asymptotic representation of (32). It can be shown that both expressions for $\boldsymbol{K}$, (16) and (33), are equivalent when the loading considered is symmetric.

Following the method developed in [Piccolroaz et al. 2007] and [Morini et al. 2013] an expression for further asymptotic coefficients can be found depending on whether the applied loading is smooth and has a Fourier transform that vanishes at a fast enough rate at infinity. If this is the case the general expression for the asymptotic coefficients can be found using

$$\boldsymbol{Y}_j = \frac{1}{2\pi i}\mathscr{Z}_j^{-1}\int_{-\infty}^{\infty} \tau^{j-1}\{[\hat{\boldsymbol{U}}]^{+T}(\tau)\mathcal{R}\langle\hat{\boldsymbol{p}}\rangle(\tau) + \langle\hat{\boldsymbol{U}}\rangle^T(\tau)\mathcal{R}[\hat{\boldsymbol{p}}](\tau)\}\,\mathrm{d}\tau. \tag{34}$$

Here, $\mathscr{Z}_j$ is also derived from the asymptotic representation of (32) and is found in Section 4.

3. Steady-state weight functions for orthotropic bimaterials

In this section, expressions for the symmetric and skew-symmetric weight function matrices corresponding to a steady-state plane strain interfacial crack in orthotropic bimaterials are reported. Substituting the solution for $\boldsymbol{w}$ found in [Yang et al. 1991], and shown in the Appendix of this paper, into (25), and using the method used in [Piccolroaz et al. 2009], yields the following linearly independent traction vectors for $-\infty < x < 0$:

$$\Upsilon^1(x) = \frac{(-x)^{-3/2}}{2\sqrt{2\pi}} \begin{pmatrix} i[(-x)^{i\epsilon} - (-x)^{-i\epsilon}] \\ \sqrt{\dfrac{H_{11}}{H_{22}}}[(-x)^{i\epsilon} + (-x)^{-i\epsilon}] \end{pmatrix}, \tag{35}$$

$$\Upsilon^2(x) = \frac{(-x)^{-3/2}}{2\sqrt{2\pi}} \begin{pmatrix} -[(-x)^{i\epsilon} + (-x)^{-i\epsilon}] \\ i\sqrt{\dfrac{H_{11}}{H_{22}}}[(-x)^{i\epsilon} - (-x)^{-i\epsilon}] \end{pmatrix}, \tag{36}$$

where H_{11} and H_{22} are parameters depending on the crack tip speed and elastic constants of both considered materials. Explicit expressions for H_{11} and H_{22} have been introduced in [Yang et al. 1991] and are given in the Appendix. The branch cut for these vectors is situated along the positive real axis and polar coordinates with angle between -2π and 0 are taken. The Fourier transforms obtained are

$$\hat{\Upsilon}^{1-}(\chi) = \frac{(i\chi)^{1/2}\sqrt{2}}{(1+4\epsilon^2)\sqrt{\pi}} \begin{pmatrix} i\left[\left(-\frac{1}{2}-i\epsilon\right)\Gamma\left(\frac{1}{2}+i\epsilon\right)(i\chi)^{-i\epsilon} - \left(-\frac{1}{2}+i\epsilon\right)\Gamma\left(\frac{1}{2}-i\epsilon\right)(i\chi)^{i\epsilon}\right] \\ \sqrt{\dfrac{H_{11}}{H_{22}}}\left[\left(-\frac{1}{2}-i\epsilon\right)\Gamma\left(\frac{1}{2}+i\epsilon\right)(i\chi)^{-i\epsilon} + \left(-\frac{1}{2}+i\epsilon\right)\Gamma\left(\frac{1}{2}-i\epsilon\right)(i\chi)^{i\epsilon}\right] \end{pmatrix}, \tag{37}$$

$$\hat{\Upsilon}^{2-}(\chi) = \frac{(i\chi)^{1/2}\sqrt{2}}{(1+4\epsilon^2)\sqrt{\pi}} \begin{pmatrix} -\left[\left(-\frac{1}{2}-i\epsilon\right)\Gamma\left(\frac{1}{2}+i\epsilon\right)(i\chi)^{-i\epsilon} + \left(-\frac{1}{2}+i\epsilon\right)\Gamma\left(\frac{1}{2}-i\epsilon\right)(i\chi)^{i\epsilon}\right] \\ i\sqrt{\dfrac{H_{11}}{H_{22}}}\left[\left(-\frac{1}{2}-i\epsilon\right)\Gamma\left(\frac{1}{2}+i\epsilon\right)(i\chi)^{-i\epsilon} - \left(-\frac{1}{2}+i\epsilon\right)\Gamma\left(\frac{1}{2}-i\epsilon\right)(i\chi)^{i\epsilon}\right] \end{pmatrix}, \tag{38}$$

where $\Gamma(\cdot)$ is the gamma function and the branch cut of $\hat{\Upsilon}^-$ is situated along the positive imaginary axis. Note that the expressions (37) and (38) are written using a different representation than was used in [Morini et al. 2013]. The reason behind this will become clearer in Section 4.

The Fourier transforms (26) and (27) can now be computed, for $\chi \in \mathbb{R}$, with the expressions for $\boldsymbol{H}$ and $\boldsymbol{W}$ found in [Yang et al. 1991] and [Morini et al. 2013], respectively:

$$[\hat{\boldsymbol{U}}]^+(\chi) = \frac{1}{|\chi|} \begin{pmatrix} -H_{11} & -i\beta\,\mathrm{sign}(\chi)\sqrt{H_{11}H_{22}} \\ i\beta\,\mathrm{sign}(\chi)\sqrt{H_{11}H_{22}} & -H_{22} \end{pmatrix} \hat{\Upsilon}^-(\chi), \tag{39}$$

$$\langle\hat{\boldsymbol{U}}\rangle(\chi) = \frac{1}{2|\chi|} \begin{pmatrix} -\delta_1 H_{11} & i\gamma\,\mathrm{sign}(\chi)\sqrt{H_{11}H_{22}} \\ -i\gamma\,\mathrm{sign}(\chi)\sqrt{H_{11}H_{22}} & -\delta_2 H_{22} \end{pmatrix} \hat{\Upsilon}^-(\chi), \tag{40}$$

where the branch cuts are now situated along the negative imaginary axis. Here β, γ, δ_1, and δ_2 are all dimensionless parameters depending on the elastic coefficients of the bimaterial and the crack tip velocity [Yang et al. 1991]. Full expressions for both matrices, $\boldsymbol{H}$ and $\boldsymbol{W}$, are given in the Appendix, including full expressions for the parameters β, γ, δ_1, and δ_2. It can be clearly seen from the results of

[Yang et al. 1991] that β is of great importance when considering oscillations near the crack tip as $\epsilon = 0$ when $\beta = 0$.

4. Evaluation of the coefficients in the asymptotic expansion of the displacement and stress fields for the steady-state crack

4.1. ***Determination of the stress intensity factor.*** It is now possible to develop a method in order to find the stress intensity factor for an orthotropic bimaterial, similar to that seen for the static crack in [Morini et al. 2013]. In the case of orthotropic materials, the matrix $\mathcal{T}(x)$ in (14) is given by

$$\mathcal{T}(x) = \begin{pmatrix} -ix^{i\epsilon} & ix^{-i\epsilon} \\ \sqrt{\dfrac{H_{11}}{H_{22}}}x^{i\epsilon} & \sqrt{\dfrac{H_{11}}{H_{22}}}x^{-i\epsilon} \end{pmatrix}. \tag{41}$$

Note that this result is equivalent to (15) with the known value of $\boldsymbol{w}$ inserted. The Fourier transform of this expansion is computed in order to find the asymptotic expansion as $\chi \to \infty$, with $\mathrm{Im}(\chi) \in (0, \infty)$. The result is

$$\hat{t}(\chi) = \frac{(-i\chi)^{-1/2}}{2\sqrt{2\pi}}\mathfrak{T}_1(\chi)\boldsymbol{K} + \frac{(-i\chi)^{-3/2}}{2\sqrt{2\pi}}\mathfrak{T}_2(\chi)\boldsymbol{Y} + \mathbb{O}((\chi)^{-5/2}), \tag{42}$$

where

$$\mathfrak{T}_1(\chi) = \begin{pmatrix} -i(-i\chi)^{-i\epsilon}\Gamma\left(\frac{1}{2}+i\epsilon\right) & i(-i\chi)^{i\epsilon}\Gamma\left(\frac{1}{2}-i\epsilon\right) \\ \sqrt{\dfrac{H_{11}}{H_{22}}}(-i\chi)^{-i\epsilon}\Gamma\left(\frac{1}{2}+i\epsilon\right) & \sqrt{\dfrac{H_{11}}{H_{22}}}(-i\chi)^{i\epsilon}\Gamma\left(\frac{1}{2}-i\epsilon\right) \end{pmatrix}, \tag{43}$$

$$\mathfrak{T}_2(\chi) = \begin{pmatrix} -i(-i\chi)^{-i\epsilon}\Gamma\left(\frac{3}{2}+i\epsilon\right) & i(-i\chi)^{i\epsilon}\Gamma\left(\frac{3}{2}-i\epsilon\right) \\ \sqrt{\dfrac{H_{11}}{H_{22}}}(-i\chi)^{-i\epsilon}\Gamma\left(\frac{3}{2}+i\epsilon\right) & \sqrt{\dfrac{H_{11}}{H_{22}}}(-i\chi)^{i\epsilon}\Gamma\left(\frac{3}{2}-i\epsilon\right) \end{pmatrix}. \tag{44}$$

These expressions differ from those seen in [Morini et al. 2013] and [Piccolroaz et al. 2007] in that they incorporate the different branch cut used in this paper. It is now possible to find the asymptotic expansion of the members of Betti's identity from (32), using expressions (39) and (40), as $\chi \to \infty$:

$$[\hat{\boldsymbol{U}}]^{+T}\mathcal{R}\hat{\boldsymbol{t}}^{+} = \chi^{-1}\mathscr{Z}_1\boldsymbol{K} + \chi^{-2}\mathscr{Z}_2\boldsymbol{Y}_2 + \chi^{-3}\mathscr{Z}_3\boldsymbol{Y}_3 + \mathbb{O}(\chi^{-4}), \quad \text{where } \mathrm{Im}(\chi) \in (0, \infty), \tag{45}$$

$$\hat{\Upsilon}^{-T}\mathcal{R}[\hat{\boldsymbol{u}}]^{-} = \chi^{-1}\mathscr{Z}_1\boldsymbol{K} + \chi^{-2}\mathscr{Z}_2\boldsymbol{Y}_2 + \chi^{-3}\mathscr{Z}_3\boldsymbol{Y}_3 + \mathbb{O}(\chi^{-4}), \quad \text{where } \mathrm{Im}(\chi) \in (-\infty, 0). \tag{46}$$

The matrices $\mathscr{Z}_1$ and $\mathscr{Z}_2$ are given by

$$\mathscr{Z}_1 = -\frac{H_{11}}{4s^{+}s^{-}(1+4\epsilon^2)}\begin{pmatrix} -\dfrac{(\beta-1)(1-2i\epsilon)}{E^2} & E^2(\beta+1)(1+2i\epsilon) \\ \dfrac{i(\beta-1)(1-2i\epsilon)}{E^2} & iE^2(\beta+1)(1+2i\epsilon) \end{pmatrix},$$

$$\mathscr{Z}_2 = -\frac{H_{11}}{4(1+4\epsilon^2)}\begin{pmatrix} -\dfrac{(\beta-1)(1-2i\epsilon)}{g^{+}s^{-}E^2} & \dfrac{E^2(\beta+1)(1+2i\epsilon)}{s^{+}g^{-}} \\ \dfrac{i(\beta-1)(1-2i\epsilon)}{g^{+}s^{-}E^2} & \dfrac{iE^2(\beta+1)(1+2i\epsilon)}{s^{+}g^{-}} \end{pmatrix},$$

where

$$E = e^{\epsilon(\pi/2)}, \quad s^{\pm} = \frac{(1+i)\sqrt{\pi}}{2\Gamma\left(\frac{1}{2} \pm i\epsilon\right)}, \quad g^{\pm} = \frac{(1-i)\sqrt{\pi}}{2\Gamma\left(\frac{3}{2} \pm i\epsilon\right)}.$$

Following the method of Morini et al. [2013], (32) is rewritten as

$$\boldsymbol{\psi}^{+}(\chi) - \boldsymbol{\psi}^{-}(\chi) = -[\hat{\boldsymbol{U}}]^{+T}\mathcal{R}\langle\hat{\boldsymbol{p}}\rangle - \langle\hat{\boldsymbol{U}}\rangle^{T}\mathcal{R}[\hat{\boldsymbol{p}}]. \tag{47}$$

Using the Plemelj formula it is possible to find $\boldsymbol{\psi}^{\pm}(\chi)$ using the formula

$$\boldsymbol{\psi}^{\pm}(\chi) = \frac{1}{2\pi i}\int_{-\infty}^{\infty} \frac{\boldsymbol{\psi}(\tau)}{\tau - \chi}\,\mathrm{d}\tau, \tag{48}$$

where $\boldsymbol{\psi}(\tau) = -[\hat{\boldsymbol{U}}]^{+T}(\tau)\mathcal{R}\langle\hat{\boldsymbol{p}}\rangle(\tau) - \langle\hat{\boldsymbol{U}}\rangle^{T}(\tau)\mathcal{R}[\hat{\boldsymbol{p}}](\tau)$. The solution of (47) is given by

$$\begin{aligned} [\hat{\boldsymbol{U}}]^{+T}\mathcal{R}\hat{\boldsymbol{t}}^{+} &= \boldsymbol{\psi}^{+}, \quad \text{where } \mathrm{Im}(\chi) \in (0, \infty), \\ \hat{\Upsilon}^{-T}\mathcal{R}[\hat{\boldsymbol{u}}]^{-} &= \boldsymbol{\psi}^{-}, \quad \text{where } \mathrm{Im}(\chi) \in (-\infty, 0). \end{aligned}$$

The asymptotic expansion of the Plemelj formula as $\chi \to \infty^{\pm}$ is given by

$$\boldsymbol{\psi}^{\pm}(\chi) = \frac{1}{2\pi i}\int_{-\infty}^{\infty} \frac{\boldsymbol{\psi}(\tau)}{\tau - \chi}\,\mathrm{d}\tau = \chi^{-1}\boldsymbol{V}_1^{\pm} + \chi^{-2}\boldsymbol{V}_2^{\pm} + \mathbb{O}(\chi^{-3}). \tag{49}$$

Comparing the terms of this asymptotic expansion with the terms of the expansions (45) and (46) it is clear that $\boldsymbol{V}_j^{\pm} = \mathscr{L}_j\boldsymbol{Y}_j$, where $\boldsymbol{Y}_1 = \boldsymbol{K}$. Using (49) it is easily seen that the stress intensity factor, $\boldsymbol{K}$, is given by

$$\boldsymbol{K} = \lim_{\chi\to\infty^{\pm}} \frac{1}{2\pi i}\mathscr{L}_1^{-1}\int_{-\infty}^{\infty} \frac{\chi(-[\hat{\boldsymbol{U}}]^{+T}(\tau)\mathcal{R}\langle\hat{\boldsymbol{p}}\rangle(\tau) - \langle\hat{\boldsymbol{U}}\rangle^{T}(\tau)\mathcal{R}[\hat{\boldsymbol{p}}](\tau))}{\tau - \chi}\,\mathrm{d}\tau, \tag{50}$$

where the explicit expression for $\mathscr{L}_1^{-1}$ is given by

$$\mathscr{L}_1^{-1} = \frac{2s^{+}s^{-}(1+4\epsilon^2)}{H_{11}}\begin{pmatrix} \dfrac{E^2}{(\beta-1)(1-2i\epsilon)} & \dfrac{iE^2}{(\beta-1)(1-2i\epsilon)} \\ -\dfrac{1}{(\beta+1)(1+2i\epsilon)E^2} & \dfrac{i}{(\beta+1)(1+2i\epsilon)E^2} \end{pmatrix}.$$

Assuming that the loading disappears in the region of the crack tip the limit in (50) exists and therefore the general expression for the stress intensity factor, $\boldsymbol{K}$, for the steady state is identical to that found in [Morini et al. 2013] (see (33)).

Now that an expression for the stress intensity factor has been found it is possible to determine the energy release rate (ERR). Using (18) the following expression is obtained for the ERR in orthotropic materials:

$$G = \tfrac{1}{4}H_{11}(1-\beta^2)|K|^2. \tag{51}$$

4.2. ***General expression for the coefficients of the higher-order terms.*** Using the asymptotic expansions (45) and (46) and the corresponding terms of (49) a general expression for the j-th coefficient of the asymptotic expansions, $\boldsymbol{Y}_i$, is found

$$\boldsymbol{V}_j^{\pm} = \lim_{\chi\to\infty^{\pm}}\left[\frac{\chi^j(-1)^{j-1}}{2\pi i(j-1)!}\int_{-\infty}^{\infty}\boldsymbol{\psi}(\tau)\frac{\mathrm{d}^{j-1}}{\mathrm{d}\chi^{j-1}}\Big(\frac{\chi^{j-1}}{\tau-\chi}\Big)\,\mathrm{d}\tau\right]. \tag{52}$$

This gives a general expression for the coefficients of the asymptotic expansion of the displacement and stress fields as

$$\boldsymbol{Y}_j = \lim_{\chi\to\infty^{\pm}}\frac{1}{2\pi i}\mathscr{L}_j^{-1}\int_{-\infty}^{\infty}\tau^{j-1}([\hat{\boldsymbol{U}}]^{+T}(\tau)\mathscr{R}\langle\hat{\boldsymbol{p}}\rangle(\tau)+\langle\hat{\boldsymbol{U}}\rangle^{T}(\tau)\mathscr{R}[\hat{\boldsymbol{p}}](\tau))\Big(\frac{\chi}{\chi-\tau}\Big)^{j}\mathrm{d}\tau. \tag{53}$$

If the loading is applied in such a way that the limit exists it is clearly seen that (53) is identical to (34). The limit in (53) can only be computed directly for $j \geq 2$ if the loading is given by a particularly smooth function which is therefore differentiable. However, this paper considers a general loading system in which case (34) cannot always be used. An example of loading for which (34) cannot be used is when point forces are applied on the crack faces [Piccolroaz et al. 2009]. To find further asymptotic terms, for arbitrary loading, an alternate method must be used.

As the function $\boldsymbol{p}$ only exists on the negative real x-axis its Fourier transform is analytic in the lower half χ-plane. Therefore, $[\hat{\boldsymbol{p}}]$ and $\langle\hat{\boldsymbol{p}}\rangle$ are also analytic in the lower half-plane. As long as the applied loading $\boldsymbol{p}$ vanishes within a region of the crack tip it is clearly seen that $[\hat{\boldsymbol{p}}]$ and $\langle\hat{\boldsymbol{p}}\rangle$ decay exponentially as χ tends to $-i\infty$. It is also known that both $[\hat{\boldsymbol{U}}]^{+}$ and $\langle\hat{\boldsymbol{U}}\rangle$ are analytic in the lower half-plane apart from the negative imaginary axis.

For computing $\boldsymbol{Y}_j$ the contour of integration shown in Figure 2 is used. However, due to exponential decay as χ goes to $-i\infty$, $L_{-\infty}$ and L_{∞} do not contribute to the total integral. Equation (53) now becomes

$$\boldsymbol{Y}_j = \lim_{\chi\to\infty^{\pm}}\left(-\frac{1}{2\pi i}\mathscr{L}_j^{-1}\left[\int_{\tilde{L}_l}\tau^{j-1}\boldsymbol{\psi}(\tau)\Big(\frac{\chi}{\chi-\tau}\Big)^{j}\mathrm{d}\tau-\int_{\tilde{L}_r}\tau^{j-1}\boldsymbol{\psi}(\tau)\Big(\frac{\chi}{\chi-\tau}\Big)^{j}\mathrm{d}\tau\right]\right). \tag{54}$$

The limit of (54) can be taken to give

$$\boldsymbol{Y}_j = -\frac{1}{2\pi i}\mathscr{L}_j^{-1}\int_{-i\infty}^{0}\tau^{j-1}[\boldsymbol{\psi}(\tau)]\,\mathrm{d}\tau, \tag{55}$$

where $[\boldsymbol{\psi}(\tau)]$ refers to the jump of the function $\boldsymbol{\psi}$ over the negative imaginary axis.

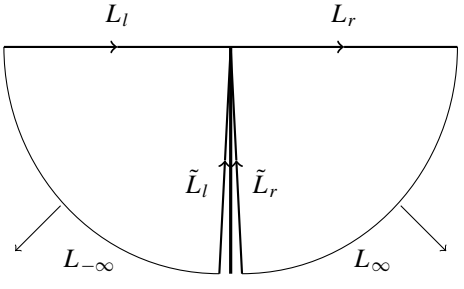

Figure 2. Integration shift in the χ-plane.

The expression (55) can be simplified further by considering the continuity of (39) and (40). The first term in both equations is analytic in the lower half-plane and therefore continuous over the negative imaginary axis. For this reason they do not contribute to the general expression for the asymptotic coefficients, (55). Therefore, (55) simplifies to give

$$\boldsymbol{Y}_j = -\frac{1}{2\pi i}\mathscr{L}_j^{-1}\int_{-i\infty}^{0}\tau^{j-1}[\boldsymbol{\phi}(\tau)]\,\mathrm{d}\tau, \tag{56}$$

where $\boldsymbol{\phi}(\tau)$ is given by

$$\boldsymbol{\phi}(\tau) = \frac{\mathrm{Re}(\boldsymbol{H})\{\hat{\Upsilon}^-(\tau)\mathscr{R}\langle\hat{\boldsymbol{p}}\rangle(\tau)\}}{|\tau|} + \frac{\mathrm{Re}(\boldsymbol{W})\{\hat{\Upsilon}^-(\tau)\mathscr{R}[\hat{\boldsymbol{p}}](\tau)\}}{2|\tau|}.$$

5. Specific examples

Specific examples for computing the stress intensity factors for orthotropic materials are now considered. Firstly, the loading on the crack faces is given by a point force of magnitude F acting perpendicular to the upper crack face a distance a behind the crack tip and two point forces, both of magnitude $F/2$, acting perpendicular to the lower crack face a distance b away from the point force acting upon the upper crack face. The loading moves at the same speed and in the same direction that the crack is propagating. This example is shown in Figure 3. The forces are represented mathematically using the Dirac delta function [Piccolroaz et al. 2009]:

$$p_+(x) = -F\delta(x+a), \quad p_-(x) = -\frac{F}{2}\delta(x+a+b) - \frac{F}{2}\delta(x+a-b). \tag{57}$$

It is now possible to decompose the loading into its symmetric and skew-symmetric components:

$$\begin{aligned}\langle p\rangle(x) &= \frac{1}{2}[p_+(x)+p_-(x)] = -\frac{F}{2}\delta(x+a) - \frac{F}{4}\delta(x+a-b) - \frac{F}{4}\delta(x+a-b),\\ [p](x) &= p_+(x) - p_-(x) = -F\delta(x+a) + \frac{F}{2}\delta(x+a+b) + \frac{F}{2}\delta(x+a-b).\end{aligned} \tag{58}$$

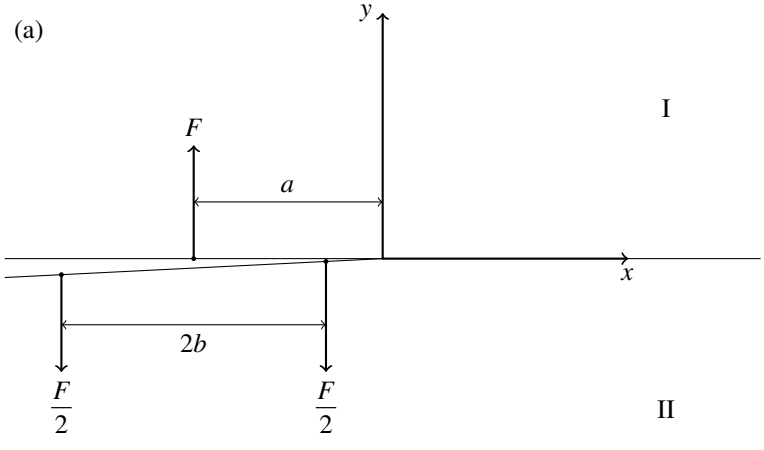

Figure 3. Mode I-dominant loading.

In order to compute the stress intensity factors the Fourier transforms of the skew-symmetric and symmetric parts of the loading are required. These are given by

$$\langle \hat{p} \rangle(\chi) = -\frac{F}{2} e^{-i\chi a} - \frac{F}{4} e^{-i\chi(a+b)} - \frac{F}{4} e^{-i\chi(a-b)}, \tag{59}$$

$$[\hat{p}](\chi) = -F e^{-i\chi a} + \frac{F}{2} e^{-i\chi(a+b)} + \frac{F}{2} e^{-i\chi(a-b)}. \tag{60}$$

It is now possible to compute expressions for the first and second-order asymptotic coefficients, $\boldsymbol{K}$ and $\boldsymbol{Y}_2$, using expressions (50) and (56), respectively.

To find an expression for $\boldsymbol{K}$ (50) is used, which is identical to using the dynamic equivalent of (33). The solution is split into parts corresponding to the symmetric and antisymmetric parts of the loading, denoted K^S and K^A, respectively:

$$K^S_{(a)} = F \frac{E^2}{(1-\beta)} \sqrt{\frac{H_{22}}{H_{11}}} \sqrt{\frac{2}{\pi}} \Lambda(1, a, b, \epsilon), \quad K^A_{(a)} = F \frac{E^2 \delta_2}{(1-\beta)} \sqrt{\frac{H_{22}}{H_{11}}} \sqrt{\frac{2}{\pi}} \Xi(1, a, b, \epsilon), \tag{61}$$

where

$$\Lambda(c, a, b, \epsilon) = a^{-c/2-i\epsilon} \left[\tfrac{1}{2} + \tfrac{1}{4}(1 + b/a)^{-c/2-i\epsilon} + \tfrac{1}{4}(1 - b/a)^{-c/2-i\epsilon} \right],$$

$$\Xi(c, a, b, \epsilon) = a^{-c/2-i\epsilon} \left[\tfrac{1}{2} - \tfrac{1}{4}(1 + b/a)^{-c/2-i\epsilon} - \tfrac{1}{4}(1 - b/a)^{-c/2-i\epsilon} \right].$$

Regarding higher-order asymptotic coefficients for the loading shown in Figure 3, the alternate method developed in Section 4.2 must be used. Once again the coefficient is split into symmetric and antisymmetric parts. The second-order term is given by

$$Y^S_{2(a)} = F \frac{E^2}{(\beta-1)} \sqrt{\frac{H_{22}}{H_{11}}} \sqrt{\frac{2}{\pi}} \Lambda(3, a, b, \epsilon), \quad Y^A_{2(a)} = F \frac{E^2 \delta_2}{(\beta-1)} \sqrt{\frac{H_{22}}{H_{11}}} \sqrt{\frac{2}{\pi}} \Xi(3, a, b, \epsilon). \tag{62}$$

A different configuration has also been considered. This other point loading system consists of point forces acting on the crack faces at the same points as previously considered but the forces are now running parallel to the crack, as opposed to the perpendicular system shown in Figure 3. This different loading is shown in Figure 4.

For this loading the following expressions are found for the symmetric and antisymmetric parts of the stress intensity factors:

$$K^S_{(b)} = i F \frac{E^2}{(1-\beta)} \sqrt{\frac{2}{\pi}} \Lambda(1, a, b, \epsilon), \quad K^A_{(b)} = i F \frac{E^2 \delta_1}{(1-\beta)} \sqrt{\frac{2}{\pi}} \Xi(1, a, b, \epsilon). \tag{63}$$

Using the method developed in Section 4.2, the symmetric and antisymmetric components of the second-order asymptotic coefficient are found:

$$Y^S_{2(b)} = i F \frac{E^2}{(\beta-1)} \sqrt{\frac{2}{\pi}} \Lambda(3, a, b, \epsilon), \quad Y^A_{2(b)} = i F \frac{E^2 \delta_1}{(\beta-1)} \sqrt{\frac{2}{\pi}} \Xi(3, a, b, \epsilon). \tag{64}$$

Having computed expressions for the stress intensity factors it is now possible to calculate the ERR for two given materials. The velocity is normalized by dividing by c_R, the lowest of the two Rayleigh wave speeds for the given materials. This is done because the Rayleigh wave speed is a limiting velocity

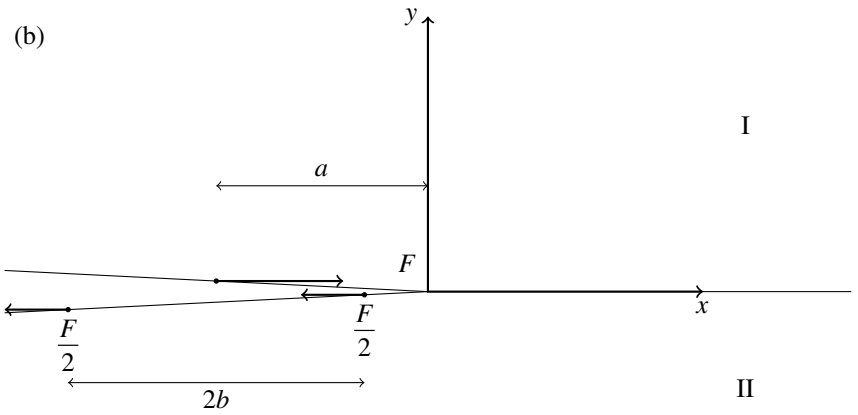

Figure 4. Mode II-dominant loading.

for which the steady-state coordinate system can be used. In the results shown the ERR is normalized as $GC_{66}^{(1)}/F^2$. Here, $C_{66}^{(1)}$ is taken as the value of C_{66} for the material above the crack. In all figures in this paper graphs labeled (a) correspond to the mode I-dominant loading whereas those labeled (b) refer to the case with mode II-dominant loading. For the purpose of calculations, a is set as 1.

Material I is the piezoceramic barium titanate. Information on this material has been obtained from [Geis et al. 2004] which states that the material is transverse isotropic, which is a subgroup of orthotropic materials. Material II is set as monocrystalline aluminum, with a cubic structure, where the material parameters have been obtained from [Bower 2009]. The properties of these materials are shown in Table 1. Using the method outlined in the Appendix it can be shown that the Rayleigh wave speed of barium titanate is $1{,}771\,\mathrm{m\,s^{-1}}$ while for aluminum it is $2{,}941\,\mathrm{m\,s^{-1}}$. Therefore the normalizing velocity, c_R, used is that of barium titanate.

Figure 5 shows the variation of the normalized ERR, as a function of the velocity, for both loadings considered. Figures 6 and 7 illustrate the symmetric and antisymmetric contributions to the ERR, corresponding to K^S and K^A, respectively. Both G^S and G^A are normalized by the total ERR G, which is associated with $K = K^S + K^A$.

It can be observed in Figure 5 that the ERR increases as the velocity increases and tends towards infinity as the velocity approaches the Rayleigh wave speed. This behavior is observed regardless of the asymmetry of the loading acting on the crack faces. It is important to note that, as velocity increases, asymmetry gives a larger ERR; therefore it can be said that symmetric loading is more energetically beneficial than any asymmetric load.

Figures 6 and 7 show that for $b/a = 0$, when both loadings become symmetric, $G^S/G = 1$ and $G^A/G = 0$; therefore, the ERR only consists of its symmetric part, regardless of velocity, which agrees

Material	C_{11} (GPa)	C_{22} (GPa)	C_{12} (GPa)	C_{66} (GPa)	ρ ($\mathrm{kg\,m^{-3}}$)
I. Barium titanate	120.3	120.3	75.2	21.0	6,020
II. Aluminum	107.3	107.3	60.9	28.3	2,700

Table 1. Material properties.

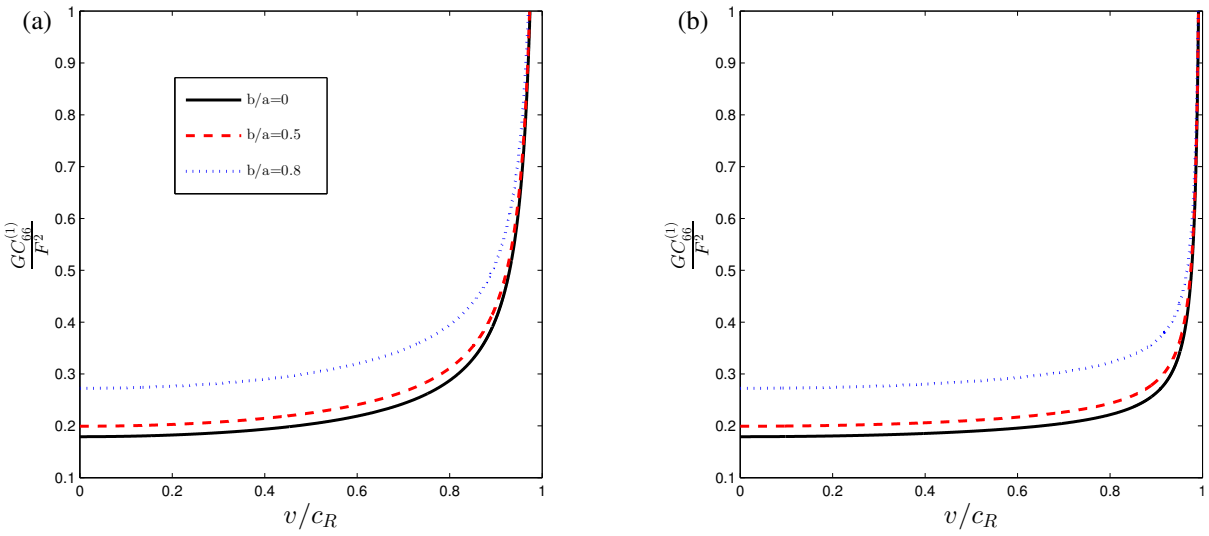

Figure 5. The normalized ERR, as a function of the velocity, for different positions of the self-balanced point forces applied to the crack surfaces, described by the ratio b/a.

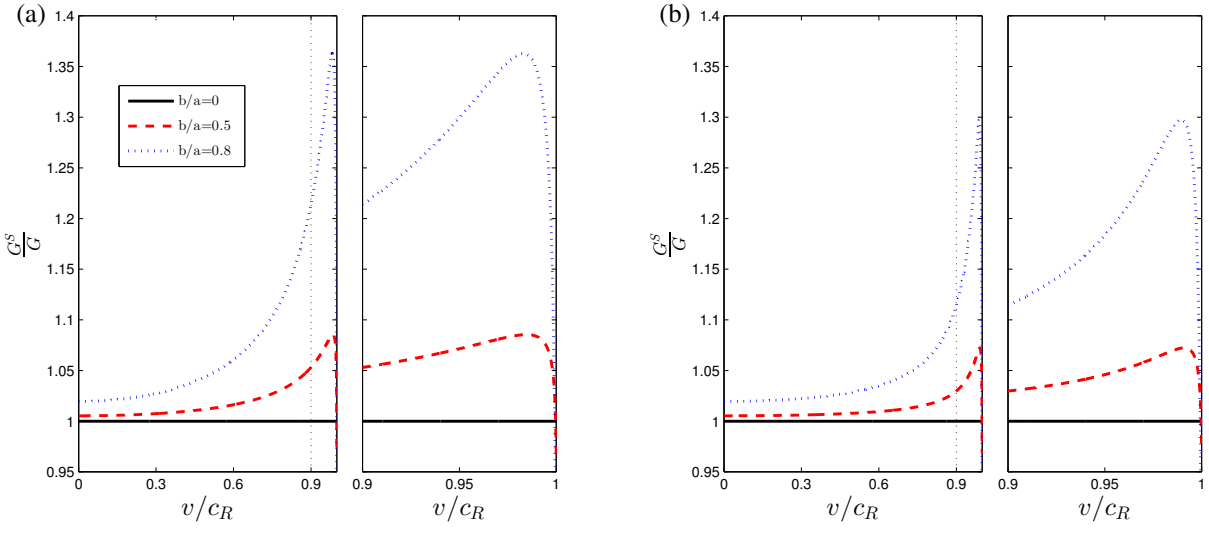

Figure 6. The normalized symmetric part of the ERR, as a function of the velocity, for different positions of the self-balanced point forces applied to the crack surfaces, described by the ratio b/a.

with the results found for isotropic and anisotropic bimaterials in [Piccolroaz et al. 2009] and [Morini et al. 2013]. When asymmetry is introduced into the loading it is observed that the symmetric contribution to the ERR is higher than the total ERR and the ratio increases as the velocity increases. Upon approaching the Rayleigh wave speed there is an unexpected sharp decrease in the ratio G^S/G. This effect should be studied further by performing experiments on crack propagation at near-Rayleigh speeds.

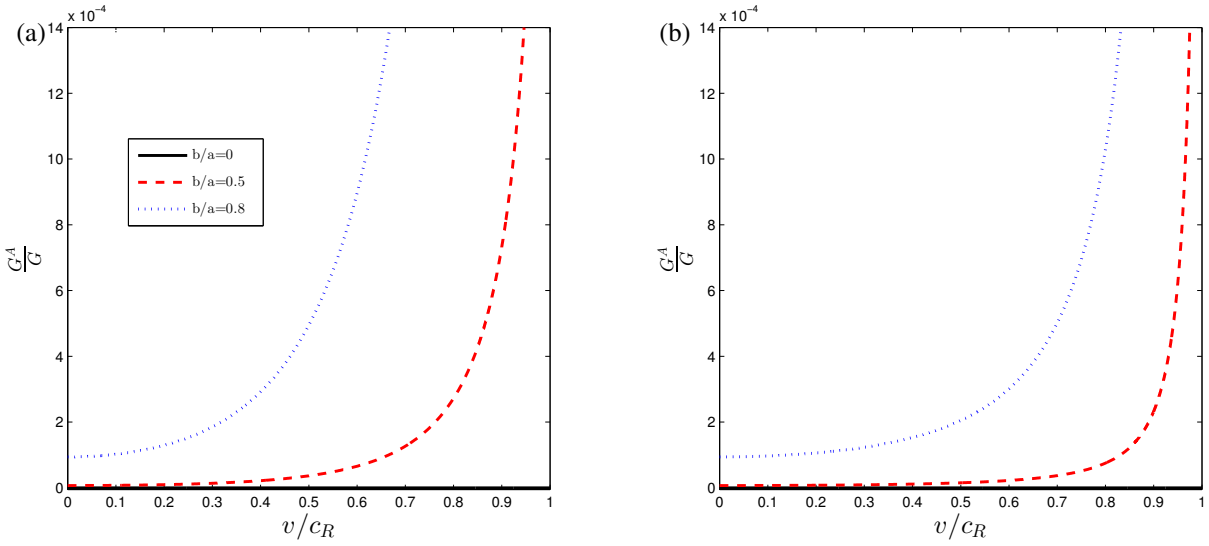

Figure 7. The normalized antisymmetric part of the ERR, as a function of the velocity, for different positions of the self-balanced point forces applied to the crack surfaces, described by the ratio b/a.

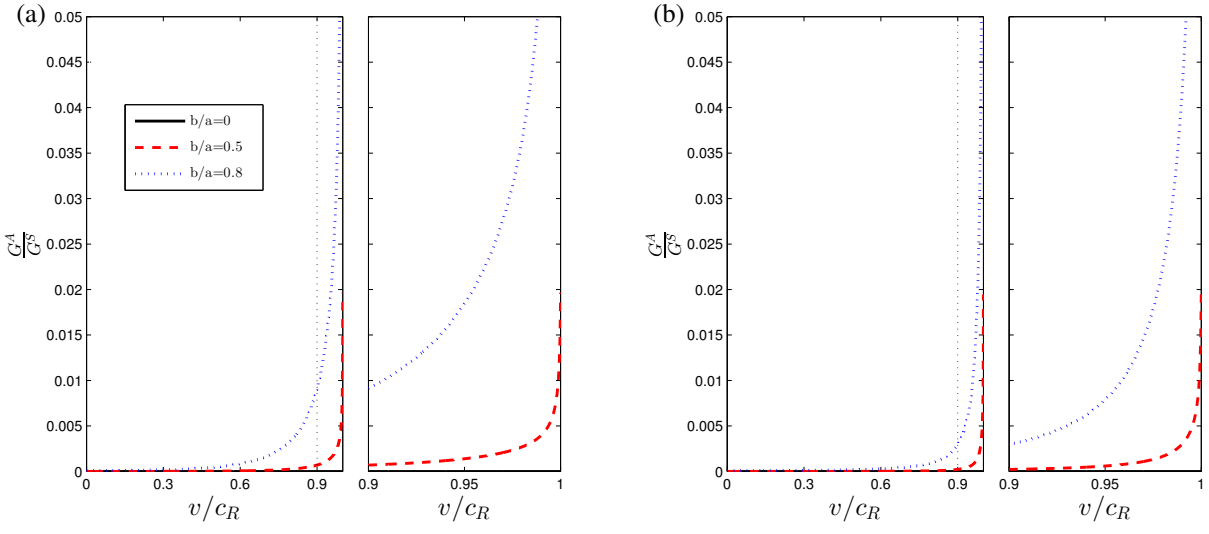

Figure 8. The ratio of antisymmetric and symmetric parts of the ERR, as a function of the velocity, for different positions of the self-balanced point forces applied to the crack surfaces, described by the ratio b/a.

In comparison to the symmetric contribution shown in Figure 6, the asymmetric part of the ERR, illustrated in Figure 7, is very small, in particular for low velocities. As the velocity starts to increase the asymmetric contribution to G becomes larger. This result is supported by Figure 8, showing the ratio G^A/G^S, which also shows an increased contribution by the asymmetric part of the loading at higher velocities.

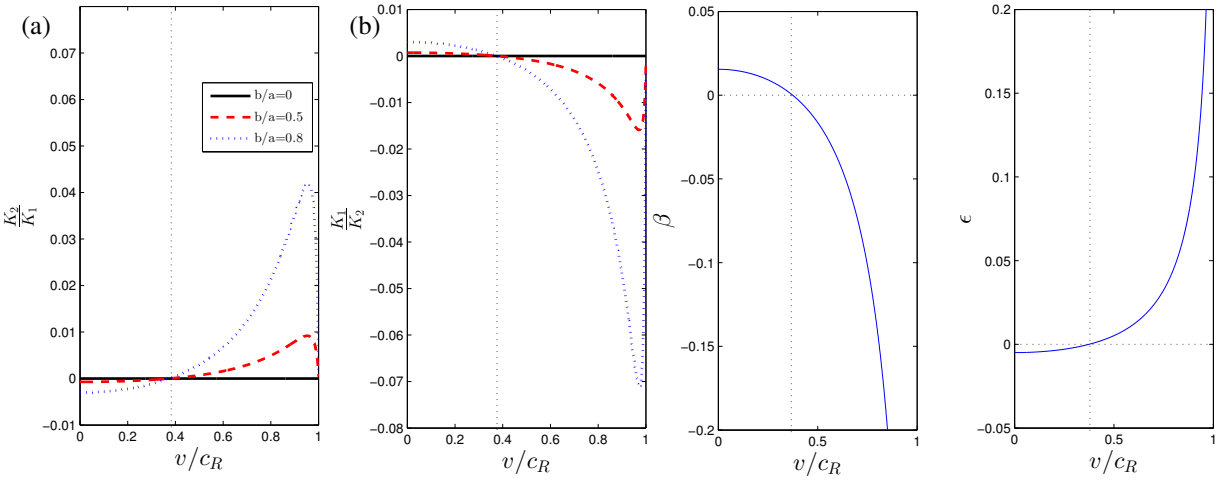

Figure 9. The ratios K_2/K_1 and K_1/K_2 for the mode I and mode II loadings, respectively. The graphs of β and ϵ, as functions of velocity, are also shown.

The dependence of the stress intensity factor, K, on the normalized crack tip speed is illustrated in Figure 9. The first graph shows the ratio K_2/K_1 for mode 1-dominant loading. Here, K_1 and K_2 are the mode 1 and 2 contributions to the stress intensity factor, respectively. For symmetric loading there is no mode 2 contribution to K, due to the fact that there is only mode 1 opening of the crack. It is important to observe that if asymmetry is introduced, for all values of b/a, there exists a velocity at which K_2 changes sign. The second image in Figure 9 shows a similar result for the mode 2-dominant loading considering the ratio K_1/K_2. In this case, it is the K_1 component which changes sign. The velocity at which this change takes place is the same for both types of loading and does not depend on the asymmetry. This velocity corresponds to the value of the crack tip speed at which the Dundurs parameter, β, vanishes. This characteristic velocity can be found by solving the algebraic equation $\beta(v) = 0$ and depends only on the elastic properties of the materials and the speed at which the crack is propagating; the asymmetry of the load does not affect the value at which the stress intensity factors have a change in sign. It is also clear from (A.7) that when β vanishes the oscillatory term, ϵ, vanishes; this has also been shown in Figure 9. This agrees with the obtained results as, when $\epsilon = 0$, it can be observed that (61) consists only of real terms and (63) only has imaginary components.

It can be said that, when the crack tip speed reaches this characteristic value of the velocity associated with $\beta = 0$, the propagation should continue along the interface in a straight line. Instead, when neither K_1 or K_2 is 0 there is a possibility of kinking or branching of the propagation. Increased magnitudes of the ratios considered in Figure 9 lead to an increased probability of crack redirection. As the velocity increases the ratios exhibit this behavior, which explains why straight propagation along the interface is unlikely for high crack speeds. These results are in agreement with many theoretical and experimental studies which have demonstrated that there exists a specific sub-Rayleigh velocity which is related to the stability of the crack propagation [Obrezanova et al. 2002a; 2002b].

The behavior of the stress intensity factor is also observed in Figure 10 for different materials in the lower half-plane. The asymmetry of the load was fixed at $b/a = 0.8$. The results in these graphs show that the previously mentioned speed at which the direction of the crack propagation changes does not

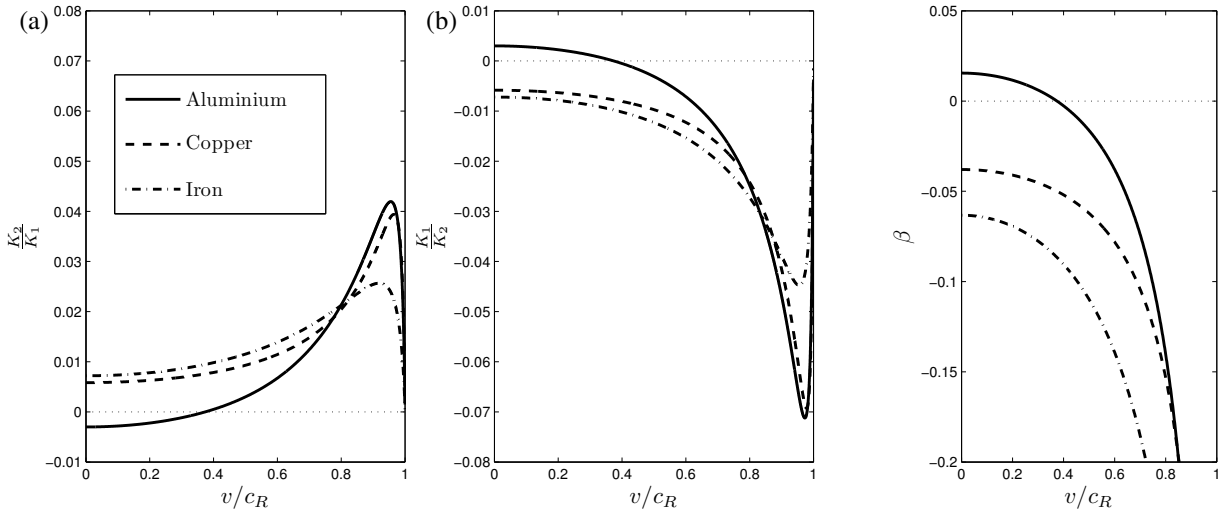

Figure 10. The change in behavior of the crack propagation when the material below the crack is changed, for fixed asymmetry of the loading.

exist for all bimaterials. This is due to the fact that there does not always exist a velocity at which $\beta = 0$. For bimaterials which do not have this characteristic velocity the change of behavior of the crack propagation would not be expected. However, the increased probability of kinking/branching at higher velocities is still observed.

Figure 11 shows the variation in the real and imaginary parts of the normalized stress intensity factor when $v = 0$ and the asymmetry of the loading is varied. The loading considered here is mode I-dominant

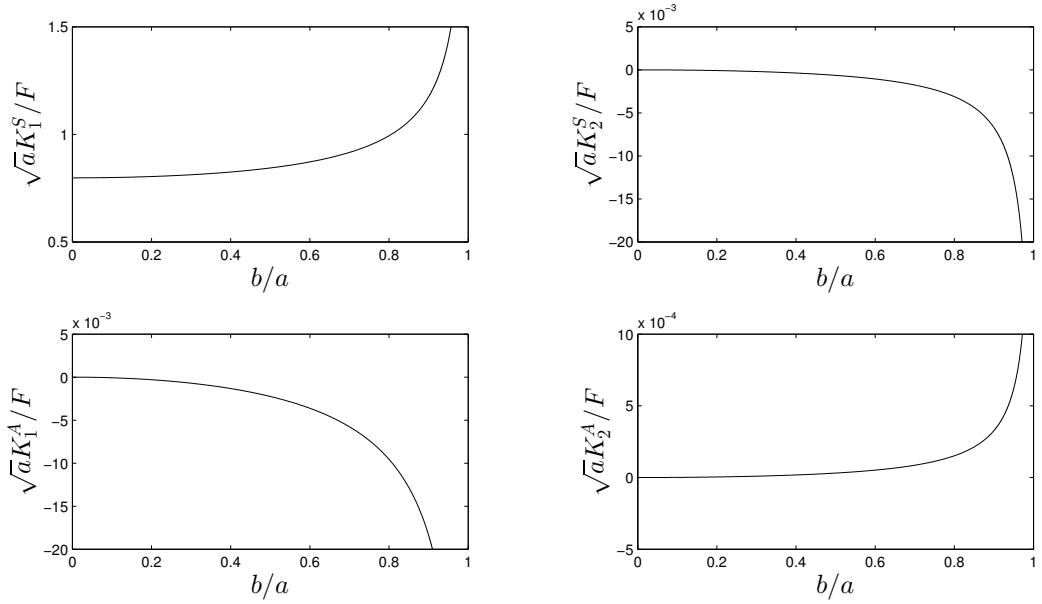

Figure 11. The normalized components of K^S and K^A for $v = 0$ with mode I-dominant loading.

so a comparison can be made to the results obtained for this system in [Morini et al. 2013]. The results shown agree with the ones there, with only the real part of the symmetric stress intensity factor existing for symmetric loading and the magnitude of all components increasing as the asymmetry becomes more profound. The behavior is not identical to that seen in [Morini et al. 2013] due to the different materials considered in this paper.

6. Conclusions

A general method for calculating stress intensity factors and higher-order terms in the asymptotic expansions of the displacement and stress fields for a dynamic steady-state crack at the interface between two dissimilar anisotropic materials has been developed. The proposed approach, based on weight functions theory and the Betti integral formula, can be applied to many crack problems in a wide range of materials, for example, several classes of anisotropic elastic media (monoclinic, orthotropic) and piezoceramics. As a particular case, a steady-state plane interfacial crack in orthotropic bimaterials has been studied. Expressions for the stress intensity factor and further higher-order asymptotic coefficients have been found for two different configurations of loading acting on the crack faces.

It has been shown in the considered examples that greater asymmetry of the loading configuration leads to an increase in the energy release rate at the crack tip and has a particularly large effect for high crack velocities. Moreover, the analysis of the stress intensity factors for both loadings shows the existence of a sub-Rayleigh velocity at which the stress intensity factor changes sign, which could lead to a change in the direction of the crack propagation. This effect was only observable when asymmetric loading was applied and may give some explanation for the fact that kinking/branching is more probable at certain velocities. As different materials for the lower half-plane are considered, it has been shown that this characteristic velocity does not exist for every bimaterial; therefore experimental study is of great importance in order to clearly detect the presence of this critical value and its physical implications on crack propagation stability.

Acknowledgments

Lewis Pryce and Gennady Mishuris acknowledge support from the FP7 IAPP project “INTERCER2”, project reference PIAP-GA-2011-286110-INTERCER2. Lorenzo Morini gratefully acknowledges financial support from the Italian Ministry of Education, University and Research in the framework of the FIRB 2010 project “Structural mechanics models for renewable energy applications”. The authors would also like to acknowledge the pleasant work environment provided at Enginsoft, Trento.

Appendix: Orthotropic Stroh matrices for a dynamic crack

For orthotropic materials the matrices $\boldsymbol{Q}$, $\boldsymbol{R}$, and $\boldsymbol{T}$ are given by

$$\boldsymbol{Q} = \begin{pmatrix} C_{11} - \rho v^2 & 0 \\ 0 & C_{66} - \rho v^2 \end{pmatrix}, \quad \boldsymbol{R} = \begin{pmatrix} 0 & C_{12} \\ C_{66} & 0 \end{pmatrix}, \quad \boldsymbol{T} = \begin{pmatrix} C_{66} & 0 \\ 0 & C_{22} \end{pmatrix}. \tag{A.1}$$

Previously, expressions were found for the Stroh matrices for an orthotropic bimaterial with a crack propagating at a constant speed, v, in [Yang et al. 1991], where the following parameters were defined:

$$\kappa_{\gamma\beta} = \frac{C_{\gamma\beta}}{C_{66}}, \quad \alpha_1 = \sqrt{1 - \frac{\rho v^2}{C_{11}}}, \quad \alpha_2 = \sqrt{1 - \frac{\rho v^2}{C_{66}}},$$
$$\xi = \alpha_1\alpha_2\sqrt{\frac{\kappa_{11}}{\kappa_{22}}}, \quad s = \frac{\alpha_2^2 + \kappa_{11}\kappa_{22}\alpha_1^2 - (1+\kappa_{12})^2}{2\alpha_1\alpha_2\sqrt{\kappa_{11}\kappa_{22}}}.$$

It is seen that the eigenvalues, with positive imaginary parts, of (6) are given by

$$p_{1,2} = \begin{cases} i\sqrt{\xi}\left(\sqrt{\dfrac{s+1}{2}} \pm \sqrt{\dfrac{s-1}{2}}\right), & \text{for} \quad s \geq 1, \\ \sqrt{\xi}\left(\pm\sqrt{\dfrac{1-s}{2}} + i\sqrt{\dfrac{1+s}{2}}\right), & \text{for} \quad -1 < s < 1. \end{cases} \tag{A.2}$$

Using the same normalization as used in [Yang et al. 1991] the matrices $\boldsymbol{A}$ and $\boldsymbol{L}$ are given by

$$\boldsymbol{A} = \begin{pmatrix} 1 & -\lambda_2^{-1} \\ -\lambda_1 & 1 \end{pmatrix}, \tag{A.3}$$

$$\boldsymbol{L} = C_{66}\begin{pmatrix} p_1 - \lambda_1 & 1 - p_2\lambda_2^{-1} \\ \kappa_{12} - \kappa_{22}p_1\lambda_1 & \kappa_{22}p_2 - \kappa_{12}\lambda_2^{-1} \end{pmatrix}, \tag{A.4}$$

where

$$\lambda_\mu = \frac{\kappa_{11}\alpha_1^2 + p_\mu^2}{(1+\kappa_{12})p_\mu}.$$

It is now possible to find an expression for the hermitian matrix $\boldsymbol{B}$:

$$\boldsymbol{B} = i\boldsymbol{A}\boldsymbol{L}^{-1} = \frac{1}{C_{66}R}\begin{pmatrix} \kappa_{22}\alpha_2^2\sqrt{2(1+s)/\xi} & i(\kappa_{22} - \kappa_{12}\alpha_2^2/\xi) \\ -i(\kappa_{22} - \kappa_{12}\alpha_2^2/\xi) & \kappa_{22}\sqrt{2\xi(1+s)} \end{pmatrix}, \tag{A.5}$$

where R is the generalized Rayleigh wave function given by

$$R = \kappa_{22}(\kappa_{22}\xi - 1 + \alpha_2^2) - \kappa_{12}^2\alpha_2^2/\xi.$$

The Rayleigh wave speed of a material can be found by solving the equation for $R = 0$.

The bimaterial matrix $\boldsymbol{H}$, from (7), has the form

$$\boldsymbol{H} = \begin{pmatrix} H_{11} & -i\beta\sqrt{H_{11}H_{22}} \\ i\beta\sqrt{H_{11}H_{22}} & H_{22} \end{pmatrix}. \tag{A.6}$$

From (A.5) it is seen that

$$H_{11} = \left[\frac{\kappa_{22}\alpha_2^2\sqrt{2(1+s)/\xi}}{C_{66}R}\right]_{\mathrm{I}} + \left[\frac{\kappa_{22}\alpha_2^2\sqrt{2(1+s)/\xi}}{C_{66}R}\right]_{\mathrm{II}},$$
$$H_{22} = \left[\frac{\kappa_{22}\sqrt{2\xi(1+s)}}{C_{66}R}\right]_{\mathrm{I}} + \left[\frac{\kappa_{22}\sqrt{2\xi(1+s)}}{C_{66}R}\right]_{\mathrm{II}},$$
$$\beta\sqrt{H_{11}H_{22}} = \left[\frac{\kappa_{22}-\kappa_{12}\alpha_2^2/\xi}{C_{66}R}\right]_{\mathrm{II}} - \left[\frac{\kappa_{22}-\kappa_{12}\alpha_2^2/\xi}{C_{66}R}\right]_{\mathrm{I}}.$$

In order to compute the weight functions the eigenvalues and eigenvectors of (9) are required. Using the representation (A.6) it is found that

$$\boldsymbol{w} = \begin{pmatrix} -\dfrac{i}{2} \\ \dfrac{1}{2}\sqrt{\dfrac{H_{11}}{H_{22}}} \end{pmatrix}, \quad \epsilon = \frac{1}{2\pi}\ln\Big(\frac{1-\beta}{1+\beta}\Big). \tag{A.7}$$

Another key component for calculating the weight functions is the bimaterial matrix $\boldsymbol{W}$, defined in (7). Using (A.5) it is seen that

$$\boldsymbol{W} = \sqrt{H_{11}H_{22}}\begin{pmatrix} \delta_1\sqrt{\dfrac{H_{11}}{H_{22}}} & i\gamma \\ -i\gamma & \delta_2\sqrt{\dfrac{H_{22}}{H_{11}}} \end{pmatrix}, \tag{A.8}$$

where

$$\gamma = \frac{\left[\dfrac{\kappa_{22}-\kappa_{12}\alpha_2^2/\xi}{C_{66}R}\right]_{\mathrm{I}} + \left[\dfrac{\kappa_{22}-\kappa_{12}\alpha_2^2/\xi}{C_{66}R}\right]_{\mathrm{II}}}{\sqrt{H_{11}H_{22}}},$$
$$\delta_1 = \frac{\left[\dfrac{\kappa_{22}\alpha_2^2\sqrt{2(1+s)/\xi}}{C_{66}R}\right]_{\mathrm{I}} - \left[\dfrac{\kappa_{22}\alpha_2^2\sqrt{2(1+s)/\xi}}{C_{66}R}\right]_{\mathrm{II}}}{H_{11}},$$
$$\delta_2 = \frac{\left[\dfrac{\kappa_{22}\sqrt{2\xi(1+s)}}{C_{66}R}\right]_{\mathrm{I}} - \left[\dfrac{\kappa_{22}\sqrt{2\xi(1+s)}}{C_{66}R}\right]_{\mathrm{II}}}{H_{22}}.$$

References

[Bercial-Velez et al. 2005] J. P. Bercial-Velez, Y. A. Antipov, and A. B. Movchan, "High-order asymptotics and perturbation problems for 3D interfacial cracks", *J. Mech. Phys. Solids* **53**:5 (2005), 1128–1162.

[Bower 2009] A. F. Bower, *Applied mechanics of solids*, 1st ed., CRC Press, Boca Raton, Florida, 2009.

[Bueckner 1985] H. F. Bueckner, "Weight functions and fundamental fields for the penny-shaped and the half plane crack in three-space", *Int. J. Solids Struct.* **23**:1 (1985), 57–93.

[Bueckner 1989] H. F. Bueckner, "Observations on weight functions", *Eng. Anal. Bound. Elem.* **6**:1 (1989), 3–18.

[Geis et al. 2004] W. Geis, G. Mishuris, and A. Sandig, "Asymptotic models for piezoelectric stack actuators with thin metal inclusions", Preprint 2004/001, Univeristy of Stuttgart, 2004, Available at http://preprints.ians.uni-stuttgart.de.

[Irwin 1957] G. R. Irwin, "Analysis of stresses and strains near the end of a crack traversing a plate", *J. Appl. Mech* **24** (1957), 361–364.

[Morini et al. 2013] L. Morini, E. Radi, A. B. Movchan, and N. V. Movchan, "Stroh formalism in analysis of skew-symmetric and symmetric weight functions for interfacial cracks", *Math. Mech. Solids* **18**:2 (2013), 135–152.

[Obrezanova et al. 2002a] O. Obrezanova, A. B. Movchan, and J. R. Willis, "Dynamic stability of a propagating crack", *J. Mech. Phys. Solids* **50**:12 (2002), 2637–2668.

[Obrezanova et al. 2002b] O. Obrezanova, A. B. Movchan, and J. R. Willis, "Stability of an advanicng crack to small perturbation of its path", *J. Mech. Phys. Solids* **50**:1 (2002), 57–80.

[Piccolroaz et al. 2007] A. Piccolroaz, G. Mishuris, and A. B. Movchan, "Evaluation of the Lazarus–Leblond constants in the asymptotic model for the interfacial wavy crack", *J. Mech. Phys. Solids* **55**:8 (2007), 1575–1600.

[Piccolroaz et al. 2009] A. Piccolroaz, G. Mishuris, and A. B. Movchan, "Symmetric and skew-symmetric weight functions in 2D perturbation models for semi-infinite interfacial cracks", *J. Mech. Phys. Solids* **57**:9 (2009), 1657–1682.

[Piccolroaz et al. 2010] A. Piccolroaz, G. Mishuris, and A. B. Movchan, "Perturbation of mode III interfacial cracks", *Int. J. Fract.* **166**:1–2 (2010), 41–51.

[Stroh 1962] A. N. Stroh, "Steady state problems in anisotropic elasticity", *J. Math. Phys* **41**:2 (1962), 77–103.

[Suo 1990] Z. Suo, "Singularities, interfaces and cracks in dissimilar anisotropic media", *Proc. R. Soc. Lond. A. Math. Phy. Sci.* **427**:1873 (1990), 331–358.

[Ting 1996] T. C. T. Ting, *Anisotropic elasticity: theory and applications*, Oxford University Press, 1996.

[Willis and Movchan 1995] J. R. Willis and A. B. Movchan, "Dynamic weight function for a moving crack. I. mode I loading", *J. Mech. Phys. Solids* **43**:3 (1995), 319–341.

[Yang et al. 1991] W. Yang, Z. Suo, and C. F. Shih, "Mechanics of dynamic debonding", *Proc. R. Soc. Lond. A. Math. Phy. Sci.* **433**:1889 (1991), 679–697.

[Yu and Suo 2000] H. H. Yu and Z. Suo, "Intersonic crack growth on an interface", *Proc. R. Soc. Lond. A. Math. Phy. Eng. Sci.* **456**:1993 (2000), 223–246.

Received 4 Jul 2013. Revised 24 Sep 2013. Accepted 6 Oct 2013.

LEWIS PRYCE: lep8@aber.ac.uk
Institute of Mathematics and Physics, Aberystwyth University, Aberystwyth, Ceredigion, SY23 3BZ, United Kingdom
and
Enginsoft Trento, Via della Stazione 27 - frazione Mattarello, 38123 Trento, Italy

LORENZO MORINI: lorenzo.morini@unitn.it
Department of Civil, Environmental and Mechanical Engineering, University of Trento, via Mesiano 77, 38123 Trento, Italy

GENNADY MISHURIS: ggm@aber.ac.uk
Institute of Mathematics and Physics, Aberystwyth University, Aberystwyth, Ceredigion, SY23 3BZ, United Kingdom
and
Enginsoft Trento, Via della Stazione 27 - frazione Mattarello, 38123 Trento, Italy

JOURNAL OF MECHANICS OF MATERIALS AND STRUCTURES
Vol. 8, No. 8-10, 2013
dx.doi.org/10.2140/jomms.2013.8.501

msp

EFFECTS OF TRANSVERSE SHEAR DEFORMATION ON THERMOMECHANICAL INSTABILITIES IN PATCHED STRUCTURES WITH EDGE DAMAGE

PEINAN GE AND WILLIAM J. BOTTEGA

The problem of a patched structure under uniform thermal loading is studied, where geometric nonlinearity and shear deformation are considered. The formulation is based on the calculus of variations with propagating boundaries, and yields the governing equations, boundary conditions, matching conditions and transversality condition. Closed form analytical solutions are obtained in terms of an (unknown) membrane force parameter, the angle of rotation due to bending and the transverse displacement. Results of numerical simulations based on those solutions are presented and critical phenomena of the composite structure are unveiled. Results of the current work are compared with previously published results where transverse shear deformation was neglected. It is seen that shear deformation plays an important role in certain situations. In particular, the effects of shear deformation on the phenomena of "slingshot buckling" and "buckle trapping" are demonstrated and discussed. The influence of the relative size of the detached region and of the difference between the material properties of the base plate and of the patch (in particular, shear moduli) on the thermomechanical instabilities are elucidated.

1. Introduction

Patched structures are widely used in a variety of engineering systems. Such a structure consists of a secondary component adhered to a primary structure. Engineers have been using patches on aircraft in recent years to alleviate the stress intensity in the vicinity of cracks in the primary structures. It is necessary to predict and characterize the functionality of a patched structure during its servicing period. In the structures of this class, the mechanical properties of the composite structure change with respect to the properties of the patch and base components. With varying the temperature environments, with ensuing increased stress and buckling, transverse shear deformation may affect the system greatly. Therefore the characterization of the shear effect is of critical importance.

It is well known that the composite structure will eventually buckle when it is subjected to temperature change. The classic papers on thermal buckling include [Timoshenko 1925; Wittrick et al. 1953; Wahl 1944]. Karlsson and Bottega [1999] studied the presence of edge contact in patched cylindrical panels, and found that edge contact often occurs, and that it can influence the debonding behavior of the structure. Karlsson and Bottega [2000a; 2000b] and Rutgerson and Bottega [2002] subsequently studied the behavior of patched plates and layered shells, respectively, subjected to uniform temperature change. Their results showed that the structure will dynamically sling to an equilibrium configuration associated with deflections in the opposite sense of the original. The phenomenon is referred to as "slingshot buckling"

Keywords: beam, buckle trapping, buckling, patch, patched structure, contact zone, plate, slingshot buckling, stability, temperature, thermal buckling, thermal load, transverse shear deformation.

by the authors. Those studies are united and compared in [Bottega 2006b]. Recently, Bottega and Carabetta [2009] studied the detachment and separation failure of layered structures under thermal loading. The behaviors of several representative structures and loadings were studied. Carabetta and Bottega [2012; 2014] studied the instability of patched structures with edge damage where a new phenomenon referred to as "buckle trapping" was unveiled. A detailed review of the pertinent literature is presented therein. In addition, Carabetta [2011] studied the interaction of thermal buckling and detachment of patched structures. The existence of intermediate propagating contact was discussed for different bond zone sizes and edge supports. These representative results significantly advance the understanding of engineering structures. However, a more sophisticated elastic theory containing shear deformation will further elucidate the phenomena of interest.

Timoshenko [1921] was the first to introduce shear deformation as well as rotatory inertia into beam theory. Shen [1998] presented a post-buckling analysis for laminated composite plates subjected to uniform or nonuniform temperature loading. Reddy [1984] adopted higher order shear deformation in the formulation to show that the characteristics of thermal post-buckling are significantly influenced by transverse shear deformation. Aydogdu [2007] applied the Ritz method and performed an analysis of thermal buckling behavior on cross-ply laminated beams. In that work, a shear deformable theory was used in conjunction with a shape function to fulfill geometric and material constraints. Zenkour and Sobhy [2010] used a sinusoidal shear deformation plate theory to model thermal buckling phenomena of sandwich plates. Different thermal loads were applied under various configurations of the plates.

The present work focuses on the response of patched plates subjected to a uniform temperature field for a variety of support conditions and material properties. We extend the model and analysis of [Carabetta and Bottega 2014] to include transverse shear deformation. The formulations are based on [Mindlin 1951, Plate Theory], a generalization of [Timoshenko 1921, Beam Theory], and the calculus of variations. Numerical simulations are performed to elucidate representative behavior of the composite structure. Of particular interest is how the inclusion of transverse shear deformation in the overall formulation affects the response of the composite structure. In addition, the effects that the length of the patch, the proportion of Poisson's ratio and Young's modulus between the patch and the base plate have on the behavior of the structure are also examined.

2. Problem statement

In this work, we study the instability of a patched structure with a preexisting detached region emanating from each edge of the patch. We advance the work of [Carabetta and Bottega 2014] and include the effect of transverse shear deformation to examine its influence on critical phenomena. In the formulation we allow for three configurations: (1) no contact of the debonded segments of the substructures; (2) the "free" edge of the debonded segment of the patch maintains sliding contact with the base plate ("edge contact"); (3) a contact zone (a region of sliding contact) adjacent to the bonded region. Each of these configurations are shown in Figure 1.

The thin patched plate is comprised of two substructures: a base plate of half-span length L, and a patch of half-span L_p centrally and partially adhered to the base structure (Figure 2). The thicknesses of the base plate and the patch are h_b and h_p, respectively. The coordinate x originates at the centerspan and runs along the reference surface — the upper surface of the base plate. All the length scales are

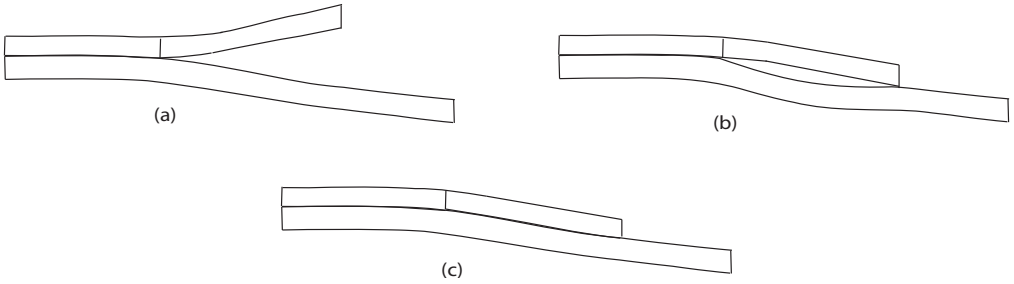

Figure 1. Deformed plate showing various configurations: (a) panel with no contact of debonded segments; (b) plate with edge contact of debonded segments; (c) plate with full contact of debonded segments of patch plate and base.

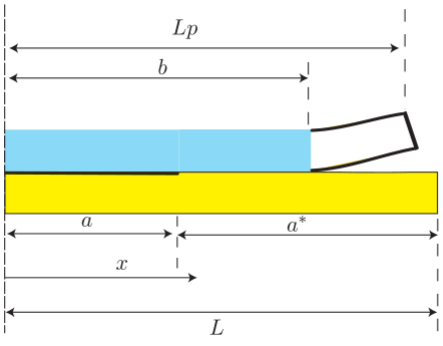

Figure 2. Half-span of structure.

normalized with respect to the half-length of the base plate and other pertinent parameters are normalized in accordance with [Bottega and Carabetta 2009]. Thus, for the structure of interest, the half-span length of the base plate is $L = 1$. The structure is mathematically partitioned into three domains: the *bond zone* $S_1 : x \in [0, a]$, the *contact zone* $S_2 : x \in [a, b]$ and the *lift zone* $S_3 : x \in [b, 1]$. The functions $w(x)$ and $w_p(x)$ (positive downward) represent the normalized transverse displacements of the base plate and of the patch, respectively. The functions $u(x)$ and $u_p(x)$ (positive outward from centerspan) denote the corresponding normalized in-plane displacements of material particles located at the centroid of the base plate and of the patch, respectively. Correspondingly, the functions $\phi(x)$ and $\phi_p(x)$ represent the angle of rotation of the cross section due to bending for the base plate and of the patch, respectively. In addition, the functions $\gamma(x)$ and $\gamma_p(x)$ represent the shear angles of the base plate and of the patch, respectively.

Paralleling the developments in [Carabetta and Bottega 2014], the membrane strain of the base plate and of the patch, $e_i(x)$ and $e_p(x)$, respectively, are given by

$$e_i = u'_{bi} + \tfrac{1}{2} {w'_{bi}}^2 - \alpha_b \Theta \qquad (i = 1, 2, 3), \tag{1}$$

$$e_p = {u'_{p_2}}^2 + \tfrac{1}{2} {w'_{p_2}}^2 - \alpha_p \Theta, \tag{2}$$

where $(\,)' = d(\,)/dx$ and α_b, α_p are described in what follows. We next adopt the normalized temperature scale of [Rutgerson and Bottega 2002; Carabetta and Bottega 2014]:

$$\Theta = \alpha \frac{\overline{\Theta} - \overline{\Theta}_0}{\overline{\Theta}_0}, \tag{3}$$

$$\alpha_b = \bar{\alpha}_b \overline{\Theta}, \qquad \alpha_p = \bar{\alpha}_p \overline{\Theta} \qquad \text{(plane stress)}, \tag{4}$$

$$\alpha_b = \bar{\alpha}_b \overline{\Theta}(1+\nu), \quad \alpha_p = \bar{\alpha}_p \overline{\Theta}(1+\nu) \qquad \text{(plane strain)}, \tag{5}$$

where the parameters $\overline{\Theta}$ and $\overline{\Theta}_0$ represent the present dimensional temperature and the reference temperature of the system, respectively, and ν is Poisson's ratio. The nondimensional coefficients of thermal expansion of the base plate and patch, $\bar{\alpha}_b$ and $\bar{\alpha}_p$ respectively, are defined in terms of their dimensional counterparts, α_b and α_p, in (4) and (5).

Paralleling the developments in [Carabetta and Bottega 2014], but now incorporating transverse shear deformation, we next formulate an energy functional in terms of the membrane energies, bending energies and shear energies of each substructure for each segment of the base panel and of the patch, and we also include constraint functionals which match the transverse displacements in the contact zone and the transverse and in-plane displacements and the angle of rotation due to bending in the bond zone. We thus formulate the energy functional Π as

$$\Pi = \sum_1^3 \left(U_B^{(i)} + U_{Bp}^{(i)} + U_M^{(i)} + U_{Mp}^{(i)} + U_S^{(i)} + U_{Sp}^{(i)}\right) - \Lambda \tag{6}$$

where

$$U_B^{(i)} = \int_{S_i} \tfrac{1}{2} D_b \kappa_i^2 \, dx, \quad U_{Bp}^{(i)} = \int_{S_i} \tfrac{1}{2} D_p \kappa_{pi}^2 \, dx \quad (i = 1, 2, 3) \tag{7}$$

are the bending energies in the base plate and patch in region S_i,

$$U_M^{(i)} = \int_{S_i} \tfrac{1}{2} C_b e_i^2 \, dx, \quad U_{Mp}^{(i)} = \int_{S_i} \tfrac{1}{2} C_p e_{pi}^2 \, dx \quad (i = 1, 2, 3) \tag{8}$$

are the membrane energies in the base plate and patch in region S_i. Further

$$U_S^{(i)} = \int_{S_i} \tfrac{1}{2} G_b \gamma_i^2 \, dx, \quad U_{Sp}^{(i)} = \int_{S_i} \tfrac{1}{2} G_p \gamma_{pi}^2 \, dx \quad (i = 1, 2, 3) \tag{9}$$

are the shear energies in the base plate and in the patch in region S_i. The constraint functional Λ in (6) is given by

$$\Lambda = \sum_1^2 \int_{S_i} \sigma_i (w_{pi} - w_i) \, dx + \int_{S_1} \tau (u_{p1}^* - u_1^*) \, dx + \int_{S_1} \lambda (\phi_{p1}^* - \phi_1^*) \, dx. \tag{10}$$

In (7)–(10), D_b and D_p are the nondimensional bending stiffnesses of the base plate and the patch, respectively, C_b and C_p are the corresponding nondimensional membrane stiffnesses, and G_b and G_p are the nondimensional shear stiffnesses. In addition, σ_i represents the interfacial normal stress, τ is the interfacial shear stress, and λ is the interfacial moment couple. According to [Mindlin 1951, Plate

Theory; Timoshenko 1921, Beam Theory; Bottega 2006a], where a shear correction and rotatory inertia are considered, the strain-displacement relation is given by

$$\frac{dw}{dx} = \phi + \gamma, \tag{11}$$

$$\gamma = \frac{V}{kGh}, \tag{12}$$

where w is the transverse displacement, ϕ is the angle of rotation due to bending and γ is the transverse shear angle of the cross section. In (12), the parameter G is the shear modulus and V is the transverse shear force. In addition, k is the "shape factor" or "shear coefficient" of the structure, which depends on the shape of the cross section. In the past decades, the shear coefficients for various cross sections of beams were derived. Examples of related work may be found in [Mindlin 1951; Cowper 1966; Ritchie et al. 1973; Hutchinson 1981; Wittrick 1986]. Incorporating (11) into the development through Equations (6)–(10), the problem is expressed in terms of the in-plane displacement, $u(x)$, the transverse displacement, $w(x)$, and the angle of rotation due to bending, $\phi(x)$. The parameters shown in the above formulation of the total potential energy of the system are defined in terms of their dimensional versions as follows:

$$\begin{aligned}
x &= \bar{x}/\bar{L}, & D_b &= 1,\\
u(x) &= \bar{u}(\bar{x})/\bar{L}, & C_b &= \bar{C}_b/\bar{D}_b,\\
w(x) &= \bar{w}(\bar{x})/\bar{L}, & D_p &= \bar{D}_p/\bar{D}_b,\\
\phi(x) &= \bar{\phi}(\bar{x}), & C_p &= \bar{C}_p/\bar{D}_b,\\
G_b &= k_b\bar{G}_b\bar{h}_b\bar{L}^2/\bar{D}_b, & G_p &= k_p\bar{G}_p\bar{h}_p\bar{L}^2/\bar{D}_b,\\
\sigma_i &= \bar{\sigma}_i\bar{L}^3/\bar{D}_b, & \tau &= \bar{\tau}\bar{L}^3/\bar{D}_b,\\
h_b &= \bar{h}_b/\bar{L}, & \lambda &= \bar{\lambda}\bar{L}^2/\bar{D}_b,\\
h_p &= \bar{h}_p/\bar{L}, & L &= 1,
\end{aligned} \tag{13}$$

where length scales have been normalized with respect to the dimensional half-span $\bar{L}$ of the base plate. Invoking the principle of stationary potential energy, which is described in the present context as $\delta\Pi = 0$, we take the appropriate variations and allow the boundary b to vary along with the displacements. This results in the corresponding governing equations, boundary and matching conditions, and transversality condition. After eliminating the Lagrange multipliers, we arrive at the self-consistent equations and conditions for the composite structure presented next.

2.1. ***Governing equations.*** Adopting the procedure presented in [Carabetta and Bottega 2014], we first obtain the relation

$$N_1^* = N_2 = N_3 = -N_0 = \text{constant}, \qquad N_{p2} = N_{p3} = 0, \tag{14}$$

where N_0 is yet to be determined. With this important result, the problem is recast into a mixed formulation, expressed in terms of the transverse displacement, $w(x)$, the angle of rotation due to bending, $\phi(x)$, and the uniform membrane force, N_0.

The equations of transverse motion and rotation then take the form

$$\begin{aligned} D^*\phi''_{b1} + (G_b + G_p)(w'_{b1} - \phi_{b1}) &= 0, \\ -N_0 w''_{b1} + (G_b + G_p)(w'_{b1} - \phi_{b1})' &= 0, \quad x \in [0, a]. \end{aligned} \tag{15}$$

We next rearrange the above equations, eliminate w_{b1} and decouple the governing equations in terms of the angle of rotation due to bending, ϕ_{b1}, and the uniform membrane force, N_0. Applying the same procedure for other regions gives the following governing equations. Hence,

$$g^*\phi'''_{b1} + N_0\phi'_{b1} = 0 \quad (0 \le x \le a), \tag{16}$$

$$g_3\phi'''_{b2} + N_0\phi'_{b2} + D_p\phi'''_{p2} = 0 \quad (a \le x \le b), \tag{17}$$

$$g_3\phi'''_{b3} + N_0\phi'_{b3} = 0 \quad (b \le x \le 1), \tag{18}$$

$$g_4\phi'''_{p3} = 0 \quad (b \le x \le L_p), \tag{19}$$

where

$$g^* = D^*\left(1 - \frac{N_0}{G_b + G_p}\right), \qquad g_3 = D_b\left(1 - \frac{N_0}{G_b}\right), \qquad g_4 = D_p\left(1 - \frac{N_0}{G_p}\right), \tag{20}$$

$$w''_{b1}(x) = -\frac{D^*}{G_b + G_p}\phi''_b + \phi_b, \qquad w'_{b2}(x) = -\frac{D_b}{G_b}\phi''_{b2} + \phi_{b2}, \qquad w'_{b3}(x) = -\frac{D_b}{G_b}\phi''_{b3} + \phi_{b3}, \tag{21}$$

$$w'_{p2}(x) = -\frac{D_p}{G_p}\phi''_{p2} + \phi_{p2}, \qquad w'_{p3}(x) = -\frac{D_p}{G_p}\phi''_{p3} + \phi_{p3}. \tag{22}$$

2.2. ***Boundary and matching conditions.*** The associated boundary and matching conditions are obtained from the variational operation as

$$\phi_{b1}(0) = 0, \quad \phi''_{b1}(0) = 0, \quad \phi_{b3}(1) = 0, \quad w_{b3}(1) = 0, \quad \phi'_{p3}(L_p) = 0, \quad \phi''_{p3}(L_p) = 0, \tag{23}$$

$$\begin{aligned} M_\lambda(a) = [D^*\phi'_b - D_b\phi'_{b2} - D_p\phi'_{p2}]_{x=a}, &\qquad \phi_{b1}(a) = \phi_{b2}(a) = \phi_{p2}(a), \\ [g^*\phi''_{b1} + N_0\phi_{b1}]_{x=a} = [g_3\phi''_{b2} + N_0\phi_{b2} + D_p\phi''_{p2}]_{x=a}, &\qquad w_{b1}(a) = w_{b2}(a) = w_{p2}(a), \end{aligned} \tag{24}$$

$$\begin{aligned} \phi'_{b2}(b) = \phi'_{b3}(b), &\qquad \phi'_{p2}(b) = \phi'_{p3}(b), \\ \phi_{b2}(b) = \phi_{b3}(b), &\qquad \phi_{p2}(b) = \phi_{p3}(b), \\ [g_3\phi''_{b2} + N_0\phi_{b2} + D_p\phi''_{p2}]_{x=b} &= [g_3\phi''_{b3} + N_0\phi_{b3} + D_p\phi''_{p3}]_{x=b}, \\ w_{b2}(b) = w_{b3}(b) &= w_{p3}(b) = w_{p2}(b) \end{aligned} \tag{25}$$

where

$$M_\lambda = m^*\Theta + \left(\rho^* + \tfrac{1}{2}h_b\right)N_0. \tag{26}$$

The parameter M_λ in the matching condition is denoted as the transverse loading parameter, which is first introduced by Karlsson and Bottega [2000a], from which the external thermal loading enters the problem for the composite structure. The two components of the loading parameter compete with each other when they have opposite sign, which is central to the "slingshot buckling" and other related issues presented in [Bottega 2006b]. The parameters m^* and ρ^* are given in Appendix A. Finally, integrating

the strain-displacement relations and imposing the boundary and matching conditions for the in-plane displacements result in the integrability condition

$$u_{b2}(1)-u_b(0)=-N_0\Big(\frac{1-a}{C_b}+\frac{a^*}{C_p}\Big)+\Big(1-a+a\frac{n^*}{C^*}\Big)\Theta-\big(\tfrac{1}{2}h_b+\rho^*\big)\phi_b(a)$$
$$-\frac{1}{2}\int_0^a w_b'^2\,dx-\frac{1}{2}\int_a^b w_{b2}'^2\,dx-\frac{1}{2}\int_b^1 w_{b3}'^2\,dx. \quad (27)$$

2.3. ***Transversality condition.*** The partially debonded structure discussed on page 503 (see especially Figure 2) is divided into 3 segments — bonded zone, contact zone and lift zone. The location of the boundary between the contact zone and the lift zone is determined by the corresponding transversality condition that is derived by taking the appropriate variations and allowing the boundary b to vary along with the displacements. This condition reduces to the equality of the total angular displacement of the patch and the base plate at the contact zone boundary. Therefore, a propagating contact boundary may occur only if the following condition is satisfied

$$w_{b3}'(b)=w_{p3}'(b), \quad (28)$$
$$w_{b3}'(b)>0, \quad (29)$$

where (29) is added to prohibit penetration of the patch to the base plate. If (28) and (29) are not satisfied, the system will possess either a full contact zone ($b=L_p$), no contact zone ($b=a$), or edge point contact, whichever possesses the lowest system energy.

2.4. ***Condition for (full) contact or lift.*** To establish whether full contact between, or lift off of, the detached segment of the patch and the base plate occurs for clamped-fixed, we establish a kinematic criterion based on physical arguments. For lift off to occur, a pseudo inflection point must occur at the bond zone boundary, $x=a$. This can be characterized by the product of the gradients of total rotations of the composite plate in the bond zone and in the contact zone, evaluated at the bond zone boundary. That is,

$$J_a\equiv w_1''(a)\cdot w_2''(a). \quad (30)$$

If

$$J_a<0, \quad (31)$$

a full contact zone is possible. If

$$J_a>0, \quad (32)$$

lift is possible. The above is coupled with the sense of the deflections when making an assessment.

2.5. ***Stability criterion.*** For a given value of the applied thermal loading, if multiple equilibrium configurations exist, it is necessary to determine which of the configurations are stable and which are unstable. In this regard, we utilize the second variation of the potential energy functional to assess the stability of each equilibrium configuration (the approach implemented in [Karlsson and Bottega 2000a]). The configuration is considered stable if the second variation of the total potential is positive definite ($\delta^2\Pi>0$). We adopt the approach discussed in [Karlsson and Bottega 2000b], in which the transverse displacements

and the axial strains are perturbed via their coefficients. Doing this, we obtain the second variation of the total potential energy in the following form,

$$\delta^2\Pi = \hat{F}(\delta M_\lambda)^2 + \zeta(\delta N_0)^2 \tag{33}$$

where Π is the total potential energy, δ is the variational operator,

$$\zeta = \frac{1}{2}\left(\frac{a}{C^*} + \frac{a^*}{C_b}\right) \quad \text{and} \quad \hat{F} = \hat{F}(N_0, a, b). \tag{34}$$

As discussed in [Carabetta and Bottega 2014], the form of the function $\hat{F}$ depends on the particular support conditions for the specific structure. Since $\zeta > 0$, the requirement of positive definiteness of the second variation reduces to the stability criterion

$$\hat{F} > 0. \tag{35}$$

In this regard, a configuration is stable when (35) is satisfied. The function $\hat{F}$ is therefore referred to as the stability function.

3. Analysis

Solving Equations (16)–(19), subject to the boundary and matching conditions of Equations (23)–(25), yields the solutions for the angle of rotation due to bending in each region. The solutions are presented for two extreme support conditions: hinged-fixed and clamped-fixed ends. The general solutions to the governing equations of Section 2, Equations (16)–(19), are found to be

$$\phi_{b1}(x) = C_1 + C_2\cos(K_b x) + C_3\sin(K_b x), \tag{36}$$

$$\phi_{b2}(x) = A_1\cosh(\mu_1 x) + A_2\sinh(\mu_1 x) + A_3\sin(\beta_1 x) + A_4\cos(\beta_1 x) + A_5, \tag{37}$$

$$\phi_{p2}(x) = P_1[A_1\cosh(\mu_1 x) + A_2\sinh(\mu_1 x)] + P_2[A_3\sin(\beta_1 x) + A_4\cos(\beta_1 x)] + A_5, \tag{38}$$

$$\phi_{b3}(x) = C_4 + C_5\cos(K_{b3} x) + C_6\sin(K_{b3} x). \tag{39}$$

The parameters μ_1, K_b, K_{b3}, β_1, P_1, and P_2 are given in Appendix B. Note that, for both support conditions, the rotations for the base plate and patch within the contact zone are not identical ($P_1 \neq 1$, and $P_2 \neq 1$) when the shear deformation is included. The relations between transverse deflection and the angle of rotation due to bending are described by (21) and (22). The expressions for the constants $C_1, \ldots, C_6$ and $A_1, \ldots, A_5$ depending on the specific support conditions imposed at $x = 1$, are cumbersome, and are omitted for brevity. It is noted that the equations presented above reduce to the solutions for a perfectly intact structure in the limiting scenario when $G_b, G_p \to \infty$.

With the analytical solution and stability criterion established, we next present the results of numerical simulations based on these solutions.

4. Results and discussion

The purpose of this study is to demonstrate the influence of transverse shear deformation on the behavior of the structure under thermal loading. This is done by comparing results of the present model with those found in [Carabetta and Bottega 2014] using the corresponding model neglecting transverse shear

deformation. In this section, numerical results are presented for structures with hinged-fixed edges and for structures with clamped-fixed ends, under uniform thermal loading. The effect of changing the shear modulus of the patch and base plate will be analyzed to reveal characteristic behavior. The corresponding thickness ratio is taken as $h_0 = 1$ and the ratio of coefficient of thermal expansion of the patch to the base is $\alpha_p^0 = 0.5$, which are consistent with those used in [Carabetta and Bottega 2014].

4.1. ***Hinged ends.*** We first consider the structure with hinged-fixed supports. That is, the edges of the base plate are hinged with respect to rotation and fixed with respect to in-plane translation. For such support conditions, no contact zone exists when the partially detached structure deflects upward, due to the lack of an inflection point or pseudo-inflection point. When in this configuration, the partially detached structure is equivalent to the intact structure having the same bond zone size in terms of global stiffness and energy. This is consistent with previous studies [Bottega and Carabetta 2009; Carabetta and Bottega 2012; Carabetta 2011]. In contrast, the structure possesses a full contact zone when it deflects downwards. Thus, as discussed in [Carabetta and Bottega 2014], a "dual nature" exists for a partially debonded structure with hinged-fixed supports. In order to appropriately capture the overall behavior of the structure under thermal loading, results of simulations for a structure with no contact zone ($b = a$) and a structure having a full contact zone ($b = L_p$) are presented together. To show the effect of transverse shear on the behavior of the structure, two cases are presented: (1) equal shear stiffness for the two layers; (2) unequal shear stiffness for the base plate and patch.

Case 1: *Equal shear stiffness* ($G_b = G_p$). The shear stiffnesses of the base plate and of the patch are identical, for equal thickness, if both the Young's modulus and Poisson's ratio are equal, per the well-known relation

$$G = \frac{E}{1+\nu}. \tag{40}$$

The results for a structure possessing a bond zone of length $a = 0.6$ and a patch length $L_p = 0.9$ are displayed in Figures 3 and 5. The papers [Carabetta and Bottega 2012; 2014; Carabetta 2011] studied the behavior of the same structure with the transverse shear deformation neglected. The results displayed in Figure 3 are regenerated according to [Carabetta and Bottega 2014]. The load-deflection path is shown in Figure 3(b) as the applied temperature change as a function of the center point deflection. The membrane force, total energy and stability function are shown as a function of the applied temperature change in parts (a), (c) and (d) of Figure 3, with the shear deformation neglected. The corresponding results, with shear deformation accounted for, are displayed in Figure 4. Comparison of Figures 3 and 4 shows virtually no difference in the response of the structure, indicating that the transverse shear has little effect for the case when $G_b = G_p$. In these figures, red color indicates the stable equilibrium configurations and blue color indicates the unstable equilibrium configurations. It is seen from Figure 4(b) that, as the temperature change is increased from zero, the structure initially deflects upward and continues to do so until the critical temperature is achieved, $\Theta_{\mathrm{cr}} = 2.2$. At this point, the configuration associated with Branch 1 becomes unstable and the structure slingshots to an alternate stable configuration on Branch 2. As the structure deflects downward, the detached "flap" of the patch comes into contact with the base plate when $w(0) \geq 0$ and a full contact configuration appears. Thus the rightmost path shown in Figure 4(b) is dismissed on physical grounds.

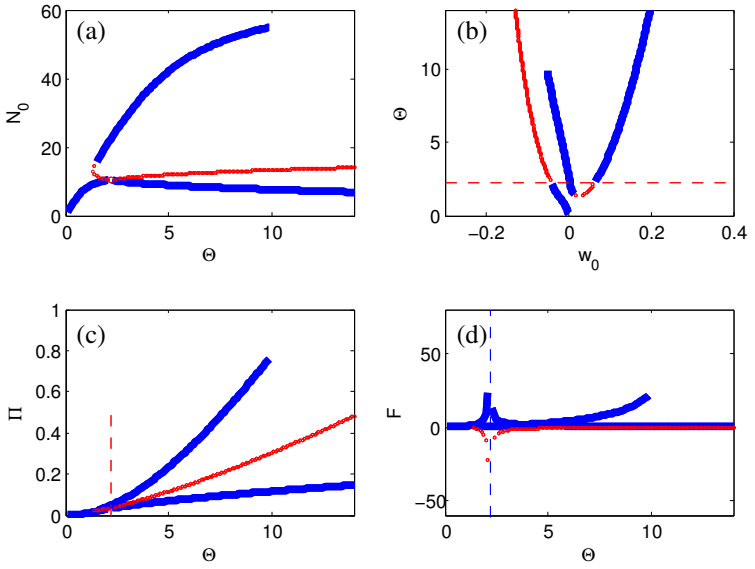

Figure 3. Behavior of hinged-fixed structure with shear deformation neglected, for a fully lifted flap, with $a = 0.6$, $L_p = 0.9$: (a) membrane force vs. temperature difference; (b) temperature difference vs. center-span transverse deflection; (c) total potential energy vs. temperature difference; (d) stability function vs. temperature difference. Red circles represent stable configurations and blue lines indicate unstable ones.

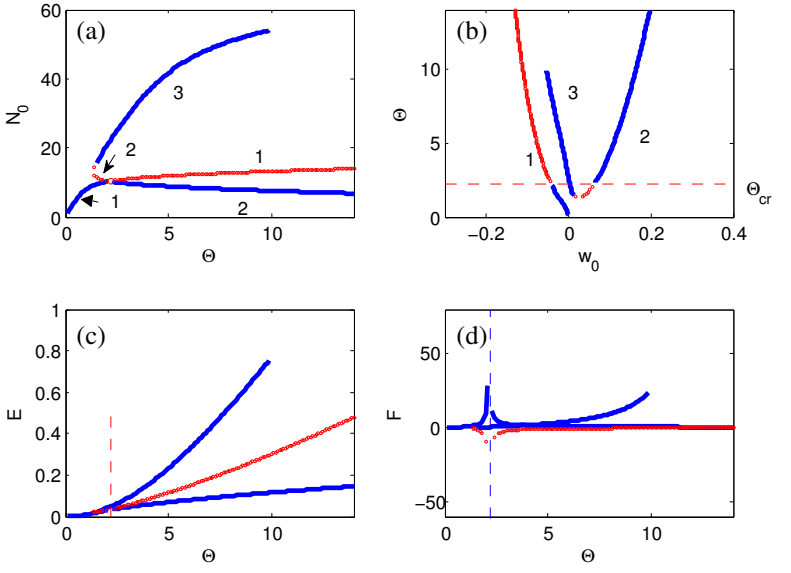

Figure 4. Behavior of hinged-fixed structure, $G_b = G_p$, for a fully lifted flap, with $a = 0.6, L_p = 0.9$: (a) membrane force vs. temperature difference; (b) temperature difference vs. center-span transverse deflection; (c) total potential energy vs. temperature difference; (d) stability function vs. temperature difference. Red circles represent stable configurations and blue lines indicate unstable ones.

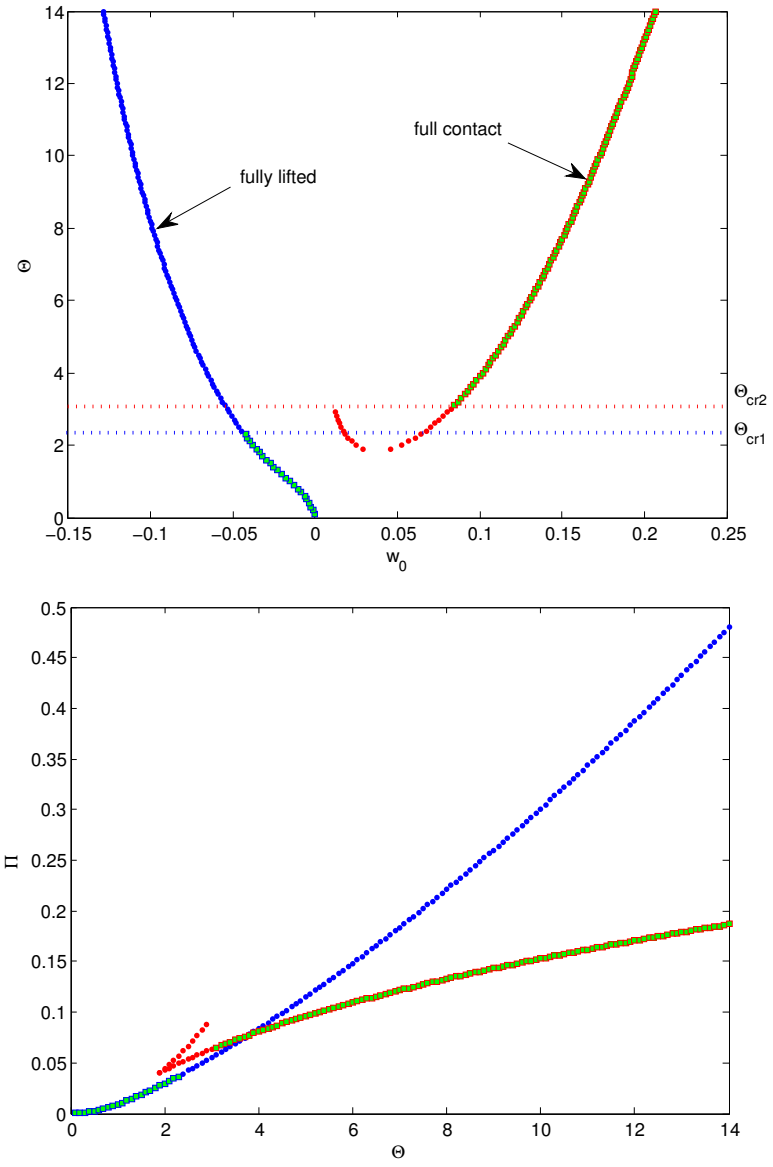

Figure 5. Thermal load-deflection paths (top) and total energy as a function of the temperature change (bottom) for hinged-fixed total structure with $G_b = G_p$, $a = 0.6$, and $L_p = 0.9$.

Figure 5 displays profiles of the temperature difference vs. centerspan displacement and the total energy vs. temperature difference, respectively for the structure. In these figures, red color corresponds to the full contact configuration and blue color to the fully lifted configuration. The squares indicate the stable equilibrium positions and the dots indicate the unstable positions. In these figures, the gap between the critical temperatures of the two configurations is shown. When the structure switches from the fully lifted configuration to the full contact configuration, there is no stable equilibrium position in

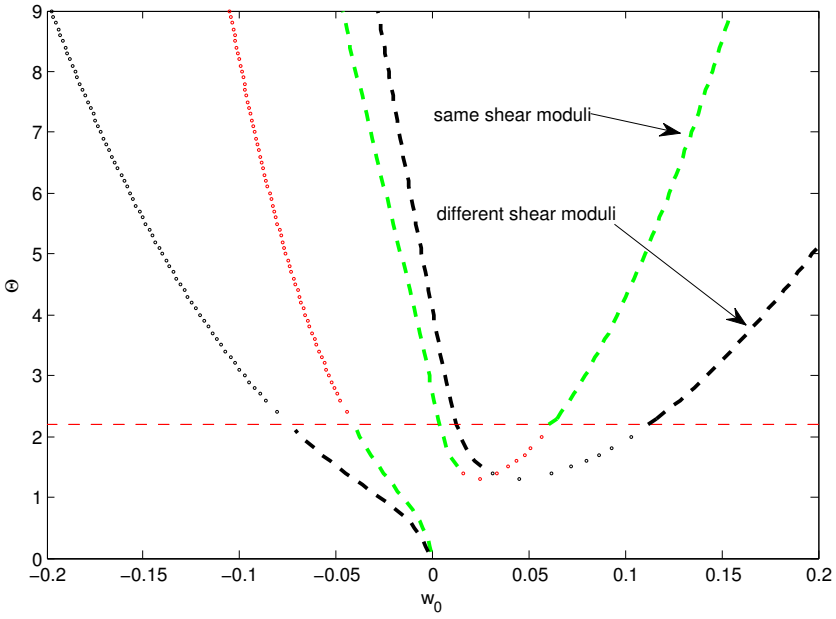

Figure 6. Comparison of thermal load-deflection paths for hinged-fixed structures with $G_p \neq G_b$ ($\nu_b/\nu_p = 0.3/0.2$) with those for $G_p = G_b$, $a = 0.6$, $L_p = 0.9$. Dashed lines represent stable configurations and circles indicate the unstable configurations.

either configuration. Thus, the structure is trapped between the two. This phenomenon, called *buckle trapping*, was established by Carabetta and Bottega [2012; 2014], who proposed the existence of an energy cusp, and hence a stable equilibrium configuration, when $w = 0$ ($\Theta_{\text{cr1}} \leq \Theta \leq \Theta_{\text{cr2}}$). Simulations for a bond zone of half-length $a = 0.8$ with the same patch length are also studied, but the results are omitted for brevity. However, It is observed that the "buckle trapping" phenomenon exists even with the shear correction for this case. It is thus seen that, in this regard, the effects of transverse shear deformation are not apparent when the base plate and the patch possess equal shear stiffness.

Case 2: *Unequal shear stiffnesses* ($G_b \neq G_p$). We next consider the case when the base plate and the patch possess unequal shear stiffness ($G_b \neq G_p$). Selected results of simulations based on the solutions discussed in Section 3 are presented in what follows.

Results for a structure possessing a bond zone of half-length $a = 0.6$ and a patch half-length $L_p = 0.9$ are displayed in Figures 6 and 7. A comparison of the thermal load-deflection paths is displayed in Figure 6 for both cases: (1) equal shear stiffness ($G_b/G_p = 1$) and (2) unequal shear stiffness ($G_b/G_p = 2.2/2.6$), between the base plate and the patch. The profile for equal shear stiffness was already discussed under Case 1. In Figure 6, the black curves correspond to $G_b \neq G_p$ case and the colored curves correspond to $G_b = G_p$ case. The dashed lines indicate stable equilibrium configurations and the circles indicate the unstable states. Although the critical temperature for both cases is the same ($\Theta_{\text{cr}} = 2.2$), the deflection corresponding to the structure with unequal shear stiffnesses is seen to be much larger than that of the structure with equal shear stiffnesses, as Θ increases. Thus, the effect of shear deformation on the behavior of the structure is apparent in this case.

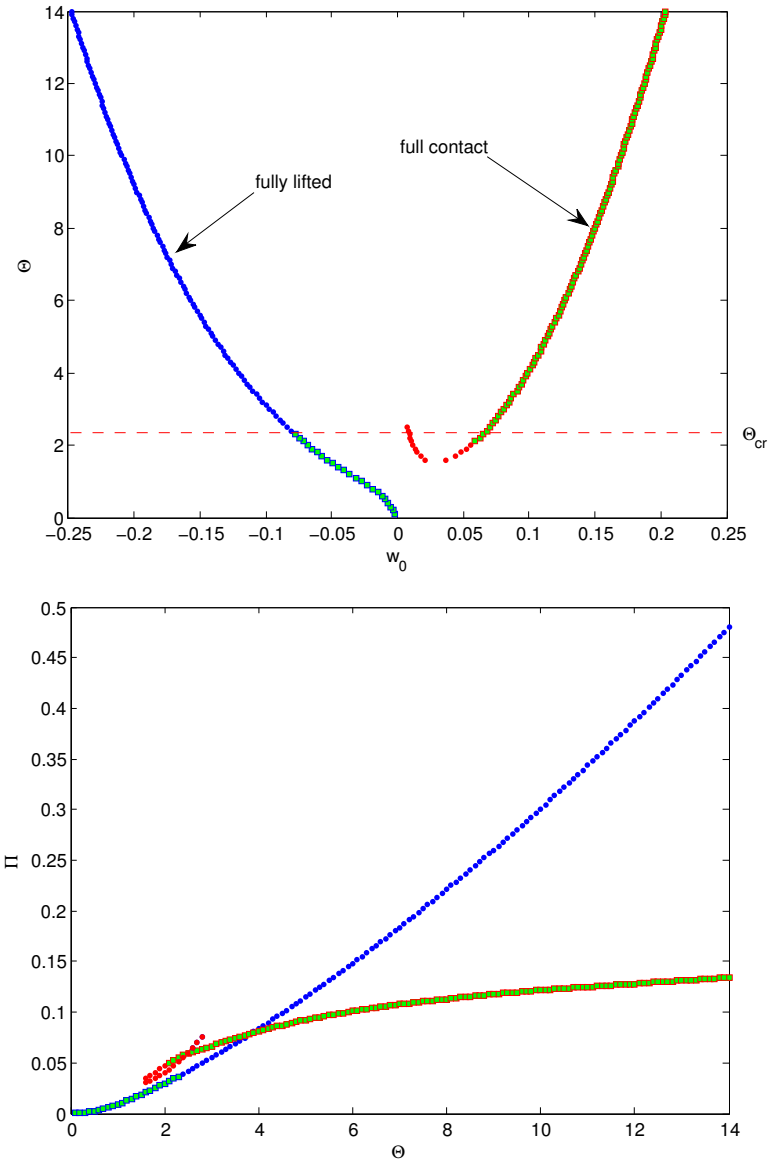

Figure 7. Thermal load-deflection paths (top) and total energy as a function of the temperature change (bottom) for hinged-fixed structure with $\nu_b/\nu_p = 0.3/0.2$, $a = 0.6$, $L_p = 0.9$.

Figure 7 shows the dual load-deflection curve and the total energy profile as a function of the temperature change (both the full contact and fully lifted configurations are presented). It was shown previously, for Case 1, that at the critical temperature, the structure buckles from the fully lifted configuration, and buckle trapping occurs before it reaches the full contact configuration. However, it is seen from Figure 7 that the partially detached structure buckles from a fully lifted configuration to a full contact configuration at the critical temperature $\Theta_{\rm cr} = 2.2$ where it is stable for the full contact configuration.

Thus, the buckle trapping phenomenon disappears for this case. We also examined the partially debonded structure with differing shear stiffnesses for a bond zone size $a = 0.8$ and observed similar behavior. The results are omitted for brevity. Comparing these results to those for the case of a structure with equal shear stiffnesses, we observe that the "buckle trapping" phenomenon does not occur when the base plate and the patch posses unequal shear stiffnesses for the case considered. This is in contrast to what was predicted by Carabetta and Bottega [2014], with the transverse shear neglected. We next proceed to the case of structures with clamped-fixed edges under uniform temperature change.

4.2. ***Clamped ends.*** We next consider the situation when the edges of the base-plate are clamped-fixed. That is, when the edges of the structure are clamped with respect to rotation and fixed with respect to both transverse and in-plane translation. The general behavior of the whole structure will be seen to be notably different from that of the structure with hinged-fixed supports described earlier. It was established in [Bottega and Carabetta 2009; Carabetta and Bottega 2014; Carabetta 2011] that a propagating intermediate contact zone is possible for certain bond zone sizes. For the present case, we demonstrate the existence of fully lifted, full contact, intermediate contact and edge contact configurations, with transverse shear effect included. As the structure deflects upward, edge contact may occur as discussed by Karlsson and Bottega [1999] for patched cylindrical panels. It is observed for the present case that, in contrast to what was observed for hinged supports, contact occurs in prebuckling and lift occurs in postbuckling. When intermediate contact occurs, the transversality condition (28) and its caveat (29) are used to determine the location of the contact zone/lift zone boundary under a certain temperature change. In this section, some representative examples will be presented to demonstrate the variety of behaviors. The first example is for the case when the shear stiffnesses of the base plate and the patch are equal.

Case 1: *Equal shear stiffness* ($G_b = G_p$). Results for a structure possessing a bond zone of half-length $a = 0.6$ and a patch half-length $L_p = 0.9$ are presented in Figures 8–11. For a structure with clamped ends, edge contact as well as full contact configurations are possible when the structure deflects upward. Unlike the situation when shear deformation is neglected, it is found presently that, when shear deformation is accounted for, an edge contact configuration may occur when the structure deflects upward. In situations when the patched structure has more than one admissible configuration for a given bond zone size, the one with the lowest total potential energy will be considered as the "preferred" configuration for a particular patch and base structure [Carabetta and Bottega 2012; 2014]. The total energies for three different configurations (full contact, no contact and edge contact) are presented in Figure 8. Based on the results of the junction rotation gradient product, J_a, presented in Figure 9, it is observed that at $\Theta = 2.4$, the full contact configuration is no longer valid as the sign of J_a becomes the same. The structure, thus, has two possible configurations — no contact or edge contact. However, it is seen from Figure 8 that the edge contact configuration has a lower potential energy at this temperature. Thus, we take the edge contact configuration as the "preferred" configuration for the system. As the temperature increases, the total energy of the edge contact configuration exceeds that of the no contact configuration, and the patched structure switches to the no contact configuration at $\Theta = 5.5$, with the patch lifting away from the base plate.

The final load-deflection profile and the total energy of the structure (only stable configurations) are presented in Figures 10 and 11, respectively. It is noticed that the structure first possesses a full contact zone and then, at $\Theta = 2.4$ it "jumps" to edge contact, and then to no contact configuration when $\Theta \geq 5.5$. The simulation results for a bond zone half-length of $a = 0.8$ are summarized in Table 1. At this point, it

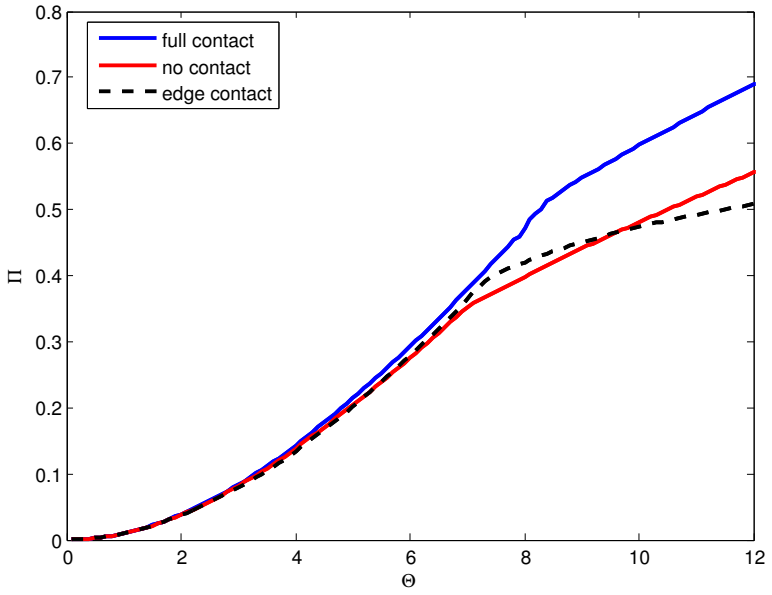

Figure 8. Comparison of total energy (full contact, fully lifted and edge contact) vs. temperature difference for clamped-fixed structure with $G_b = G_p$, $a = 0.6$, $L_p = 0.9$.

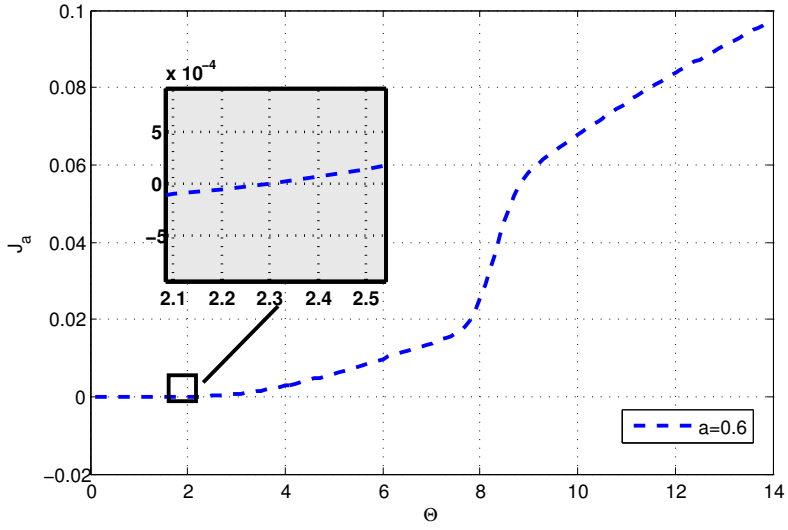

Figure 9. Junction parameter, J_a, as a function of the temperature difference for clamped-fixed structure with $G_b = G_p$, $a = 0.6$, $L_p = 0.9$.

is concluded that, for the case with equal shear stiffness, the patched plate possesses three configurations during the temperature increases: full contact, edge contact and no contact. Intermediate contact does not occur.

Next, let us consider the case when the base plate and the patch have different shear stiffnesses.

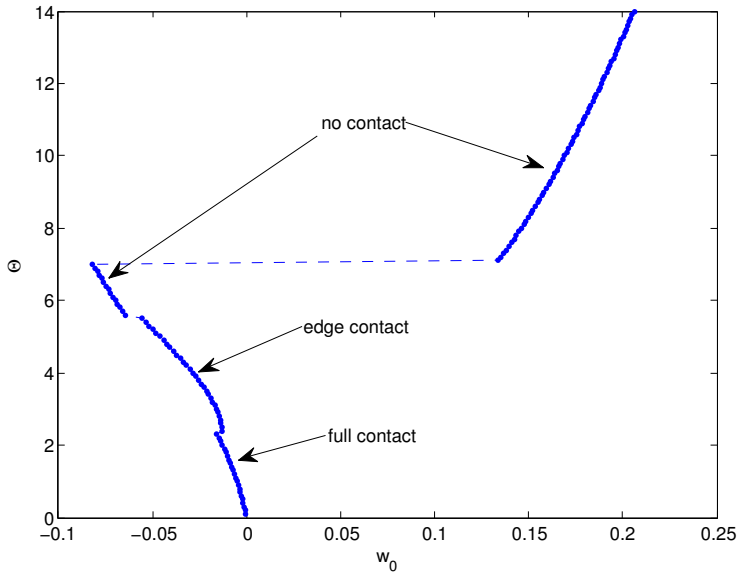

Figure 10. Thermal load-deflection paths for clamped-fixed structure with $G_b = G_p$, $a = 0.6$, $L_p = 0.9$.

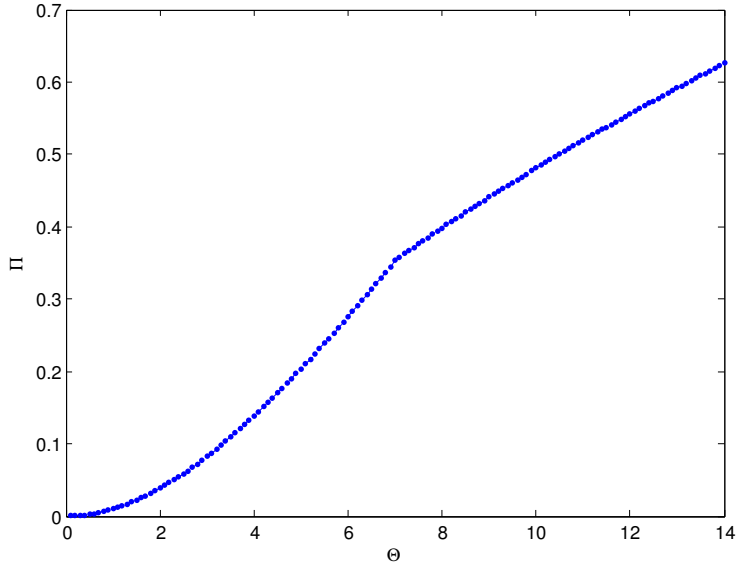

Figure 11. Clamped-fixed structure, $G_b = G_p$, total energy vs. temperature difference; $a = 0.6$, $L_p = 0.9$.

Case 2: *Unequal shear stiffnesses* ($G_b \neq G_p$). In this section, we consider the case when the shear stiffnesses of the patch and of the base plate are unequal. We remark that this is equivalent to the substructures possessing different Poisson's ratios and/or different Young's moduli per the well known relation (40).

	$E_b = E_p$			$\nu_b = \nu_p$		$E_b = E_p$ $\nu_b = \nu_p$
	$\frac{\nu_b}{\nu_p} = \frac{0.3}{0.25}$	$\frac{\nu_b}{\nu_p} = \frac{0.25}{0.3}$	$\frac{\nu_b}{\nu_p} = \frac{0.1}{0.3}$	$\frac{E_b}{E_p} = 0.1$	$\frac{E_b}{E_p} = 10$	$G_b = G_p$
$a = 0.8$	Full $\Downarrow \theta = 4.3$ No	Full $\Downarrow \theta = 4.2$ No	Full $\Downarrow \theta = 4.2$ No	Full $\Downarrow \theta = 3.3$ No	Full $\Downarrow \theta = 2.5$ No	Full $\Downarrow \theta = 4$ No
$a = 0.6$	Full $\Downarrow \theta = 1.8$ Edge $\Downarrow \theta = 5.6$ No	Full $\Downarrow \theta = 2$ Edge $\Downarrow \theta = 5.5$ No	Full $\Downarrow \theta = 2.6$ Edge $\Downarrow \theta = 5.5$ No	Full $\Downarrow \theta = 3.2$ No	Full $\Downarrow \theta = 2.5$ No	Full $\Downarrow \theta = 2.4$ Edge $\Downarrow \theta = 5.5$ No

Table 1. Summary of the simulation results for clamped-fixed edge. "Full" represents "full contact", and likewise for "Edge" and "No".

As discussed in the previous section, the analytical solution for this situation differs substantially from that of the case with equal shear stiffness. It is anticipated some interesting behaviors of the patched structure will be unveiled.

1. *Different Poisson's ratios and equal Young's moduli.* Results for a structure possessing a bond zone size of $a = 0.6$ and a patch half-length $L_p = 0.9$ are presented in Figures 12–15. To identify the existence of the contact zone and edge contact configurations, we combine the results of the junction rotation gradient product, J_a, in Figure 13 with those for the total potential energy of the three configurations presented in Figure 12. In Figure 13, the full contact configuration is no longer valid when the sign of $J_a \equiv J_a \equiv w_1''(a) \cdot w_2''(a)$ changes. Thus, the structure "jumps" to a configuration with edge contact when the temperature achieves the value $\Theta = 1.7$. At this point, the system assumes a configuration with edge contact, which has a lower total potential energy. The structure then switches to a configuration with no contact, when $\Theta = 5.3$. The trend is similar to that for the case of equal shear stiffness, however the critical "jump" temperature changes substantially. The results displayed in Figures 14 and 15 show the "actual" load-deflection paths and the total energy, respectively. It is noticed that the structure initially possesses a full contact zone, but at $\Theta = 1.7$, it "jumps" to a configuration with edge contact, and then to a configuration with no contact when $\Theta = 5.3$. Results are also obtained for the case of a contact zone length of $a = 0.8$ and for different Poisson's ratios of the two layers. Characteristic behavior for this case is summarized in Table 1 along with those for a structure with a bond zone half-length of $a = 0.6$. Based on these results, we see that for different Poisson's ratios, the structure follows a similar trend as for $a = 0.8$. We next consider the effect of Young's modulus on the behavior of the structure.

2. *Different Young's moduli and equal Poisson's ratio.* Different Young's moduli will result in different shear stiffnesses between the patch and the base plate, per (40). However, unlike for Poisson's ratio, Young's modulus will also affect the membrane energy and bending energy of the system.

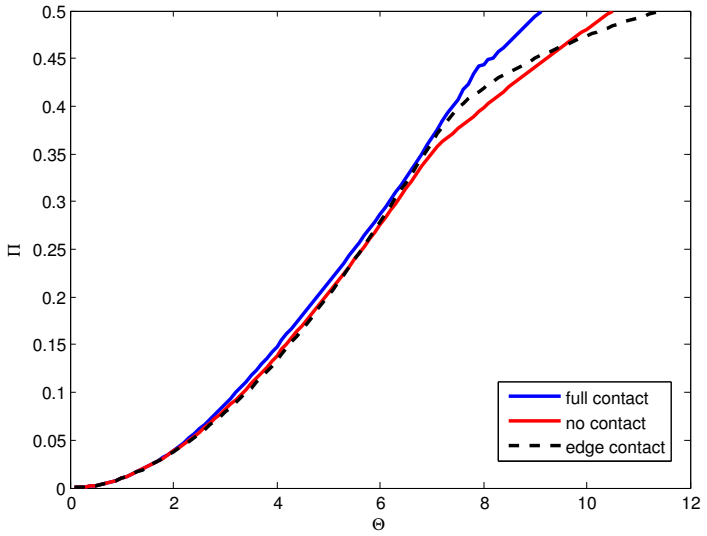

Figure 12. Comparison of total energy (full contact, fully lifted and edge contact) as a function of the temperature difference for clamped-fixed structure with $\nu_b/\nu_p = 0.3/0.2$, $a = 0.6$, $L_p = 0.9$.

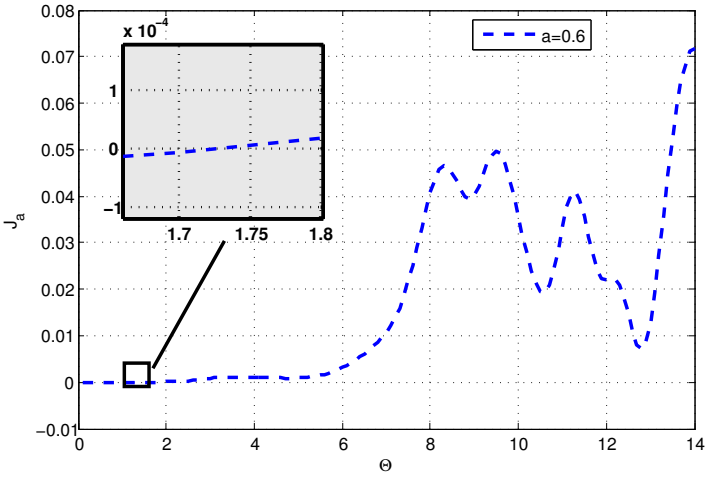

Figure 13. Junction parameter, J_a, as a function of the temperature difference for clamped-fixed structure with $\nu_b/\nu_p = 0.3/0.2$, $a = 0.6$, $L_p = 0.9$.

It is therefore essential to study the behavior of the patched structure when Young's modulus for the patch and that of the base plate differ. Results for the case when the ratio of Young's modulus of the base plate to that of the patch is $E_b/E_p = 0.1$ are displayed in Figures 16–18 for a structure that possesses a bond zone half-length of $a = 0.6$. The transversality condition is then examined to check the existence of an intermediate contact zone and to determine the location of the contact point. It is seen from Figure 16 that when the structure deflects upward, it will initially possess a full contact zone until the critical temperature is reached. At this temperature, the structure buckles downward. We note

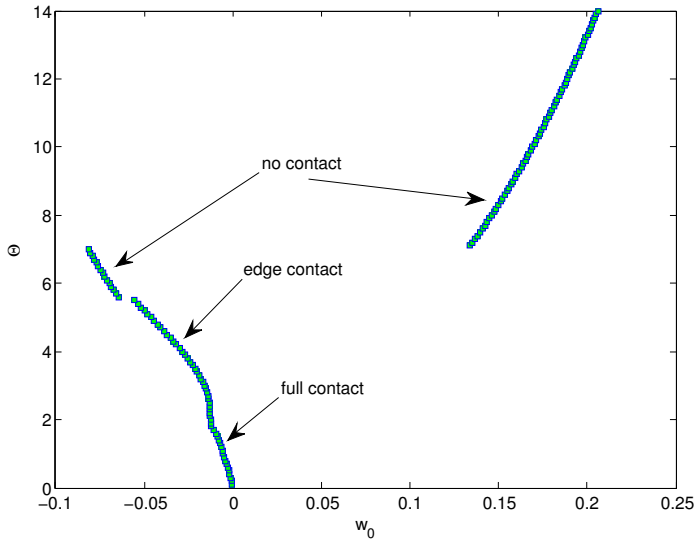

Figure 14. Thermal load-deflection paths for clamped-fixed structure with $\nu_b/\nu_p = 0.3/0.2$, $a = 0.6$, $L_p = 0.9$.

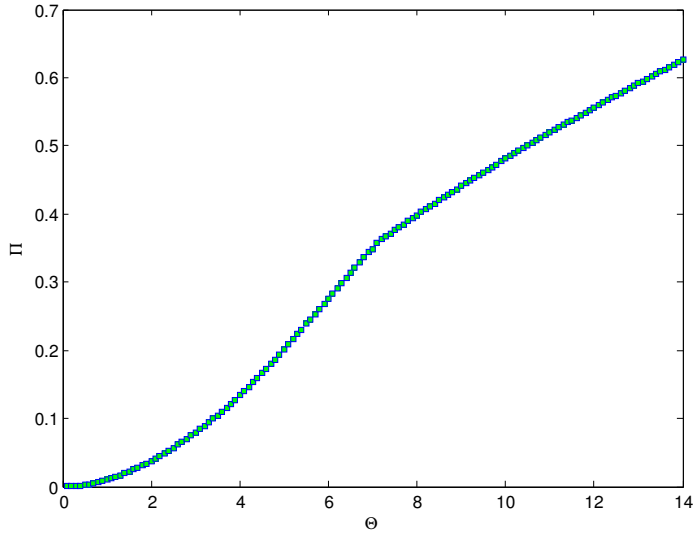

Figure 15. Clamped-fixed structure, $\nu_b/\nu_p = 0.3/0.2$, total energy vs. temperature difference; $a = 0.6$, $L_p = 0.9$.

that, for this range of temperatures, the sign of J_a is negative, which indicates that the structure will not possess a contact zone when it deflects downward. For this case, we also find that there is no edge contact configuration during the temperature increase. Therefore, at the critical temperature, the structure slingshots from a configuration with full contact to a configuration with no contact. The "actual" load-deflection curve and the total energy profile (stable configurations) of the system are shown in Figures 17

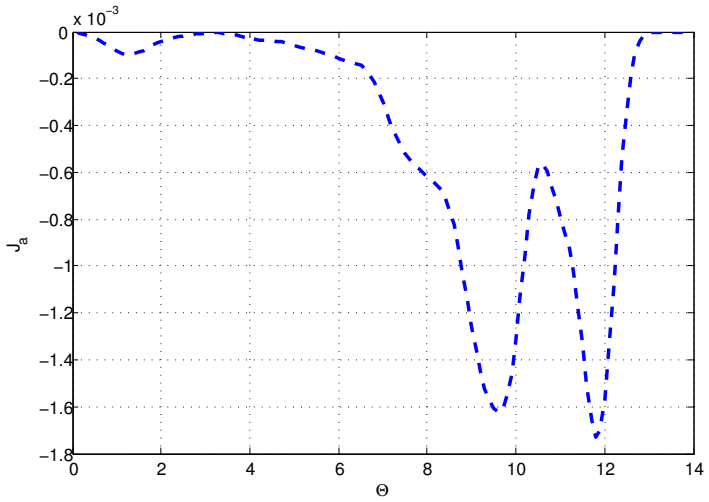

Figure 16. Junction parameter, J_a, as a function of the temperature difference for clamped-fixed structure with $E_b/E_p = 0.1$, $a = 0.6$, $L_p = 0.9$.

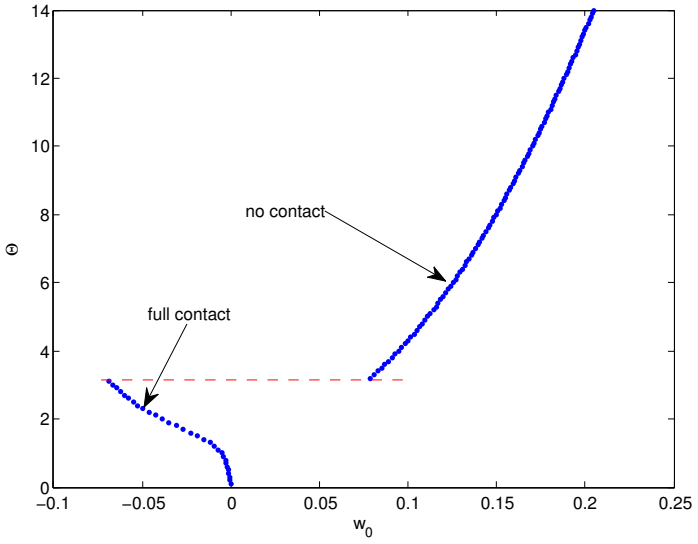

Figure 17. Clamped-fixed structure, $E_b/E_p = 0.1$, center-span displacement vs. temperature difference; $a = 0.6$, $L_p = 0.9$.

and 18, respectively. It is seen that, as the temperature is increased, the structure first possesses a full contact zone and then "jumps" to a no contact configuration at $\Theta = 3.2$.

A summary of characteristic behavior, and its relation to bond zone size, Young's modulus, and Poisson's ratio of the layers is presented in Table 1. The morphological "transition" temperatures, at which the structure will switch from one type of configuration to another type of configuration (e.g., full contact, edge contact, no contact) are shown separately for each case. It is seen that edge contact will not occur, for the larger bond zone size considered, $a = 0.8$. In contrast, it seen that edge contact often occurs for

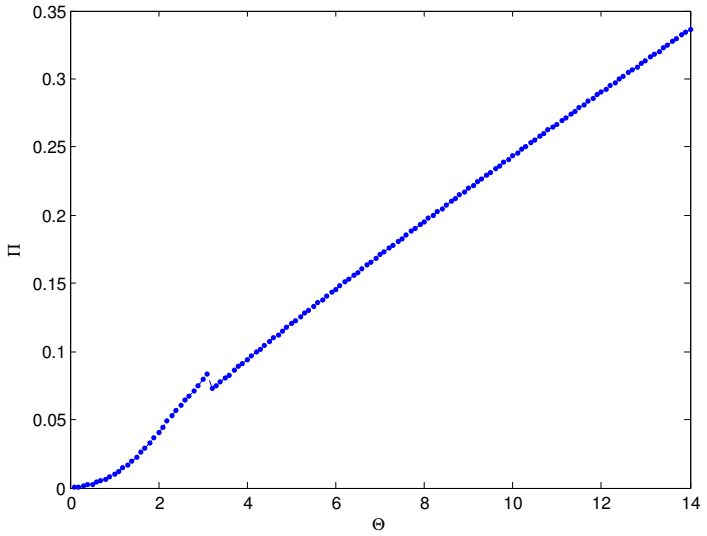

Figure 18. Clamped-fixed structure, $E_b/E_p = 0.1$, total energy vs. temperature difference; $a = 0.6$, $L_p = 0.9$.

the other bond zone size considered, $a = 0.6$, except for the case when the two layers have the same Young's modulus, but different Poisson's ratio. Thus, the morphology of the partially detached patched structure is very sensitive to the material properties of the constituent structures.

5. Conclusions

The current work includes transverse shear deformation and, in this regard, advances on specific prior studies concerning thermal instabilities in patched beam-plates with partial edge detachment. The resulting governing equations, internal and external boundary conditions, transversality condition and stability criterion are derived using a variational formulation. Closed form analytical solutions to the governing equations are determined and simulations based on these solutions are performed. The associated analysis and numerical simulations reveal representative and critical behavior of the partially detached structure under uniform temperature change for both hinged-fixed and clamped-fixed edges. The influence of transverse shear on critical behavior is assessed through examination of these results. For structures with hinged-fixed supports, when the shear moduli of the patch and of the base plate are equal, it is observed that transverse shear deformation has minimal influence for the representative cases considered. It is also seen that the phenomenon of "buckle-trapping" still exists (first revealed in a prior study using a classical model — no transverse shear deformation). However, behavior is altered and "buckle trapping" is not observed to occur when the shear moduli of the substructures are unequal. This is in contrast to prior results predicted using the simpler (no transverse shear) model. One concludes from this that the simpler model for the structure, that which neglects transverse shear deformation, is inadequate in this case. Structures with clamped-fixed supports allow for several possible local configurations of the detached segment of patch and base plate: full contact, no contact and edge contact. Those that are not physically realizable are disqualified, based on local kinematic conditions and the relative magnitudes of

the total potential energies for each case. For these structures, we also consider the situation where the patch and base plate possess the same shear stiffnesses but have different Poisson's ratios and different Young's moduli. Results for structures with clamped-fixed supports are seen to differ significantly from those of previous studies using the simpler (no transverse shear) model. For the cases considered here, propagating intermediate contact zone configurations (predicted by the model without shear deformation) are not observed. However, edge contact configurations not observed with the simpler model, are often seen to occur for structures with relatively small bond zone sizes in the results of the present analysis. To conclude, based on the results of the present study, it is found that transverse shear deformation generally has substantial influence on critical behavior of the structures of interest.

Appendix A. Stiffnesses of composite structure in bond zone

$$A^* = D_b + D_p + (h_b/2)^2 C_b + (h_p/2)^2 C_p, \tag{A.1}$$

$$B^* = (h_p/2)C_p - (h_b/2)C_b, \tag{A.2}$$

$$C^* = C_p + C_b, \quad D^* = A^* - \rho^* B^*, \tag{A.3}$$

$$\rho^* = B^*/C^*, \tag{A.4}$$

$$n^* = C_b\alpha_b + C_p\alpha_p, \tag{A.5}$$

$$\mu^* = \tfrac{1}{2}h_p C_p \alpha_p - \tfrac{1}{2}h_b C_b \alpha_b, \tag{A.6}$$

$$m^* = \mu^* - \rho^* n^*. \tag{A.7}$$

The quantity ρ^* is seen to give the transverse location of the centroid of the composite structure with respect to the reference surface.

Appendix B. Solution parameters

$$\mu_1 = \frac{\hat{b} - \sqrt{R}}{-2\hat{a}}, \quad \beta_1 = \frac{\hat{b} + \sqrt{R}}{-2\hat{a}}, \qquad P_1 = \frac{1 - \frac{D_b}{G_b}\alpha_1^2}{1 - \frac{D_p}{G_p}\alpha_1^2}, \qquad P_2 = \frac{1 - \frac{D_b}{G_b}\beta_1^2}{1 - \frac{D_p}{G_p}\beta_1^2} \text{ (general case)}, \tag{B.1}$$

$$\mu_1 = \sqrt{\frac{G_b}{D_b}}, \quad \beta_1 = \sqrt{\frac{N_0}{D_b\left(2 - \frac{N_0}{G_b}\right)}}, \quad P_1 = -1, \qquad P_2 = 1 \text{ (special case } G_p = G_b), \tag{B.2}$$

$$\hat{b} = -\left(D_b + D_p - N_0\left(\tfrac{D_b}{G_b} + \tfrac{D_p}{G_p}\right)\right), \quad \hat{c} = -N_0, \qquad K_b = \sqrt{N_0/g^*}, \tag{B.3}$$

$$\hat{a} = \frac{D_b D_p}{G_b G_p}(G_b + G_p - N_0), \qquad R = \hat{b}^2 - 4\hat{a}\hat{c}, \quad K_{b3} = \sqrt{N_0/g_3}. \tag{B.4}$$

References

[Aydogdu 2007] M. Aydogdu, "Thermal buckling analysis of cross-ply laminated composite beams with general boundary conditions", *Compos. Sci. Technol.* **67**:6 (2007), 1096–1104.

[Bottega 2006a] W. J. Bottega, *Engineering vibrations*, CRC Press, Boca Raton, FL, 2006.

[Bottega 2006b] W. J. Bottega, "Sling-shot buckling of composite structures under thermo-mechanical loading", *Int. J. Mech. Sci* **48**:5 (2006), 568–578.

[Bottega and Carabetta 2009] W. J. Bottega and P. M. Carabetta, "On the detachment of patched panels under thermomechanical loading", *J. Mech. Mater. Struct.* **4**:7–8 (2009), 1227–1250.

[Carabetta 2011] P. M. Carabetta, *On the interaction of thermal buckling and debonding of patched structures*, Ph.D. thesis, Rutgers University, New Brunswick, 2011, available at http://rucore.libraries.rutgers.edu/rutgers-lib/33593/.

[Carabetta and Bottega 2012] P. M. Carabetta and W. J. Bottega, "On the interaction of thermally induced buckling and debond propagation in patched structures", *J. Appl. Mech.* **79**:6 (2012), 061012.

[Carabetta and Bottega 2014] P. M. Carabetta and W. J. Bottega, "Thermo-mechanical instabilities in patched structures with edge damage", *Int. J. Non-linear Mech.* **58** (2014), 89–98.

[Cowper 1966] G. R. Cowper, "The shear coefficient in Timoshenko's beam theory", *J. Appl. Mech.* **33**:2 (1966), 335–340.

[Hutchinson 1981] J. R. Hutchinson, "Transverse vibrations of beams, exact versus approximate solutions", *ASME J. Appl. Mech.* **48**:4 (1981), 923–928.

[Karlsson and Bottega 1999] A. M. Karlsson and W. J. Bottega, "The presence of edge contact and its influence on the debonding of patched panels", *Int. J. Fract.* **96**:4 (1999), 383–406.

[Karlsson and Bottega 2000a] A. M. Karlsson and W. J. Bottega, "On thermal buckling of patched beam-plates", *Int. J. Solids Struct.* **37**:34 (2000), 4655–4690.

[Karlsson and Bottega 2000b] A. M. Karlsson and W. J. Bottega, "Thermo-mechanical response of patched plates", *AIAA Journal* **38**:6 (2000), 1055–1062.

[Mindlin 1951] R. D. Mindlin, "Influence of rotary inertia and shear on flexural motions of isotropic elastic plates", *ASME J. Appl. Mech.* **18** (1951), 31–38.

[Reddy 1984] J. N. Reddy, "A simple higher-order theory for laminated composite plates", *J. Appl. Mech.* **51**:4 (1984), 745–752.

[Ritchie et al. 1973] R. O. Ritchie, J. F. Knott, and J. R. Rice, "On the relationship between critical tensile stress and fracture toughness in mild steel", *J. Mech. Phys. Solids* **21**:6 (1973), 395–410.

[Rutgerson and Bottega 2002] S. E. Rutgerson and W. J. Bottega, "Thermo-elastic buckling of layered shell segments", *Int. J. Solids Struct.* **39**:19 (2002), 4867–4887.

[Shen 1998] H.-S. Shen, "Thermomechanical post-buckling analysis of imperfect laminated plates using a higher-order shear-deformation theory", *Comput. Struct.* **66**:4 (1998), 395–409.

[Timoshenko 1921] S. P. Timoshenko, "LXVI. On the correction for shear of the differential equation for transverse vibrations of prismatic bars", *The London, Edinburgh, and Dublin Philosophical Magazine and Journal of Science* **41**:245 (1921), 744–746.

[Timoshenko 1925] S. P. Timoshenko, "Analysis of bi-metal thermostats", *J. Opt. Soc. Am,* **11**:3 (1925), 233–255.

[Wahl 1944] A. M. Wahl, "Analysis of Valverde thermostat", *J. Appl. Mech.* **11** (1944), A183–A189.

[Wittrick 1986] W. H. Wittrick, "Analytical, three-dimensional elasticity solutions to some plate problems, and some observations on Mindlin's plate theory", *Int. J. Solids Struct.* **23**:4 (1986), 441–464.

[Wittrick et al. 1953] W. H. Wittrick, D. M. Myers, and W. R. Blunden, "Stability of a bimetallic disk", *Quart. J. Mech. Appl. Math.* **6**:1 (1953), 15–31.

[Zenkour and Sobhy 2010] A. M. Zenkour and M. Sobhy, "Thermal buckling of various types of FGM sandwich plates", *Composite Structures* **93**:1 (2010), 93–102.

Received 16 Jul 2013. Revised 26 Sep 2013. Accepted 27 Oct 2013.

PEINAN GE: pelange@eden.rutgers.edu
Department of Mechanical and Aerospace Engineering, Rutgers University, 98 Brett Road, Piscatway, NJ 08854-8058, United States

WILLIAM J. BOTTEGA: bottega@rci.rutgers.edu
Department of Mechanical and Aerospace Engineering, Rutgers University, Campus at New Brunswick, 98 Brett Road, Piscataway, NJ 08854-8058, United States

SUBMISSION GUIDELINES

ORIGINALITY

Authors may submit manuscripts in PDF format online at the Submissions page. Submission of a manuscript acknowledges that the manuscript is original and has neither previously, nor simultaneously, in whole or in part, been submitted elsewhere. Information regarding the preparation of manuscripts is provided below. Correspondence by email is requested for convenience and speed. For further information, write to contact@msp.org.

LANGUAGE

Manuscripts must be in English. A brief abstract of about 150 words or less must be included. The abstract should be self-contained and not make any reference to the bibliography. Also required are keywords and subject classification for the article, and, for each author, postal address, affiliation (if appropriate), and email address if available. A home-page URL is optional.

FORMAT

Authors can use their preferred manuscript-preparation software, including for example Microsoft Word or any variant of TEX. The journal itself is produced in LATEX, so accepted articles prepared using other software will be converted to LATEX at production time. Authors wishing to prepare their document in LATEX can follow the example file at www.jomms.net (but the use of other class files is acceptable). At submission time only a PDF file is required. After acceptance, authors must submit all source material (see especially Figures below).

REFERENCES

Bibliographical references should be complete, including article titles and page ranges. All references in the bibliography should be cited in the text. The use of BibTEX is preferred but not required. Tags will be converted to the house format (see a current issue for examples); however, for submission you may use the format of your choice. Links will be provided to all literature with known web locations; authors can supply their own links in addition to those provided by the editorial process.

FIGURES

Figures must be of publication quality. After acceptance, you will need to submit the original source files in vector format for all diagrams and graphs in your manuscript: vector EPS or vector PDF files are the most useful. (EPS stands for Encapsulated PostScript.)

Most drawing and graphing packages—Mathematica, Adobe Illustrator, Corel Draw, MATLAB, etc.—allow the user to save files in one of these formats. Make sure that what you're saving is vector graphics and not a bitmap. If you need help, please write to graphics@msp.org with as many details as you can about how your graphics were generated.

Please also include the original data for any plots. This is particularly important if you are unable to save Excel-generated plots in vector format. Saving them as bitmaps is not useful; please send the Excel (.xls) spreadsheets instead. Bundle your figure files into a single archive (using zip, tar, rar or other format of your choice) and upload on the link you been given at acceptance time.

Each figure should be captioned and numbered so that it can float. Small figures occupying no more than three lines of vertical space can be kept in the text ("the curve looks like this:"). It is acceptable to submit a manuscript with all figures at the end, if their placement is specified in the text by means of comments such as "Place Figure 1 here". The same considerations apply to tables.

WHITE SPACE

Forced line breaks or page breaks should not be inserted in the document. There is no point in your trying to optimize line and page breaks in the original manuscript. The manuscript will be reformatted to use the journal's preferred fonts and layout.

PROOFS

Page proofs will be made available to authors (or to the designated corresponding author) at a Web site in PDF format. Failure to acknowledge the receipt of proofs or to return corrections within the requested deadline may cause publication to be postponed.

Journal of Mechanics of Materials and Structures

Volume 8, No. 8-10 October-December 2013

1559-3959(2013)8:8;1-4